Western Graduate&PostdoctoralStudies

Western University
Scholarship@Western

Electronic Thesis and Dissertation Repository

4-8-2021 2:00 PM

Geological, mineralogical and geochemical process controls on Ni tenor variations in the metasedimentary-hosted Thompson 1D orebody at Vale's Thompson mine (T3), Northern Manitoba, Canada

Povilas G. Grigutis, *The University of Western Ontario*

Supervisor: Linnen, Robert, *The University of Western Ontario*
Co-Supervisor: Lightfoot, Peter C., *The University of Western Ontario*
A thesis submitted in partial fulfillment of the requirements for the Master of Science degree in Geology
© Povilas G. Grigutis 2021

Follow this and additional works at: https://ir.lib.uwo.ca/etd

Part of the Geology Commons

Recommended Citation

Grigutis, Povilas G., "Geological, mineralogical and geochemical process controls on Ni tenor variations in the metasedimentary-hosted Thompson 1D orebody at Vale's Thompson mine (T3), Northern Manitoba, Canada" (2021). *Electronic Thesis and Dissertation Repository*. 7727.
https://ir.lib.uwo.ca/etd/7727

This Dissertation/Thesis is brought to you for free and open access by Scholarship@Western. It has been accepted for inclusion in Electronic Thesis and Dissertation Repository by an authorized administrator of Scholarship@Western. For more information, please contact wlswadmin@uwo.ca.

Abstract

The Proterozoic Thompson Nickel Belt (TNB) contains rift-related mafic-ultramafic igneous rocks, in a collisional belt at the NW margin of the Archean Superior province in Northern Manitoba, Canada. The TNB hosts world class Ni-Cu-(PGE) mineralization, that has undergone polyphase deformation (D_1 – D_4) and upper amphibolite to lower granulite facies metamorphism, up to ~750ºC and 7.5 kbars (Lightfoot et al., 2017). Komatiitic magmas (1880 ± 5 Ma; Hulbert et al., 2005) fertile in Ni & PGE elements intruded Ospwagan Group metasedimentary sequences and through sulfur assimilation and segregation produced primary magmatic sulfides (Lesher and Burnham, 2001).

The TNB metasedimentary-hosted ores of the Thompson Deposit (T1 and T3) are interpreted to have formed from the complete remobilization and relocation of sulfides from primary ultramafic boudins (Bleeker, 1990). The aim of this study was to assess geological, mineralogical and geochemical controls on the Ni tenor of sulfide (% Ni normalized to 100% sulfide), and to understand why Ni tenor in the metasedimentary-hosted Thompson deposits is higher than those of primary ultramafic associated mineralization, like the Pipe and Birchtree Deposits. The research focused on the Thompson 1D orebody at T3 mine because of the large variability of nickel tenor, ranging from <200ppm Ni in barren sulfide to very high (8-16 wt% Ni).

The two most significant findings of this study are that; Ni-Co-Pd tenors are highest in shear-hosted massive sulfides and that there is a positive correlation between pyrite modal abundance and Ni-Co tenor. Pyrite is interpreted to be paragenetically-late, which strongly indicates a metamorphic modification of the ores. Understanding the processes responsible for pyrite generation is crucial to deconvoluting the cause of the Ni tenor variability across the Thompson 1D deposit.

This study is the first to document the occurrence of polymetallic sulfide melt inclusions at Thompson, which indicates that partial melting of sulfide ores occurred during peak metamorphic conditions and modified the ores at Thompson.

A staged mechanism for the formation of Thompson sulfide deposits is proposed, in which three principle stages exist: komatiitic emplacement and a primary magmatic origin for the sulfides; high P-T MSS reformation and repositioning of primary ultramafic sulfide, and partial melts, into sedimentary country rocks; and modification by hydrothermal fluids, contemporaneous localized partial melting, and shear-melting, which further modified the remobilized ores.

Research in this study has helped move the ore genesis models for Thompson forward and although nickel tenor upgrading of ores is not entirely explained, it seems to be related to pyrite and the late tectonic-metamorphic history of the deposit.

Keywords

Thompson Nickel Belt, sulfide, metasedimentary, komatiite, nickel, tenor, post-ore modification, pyrite, sulfide melt inclusions, partial melting

Summary for Lay Audience

The Thompson Nickel Belt is a collisional craton margin located along the northwestern edge of the Superior Igneous Province (Canadian Shield). This region underwent a classic rift-drift-collision sequence (Wilson Cycle) providing an optimal location for ultramafic komatiitic magmas to be emplaced into sulfide-bearing, sedimentary rocks (Ospwagan Group). This resulted in the production of primary magmatic sulfides which are host to world-class nickel mineralization. The rocks underwent high pressure-temperature (7.5 kbars and ~750ºC) metamorphism and deformation. The magmatic sulfides were remobilized from primary ultramafic intrusions into the neighbouring meta-sedimentary rocks, forming the Thompson deposits. The purpose of this study was to determine geological, mineralogical and geochemical factors that might be responsible for the higher nickel grades (tenor) in the remobilized, metasedimentary-hosted Thompson deposit compared to those of the primary ultramafic-associated deposits. Research focused on the 1D sulfide deposit at Thompson mine (T3), where nickel tenors are highly variable, ranging from <200 ppm Ni to very high (8-16 wt% Ni). The two most significant findings of this study are that nickel grades seem to be highest in shear-hosted massive sulfides and a positive correlation between pyrite modal abundance and nickel grade exists. The mineral pyrite is interpreted to be paragenetically-late, which strongly indicates a metamorphic modification of the ores, and possible link to explaining the highly variable sulfide grades. Additionally, this study is the first to document the occurrence of sulfide melt inclusions at Thompson, which indicate that partial melting of sulfide ores occurred during peak metamorphic conditions. A three-part, model is proposed to explain the formation of the remobilized Thompson metasedimentary-hosted sulfide deposits: a primary magmatic origin for magmatic sulfides; high pressure-temperature metamorphism, transport and partial melting of these primary sulfides; and, ensuing post-ore modifications of sulfides by contemporaneous hydrothermal fluids and localized shear-melting.

Acknowledgements

I am indebted to my supervisors, Dr. R. Linnen and Dr. P.C. Lightfoot for their time, patience and constructive criticism during the preparation of this project. Their valuable ideas contributed greatly to the research and writing of this thesis, and I could not have done it without them. Thank you for coaching me both academically and outside the research lab. I would like to thank; Marc Beauchamp for the countless hours in sample preparation and EMPA data collection, as well as Dr. Micha Pazner for giving me that first opportunity.

Funding for this project over the last several years was provided by Vale and an NSERC Discovery grant to Dr.R.Linnen. Additional financial support was provided through Western University Graduate Teaching Assistantships and Earth Sciences scholarships.

I am grateful to the Vale geological staff in the Manitoba Division for their effort in training me for underground field work, sample collection and overall contributions during my time in Thompson and afterwards: Rob Stewart, Stephen Kirby-McDougall, Dave Duarte, Angela Kennedy, Sam Davies, Raymond Kitchen, Luke Maddigan, Robert Southern, Dennis Hanson, Dallas Dixon, Ethan Amyotte, Kathryn Windeler, Shannon Huebert.

Lastly, I would like to thank my family for their ongoing support during both my undergraduate and graduate studies. Also, to the Western Earth Sciences community and close friends for the rewarding memories, experiences and those days in need of extra motivation to push through. Thank you everyone.

Table of Contents

List of Abbreviations

TNB: Thompson Nickel Belt

THO: Trans Hudson Orogen

CSBZ: Churchill-Superior Boundary Zone

Ni-Cu-PGE: Nickel, copper, platinum-group elements

PGM: platinum group metals

Inco: The International Nickel Company

MSS: monosulfide solid solution

ISS: intermediate solid solution

FW/HW: footwall/ hanging wall

FW Deep: footwall deep zone

1D Orebody: Thompson mine orebody (focus of study)

602: the 1D Lower, between mine levels 3700 to 4160

P_2 Pipe Formation schist: the primary host unit to sulfide mineralization at Thompson

P-T: pressure-temperature

LOR: limit of reporting

ICP-AES: Inductively coupled plasma atomic emission spectroscopy

EPMA: electron probe microanalysis

EDS/WDS: energy dispersive spectrometry/ wavelength dispersive spectrometry

B-SEM: benchtop scanning electron microscope

BSE/SEI: backscatter electron/secondary electron images

Po-Py-Pn-Ccp-Gdf: pyrrhotite-pyrite-pentlandite-chalcopyrite-gersdorffite

SMI: sulfide melt inclusions

PMSA: primary magmatic sulfide assemblage

SCH: schist

PSCH: pegmatite schist

SUMX: sulfide-matrix ore

MSCH: mineralized schist

MASV: massive sulfide ore

SM: semi-massive sulfide ore

NT: net-textured ore

MIF: mineralized iron-formation

MSCHR: mineralized shear

DISS: disseminated

PEG: pegmatite

List of Appendices *(all digital)*

List of Figures

List of Tables

Chapter 1: Introduction

1.1 Overview

The Thompson Nickel Belt (TNB) is a narrow, collisional terrain in Northern Manitoba that hosts remnants of Archean Superior Province rocks, autochthonous Proterozoic sedimentary sequences (Ospwagan Group) and allochthonous Proterozoic rocks of the deformed Trans Hudson Orogen (Layton-Matthews et al., 2007). The TNB hosts several world-class Ni-Co-Cu-PGE sulfide deposits that make up one of four principal nickel camps in Canada and the fifth largest known nickel camp in the world based on contained nickel (Lightfoot et al., 2017).

The International Nickel Company (Inco) began exploration of the TNB in 1946 with geological and geophysical programs accompanied by diamond drilling, which led to the discovery of the Moak deposit in 1952, the Thompson deposit in 1956, the Pipe deposits in 1957 and the Birchtree deposit in 1962 (Fraser, 1985). Initial mine construction at the world-class Thompson deposit began in 1959, with production starting in 1961 (Fraser, 1985). The Thompson mine is located 740 kilometers north of Winnipeg and has a past production of 2500 kilotons of nickel produced to date (Lightfoot et al., 2017), which is approximately double the historic resource of Kambalda (1200 kt Ni; Hoatson et al., 2006; Mudd, 2010).

According to mineral reserve estimates provided by Golder Associates Ltd. (Golder) in 2010 with requirements conforming to the Securities Exchange Commission's Industry Guide 7 and to Canadian National Instrument (NI) 43-101, Thompson mine has proven and probable reserves of 19.5 million tonnes grading at 1.73% Ni and 0.11% Cu (Golder Associates Ltd., 2010) with unreported resources by Vale (Lightfoot and Evans-Lamswood, 2015).

The majority of sulfide deposits in the TNB formed from the intrusion of komatiitic magmas into the metasedimentary sequences of the Ospwagan Group, which was ensued by assimilation of S-rich sedimentary rocks, sulfide saturation, segregation and concentration of Ni sulfide deposits (Lightfoot et al., 2017). The metasedimentary-hosted sulfides of the Thompson mine are interpreted to have formed from the complete remobilization and relocation of these sulfides from primary ultramafic intrusions (Bleeker, 1990). The sulfide ore bodies subsequently experienced multiple phases of deformation (D_1 to D_4), and their distributions are largely controlled by doubly-plunging F_3 structures that have relocalized the sulfide bodies within open-space dilation zones in fold hinges and limbs, along the eastern flank of the Thompson Dome structure (Lightfoot et al., 2017).

1.2 Previous Work

It has long been debated whether primary magmatic or secondary post-magmatic processes govern high-Ni tenor (i.e., Ni abundance recalculated into 100% sulfide) mineralization within the deformed Thompson deposit. Previous academic and government-directed studies have focused on understanding the genesis and classification of ultramafic bodies of the TNB and their roles in sulfide generation (Lesher and Keays, 2002; Layton-Matthews et al., 2007; Lightfoot and Evans-

Lamswood, 2015; Franchuk et al., 2016). Sulfide and silicate textures in nickel sulfide deposits have been well documented (Burnham et al., 2009; Barnes et al., 2018). Similarly, the geological, structural and tectono-metamorphic history of the TNB is well understood (Peredery, 1982; Bleeker, 1990; Monteiro and Krstic, 2006; Burnham et al., 2009; Machado et al., 2011; Lightfoot et al., 2017). An excellent stratigraphic context of all lithologies, and implementation in exploration by Thompson geologists, has aided in the discovery of new sulfide deposits within the TNB (Bleeker, 1990; Bleeker and Macek, 1996). Furthermore, numerous studies have focused on the geochemistry of the sulfide and silicate host rocks and their roles in sulfide mineralization (Bleeker, 1990; Burnham et al. 2009; Lightfoot et al., 2017). However, little is known about the processes that generate the variation in sulfide chemistry between and within the different ore bodies.

1.3 Purpose and Scope of Study

The aim is to assess the Ni tenor variations between different ore types in the Thompson 1D and to understand why Ni tenor of metasedimentary-hosted sulfide ores is higher than the primary ultramafic associated mineralization. This will be accomplished by taking into consideration the deposit geology, complex mineralogy and variable mineral chemistry in order to determine the effects of remobilization of ores during upper amphibolite to lower granulite facies metamorphism and polyphase deformation (D_1 to D_4). The aim is also to understand post-ore modification processes and their effect on tenor variability across the Thompson 1D orebody. Lastly, to determine which process controls are important as exploration vectors towards high Ni tenor sulfide mineralization within the TNB and other nickel-sulfide camps globally.

At the Thompson Deposits, metasedimentary-hosted sulfides generally have higher Ni tenors (8 to 16 wt% Ni) than most, but not all, primary ultramafic associated mineralization (4-8 wt%), like the Pipe and Birchtree deposits (House, 2009). The exception being the Ni-PGE-rich ultramafic-associated mineralization at South Manasan, which has a much higher range in nickel tenor (10 to 39 wt% Ni; Franchuk et al., 2016) relative to the Thompson Deposits. The metasediment-hosted sulfides have some of the highest nickel tenors in the TNB, therefore understanding the processes that control Ni tenor are important for future discoveries of high-tenor mineralization.

The Thompson deposit is predominantly broken up into the T1 and T3 deposits, with underground shafts at both. The focus of this study was on the highly deformed and metamorphosed 1D orebody (Upper and Lower) at T3. As alluded to, the 1D orebody was selected as the target sulfide body for this research study due to the intense deformation history, textural complexity and Ni tenor variability, as well as the access available to drill core and mine workings. The Ni tenor of the Thompson 1D is highly variable (<200 ppm Ni to >16 wt% Ni) and the majority of sulfides are hosted by meta-sedimentary rather than ultramafic rocks (Lightfoot et al., 2017). Underground access to the 1D was available during the summer of 2017, where a detailed mapping and sampling program was completed.

Spatial relationships in the Thompson 1D orebody were documented through underground mapping. Underground mineralization styles were established and their relationships to nickel tenor were investigated. Sulfides from 26 different stopes with Ni tenors that varied from barren through low to very high were sampled, along with the host meta-sedimentary rocks located proximal to mineralization. A series of samples from four drill holes that cut through multiple lenses of sulfide mineralization in the Lower 1D orebody, along with two regional drill holes, were investigated. Detailed petrographic analysis on all underground grab and drill hole (DH#1365050) samples has identified five main sulfide mineralization styles and a complex suite of metamorphic and deformation textures.

Textural analyses of mineralization styles were completed to establish if a correlation exists between ore type and nickel tenor, with shear-hosted sulfides showing the highest Ni-Co-Pd tenors across the deposit. The relationship between pyrite abundance and elevated Ni tenor indicates a strong role for metamorphic modification of ores and understanding the genesis of pyrite has been key to determining processes responsible for the great variability in Ni tenor across the deposit. Furthermore, the present study is the first to evidently document sulfide melt inclusions within metamorphic silicate assemblages at Thompson, which supports that a sulfide melt formed from localized partial melting of pre-existing ore during metamorphism.

Lithogeochemical data was acquired on representative mineralized sulfide and unmineralized country-rock samples, to establish baseline elemental abundances on different sulfide and silicate assemblages. Point analyses and trace element mapping of sulfide minerals was undertaken to establish if minerals from different areas of the Thompson 1D orebody varied in composition. Trace element compositions and their distributions in biotite and garnet grains were also studied to determine if a halo exists in the pelitic schists surrounding sulfide mineralization. Elevated Ni and Cr concentrations in mica grains throughout meta-sedimentary country rocks proximal to sulfide mineralization has been documented.

Geological, mineralogical and geochemical process controls on relocation and tenor variability of metasedimentary-hosted ores are presented, and several genetic models for the genesis and modification of Thompson ores are discussed; a primary magmatic model, high P-T ductile emplacement of sulfides via *sulfide kinesis*, ingress of oxidizing fluids, retrograde metamorphic fluids and evidence for localized partial melting of ores. A ‘staged mechanism’ model based primarily on three key principles is proposed for the formation and modification of the Thompson deposits.

Chapter 2: Thompson Nickel Belt

2.1 Regional Geology

The Thompson Nickel Belt is located at the NW margin of the Superior Craton and is part of an assemblage of rocks including basaltic and intrusive mafic-ultramafic magmas emplaced at the northern margin of the Superior craton at circa 1.85 Ga **(Figure 2-1)** (Lightfoot, 2016). This assemblage of rocks is associated with the camp-scale ore deposits at Thompson and Raglan (Lightfoot, 2016).

The formation of the belt is a direct response to the long-lived tectonic processes controlling the disamalgamation and amalgamation of supercontinents (Lightfoot, 2016). The break-up of Neoarchean supercontinents between 2.2 and 2.1 Ga (Machado et al., 2011) led to continuous rifting at the craton margins that produced extensive ocean basins, which later re-assembled as oceanic lithosphere was subducted (Machado et al., 2011). Subduction was accompanied-by and succeeded-by island arc magmatism, the development of continental arc magmatism and then continent-continent collisions between 1.85 and 1.80 Ga (Lucas et al., 1996; Ansdell, 2005; Corrigan et al., 2005). This rift-drift-collision sequence between 2.1 – 1.8 Ga is a textbook Wilson Cycle process that produced the Paleoproterozoic Trans Hudson Orogen (THO) (Machado et al., 2011). The THO is made up of accreted intra-oceanic terranes and stretches for ~4,600 km from South Dakota to Baffin Island (Machado et al., 2011). The TNB formed during the collision of the THO with the Canadian Shield between ~1.9 - 1.7 Ga (Machado et al., 2011; Lightfoot et al., 2017).

The Proterozoic Thompson Nickel Belt (TNB) is the NW rifted collisional craton margin of the Archean Superior Province in Northern Manitoba, Canada (Bleeker, 1990). A NNE-trending structure that occupies the Churchill-Superior Boundary Zone (CSBZ) **(Figure 2-1)**, which separates 3.1 – 2.6 Ga autochthonous Archean Superior Province gneisses in the east from 1.92 – 1.83 Ga allochthonous Proterozoic domain of the Trans Hudson Orogen (THO) in the west (Burnham et al., 2009). The Thompson belt is fault-bounded to both the northwest and southeast. In the northwest, the belt is in fault contact with the migmatitic gneisses of the Kisseynew Domain (Churchill Province) (Peredery, 1982). The gneisses are deformed and metamorphosed to upper amphibolite and lower granulite facies (Elphick, 1972; McRitchie, 1995) and are overprinted by the northeasterly trending Trans-Hudsonian collisional fabric (Peredery, 1982). In the southeast, the belt has a fault contact with the Pikwitonei Domain (Superior Province), which consists of felsic and mafic granulite gneisses that were intruded by numerous mafic-ultramafic dykes (Peredery, 1982). The Pikwitonei gneisses are overprinted by a weak northeast-trending Trans-Hudsonian fabric (Hubregtse, 1980). The TNB is underlain by the Archean Thompson Belt gneisses, which are tectonically complex and extensively migmatized (Peredery, 1982). The gneisses contain metavolcanic and metasedimentary units, and are cut by mafic, ultramafic and felsic dykes (Peredery, 1982). The TNB gneisses are the basement rocks on which the rest of the Ospwagan Group was deposited.

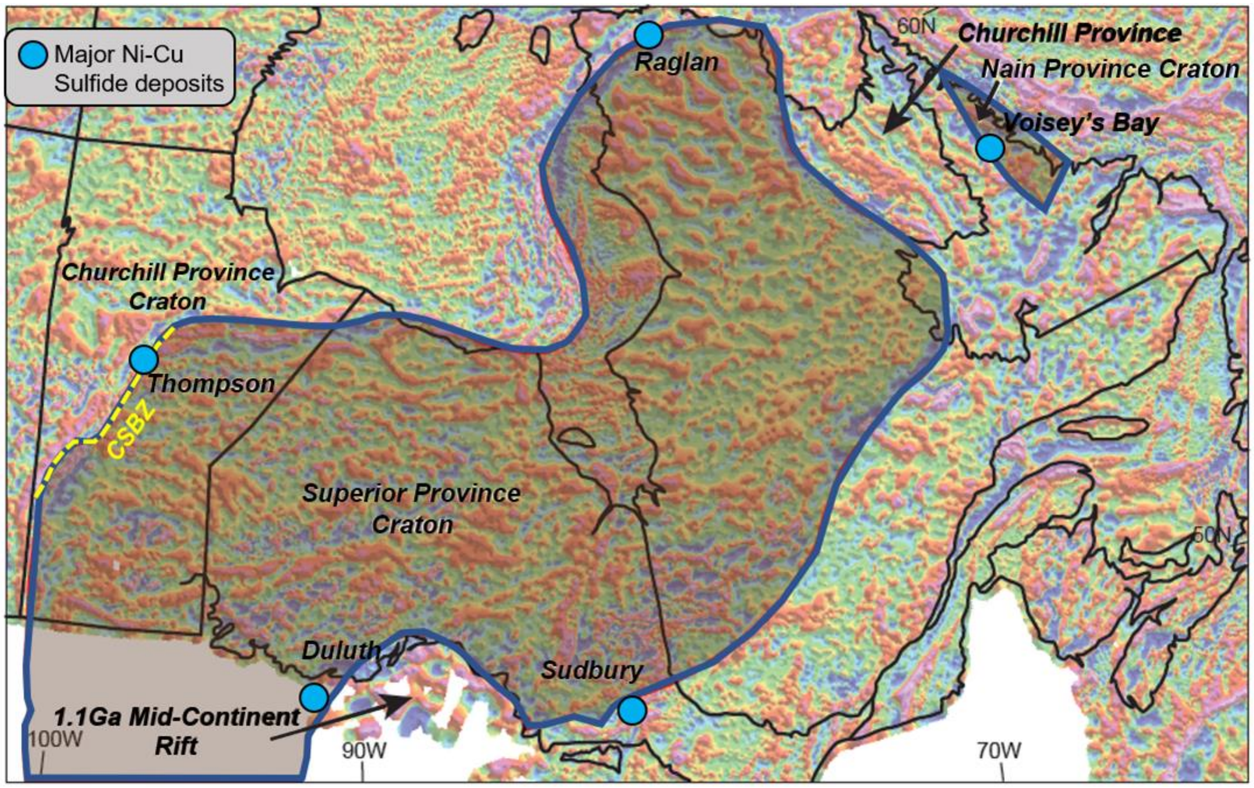

Figure 2-1: Boundary of the Superior Province, Churchill Province and Nain Province cratons superimposed on a 1VD gravity map. Note, the occurrence of the Thompson deposit along the Churchill-Superior Boundary Zone (CSBZ) (yellow dashed line). Camp-scale Ni-Cu sulfide deposits (Thompson, Duluth, Raglan, Voisey's Bay, Sudbury) occur along the margins of large igneous provinces. (Modified from Lightfoot, 2016; Fig 2.1, pg. 71).

The strongly deformed and metamorphosed TNB is 10-35 km wide and approximately 400km long **(Figure 2-2A),** consists of Archean basement gneisses, Early Proterozoic Ospwagan Group metasedimentary rocks, mafic-ultramafic intrusive and volcanic rocks **(Figure 2-2A)** (McRitchie, 1995). Tectonism subjected the TNB rocks to polyphase deformation and upper amphibolite to lower granulite grade metamorphism, reaching peak P-T conditions of ~750ºC and 7.5 kbars (Lightfoot et al., 2017). The TNB is structurally interpreted as F_1 Nappes that were refolded by large-scale F_3 fold structures during D_3 deformation. F_3 structures are steeply dipping, dome and basin-type complexes (Macek et al., 2006). The tectono-metamorphic evolution of the TNB simultaneously developed large-scale shear structures that are interpreted to have controlled the emplacement of sulfide lenses and granitoid pegmatites (Machado et al., 2011).

The generation of felsic magmatism coincided with the closing of the Manikewan Ocean in the final stages of continent-continent collision that formed the Trans-Hudson Orogen (Machado et al., 2011). Multiple ages for felsic magmatism have been recorded in the TNB stratigraphy. A diverse suite of granitoid rocks were emplaced as plutons, sills and pegmatite dykes in Archean gneisses of the TNB, with known U-Pb zircon ages that vary from 1885 ± 5 Ma (Clark Lake pluton; Percival et al., 2004) to 1726 ± 12 Ma (Sasagiu rapids pegmatite; Machado et al., 1990). Furthermore, granitic intrusions intrude Grass River Group metasediments and vary in age from 1891 ± 5 Ma (Percival et al., 2004) to 1863 ± 6 Ma (Zwanzig et al., 2003), as well as pegmatite dykes, with the youngest being dated at 1788 ± 2 Ma (Machado et al., 2011). Additional ages determined by U/Pb zircon dating place pegmatite pods throughout the TNB at 1820 ± 5 (Machado et al., 1987); pegmatites at 1786 – 1768 Ma (Machado et al., 1987); and several pegmatites from Thompson mine at 1770 ± 2 Ma, 1766 ± 2 Ma, 1772 ± 3 Ma (Machado et al., 2011). Using zircon U-Pb dates, Machado et al. (2011) proposed that there were three major stages of pegmatite development in the TNB:

Stage 1 comprises the oldest granitoid intrusions, which are associated with felsic magmatism that was coeval with the Molson dyke swarm; 1891 – 1871 Ma. In Stage 2, a younger period of felsic magmatism was generated during the final stages of continent-continent collisions along the Superior craton, during local shear development and high-grade metamorphism just prior to peak D_2 deformation (1850 – 1785 Ma).

Stage 3 consisted of the final pulse of pegmatitic emplacement, which post-dates peak metamorphism and is associated with prolonged crustal thickening and melting 50 million years after terminal collision at 1780 – 1750 Ma.

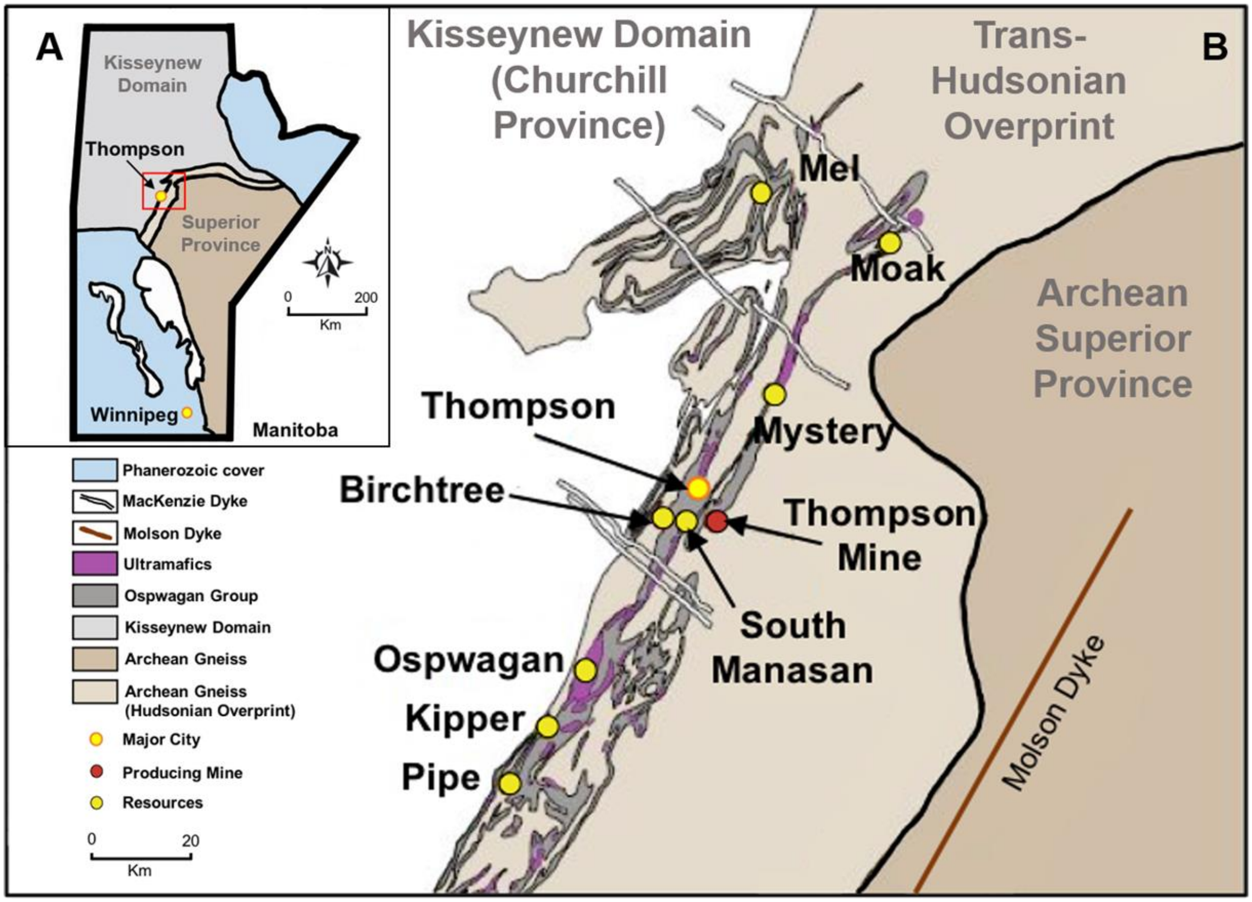

Figure 2-2: A) Location of the Thompson Nickel Belt in Northern Manitoba – located in between the southeastern portion of the Paleoproterozoic Kisseynew Domain (Churchill Province) and the northwestern edge of the Archean Superior Province. The 'red box' is depicted in 'B' B) Regional geology of the belt showing the locations of the city of Thompson, and the various mines and deposits within the northern section of the belt. (Modified from Lightfoot et al., 2017).

2.2 Early Proterozoic Ospwagan Group

The Ospwagan Group sediments, specifically the Pipe Formation members, are the primary host rocks for Ni sulfide mineralization within the TNB. The Ospwagan

Group is interpreted as having been deposited as passive margin sediments on a continental margin near the Superior plate boundary zone (Scoates et al., 1977). Active rifting of the continental platform gave rise to komatiitic magmas that intruded the S-rich sediments, causing sulfur saturation and sulfide melt generation (Lesher et al., 2001). A portion of these primary sulfides were remobilized and relocated into the host Ospwagan Group sediments (Bleeker, 1990), during high P-T repositioning of ductile, primary ultramafic sulfides during D_1 – D_2 (**Sections 8.4.2** and **8.6**) (Monteiro and Krstic, 2006; Lightfoot et al., 2017). The continental passive margin was heavily deformed into what was known as the Trans-Hudson orogen (THO), which later collided with the Canadian Shield between 1.8 - 1.7 Ga to form the TNB (Lightfoot et al., 2017).

Detrital zircon ages from Ospwagan sedimentary rocks indicate that deposition took place after 2.23 Ga (Machado et al., 2011), and possibly up to 1.97 Ga (Bleeker and Hamilton, 2001). The Ospwagan Group sedimentary rocks which are now strongly metamorphosed, rest unconformably on deformed and variably migmatized Archean TNB basement gneisses, which are derived from Pikwitonei granulite protoliths of the Superior Province (Bleeker, 1990), with protolith ages between 3.2 – 3.0 and 2.8 – 2.6 Ga (Machado et al., 1990).

2.2.1 Lithostratigraphy of the TNB

Bleeker (1990) divided The Early Proterozoic Ospwagan Group into four distinct metasedimentary formations, and an additional overlying mafic volcanic unit called the

Bah Lake assemblage (Zwanzig and Böhm, 2002). According to Bleeker (1990) the Ospwagan Group lithostratigraphy is as follows:

The basal unit, known as the Manasan Formation was unconformably deposited on top of Archean basement rocks. The lower M_1 member consists of layered impure quartzites and arkosic arenites, with a small pebble conglomerate layer directly on the contact with Archean gneiss. The overlying M_2 member consists of a quartz-feldspar-muscovite-biotite schist. Bleeker (1990) interpreted this unit to represent transgression in response to passive margin subsidence.

Overlying the Manasan Formation are the calcareous sediments of the Thompson Formation. This is a mixture of marble, chert, skarn and dolomitic carbonate with minor interlayered semi-pelitic schists. The Thompson unit represents the establishment of a stable platform (Bleeker, 1990).

The Pipe Formation overlies the Thompson Formation. The P_1 member consists of silicate + sulfide facies iron formations, laminated graphitic pelitic schists, chert lenses and pyrrhotite laminations (up to 30cm thick) (Bleeker, 1990). The P_2 member overlies the P_1 and consists of pelitic schists, commonly with porphyroblasts of garnet, staurolite and sillimanite (Layton-Matthewss et al., 2007). Thin beds of chert and calc-silicate layers are also common. The P_2 member of the Pipe Formation is the primary host unit for economic sulfide mineralization at Thompson mine (Bleeker, 1990; Lightfoot et al., 2017). The P_3 member consists of pelitic schists with calc-silicate intercalations, well-banded silicate facies iron formations, a dolomite marble unit, and chert lenses. Bleeker (1990) interprets that the Pipe Formation represented periods of prolonged chemical sedimentation and non-deposition alternating with periods of turbiditic sedimentation. Additionally, the P_1 and P_3 members are comprised of hybrid ferruginous rocks formed from the intermixing of siliclastic pelitic sediments and iron-rich precipitates, with the former being host to the Pipe and Birchtree deposits (Lightfoot et al., 2017). The P_2 member is dominantly a mica- and graphite-rich schist derived from deep water graphitic shales and is host to nickel sulfide mineralization that make up the Thompson deposits (Lightfoot et al., 2017).

The Setting Formation overlies the Pipe formation and consists of clastic sediments; thick interlayered quartzites, pelitic schists, lithic greywackes and mudstones (Bleeker, 1990; Lightfoot et al., 2017). These clastic fore-deep sediments are largely associated with felsic volcanics and are overlain by the Bah Lake Formation, which is the main sequence of mafic to ultramafic volcanic rocks at Thompson. The Bah Lake unit consists of basaltic volcanic flows - commonly associated with pillow basalts, and ultramafic sills (Bleeker, 1990; Lightfoot et al., 2017).

2.3 Structural and Metamorphic History of the Belt

A primary magmatic sulfide assemblage (Stage 1; D_0) would have existed ~1880 Ma (Hulbert et al., 2005) and defined by sulfide ores associated with ultramafic bodies. A general consensus is that the primary magmatic sulfides were remobilized into the surrounding metasedimentary rocks during high P-T prograde (Stage 2; D_1-D_2) and retrograde (Stage 3; D_3-D_4) metamorphism and deformation (**Figure 2-3**). Studies of the tectono-metamorphic evolution of the TNB help to constrain an understanding of how the sulfide mineralization has been remobilized to its present location within the

Ospwagan metasedimentary rocks. Four major deformation events (D_1 to D_4) of the TNB have been interpreted by Bleeker (1990):

D_1 is interpreted to be a result of a major regional compressional event that produced recumbent F_1 isoclinal folds and nappe structures during prograde metamorphism **(Figure 2-3).** The Thompson deposits occur on an overturned limb of an F_1 Nappe structure (Bleeker, 1990). Nappe emplacement is interpreted to have occurred prior to emplacement of the Molson dykes, which are dated by U-Pb zircon/baddeleyite ages to be at 1883 ± 2 Ma (Heaman et al., 1986, 2009). Machado et al. (2011) places the emplacement of the NNE trending Molson dyke event between 1900-1877 Ma. The Molson dykes cross cut F_1 folds, therefore D_1 deformation ceased prior to the emplacement of the Molson dyke swarm (Bleeker, 1990).

The D_2 event post-dates the emplacement of Molson Dykes and caused F_1 folds to be overprinted by F_2 structures during high-grade metamorphic conditions (Bleeker, 1990). D_2 was a compressive event that formed as a result of continental loading and produced tight to isoclinal folds **(Figure 2-3)** (Lightfoot et al., 2017). Based on U-Pb monazite ages, Couëslan et al. (2013) interpreted that peak metamorphism occurred at the end of D_2, between 1779 and 1776 Ma. The peak metamorphic facies are upper amphibolite to lower granulite at a temperature of ~750 ºC and pressure of 7.5 kbar in ore hosting pelitic schists (Lightfoot et al., 2017).

The D_3 event is interpreted to be a sinistral transpression event, responsible for refolding F_1 and F_2 folds by tight, upright, doubly-plunging F_3 folds **(Figure 2-3)** (Lightfoot et al., 2017). The D_3 event is associated with retrograde metamorphism and most TNB pegmatites are folded by the resulting F_3 structures ~1770 Ma (Bleeker, 1990). D_3 sinistral transpression produced numerous dome and basin structures all forming at a condition of ~500 ºC and 2-4 kbars (Bleeker and Macek, 1996), including the overturned Thompson Dome **(Section 3.1)** (Lightfoot et al., 2017). Doubly plunging, F_3 folds are the dominant ore controlling structures; aligning the geometry of the ore zones to be parallel to F_3 fold axes (Lightfoot et al., 2017). F_4 folds were developed on the limbs of steep F_3 folds, and subvertical F_5 folds were developed but only locally (Bleeker, 1990).

The D_4 event was a late-tectonic event with dextral transpression, generating brittle reverse faults and brittle-ductile deformation **(Figure 2-3)** associated with the Churchill-Superior boundary fault (Bleeker 1990). D_4 is associated with retrograde, greenschist facies metamorphism and is deemed the main ore brecciation event occurring <1770 Ma (Bleeker, 1990). D_4 is expressed by F_6 F_7 folds, producing dextral pseudotachylitic-generating faults and large-scale brecciation (Bleeker, 1990).

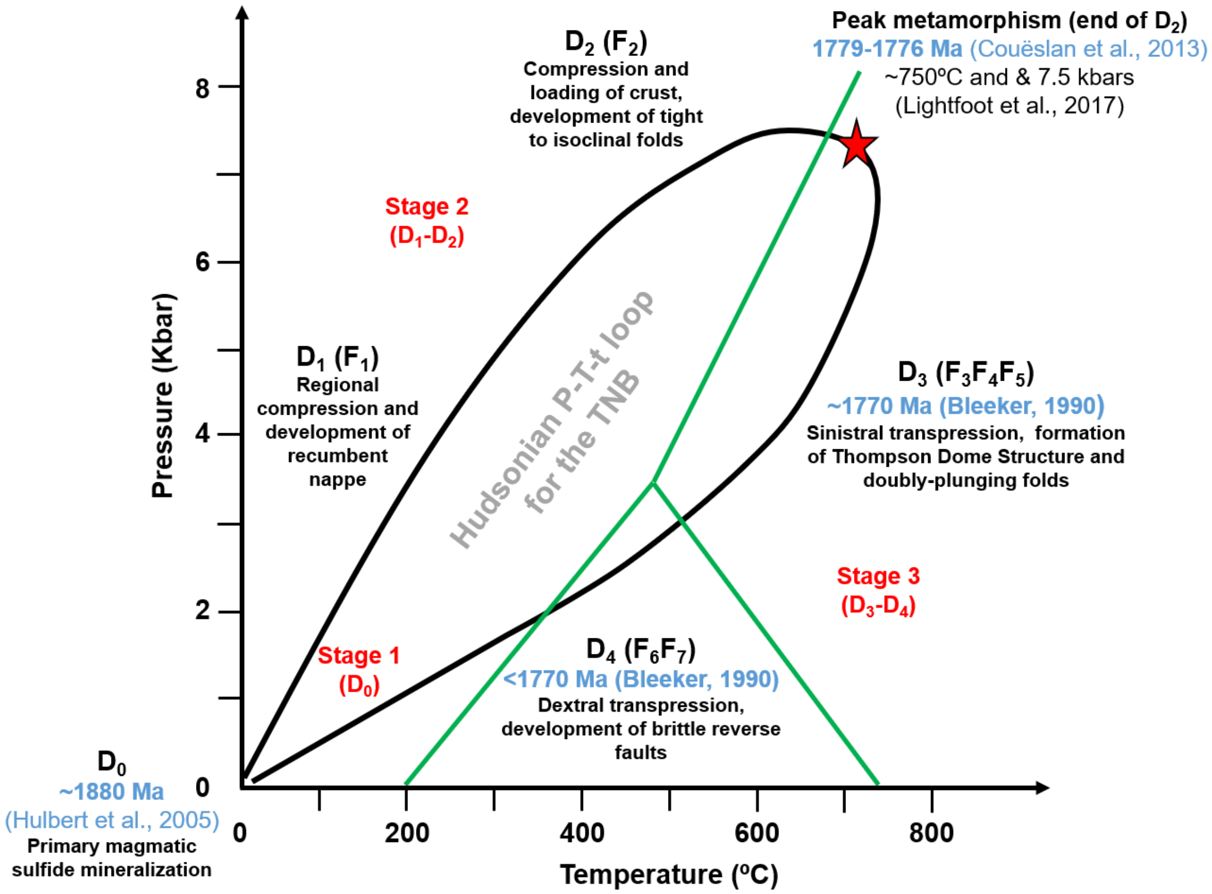

Figure 2-3: Generalized P-T-t loop of the Hudsonian deformation event for the Thompson Nickel Belt (TNB). Stage 1 - primary magmatic stage (D_0); Stage 2 – prograde metamorphism (D_1-D_2); Stage 3 – retrograde metamorphism (D_3-D_4). The 'red star' marks the peak metamorphic conditions (late-D_2) for Thompson. (Modified after; Bleeker and Macek (1996) and Lightfoot et al. (2017)).

2.4 Nickel Sulfide Mineralization

Transtensional faults, characterized by both normal and strike-slip faulting, were generated by an early stage of rifting that occurred near the end of the deposition of the Ospwagan Group sediments (Lightfoot et al., 2017). This provided the conduits for magma transport from the mantle (Barnes and Lightfoot, 2005; McRitchie, 1995; Naldrett et al., 2000; Zwanzig, 2005). A high degree of partial melting of the mantle resulted in komatiitic magmas that were fertile in Ni & PGE, which ascended along fault conduits and were transported into the Ospwagan group sediments as sills (Barnes and Lightfoot, 2005). The komatiitic magmas intruded along S-rich sediment horizons and into sulfide facies iron formations in the Ospwagan sediments, where magmatic sulfide melt was produced through assimilation of sedimentary sulfide (Bleeker, 1990). The nickel sulfide mineralization is interpreted to have been produced by saturation of the komatiitic magma in immiscible magmatic sulfide (Lesher and Burnham, 2001). Based on Re-Os isotope geochronology from sulfide ore samples from the TNB, the timing of sulfide mineralization is constrained to 1885 ± 49 Ma (Hulbert et al., 2005). However, U-Pb zircon ages from the same study constrain the age of the intrusions hosting the sulfide mineralization to 1880 ± 5 Ma (Hulbert et al., 2005). The tectonic activity associated with the Trans-Hudson orogeny at 1.7 Ga pervasively deformed the rocks and it was accompanied by upper amphibolite to lower granulite facies metamorphism (Bleeker, 1990). Sulfides were remobilized into boudin necks/shadow zones of the ultramafic bodies, or transported further away and accumulated in fold hinges, limbs and open-space dilation zones in the neighbouring P_2 schists (House, 2009; Lightfoot et al., 2017). Sulfide lenses are brecciated, inclusion-bearing, and commonly occur along shear zones.

The nickel sulfide ore deposits at Thompson mine are metasediment-hosted, and they appear to be formed by the remobilization of sulfides from the parent intrusion (Lightfoot et al., 2017). At Thompson, the Ni tenors tend to be higher in the metasedimentary rocks (8 to16 wt% Ni), compared to those found in many, but not all of the ultramafic-hosted deposits (Pipe & Birchtree; 4 to 8 wt% Ni (House, 2009; Lightfoot et al., 2017; Franchuk et al., 2016)

2.4.1 Deposit Types

The TNB has three principle types of nickel mineral deposits as described by Lightfoot et al., (2017):

1. Ultramafic-hosted deposits where mineralization is hosted within/around ultramafic intrusions (Pipe & South Manasan deposits).
2. Ultramafic and adjacent metasedimentary hosted deposits where mineralization is associated with both ultramafic intrusions and metasediments (Birchtree deposit).
3. Strictly metasediment hosted deposits where mineralization is within Pipe Formation metasediments (Thompson deposits).

Chapter 3: Local Geology

3.1 Thompson Dome Structure

The Thompson Dome comprises an inverted stratigraphy that formed as a nappe and was then folded by upright, doubly-plunging F_3 folds that were a result of the main D_3 sinistral transpressive event (Bleeker, 1990). The D_3 event locally modified the flat-lying Thompson ores, into their present subvertical positions (Bleeker, 1990). As a result, high-Ni-tenor sulfide mineralization is localized along doubly-plunging F_3 folds on the eastern and southernmost limbs of the Dome structure **(Figure 3-2)** (Lightfoot et al., 2017).

The inverted Dome structure consists of Setting Formation quartzites at the core, and Archean basement gneisses on the outer limbs; with the Pipe, Thompson and Manasan Formation metasediments sandwiched in between **(Figure 3-1)** (Lightfoot et al., 2017). The Thompson deposits (T1 and T3) are located on the southern and eastern flanks of the F_3 Thompson Dome structure, respectively **(Figure 3-1).**

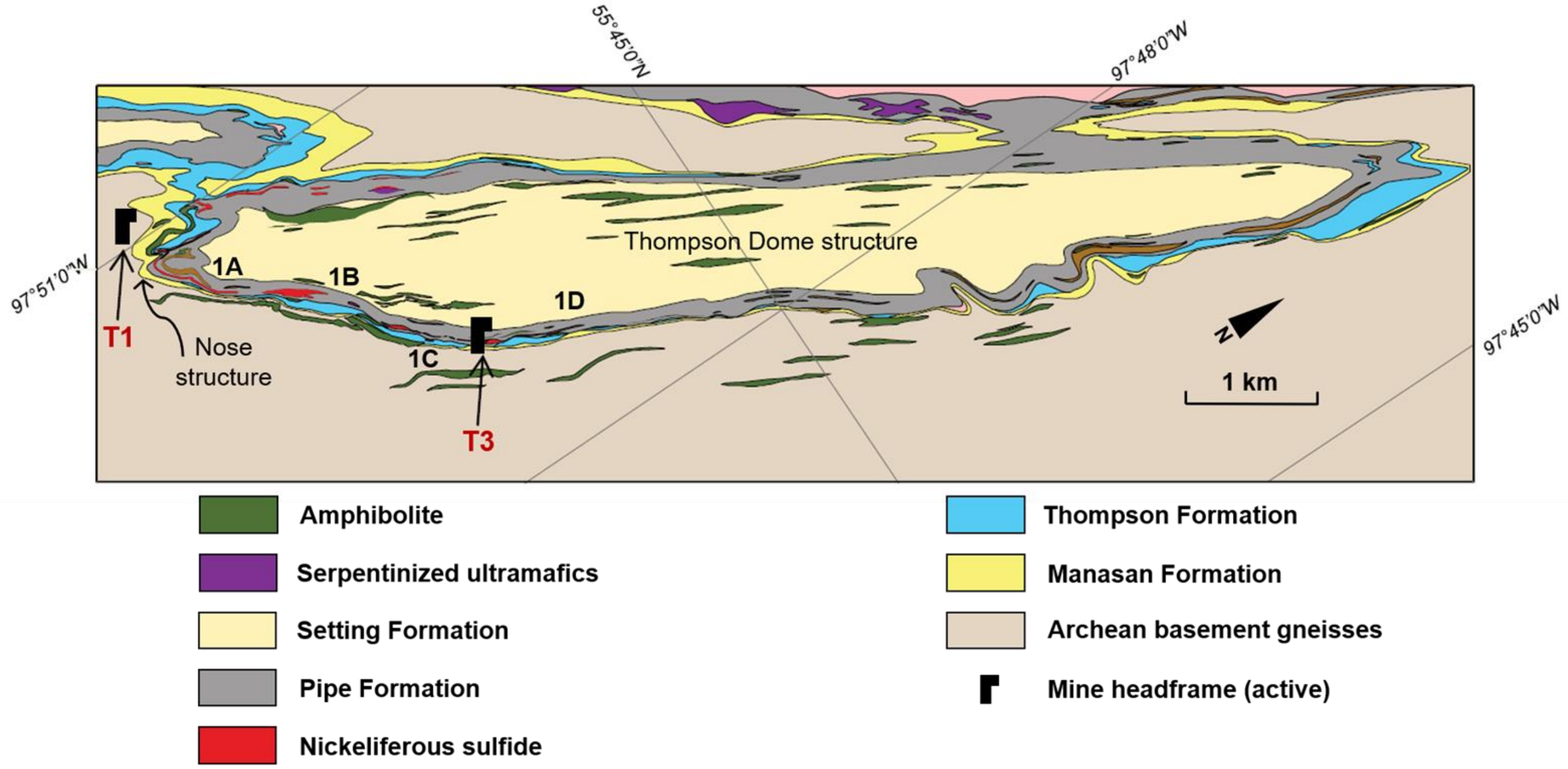

Figure 3-1: Geological plan map of the inverted Thompson Dome structure showing the T1 and T3 headframes, dome stratigraphy, amphibolite dykes, and nickeliferous sulfide. The relative location of the 1A, 1B, 1C and 1D zones is presented. Note the arrow pointing at the Thompson Dome Nose structure. (Modified from Lightfoot et al., 2017).

3.2 Thompson Deposits

The T1 mine hosts the 2-shear, 3-shear, 3-4 shear, 2-3 nose, south plunging Nose structure, 1A and 1B ore zones, depicted on **Figure 3-2.** The Nose structure is the southeastern most region of the Dome structure, and consists of a south-plunging, south fold closure (Bleeker, 1990). Sulfide mineralization is associated with dilation zones around the fold closure (Bleeker, 1990). The 1A is a south-plunging orebody at the southernmost region on the eastern limb of the Dome structure **(Figure 3-2).** The 1B is also a south-plunging orebody, located just north of the 1A zone on the eastern limb **(Figure 3-2).** Sulfide mineralization in the 1A and 1B ore bodies is controlled by dilation zones that are concordant to doubly-plunging F_3 folds (Lightfoot et al., 2017). T1 sulfide mineralization consists of massive to semi-massive lenses in pelitic schists that are closely associated with ultramafic boudins, similar to the Birchtree ores (Liwanag et al., 2001). However, several sulfide lenses also occur more distally from ultramafic intrusions. Brecciated, ultramafic inclusions are more common in T1 ores.

The T3 mine hosts the 1C and 1D orebodies. The 1C orebody is both present near surface at the T1 open-pit and extends down-dip towards the T3 shaft. The 1C orebody is currently being mined from both the T1 and T3 shafts **(Figure 3-2).** Layton-Matthews et al. (2007) describes the 1C orebody as massive sulfide lenses within pelitic schists and ultramafic breccias, along with disseminated and net-textured ores associated with ultramafic boudins. The 1C ores have coarser-grained pentlandite, which forms parallel bands within a dominantly pyrrhotite matrix (Layton-Matthews et al., 2007). The 1C sulfides are inclusion-bearing; pelitic schist fragments, single laths of biotite, quartz and garnet, as well as pegmatitic inclusions.

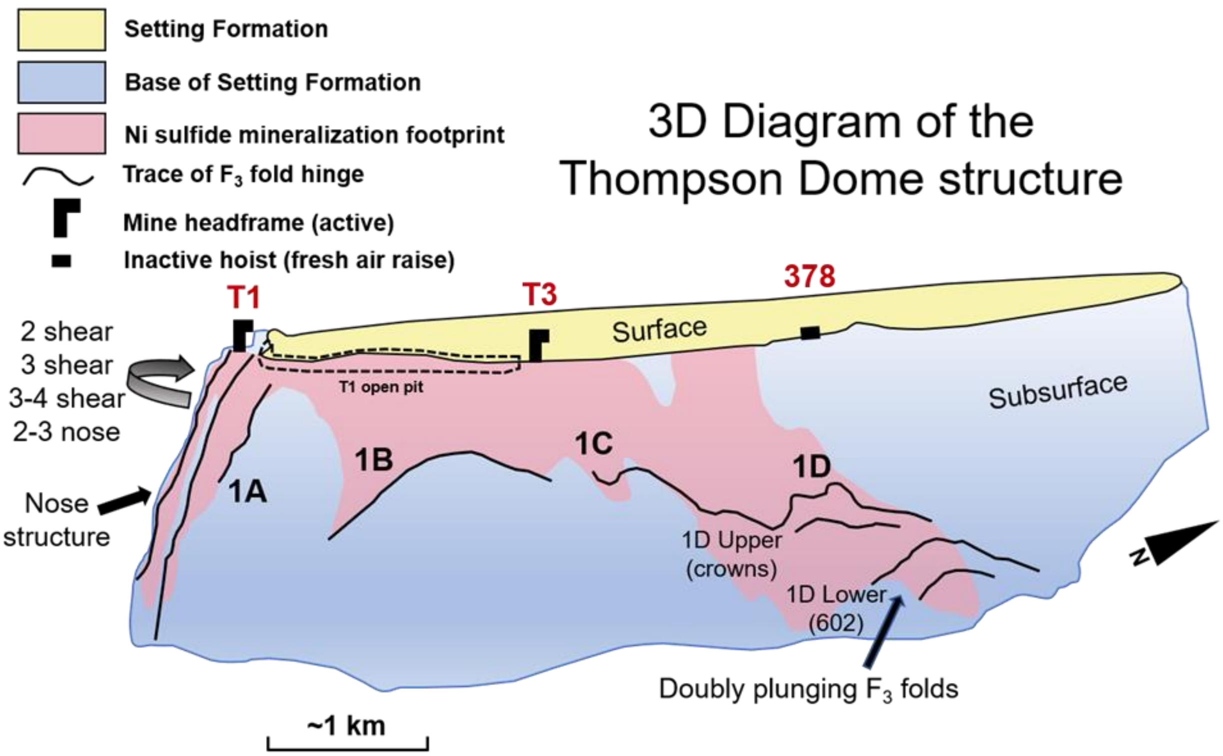

Figure 3-2: A 3D diagram showing the surface of the Setting Formation (yellow), base of the Setting Formation (blue) and the footprint of Ni sulfide mineralization (pink), in a 3D diagram view of the Thompson Dome structure. Location of the T1 ore bodies (2 shear, 3 shear, 3-4 shear, 2-3 nose, nose structure, 1A and 1B) and T3 ore bodies (1C and 1D) are shown on the southern and eastern flanks of the Dome. The diagram also shows the location of the T1 and T3 headframes, T1 open-pit, and the 378 hoist. F_3 fold hinges are depicted as 'bolded black lines'. At the 1D orebody (Upper-crowns; Lower-602), the location of doubly plunging F_3 structures are shown – high tenor Ni sulfide mineralization aligns along the doubly plunging F_3 folds (Modified from Lightfoot et al., 2012 and Lightfoot et al., 2017).

3.3 The 1D Orebody

The 1D orebody is a linear, east-dipping (45˚) orebody that has filled dilation zones around F_2 fold hinges on the flanks of doubly-plunging F_3 folds **(Figures 3-2 and 3-3)** (Lightfoot et al., 2017). **Figure 3-3** shows a North-facing vertical geology section through the Thompson 1D orebody at line 36940 South, on the eastern flank of the Thompson Dome Structure. The 1D orebody stratigraphy, mine levels and location of ultramafic boudins and nickel sulfide lenses are depicted. The P_2 member of the Pipe Formation metasediments (Ospwagan Group) is the primary host unit to sulfide mineralization at Thompson and the 1D orebody. Mineralization consists of stacked lenses infolded with P_3 metasediments and Setting Formation quartzites (Lightfoot et al., 2017). The stratigraphic package is overturned, folded, attenuated and thickened by high P-T deformation processes **(Figure 3-3)** (Lightfoot et al., 2017).

The 1D orebody is further subdivided into two zones: the 1D Upper (crowns) and 1D Lower (602). The 1D Upper (crowns) occurs on mine levels 2400 to 3500. The 1D Upper consists of massive to semi-massive sulfides that have been emplaced along hinges of tight isoclinal F_2 folds (Lightfoot et al., 2017), located below synformal closures ("sag downs") in the Thompson Formation calc-silicate rocks, termed 'skarns' by Vale geologists. The 1D Upper ores generally lack ultramafic inclusions (Lightfoot et al., 2017), are closely associated with shears, and commonly have been intruded by late pegmatites (Layton-Matthews et al., 2007). The 1D Lower, between mine levels 3700 to 4160 is considered the 602 zone **(Figure 3-3)**, which is further subdivided into North Extension (3590 to 3990) and South Extension (3500 to 4160) zones. The 1D Lower consists of massive to semi-massive, conformable sulfides in F_2 fold hinges and along F_3 limbs (Lightfoot et al., 2017). Minor ultramafic bodies are present in the 1D Lower (602) and sulfide ores are concentrated in larger, open-style folds (Lightfoot et al., 2017). Both the 1D Upper and Lower sulfides can either be inclusion-poor or inclusion-bearing (biotite laths, quartz grains, folded P_2 schist wall rock, ultramafic and pegmatitic porphyroclasts). The 1D Lower extends past the 602 zone into several deeper zones, with an increase in ultramafic presence (Midband zone) as you approach F_3 fold hinges **(Figure 3-3)**. Below the 602; the Footwall Deep (4350 to 4800), Hangingwall Deep (4400) and Midband (4070 to 4900) zones occur. Of which, minor mapping and grab sample collection was also completed for both the FW Deep and Midband zones.

The 1D orebody (Upper and Lower) is uniquely different when compared to other mineral zones in the TNB; the presence of large-scale shear structures, multi-pulse pegmatite intrusions, abundant sub-rounded inclusions in sulfides, are indicative of higher degrees of deformation (Bleeker, 1990; Layton-Matthews et al., 2007). The 1D ores are hosted by the metasediments of the Pipe and Thompson Formations, and lack a close association with ultramafic boudins that are characteristic of sulfide mineralization in the T1 mine and 1C ores (Layton-Matthews et al., 2007). There are some larger ultramafic boudins in the fold structures **(Figure 3-3)**, which likely act as a control on the localization of fold hinges (Lightfoot et al., 2017). The Ni tenor of sulfide in the 1D is highly variable, ranging from massive sulfides that are barren of Ni (<200 ppm), to sulfides that are highly nickeliferous (>16 wt% Ni in 100% sulfide).

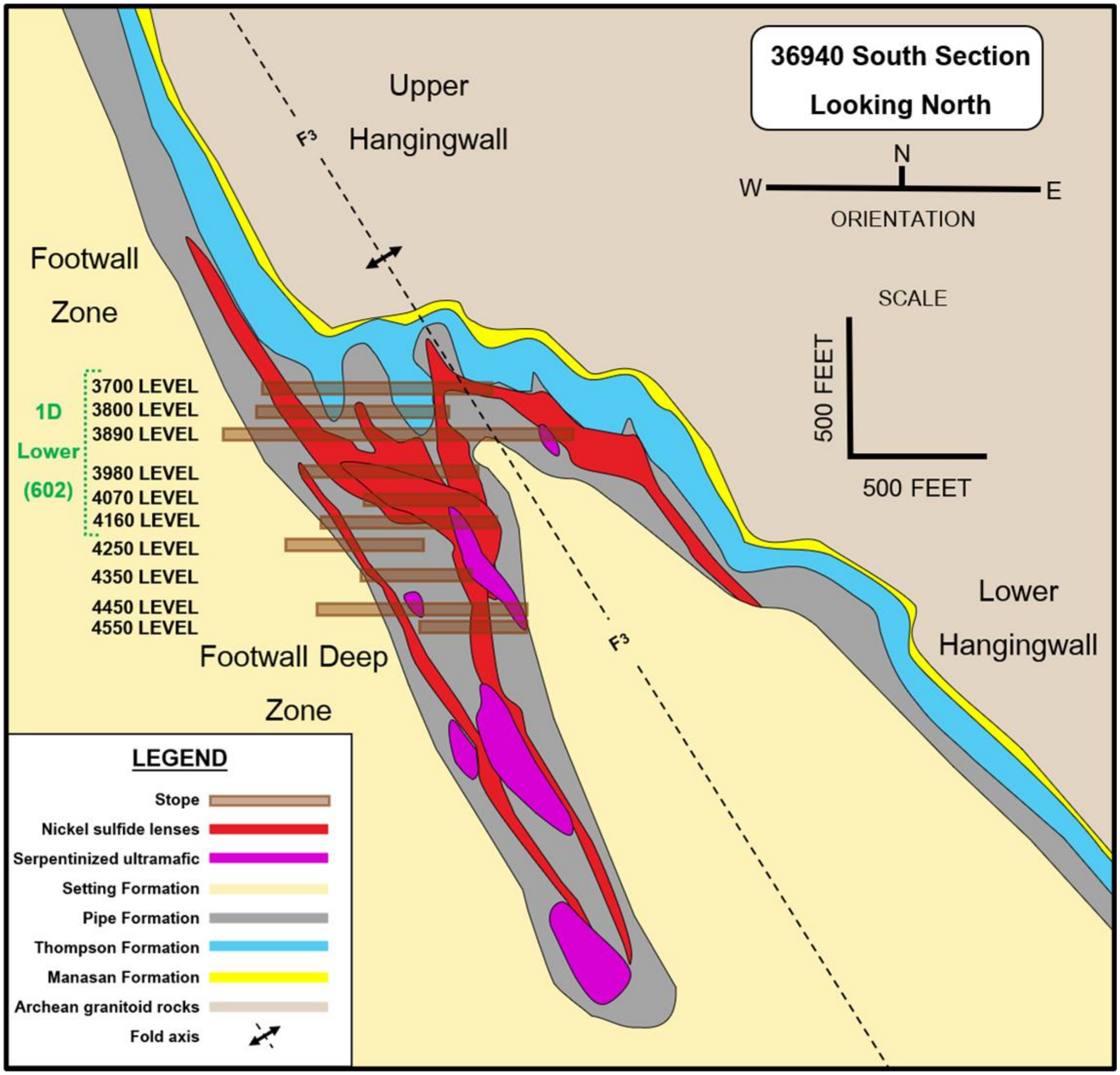

Figure 3-3: Geological section through the Thompson 1D orebody. A North-facing, 2D vertical cross section (at line 36,940 South) was taken through the 1D orebody and digitized. Relationships between country-rock stratigraphy (Ospwagan Group), ultramafic boudins and nickel sulfide mineralization are depicted.

Chapter 4: Materials and Methods

4.1 Field Methods

4.1.1 Detailed Underground Mapping

Underground mapping of face, wall, and back maps of 26 stopes from 11 different levels between 3590 – 4550 ft were mapped at the T3 mine. Mapping was focused in the Lower 1D orebody (602), but stopes from Footwall Deep and Midband orebodies were also mapped. Underground spatial associations, strikes and dips, structures, lithologies and mineralization styles were documented and recorded on grid paper. Grab sample locations were recorded by taking measurements from installed survey plugs using a ‘Leica DISTO Laser Measurer’ to accurately determine distances and face measurements. Face/back/wall sketches were later digitized, and underground measurements were uploaded on the Maptek Vulcan software by Vale Canada Ltd. geologists. Mine level plan and face maps (.pdf) for all stopes and underground samples are provided in **Appendix 1.**

4.1.2 Drill Core Logging

A total of six drill holes were logged, sampled and assayed. Drill core logging systematically recorded lithology, mineralogy, structures, alteration zones, sulfide mineralization, angle of foliation to core axis, pegmatite and ultramafic occurrences.

Core intervals were determined using a standard tape measure and all data was recorded on DH Logger and transferred into Datamine as drill core strings.

The sampling strategy consisted of identifying and sampling the prominent mineralized zones as well as the suite of P_2 schist wall rocks that surround the mineralization. Samples were taken at intervals of 1, 5 and 10 metre spacing before and after a mineralization zone in order to look for changes in the P_2 metasedimentary rocks adjacent to the mineralization. The six drill holes selected were:

Drill hole #1365050 (T3 mine, Lower 1D orebody (602), 4070 level) was selected because it cross cuts several distinct zones of massive and semi-massive sulfide mineralization within the Lower 1D orebody. A total of 36 core samples were taken, assayed and standard polished thin sections were made. However, only half (18/37) of the thin sections had petrography done on them **(Appendix 5).** K-feldspar staining of all 36 thin section blocks was completed (Section 4.4).

Three ‘fanned’ drill holes that intersect North Hangingwall mineralization at shallow dip (DH#1341100), moderate dip (DH#1226310) and steep dip (DH#1185670) were selected. The holes intersect sulfide mineralization as well as metasedimentary rock with barren sulfide horizons. A total of 62 core samples were taken and assayed.

Two regional drill holes were selected for investigation, DH#1238990 and DH#892880. The purpose of sampling the regional holes was to provide independent data for barren sulfide horizons and to collect information on the unaltered lithogeochemical variation of the P_2 metasedimentary unit. A total of 34 core samples were taken and assayed.

Due to time constraints on the project, only DH#1365050 was selected for detailed petrographic analysis and investigation (**Section 5.5.1**). However, corresponding sample assay data for all six drill holes as well as drill logs are provided in **Appendix 2.**

4.1.3 Sampling Strategy

The sampling strategy adopted for this project consisted of mapping various stopes and sulfide bodies that develop representative examples of the different styles of mineralization. Different mineralization styles were identified and sampled to establish whether mineralization style has an important control on tenor. Additionally, sampling of each ore type provided a basis to texturally classify the sulfide assemblages for each of the different styles of mineralization. Metasedimentary P_2 schist units that enclose the sulfide horizons were also sampled for lithogeochemical analysis.

Twenty-six mine stopes, across 11 different levels at T3-mine, and from 5 mine complexes (602, North Extension, South Extension, Midband, Footwall Deep) were sampled - see **Section 5.1.4; Table 5-1**. The metal tenor of the sulfide was not known at the time of sampling as assays were not available from the face until after sampling. Therefore, the underground sample collection technique consisted of taking many samples that allowed a wide array of different parameters, possibly related to diversity in Ni tenor to be tested. The most important parameters considered during the sampling campaign were:

- Sulfides occurring near shear zones were deemed interesting because shears are potential mobilization corridors for hydrothermal fluids. These fluids could enrich or deplete sulfide ore bodies in nickel and other elements;

- Sulfide ores with garnets, as nickel and cobalt are known to partition into the dodecahedral sites of aluminous garnets (Ross et al., 1996; Canil, 1999);

- Brecciated, inclusion-bearing sulfides. Specifically, sulfide ore with semi-rounded pegmatitic inclusions within them. Determining the mineral composition of such pegmatitic inclusions would aid in understanding if leaching or replacement of feldspars via potassic metasomatism occurred, and whether chemical enrichment of surrounding sulfides took place;

- Sulfides occurring in the vicinity of pegmatite intrusions, to determine if pegmatites played a role in tenor upgrading of the ores;

- Visual proportions of coarse-grained and fine-grained sulfide ore, to determine if recrystallization of sulfides occurred;

A total of 235 samples from both underground stopes and drill core were taken. Elemental analyses and geochemical whole rock assay data were determined by ALS Canada Ltd. for all 235 samples. An excel spreadsheet with the raw geochemical data can be found in **Appendix 3.** Limit of reporting (LOR) is the minimum recorded concentration of an element in a sample that can be reliably detected by the laboratory. ALS Canada Ltd. analyzed the following elements and provided their respective LOR's – Cu (0.002 wt%); Ni (0.002 wt%); Co (0.002 wt%); Fe (0.05 wt%); As (0.01 wt%); Pb (2 ppm); Zn (0.002 wt%); S (0.01 wt%); Mg (0.01 wt%); C (0.01 wt%); As (2 ppm); Au

(0.001 ppm); Pt (0.005 ppm); Pd (0.001 ppm). Inductively coupled plasma atomic emission spectroscopy (ICP-AES) was used for all analyses except carbon. Total carbon was determined using the LECO instrument.

QA/QC requirements were followed using the National-Instrument 43-101 guidelines - where a standard was added every twenty-fifth sample to maintain quality control. ‘Certified values’ are the accepted laboratory means for all elemental concentrations in a standard after outlier filtering. Three internal standards provided by Vale Canada Ltd. were used, their descriptions and certified values are as follows:

TH_1: A 60-gram sealed laminated foil packet with source material that includes medium grade Ni-Cu magmatic sulfide ores from the Thompson Nickel Belt in Manitoba, Canada. Certified values for all elemental concentrations in TH_1 can be found in **Appendix 4;**

TH_2: A 60-gram sealed laminated foil packet with source material that includes high-grade Ni-Cu magmatic sulfide ores from the Thompson Nickel Belt in Manitoba, Canada. Certified values for all elemental concentrations in TH_2 can be found in **Appendix 4;**

Raw Blank Quartz: source material is from Lawson Quarry Quartzite in Sudbury. Material is collected by Vale Canada Ltd. personnel and sent to ALS Canada Ltd. laboratories where the material is crushed (½ inch), screened (through 1/8 mesh) and bagged in approximately 500g units. The quartzite has been checked to ensure that the concentrations of main metals are negligible (below detection limits). Minor Fe and S are present (due to trace pyrite). Assay results on the quartzite do not exceed allowable ‘upper limits’ (10 x detection limit - except for S, Fe and MgO) of elements. Upper limits of elements are: Cu (0.02 wt%), Ni (0.02 wt%), Co (0.02 wt%), Fe (0.71 wt%), As (0.1 wt%), Pb (0.1 wt%), Zn (0.1 wt%), S (0.14 wt%), MgO (0.33 wt%), C (0.1 w%), As (20 ppm), Pb (20 ppm), Au (0.01 ppm), Pt (0.05 ppm), Pd (0.01 ppm).

Of 235 total samples, 135 were chosen for detailed geological, mineralogical and geochemical analysis:

A total of 99 underground grab samples, 77 sulfide ore and 22 metasedimentary rock samples, were collected. Petrographic analysis of all 77 sulfide samples was completed (**Section 4.2.1**).

A total of 133 drill core samples, across six different drill holes were collected. Assay data for all 133 drill core samples was completed. However, only 18/36 drill core samples (DH# 1365050) were chosen for detailed petrographic analysis.

All drill hole and underground grab sample locations with corresponding sample assay data can be found in **Appendix 2.** Petrographic sample descriptions of drill hole and underground grab samples can be found in **Appendix 5.**

Samples were washed, cut and photographed. Photos of underground ore samples, underground Lithogeochemical samples and drill holes can be found in **Appendix 6.** Thin section blocks were prepared at the Vale Manitoba Operations core shack and sent to Vancouver Petrographics Ltd., where standard polished thin sections were made of all underground grab and drill core samples. K-feldspar staining (**Section 4.4**) was also completed on select thin sections blocks by Vancouver Petrographics Ltd. See **Appendix 7** for photos of thin section blocks and scans of corresponding standard thin sections.

4.2 Analytical Methods

The following analytical methods were used to aid in establishing geological, mineralogical and geochemical controls on the compositional diversity in Thompson 1D sulfide mineralization of Thompson mine (T3).

4.2.1 Petrography

Understanding the mineralogy of sulfides in relation to metamorphism and deformation is key to understanding the controls of metal tenor of sulfide. Detailed petrographic studies of the sulfide assemblages from the Thompson 1D orebody were completed.

A total of 135 standard polished thin sections (26 x 46 mm) were prepared by Vancouver Petrographics Ltd. Detailed petrographic analysis of 95 thin sections was completed - 77 underground sulfide ore and 18 drill hole (DH#1365050) samples. Petrographic analysis was completed in transmitted and reflected light using an Olympus Model BX51 microscope at the Earth and Planetary Materials Analysis (EPMA) Laboratory at Western University. Silicate, sulfide and oxide mineral assemblages were determined, and modal abundances were recorded. Mineralization styles, timing relationships between minerals, alteration assemblages of both sulfide and wall rock, and a complex suite of textures were determined and recorded for each silicate and sulfide assemblage in their respective ‘Mineralogy’ chapters **(Sections 6** and **7).** All petrographic sample descriptions can be found in **Appendix 5** and microscope photos in transmitted and reflected light can be found in **Appendix 6.**

Several thin sections were specifically made to examine locally developed and/or atypical sulfide assemblages and textural styles using the microscope. This could result in skewed or biased outcomes from the examination of the thin sections where the sample does not have a representative texture or sulfide abundance. In order to work with unbiased data, all thin sections that were identified as 'unrepresentative' were omitted from the graphs and tables in the results sections **(Sections 6** and **7).** All 'unrepresentative' and omitted samples are nevertheless given in **Appendix 2** with an asterisk (*) denoted beside them.

It was recognized that pyrite is quite abundant in some samples and exhibits specific textural associations. At the time of sample collection, several massive and semi-massive sulfide samples showing atypical pyrite porphyroclasts (up to 6 cm) were collected. Thin sections were made in order to analyze the compositions and textures of these pyrite porphyroclasts. Because of the coarse grain size, these samples are biased (denoted by an * in **Appendix 2**) and were not used in the analyses of the sulfide mineral proportions of the Thompson 1D orebody. However, pyrite grain sizes for the remaining representative thin sections (26 x 46 mm) were typically <3 mm (<0.3 cm), with some grains up to 5 mm (0.5 cm). These pyrite grains provided a more representative grain size distribution when compared to thin section size, resulting in representative modal abundance estimates.

All modal abundances of sulfides/silicates/oxides from petrographic thin section analysis under a microscope were estimated 'visually'. In order to test if modal estimates were accurate, pyrite ‘visual’ abundances were compared to the modal abundances calculated from digital photographs **(Table 4-1)** using the digital image processing software, ImageJ (Abramoff et al., 2004).

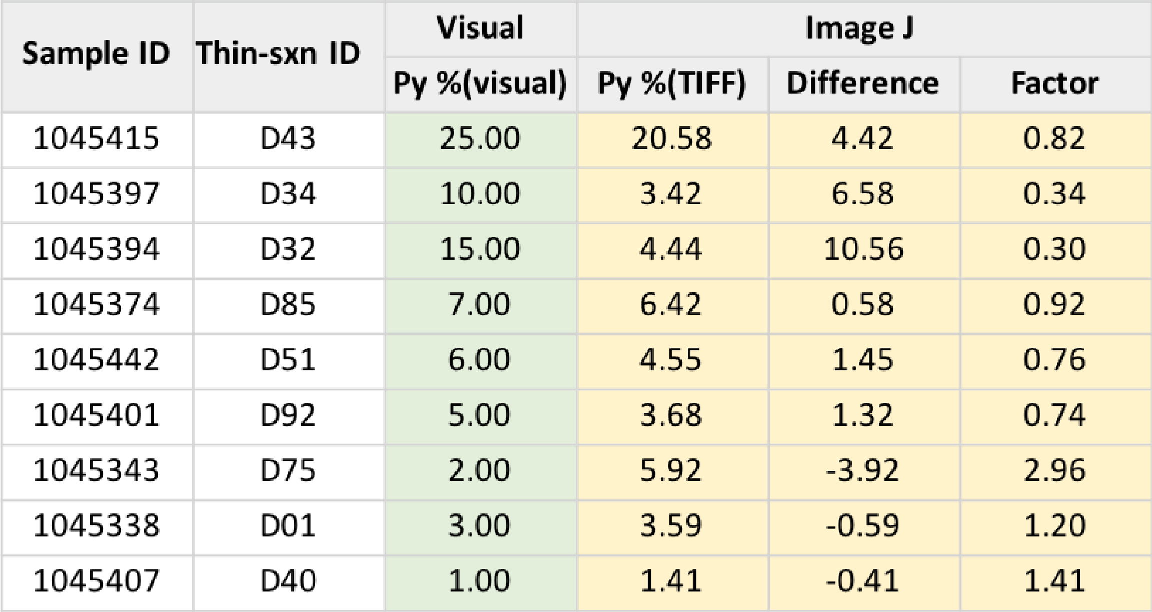

Sample ID	Thin-sxn ID	Visual	Image J		
		Py %(visual)	Py %(TIFF)	Difference	Factor
1045415	D43	25.00	20.58	4.42	0.82
1045397	D34	10.00	3.42	6.58	0.34
1045394	D32	15.00	4.44	10.56	0.30
1045374	D85	7.00	6.42	0.58	0.92
1045442	D51	6.00	4.55	1.45	0.76
1045401	D92	5.00	3.68	1.32	0.74
1045343	D75	2.00	5.92	-3.92	2.96
1045338	D01	3.00	3.59	-0.59	1.20
1045407	D40	1.00	1.41	-0.41	1.41

Table 4-1: Compares the pyrite modal abundances of 6 thin-section samples using two methods; visual and ImageJ. Visual modal abundances (green) were determined through petrographic analysis of thin sections. In the other method, thin section maps were created using electron probe microanalyzer (EPMA), then pyrite modal abundances were determined using ImageJ (Abramoff et al., 2004). TIFF files were used for modal determination. ***Py%*** *= determined pyrite modal abundance.* ***Difference*** *= (Py% visual – Py% TIFF). A positive difference value = ‘overestimation’ of pyrite modal abundances visually. Whereas a negative difference value = ‘underestimation’ of pyrite modal abundances visually.* ***Factor*** *= multiplying factor used to convert Py% (visual) to the determined Py% (TIFF) value. Factor values <1.0 = ‘overestimation’ visually. Factor values >1.0 = ‘underestimation visually’. In general, pyrite visual estimates were ‘strongly overestimated’ in 1/3 of data (1045415, 1045397, 1045394), ‘slightly overestimated’ in 1/3 of data (1045374, 1045442, 1045401), and ‘slightly underestimated’ in 1/3 of data (1045343, 1045338, 1045407). In conclusion, pyrite modal abundances determined visually through petrographic analysis are ‘overestimated’ when compared to modal abundances determined from the ImageJ. See Appendix 8.*

Using the electron probe microanalyzer (EPMA), digital thin section maps were created of six thin sections. Maps were exported as Tagged Image File Format (TIFF) to ImageJ. The TIFF files were of very high quality and provided a 1 – 5000 colour grey scale; which allowed the different sulfide and silicate minerals to be discriminated from each other. Petrographic analysis was used to confirm the mineralogy. Modal abundances were determined ‘digitally’ using ImageJ and then compared to the modal abundances determined ‘visually’ from petrographic analysis **(Table 4-1).** All ImageJ results and .tiff data files can be found in **Appendix 8.**

In conclusion, pyrite modal percentages were overestimated ‘visually’ compared to the modal estimates determined ‘digitally’ using the TIFF thin section maps on ImageJ. Notwithstanding, it is important to note that during petrographic analysis, the relative abundance of the visual estimates is consistent with ImageJ analyses.

4.2.2 Benchtop – SEM

A benchtop scanning electron microscope (B-SEM) was used to identify and establish semi-quantitative estimates of the compositions of minerals. Data was acquired at the Experimental Petrology Laboratory in Biological & Geological Sciences (Rm# 0172) at Western University using a JEOL JCM-6000 NeoScope benchtop SEM, equipped with JEOL JED-2300 energy dispersive X-ray analysis. Non-carbon coated thin sections were placed on an aluminum sample-holder, fastened with black, conductive adhesive tape, and loaded into the B-SEM. Standard configurations were used; low vacuum settings, an accelerating voltage of 15 keV, a standard filament, and a high probe current. Element spot-analysis was conducted on various sulfide minerals to determine baseline elemental concentrations, which were normalized to 100% by the JEOL software. The B-SEM data of select analyzed thin sections were exported via .pdf or .ppt files **(Appendix 9).** Pyrrhotite, pentlandite, pyrite, chalcopyrite, gersdorffite, biotite, garnet and quartz, were selected for further analysis using the electron probe microanalyzer (EPMA).

4.2.3 EPMA

The electron probe micro analyzer (EPMA) was used for spot analyses and trace element mapping of sulfide and silicate grains. Data was acquired at the Earth and Planetary Materials Analysis (EPMA) Laboratory at Western University using a JEOL JXA-8530F microprobe. **Table 4-2** summarizes all EPMA elemental spot analyses and mapping data for sulfide and silicate minerals; and whether backscatter electron (BSE), energy dispersive spectrometry (EDS) maps, wavelength dispersive spectrometry (WDS) maps, or cathodoluminescence (CL) maps were completed. Pyrite flames and sulfide melt inclusions (SMI) denoted by an italicized asterisk (*) were also included in **Table 4-2** and **Table 4-3** as a separate group - spot analyses and element maps were created for both. Furthermore, cathodoluminescence maps were only completed for quartz grains, no spot analyses were done.

Elements with minor concentrations that potentially have petrogenetic significance were analyzed using WDS; as greater resolution maps were possible owing to the lower detection limits compared to EDS (Reed, 2005). Minerals of the same type were analyzed by the EPMA on a given day, in order to retain standard calibration and consistency in data reporting. **Table 4-3** summarizes all calibration parameters used for each mineral during EPMA spot analyses; type of standards and origin, analysis (spectrometer) crystals used, counting times, beam conditions, element overlaps, correction factors applied and reasoning behind corrections are also reported. The limit of detection (LOD) for each element within a silicate or sulfide mineral is reported in the ‘Mineral Chemistry’ chapter for the respective mineral **(Sections 6** and **7).**

Before every EPMA session, oxidation was removed from thin sections using 1µm diamond wax (Struers DP-Stick) and a polishing pad. Acetone was applied to thin sections after the polishing stage and buffered by KIMTECH – Kimwipes. Thin sections were carbon-coated immediately prior to EPMA analysis.

The electron microprobe had the following operating conditions: an accelerating voltage between 15.0 and 20.0 kiloelectron volts (keV) – with the latter being used more commonly, and a beam current of 20-100 nanoamperes (nA). Pixel sizes for element maps ranged from 0.3 to 5.0 micrometres (µm) – with the former being used for smaller grains (<100 µm) that required higher resolution. Pixel sizes of 3 to 5 µm were more common for silicate element maps (biotite, garnet). Dwell times were 10 milliseconds for all grain sizes. Counts ranged from 50 to 5000 with errors up to ± 40. Counting times for all minerals were on average, 30 seconds for peak, 15 seconds for upper background and 15 seconds for lower backgrounds, for all elements analysed. Pixel sizes of 1 µm with accelerating voltages of 20 keV and dwell times of 10 milliseconds were the most common operating parameters.

Spot analysis data was exported as excel documents and element maps were exported as .pdf files. All EPMA mineral chemical data (excel spreadsheets) for silicate and sulfide minerals probed, and their corresponding trace element maps and supplementary petrographical data can be found in **Appendix 9.** Relative errors and detection limits for every mineral are discussed in the silicate and sulfide results; **Sections 6** and **7.**

Table 4-2: Summary of EPMA spot analysis and mapping data for sulfide and silicate minerals. Major elements for each mineral/group are 'bolded and in red'. SEI – secondary electron images; EDS – energy dispersive spectrometry; WDS – wavelength dispersive spectrometry; CL – Cathodoluminescence; n/a – no data available; asterisk (*) – not actual 'minerals' but separate grouped data; SMIs – sulfide melt inclusions.

Minerals	Backscatter images?	SEI images?	Spot analyses?	Number of grains?	Number of thin sections?	EDS element maps	WDS element maps	Other elements analyzed	Element maps?	CL maps?
Biotite	Yes	Yes	199	43	16	**Fe, Al,** Cl, **K,** Na, **Si, Ti,**	Co, **Cr, Mg,** Ni, F	n/a	Yes	n/a
Garnet	Yes	Yes	46	8	4	**Al,** Ca, **Mn, Si,** Ti	Co, Cr, **Fe, Mg,** Ni	n/a	Yes	n/a
Quartz	Yes	Yes	n/a	5	3	n/a	n/a	n/a	n/a	Yes
Pyrrhotite	Yes	Yes	188	44	15	Al, Bi, Ca, Cu, **Fe,** Na, Pb, Si	As, Co, Mg, **Ni, S**	Pt, Pd, Se	Yes	n/a
Pentlandite	Yes	Yes	88	46	14	Bi, **Fe, S**	**Ni, Co,** Pt, Pd, As	Ag	Yes	n/a
Pyrite	Yes	Yes	63	13	6	Al, Bi, Ca, Cu, **Fe,** Na, Pb, Si	**Co,** Mg, **Ni, S,** As	n/a	Yes	n/a
Gersdorffite	Yes	Yes	40	8	4	Au, Bi, Cu, **Fe,** Ir, Pt, Rh, **S,** Sb, **Te**	**Ni, As, Co, Pd,** Ag	n/a	Yes	n/a
Chalcopyrite	Yes	Yes	22	7	4	n/a	n/a	**Cu, Fe, S**	Yes	n/a
**pyrite flames*	Yes	Yes	n/a	14	5	Cu, **Fe, S**	As, **Co,** Mn, **Ni**	n/a	Yes	n/a
**SMIs*	Yes	Yes	54	12	4	**S**	**Ni, Co,** As, **Fe,** Cu	n/a	Yes	n/a

Table 4-3: Summary of calibration parameters used for every mineral/group during EPMA spot analysis. Table outlines type of standard used and origin, analysis (spectrometer) crystals used, counting times, beam conditions, elemental overlaps, correction factors applied and reasoning for corrections. Asterisk (*) – denotes not actual 'minerals' but separate grouped data; SMIs – sulfide melt inclusions. Note, no EPMA spot analysis on Quartz grains was done.

Minerals	**Types of element standards used and origin**	**Analysis crystals (spectrometers) used**	**Counting times**	**Beam conditions**	**Overlaps**	**Correction factors applied?**	**Reasoning for correction**
Biotite	Si, Al - Hornblende (Smithsonian USNM 143965 - Kakanui, New Zealand), K - Orthoclase (C.M. Taylor), Mg - Diopside (Smithsonian USNM 117733 - Natural Bridge, NY), Na - Albite (Amelia County, VA, USA), F - Fluorite (Astimex, synthetic Harshaw Chemical Corp, USA), Cl - Sodalite (Geller MicroAnalytical), Fe - Fayalite (unknown), Ti - Rutile (unknown), Co - Cobalt (Astimex-99.995% wire, Alfa Aesar, USA), Ni - Nickel (Astimex-99.97% wire, Alfa Aesar, USA), Cr - Chromium (Astimex-99.997% chip, Alfa Aesar, USA)	Si-TAP, Al-TAP, K-PETL, Mg-TAP, Na-TAP, F-TAP, Cl-PETL, Fe-LIF, Ti-PETL, Co-LIFH, Ni-LIFH, Cr-LIF	30 sec. peak, 15 sec. upper background, 15 sec. lower background for all elements	20 kV accelerating voltage, 20 nA probe current, 5 um spot size			
Garnet	Si, Al, Fe - Almandine (Astimex-New York State, USA), Mg - Pyrope (Astimex-Monastery Mine, Republic of South Africa), Ca - Grossular (unknown), Mn - Spessartine (Spessartine #3b-C.M. Taylor), Cr - Chromite (Smithsonian USNM 117075 - Tiebaghi Mine, New Caledonia), Ni - Nickel (Astimex-99.97% wire, Alfa Aesar, USA), Co - Cobalt (Astimex-99.995% wire, Alfa Aesar, USA)	Si-TAP, Al-TAP, Fe-LIF, Mg-TAP, Ca-PETL, Mn-LIF, Cr-LIFH, Ni-LIFH, Co-LIFL	30 sec. peak, 15 sec. upper background, 15 sec. lower background for all elements	15 kV accelerating voltage, 40 nA probe current, 1 um spot size	Fe/Co	Yes	Cobalt standard with slightly elevated cobalt abundances caused by a slight 'oxidation layer' interacting with counts, or attributed to non-homogeneity of cobalt in natural sample
Pyrrhotite	Fe, S - Pyrite (Astimex-Locality unknown), Ni - Pentlandite (Astimex-Sudbury Igneous Complex, Canada), Co - Cobalt (Astimex-99.995% wire, Alfa Aesar, USA), As - Arsenopyrite (Astimex-Yaogangxian Mine, Hunan Province, China), Cu - Chalcopyrite (unknown), Pt - Platinum (Astimex-99.95% wire, Alfa Aesar, USA), Pd - Palladium (Astimex-99.99% wire, Alfa Aeasar, USA), Bi - Bismuth (Astimex-99.999% Johnson Matthey Chemicals, USA), Se - Selenium (Astimex-99.999% pieces, Alfa Aesar, USA)	Fe-LIF, S-PETJ, Ni-LIFL, Co-LIFH, As-TAP, Cu-LIFL, Pt-PETH, Pd-PETH, Se-LIFL, Bi-PETH	30 sec. peak, 15 sec. upper background, 15 sec. lower background for all elements	20 kV accelerating voltage, 50 nA probe current, 1 um spot size	Fe/As	Yes	Overlap of Fe and S elevating the As counts, therefore correction applied
Pentlandite	Fe, S, Ni - Pentlandite (Astimex-Sudbury Igneous Complex, Canada), As - Arsenopyrite (Astimex-Yaogangxian Mine, Hunan Province, China), Co - Cobalt (Astimex-99.995% wire, Alfa Aesar, USA), Pt - Platinum (Astimex-99.95% wire, Alfa Aesar, USA), Pd - Palladium (Astimex-99.99% wire, Alfa Aeasar, USA), Bi - Bismuth (Astimex-99.999% Johnson Matthey Chemicals, USA), Ag - Silver (Astimex-99.9985% wire, Johnson Matthey Chemicals, USA)	Fe-LIF, S-PETJ, Ni-LIF, As-TAP, Co-LIFL, Pt-PETH, Pd-PETH, Bi-LIFL, Ag-PETH	30 sec. peak, 15 sec. upper background, 15 sec. lower background for all elements	20 kV accelerating voltage, 50 nA probe current, 1 um spot size	Fe/As and Fe/Co	Yes	Trace counts of arsenic could be present in the 'natural' sample. Or the arsenic peaks caused by slight overlaps of major elements (Fe and S). Cobalt standard with slightly elevated cobalt abundances caused by a slight 'oxidation layer' interacting with counts, or attributed to non-homogeneity of cobalt in natural sample
Pyrite	Fe, S - Pyrite (Astimex-Locality unknown), Ni - Pentlandite (Astimex-Sudbury Igneous Complex, Canada), Co - Cobalt (Astimex-99.995% wire, Alfa Aesar, USA), As - Arsenopyrite (Astimex-Yaogangxian Mine, Hunan Province, China), Cu - Chalcopyrite (unknown)	Fe-LIF, S-PETJ, Ni-LIFL, Co-LIFH, As-TAP, Cu-LIFL	30 sec. peak, 15 sec. upper background, 15 sec. lower background for all elements	20 kV accelerating voltage, 50 nA probe current, 1 um spot size	Fe/As	Yes	Overlap of Fe and S elevating the As counts, therefore correction applied
Gersdorffite	As, S, Fe - Arsenopyrite (Astimex-Yaogangxian Mine, Hunan Province, China), Ni - Pentlandite (Astimex-Sudbury Igneous Complex, Canada), Ag - Silver (Astimex-99.9985% wire, Alfa Aeasar, USA), Co - Cobalt (Astimex-99.995% wire, Alfa Aesar, USA), Pd - Palladium (Astimex-99.99% wire, Alfa Aesar, USA), Pt - Platinum (Astimex-99.95% wire, Alfa Aesar, USA), Rh - Rhodium (Astimex-99.8% sheet, Matthey Bishop, USA), Sb - Antimony (Astimex-99.9999% shot, Alfa Aeasar, USA), Bi - Bismuth (Astimex-99.999%, Johnson Matthey Chemicals, USA), Au - Gold (Astimex-99.95% wire, Engelhard Metals, USA), Te - Tellurium (Astimex-99.9998% chip, Alfa Aesar, USA), Ir - Iridium (Astimex-99.8% wire, Alfa Aesar, USA), Cu - Copper (Astimex-99.999% wire, Johnson Matthey Chemicals, USA)	As-TAP, S-PETJ, Fe-LIF, Ni-LIF, Ag-PETL, Co-LIF, Pd-PETL, Pt-PETH, Rh-PETL, Sb-PETH, Bi-PETH, Au-PETH, Te-PETH, Ir-PETL, Cu-LIF	40 sec. peak, 20 sec. upper background, 20 sec. lower background for all elements	20 kV accelerating voltage, 100 nA probe current, 1 um spot size	Pt/Ir	Yes	Overlap of Pt and Ir elevating the Pt counts, therefore correction applied
Chalcopyrite	Fe, S - Pyrite (Astimex-Locality unknown), Ni - Pentlandite (Astimex-Sudbury Igneous Complex, Canada), Co - Cobalt (Astimex-99.995% wire, Alfa Aesar, USA), As - Arsenopyrite (Astimex-Yaogangxian Mine, Hunan Province, China), Cu - Chalcopyrite (unknown)	Fe-LIF, S-PETJ, Ni-LIFL, Co-LIFH, As-TAP, Cu-LIFL	30 sec. peak, 15 sec. upper background, 15 sec. lower background for all elements	20 kV accelerating voltage, 50 nA probe current, 1 um spot size			
**pyrite flames*	Fe, S - Pyrite (Astimex-Locality unknown), Ni - Pentlandite (Astimex-Sudbury Igneous Complex, Canada), Co - Cobalt (Astimex-99.995% wire, Alfa Aesar, USA), As - Arsenopyrite (Astimex-Yaogangxian Mine, Hunan Province, China)	Fe-LIF, S-PETJ, Ni-LIFL, Co-LIFH, As-TAP	30 sec. peak, 15 sec. upper background, 15 sec. lower background for all elements	20 kV accelerating voltage, 50 nA probe current, 1 um spot size			
**SMIs*	Fe, S - Pyrite (Astimex-Locality unknown), Ni - Pentlandite (Astimex-Sudbury Igneous Complex, Canada), Co - Cobalt (Astimex-99.995% wire, Alfa Aesar, USA), As - Arsenopyrite (Astimex-Yaogangxian Mine, Hunan Province, China), Cu - Chalcopyrite (unknown)	Fe-LIF, S-PETJ, Ni-LIFL, Co-LIFH, As-TAP, Cu-LIFL	20 sec. peak, 10 sec. upper background, 10 sec. lower background for Fe, Ni, S, Cu and 40 sec. peak, 20 sec. upper background, 20 sec. lower background for Co and As	15 kV accelerating voltage, 50 nA probe current, 1 um spot size	Fe/Co	Yes	Cobalt standard with slightly elevated cobalt abundances caused by a slight 'oxidation layer' interacting with counts, or attributed to non-homogeneity of cobalt in natural sample

4.3 Nickel Tenor Calculation

Nickel tenor is expressed as weight % nickel in 100% sulfide. It is the universal way of comparing deposits with variable sulfide contents. The raw geochemical assay data was transformed into tenor percentages. Calculations of the tenors of sulfide and metal analyses are given in **Appendix 10.** Nickel tenor was determined using the 'normative sulfide method' as proposed by Naldrett et al. (2000):

An example calculation of the 'normative sulfide method' is shown below in **Table 4-4**. Weight % values of Ni, Cu, S and Co from whole rock data were divided by their respective molecular weights and converted to moles. The molar nickel and cobalt values were assigned to pentlandite; the number of moles of pentlandite ($Fe_{4.5}Ni_{4.5}S_8$) was calculated by dividing moles of Ni + Co by 4.5 to produce one mole of Ni in pentlandite. One mole Ni was multiplied by eight moles of S to produce total moles of S in pentlandite. The eight moles of sulfur required to make each mole of pentlandite was subtracted from the total sulfur content to give residual sulfur. Copper was assigned to chalcopyrite and the number of moles of chalcopyrite ($CuFeS_2$) was calculated by assigning one mole of Cu to chalcopyrite. Each mole Cu was multiplied by two moles of S to produce total moles of S in chalcopyrite. The moles of sulfur required to make chalcopyrite was subtracted from the residual sulfur value to give a corrected residual sulfur number. Note, Fe was assumed to be in excess for both pentlandite and chalcopyrite calculations. The residual sulfur value was assigned to make pyrrhotite (FeS) – however, this method results in a slight underestimation by using ideal FeS (Kerr, 2003). Total % sulfur containing 100% sulfides was then calculated from the weight proportions of the three sulfide minerals and their respective sulfur contents. Tenors (Ni, Cu, Co) were then calculated by dividing the respective elemental weight % values by the total % sulfur in the system and multiplying by 100. Platinum and palladium tenors were also calculated in this way.

However, several uncertainties associated with tenor calculations have been outlined by Kerr (2003): sulfide mineralogy assumes a standard magmatic assemblage (Thompson 1D ores may have had a primary magmatic origin, but have since been remobilized and relocated by secondary post-magmatic processes); the possibility of metal contents in silicates or oxides (as documented by the elevated Ni contents of mica in this study; **Sections 6.1.2** and **8.3.1**); the 'residual sulfur' of the system is assumed to create pyrrhotite, widely ignoring pyrite abundance (as will be discussed in detail below); and that threshold S concentrations are required for tenor calculations. These possible inaccuracies must be considered when comparing data from different localities and/or when mineralization types are contrasted (Kerr, 2003). Notwithstanding, the 'normative sulfide method' has been accepted common practice amongst the TNB deposits, and all tenor calculations within this study of the Thompson 1D are presented as such.

Table 4-4: An example tenor calculation showing the 'normative sulfide method'. This is an idealized tenor calculation where all the residual sulfur in the rock is assumed to make pyrrhotite – ignoring pyrite. This method was used in determining tenors for all sulfide samples in the Thompson 1D (this study). Wholerock assay data for elements was determined through ICP-AES (Inductively Coupled Plasma Atomic Emission Spectroscopy).

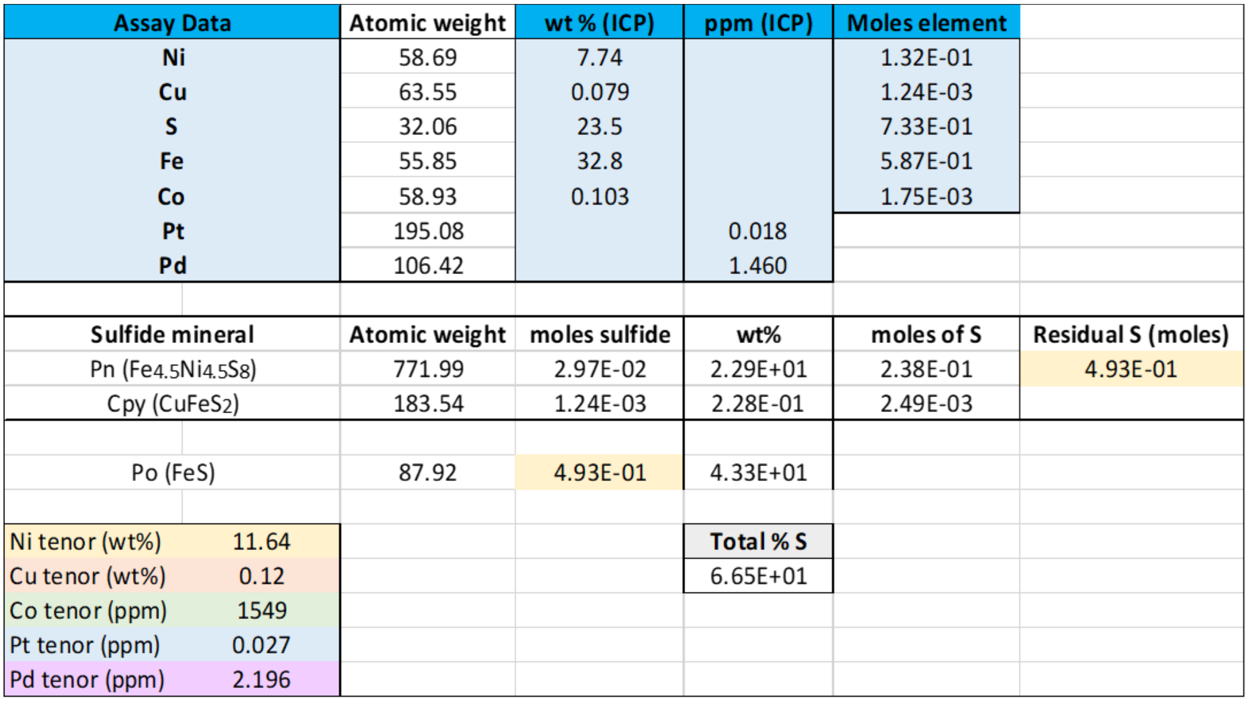

Assay Data	Atomic weight	wt % (ICP)	ppm (ICP)	Moles element	
Ni	58.69	7.74		1.32E-01	
Cu	63.55	0.079		1.24E-03	
S	32.06	23.5		7.33E-01	
Fe	55.85	32.8		5.87E-01	
Co	58.93	0.103		1.75E-03	
Pt	195.08		0.018		
Pd	106.42		1.460		
Sulfide mineral	**Atomic weight**	**moles sulfide**	**wt%**	**moles of S**	**Residual S (moles)**
Pn ($Fe_{4.5}Ni_{4.5}S_8$)	771.99	2.97E-02	2.29E+01	2.38E-01	4.93E-01
Cpy ($CuFeS_2$)	183.54	1.24E-03	2.28E-01	2.49E-03	
Po (FeS)	87.92	4.93E-01	4.33E+01		
Ni tenor (wt%) 11.64			**Total % S**		
Cu tenor (wt%) 0.12			6.65E+01		
Co tenor (ppm) 1549					
Pt tenor (ppm) 0.027					
Pd tenor (ppm) 2.196					

Note, that this is an idealized tenor calculation where all the residual sulfur in the rock is assumed to make pyrrhotite. However, some of the sulfur in the rock is contained within pyrite, which was ignored in the above normative sulfide calculations. On average there is a 1:6 ratio of pyrite to pyrrhotite in the petrographic thin sections. Therefore, we have to analyze the source of error and take into consideration the residual amount of sulfur used to make pyrite and determine how this effects tenor. A revised calculation of the 'normative sulfide method' is shown below in **Table 4-5**, taking into consideration a 1:5 pyrite to pyrrhotite ratio, which is a slight overestimation of pyrite content for the sake of the discussion:

Taking the residual sulfur (moles) determined from the idealized tenor calculation in **Table 4-4**, we present a 1:5 ratio and assign 20% of that residual sulfur to pyrite (0.2

* 4.93×10^{-1}) and the remaining 80% to pyrrhotite ($0.8 * 4.93 \times 10^{-1}$). The total weight (wt%) of pyrrhotite and pyrite is determined by multiplying the atomic weight of each element by the moles of sulfide. The total weights of pyrrhotite and pyrite are combined and added to the total weights of pentlandite and chalcopyrite determined from **Table 4-4**, resulting in a revised total % sulfur in the system. Tenors (Ni, Cu, Co, Pt, Pd) were then re-calculated by dividing the same elemental weight % values in **Table 4-4** by the new total % sulfur in the system **(Table 4-5)** and multiplying by 100. For a rock with 20% pyrite to 80% pyrrhotite (1:5 ratio), the whole rock Ni tenor of the sample increases by only 0.5 wt% (11.64 wt% Ni in **Table 4-4** to 12.14 wt% Ni in **Table 4-5**). Additionally, Table 4-2 shows how the tenor values (Ni, Cu, Co, Pt, Pd) change when 0% pyrite (**Table 4-4**), 5% pyrite, 10% pyrite, 15% pyrite and 20% pyrite is accounted for in the system. For every additional 5% increase in pyrite (standard composition), the tenor of the sulfide system increases by 0.12% wt% Ni, 16 ppm Co and 0.023 ppm Pd tenor - whilst Cu and Pt tenors stay relatively constant with increasing pyrite. In conclusion, the change in tenor is not significant and therefore we conclude that the effect of pyrite on tenor calculations is relatively small. All tenor values in this research study were calculated using the normative sulfide method expressed in **Table 4-4**, with pyrite being ignored. An excel spreadsheet showing the tenor calculations in **Table 4-4** and **Table 4-5** can be found in **Appendix 10.**

Table 4-5: A revised calculation of the 'normative sulfide method' taking into consideration the residual amount of sulfur used to make pyrite. Tenors (Ni, Cu, Co, Pt, Pd) are expressed with changes to the amount of pyrite in the sulfide system (0%, 5%, 10%, 15%, 20%). Note: this is a 'snapshot' of the tenor calculation spreadsheet in ***Appendix 10****, therefore the 'Total % S' number is variable based on which pyrite % is selected. In this snapshot, the 'Total % S' is representing the 20% pyrite box selection. However, data for each pyrite % column is correct and has been presented correctly.* In conclusion, the change in tenor is not significant and therefore we conclude that the effect of pyrite on tenor calculations is relatively small.

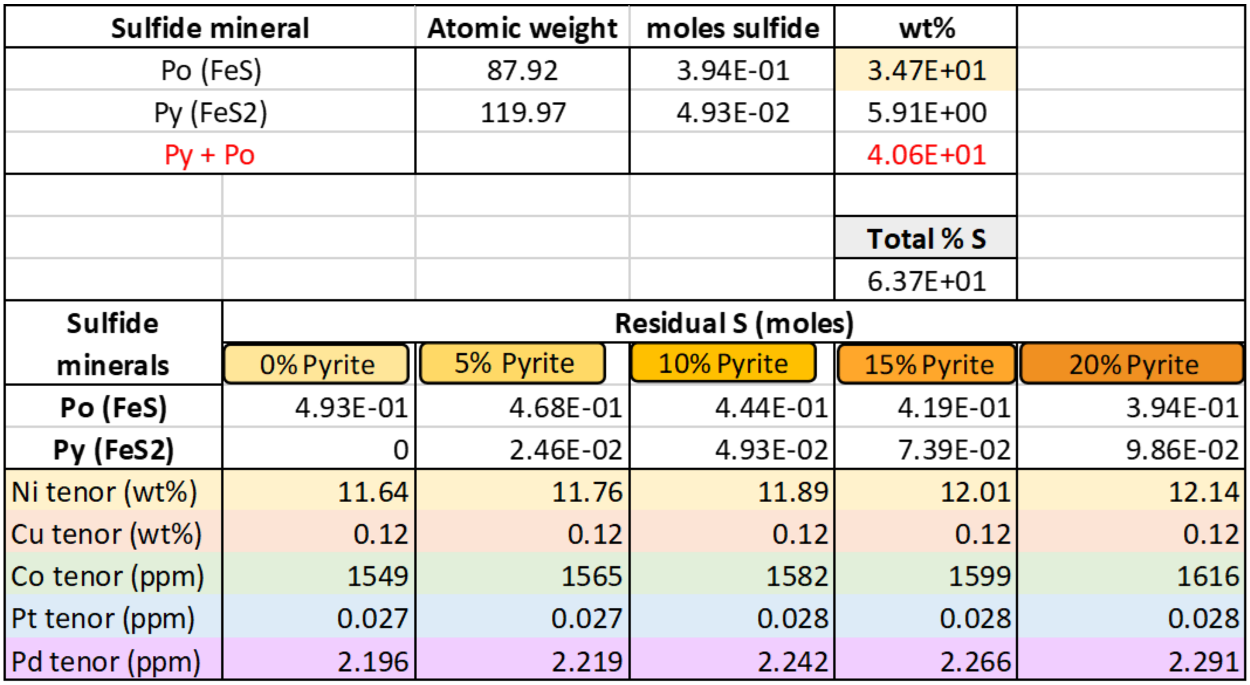

Sulfide mineral	Atomic weight	moles sulfide	wt%	
Po (FeS)	87.92	3.94E-01	3.47E+01	
Py (FeS2)	119.97	4.93E-02	5.91E+00	
Py + Po			4.06E+01	
			Total % S	
			6.37E+01	

Sulfide minerals	**Residual S (moles)**				
	0% Pyrite	5% Pyrite	10% Pyrite	15% Pyrite	20% Pyrite
Po (FeS)	4.93E-01	4.68E-01	4.44E-01	4.19E-01	3.94E-01
Py (FeS2)	0	2.46E-02	4.93E-02	7.39E-02	9.86E-02
Ni tenor (wt%)	11.64	11.76	11.89	12.01	12.14
Cu tenor (wt%)	0.12	0.12	0.12	0.12	0.12
Co tenor (ppm)	1549	1565	1582	1599	1616
Pt tenor (ppm)	0.027	0.027	0.028	0.028	0.028
Pd tenor (ppm)	2.196	2.219	2.242	2.266	2.291

4.4 K-feldspar Staining

A total of 87 thin section blocks comprising of various underground sulfide mineralization assemblages (massive, semi-massive, concordant) and P_2 meta-sediments (biotite-schists, pegmatite-schists) were sent out for K-feldspar staining to Vancouver Petrographics Ltd. The purpose of K-feldspar staining was to test whether the rounded, pegmatitic porphyroclasts (**Section 5.1.3**) that occur within the sulfide mineral zones, are quartz or feldspar-rich. Photos of K-feldspar-stained thin section blocks, and overall observations can be found in **Appendix 11.**

Almost all the massive sulfide thin section blocks have minimal to no K-feldspar porphyroclasts. However, several of the thin-section blocks do have plagioclase porphyroclasts (<1cm) that are enclosed in a sulfide matrix.

The semi-massive sulfide thin-section blocks have plagioclase porphyroclasts along with several K-feldspar porphyroclasts. However, the K-feldspar occurrences are less spherical than the plagioclase porphyroclasts. The K-feldspar rims plagioclase porphyroclasts, or K-feldspar can occur at the core of plagioclase dominant porphyroclasts. This K-feldspar has been corroded and overgrown by plagioclase, with the latter becoming the dominant feldspar in the porphyroclasts. Myrmekitic boundaries of K-feldspar occur in these feldspar porphyroclasts. Furthermore, 'deteriorated' K-feldspar porphyroclasts occur in the vicinity of granular pentlandite eyes. In semi-massive sulfide thin-section blocks it is rare to come across non-deteriorated K-feldspar porphyroclasts within the sulfide ore.

However, K-feldspar does occur in fractures cutting quartz grains/veinlets, representing a hydrothermal origin. Moreover, K-feldspar occurs as fine-grained wisps within the biotite-schist foliation but is more abundant where minor disseminated sulfides are present. Another observation is that where garnet is abundant, plagioclase porphyroclasts occur, but minimal K-feldspar porphyroclasts are present. In conclusion, K-feldspar porphyroclasts rarely occur in massive sulfide thin section blocks and are only present in minor abundances within semi-massive blocks. However, K-feldspar porphyroclasts are abundant in biotite-schist blocks neighbouring sulfide mineral zones.

4.5 Box and Whisker Plots

In the succeeding results sections **(Sections 6** and **7),** box and whisker plots using ioGas^{TM} (geoanalytical program) have been used to interpret data and display findings. Excel spreadsheets and accompanying ioGas^{TM} data files for all plotted figures and tables in this study can be found in **Appendix 12.** A brief overview of box and whisker terminology is necessary to understand how results have been represented.

Box and whisker plots (or box plots) are sets of columns and whiskers that summarize a specific set of data. This method provides a graphical representation using a five-number summary; minimum, first quartile, median, third quartile, and maximum. Group sizes are stated by a number value associated with a specific column. A column (or box) is drawn from the first quartile (Q1) to the third quartile (Q3) of data, with a vertical line going through the box at the median value. The central box represents 50% of the data from Q1 to Q3. Whiskers extrude from either side of the box and represent the extreme minimum and maximum values that are not considered outliers. The mean is represented by a solid black circle placed within the box. The mean represents the average value for a specific set of data displayed by the box. There are two types of outliers: a close outlier (hollow circle) and a far outlier (hollow triangle). A close outlier is represented as a data point further than 1.5 * (Q3 - Q1) from the box. A far outlier is represented as a data point further than 3.0 * (Q3-Q1) from the box.

Chapter 5: Geological Controls on the 1D Orebody

Different styles of ore mineralization in the T3 mine were investigated and mapped. The mapping effort centered on the 602 complex, known as the 1D Lower zone (3700 to 4160 levels) **(Figure 3-3),** because of the heterogeneity in nickel tenor between sulfide lenses. However, some mapping was also completed in the Footwall Deep (4350 to 4850 levels) and Midband complexes (4070 to 4900 levels).

During mapping of individual stopes underground, several key aspects were recorded: the lithologies of main units, occurrence of shears and faults, pegmatite abundance, ultramafic boudins, sulfide mineralization and mineral associations. These geological observations along with timing relationships are important in understanding the thermo-evolution and mineral controls of the 1D orebody.

5.1 Lithologies and Temporal Relationships Between Rock Units

5.1.1 P_2 Member Schist

The P_2 member of the Pipe Formation is the main host to sulfide ore within the TNB. It is the most aluminum-rich (10 - 25 wt% Al_2O_3) metasedimentary unit within the Ospwagan Group (Burnham et al., 2009) and is characterized as mica-graphite schist with abundant porphyroblasts of garnet (up to 3cm), andalusite (<1cm), staurolite (<1cm), and fibrous sillimanite wisps (<10cm), which are concordant to schist foliation. The P_2 schists are steeply dipping, on average between 60-80º (from underground measurements in this study); interlayered with lenses of fine-grained chert (<5cm), calc-silicate and silicate facies iron formation (Layton-Matthews et al., 2007). The P_2 member is commonly pegmatite-rich, deemed pegmatite-schists (PSch) by Vale Canada Ltd. geologists. Pegmatite-schists host a vast number of pegmatitic swets and wisps (<10 cm), boudined veinlets and dykes, that have been heavily stretched, deformed and incorporated within the P_2 pelitic schist unit.

Nickel contents of P_2 member pelitic schists near sulfide horizons and in barren sulfide horizons of the TNB were compared. Seventeen underground samples of P_2 pelitic schists from the Thompson 1D orebody and fourteen drill core samples of P_2 pelitic schists from regional drill holes (DH#1238990 and DH#892880) several kilometers away from the Thompson 1D, were collected, assayed, and compared. The P_2 pelitic schist samples from sulfide barren regional drill holes contained whole rock values of 54 ppm Ni on average. Whereas P_2 pelitic schist samples taken from the Thompson 1D contained whole rock values of 178 ppm Ni on average. The reader is referred to **Appendix 3** for the whole rock assay data of samples.

5.1.2 Ultramafic Units

Ultramafic boudins are more commonly observed in the 1C, compared to the 1D ore zones. In most instances, ultramafic boudins have experienced hydration, either high degrees of pervasive serpentinization or talc-carbonate alteration. Biotite and fibrous anthophyllite commonly occur as haloes (up to ~30 cm) around ultramafic bodies. Ultramafic bodies as well as their biotite and anthophyllite haloes contain abundant garnet porphyroblasts (<2cm). All ultramafic bodies are tabular in shape, with signs of strong deformation. Ultramafic lenses are boudinaged with sulfide mineralization being present as shadow zones around the ultramafic bodies. The ultramafic bodies have experienced multiple phases of deformation, similar to the schist country rocks, indicating that the ultramafic bodies intruded syn- to post- sedimentation of Ospwagan sediments, but prior to initial deformation (Bleeker, 1990; Layton-Matthews et al., 2007). Three main ultramafic bodies were identified in both the 1C and 1D zones (pers. comm., Vale Canada Ltd. Geologists): pyroxenites, peridotites and amphibolites, but the classification of these ultramafic boudins is beyond the scope of the research of this study. The reader is referred to Layton-Matthews et al. (2007) and Franchuk et al. (2016) for further information on classification of ultramafic intrusions within the TNB.

5.1.3 Pegmatites

As discussed in **Section 2.**1, three main stages of pegmatite emplacement occurred throughout the evolution of the TNB (Machado et al., 2011); pre-, syn- and post- sulfide mineralization and remobilization. Underground observations and timing relationships of pegmatites at T3 (this study) support this conclusion.

Pegmatite-schists (PSch) host a vast number of pegmatitic swets and wisps (<10 cm), boudined veinlets and dykes, that have been heavily stretched, deformed and incorporated within the P_2 schist unit **(Figure 5-1).** Abundant pegmatite dykes are concordant to highly deformed P_2 schist foliation in the 1D orebody, as seen in **Figure**

5-1. Furthermore, there are abundant pinch and swell structures of pegmatites commonly occurring in heavily folded regions in the 1D **(Figure 5-2).**

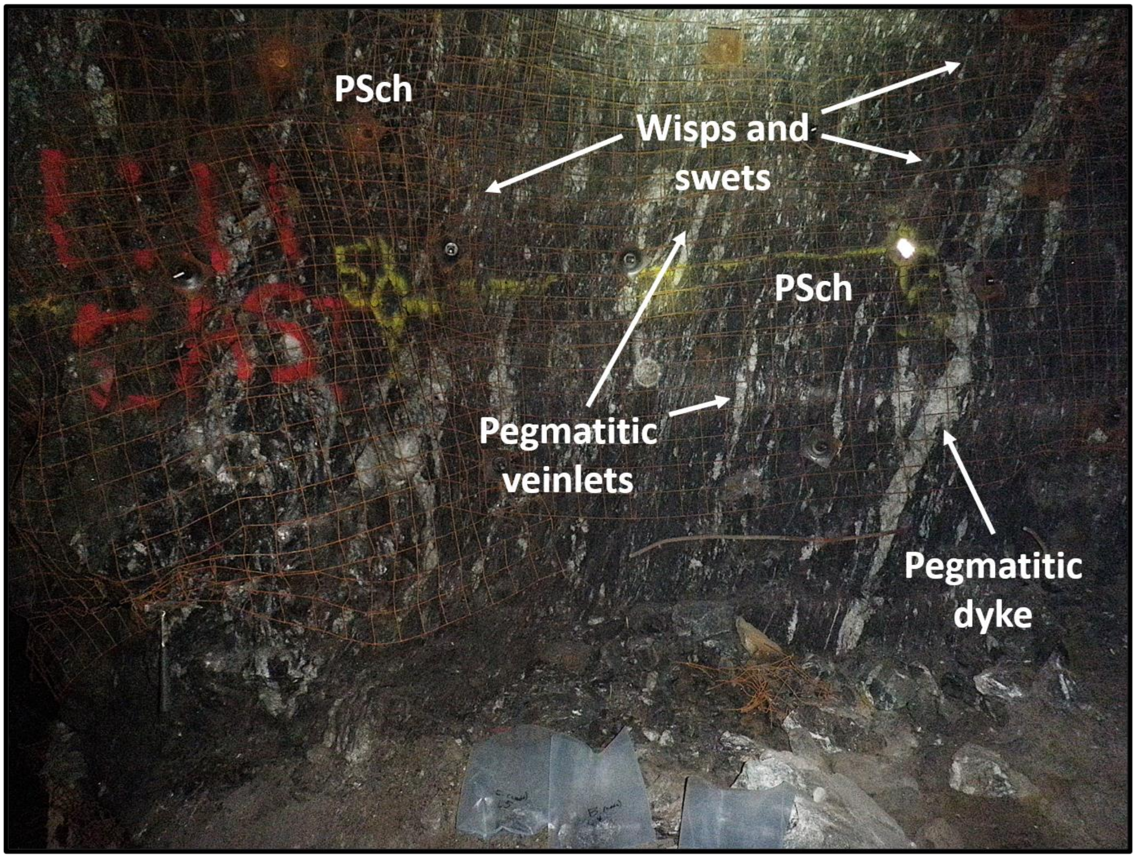

Figure 5-1: Underground photograph in the 1D orebody shows the pegmatite schist unit (PSch). Abundant pegmatitic swets, wisps and veinlets that have been heavily stretched, deformed and now incorporated within the P2 schist unit. The pegmatite dyke (right side of photo) forms parallel to the P2 schist foliation. Metal screen for scale – three squares = 1 foot (~30 cm). Abbreviations: PSch (pegmatite-schist).

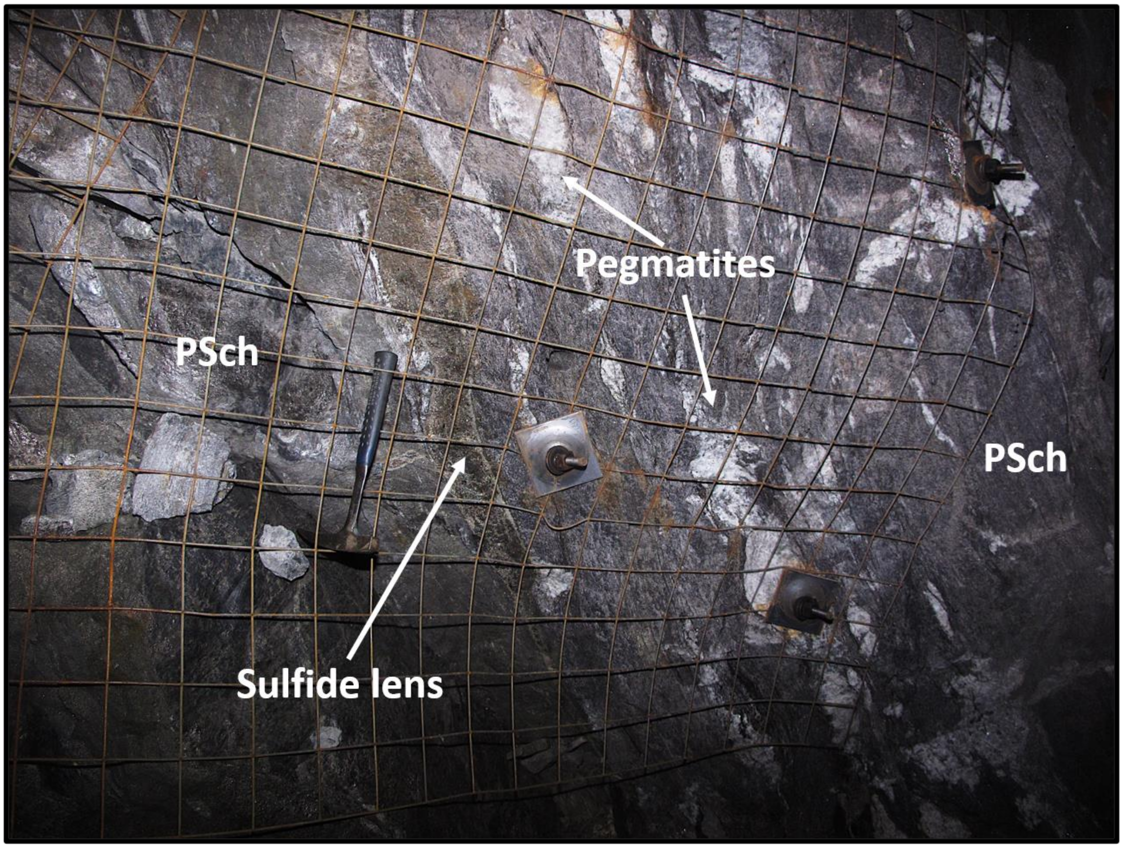

Figure 5-2: Underground photograph in the 1D orebody showing abundant pinch and swell pegmatites aligned concordant to P_2 PSch foliation. Notice the sulfide body forming concordant to the boudined pegmatites and PSch beds. Metal screen for scale – three squares = 1 foot (~30 cm). Abbreviations: PSch (pegmatite-schist).

The deformed nature of the pegmatite dykes indicate that they were deformed synchronously with the schists, which provides evidence for a very early stage of pegmatite emplacement at Thompson. Machado et al. (2011) proposed that the first pulse of felsic magmatism in the TNB was coeval with the Molson dyke swarm; 1891 – 1871 Ma (Machado et al. 2011) or 1883 ± 2 Ma (Heaman et al., 1986, 2009) (**Section 2.1**). The Molson dykes cross cut F_1 Nappe folds, therefore D_1 deformation ceased prior to the emplacement of the Molson dyke swarm (Bleeker, 1990) **(Section 2.3).**

Therefore, early pegmatite emplacement would have also post-dated regional compression (D_1) and development of F_1 folds (Bleeker, 1990; Machado et al., 2011).

Additionally, several pegmatites have been observed to cross-cut pegmatite-schist (PSch) in the Thompson 1D. These pegmatites intrude pre-existing, deformed, pegmatite dykes and veinlets. This younger generation of pegmatites can form syn-anticlinal folds in heavily deformed areas. This suggests at least two different generations of pegmatitic intrusions in the Thompson 1D orebody. Machado et al. (2011) classifies these younger pegmatites as a later pulse of pegmatitic generation, emplaced pre-to-syn peak metamorphism (end of D_2), which are subsequently deformed by F_2 and F_3 folds at the end of D_2. It is interpreted that this younger generation of pegmatite dykes were syngenetic to sulfide remobilization in the TNB and were emplaced 1850 to 1785 Ma (Machado et al., 2011).

Moreover, several pegmatite bodies crosscut both PSch foliation (first generation), and older boudinaged pegmatite bodies (second generation). These pegmatites are less deformed than their earlier counterparts. They are not extensively boudinaged, however, they have non-linear contacts with a swelled nature, which is evidence of being slightly deformed. This provides evidence for a third generation of pegmatite veins in the Thompson 1D and would suggest an even younger pegmatitic pulse that occurred after peak metamorphism (post D_2) and post sulfide re-emplacement (Machado et al., 2011). Machado et al. (2011) classifies these pegmatites belonging to a third stage of pegmatitic generation in the TNB, that were emplaced between 1780 and 1750 Ma.

In this study, it was noted that pegmatites (second and third generation) commonly occur near sulfide lenses, either bordering sulfide horizons or crosscutting them. In the case of the former, pegmatites are emplaced along shear zones, which also border Ni sulfide mineralization. In the case of the latter, pegmatites that cut various sulfide horizons were observed at multiple locations within the Thompson 1D.

All three generations of pegmatites are felsic, consisting of very coarse-grained (several cm) quartz and feldspar grains, as well as muscovite and biotite laths. The feldspars in pegmatites are either; entirely white **(Figure 5-3A)** as is more common in the first PSch generation of pegmatites, pink **(Figure 5-3B)**, or both. Pegmatites typically contain coarse-grained, black biotite laths that are interlocked with the feldspars **(Figure 5-3 A, B).**

Fuchsite (chromium-rich mica) is an apple-green alteration mineral that commonly occurs within the altered pegmatites. Fuchsite also occurs within the schist, as concordant veinlets near the contacts with pegmatite bodies. Fuchsite-rich pegmatitic porphyroclasts are also commonly incorporated within inclusion-bearing sulfide ore throughout the 1D orebody. Fuchsite is a common mineral in Archean supracrustal belts, in komatiite dominated source terrains, commonly attributed to metasomatism and/or metamorphism (Martyn and Johnson, 1986). Fuchsite may also be indicative of high chromium content of pelitic sediments (Martyn and Johnson, 1986). Burnham et al. (2009) reports on average ~100ppm Cr in P_2 member pelitic schists of the Pipe Formation. Fuchsite does not occur in the primary magmatic crystallization process (Martyn and Johnson, 1986), and therefore may reflect a variety of post-magmatic processes beyond the scope of the study. Illite (secondary clay mineral) occurs as a yellow alteration mineral within pegmatites, as a replacement product of muscovite and feldspars.

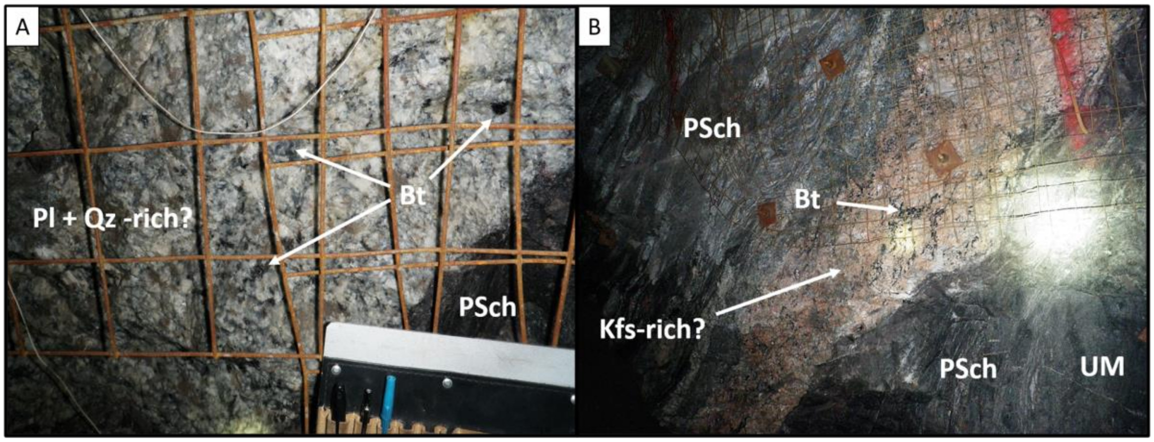

Figure 5-3 A) Pegmatite in the Thompson 1D are made up of dominantly white minerals, plagioclase + quartz-rich? Black biotite laths interlocked with felsic minerals. B) Pegmatite in the Thompson 1D made up of dominantly pink minerals, K-feldspar-rich? Black biotite laths are interlocked with felsic minerals. Abbreviations; PSch – pegmatite-schist; UM – ultramafic; Pl – plagioclase; Kfs – K-feldspar; Bt – biotite. Metal screen for scale – three squares = 1 foot (~30 cm).

Furthermore, several silicate ‘concretions’ occur wrapped by P_2 schists. These concretions are usually oval or round shaped, <1 meter in size, and commonly banded with white, brown-black-pink colored layers. The brown-black and pink-rich layers are very fine-grained, whereas the white layers are more medium to coarse-grained. The white layers resemble pegmatitic type mineral assemblages – plagioclase and quartz grains (<5 mm) interlocked by biotite and mica laths. These ‘concretions’ are rare and will not be discussed further.

5.1.4 Sulfides

A detailed description of the main sulfide minerals in the 1D orebody, is documented in Chapter 7, however, a general overview of sulfides and their timing relationships will be discussed here. The main sulfide minerals in the 1D orebody, are from greatest to least abundant: pyrrhotite, pentlandite, pyrite, chalcopyrite and gersdorffite. Pyrrhotite is the dominant sulfide assemblage that hosts all other sulfides and is generally fine-grained (<1cm). Pyrrhotite grain contacts are generally difficult to see in hand sample. Pentlandite is the dominant Ni-bearing sulfide in the TNB, and generally occurs as euhedral pentlandite ‘eyes’ (up to 5 cm) within pyrrhotite-rich matrix. Granular pentlandite eyes are aligned into trails (several cm long) and loop-textures, which are evident in hand samples. Pyrite in the 1D orebody is generally fine-grained (<1cm), and characteristically is wrapped around pentlandite eyes in hand samples. Chalcopyrite is the dominant Cu-bearing sulfide and generally occurs as anhedral, fracture-infill within schist wall rock and silicate intrusions trapped in the sulfide matrix. Gersdorffite occurs as euhedral grains hosted within pyrrhotite and pentlandite grains and generally it is too fine grained (<5 mm) to be identified in hand sample.

The mineralization styles characterized during underground mapping, key geological features and the dominant mineralization styles that occur on every mine level are summarized in **Table 5-1.** This includes a list of all samples collected, their mineralization styles, locations and Ni, Co, Cu, Pt, Pd tenors. Sulfide bodies in the 1D orebody are dominantly massive to semi-massive lenses and concordant vein-sets. The sulfide mineralization has been classified into five main styles, which are discussed below. Sulfide ores are typically inclusion-bearing (biotite and graphite laths, garnet porphyroblasts), with numerous brecciated clasts of foliated P_2 schist wall rock, ultramafic and/or pegmatite porphyroclasts within the sulfide matrix. Sulfides are strongly deformed, concordant to steeply-dipping P_2 schist fold limbs, and are concentrated in fold hinges, limbs and dilation zones in the wall rock **(Table 5-1)** (House 2009). In the Thompson 1D, higher nickel tenor sulfide lenses tend to be associated with shears that run along fold limbs and the general structural trend of F_3 folds, as opposed to fold hinges **(Table 5-1).** From **Table 5-1** it is evident that shear-hosted mineralization is the dominant ore type in the 1D orebody.

Sulfide mineralization occurred after sedimentation of the Ospwagan group had concluded (Bleeker, 1990), with U-Pb zircon age dating constraining sulfide mineralization to 1880 ± 5 Ma (Hulbert et al., 2005). The TNB country-rocks have experienced at least four stages of deformation and metamorphism (Bleeker, 1990), which have remobilized the sulfides from primary ultramafic intrusions into secondary-hosted metasediments of the Ospwagan group during D_1 to D_4 (House, 2009; Lightfoot et al., 2017). Doubly-plunging, F_3 folds caused by D_3 deformation are the dominant sulfide ore controlling structures; aligning the geometry of the sulfides to be parallel to F_3 fold axes (Lightfoot et al., 2017). The Ni tenors in the metasediment-hosted sulfides of the 1D orebody range from 4-16 wt% (Lightfoot et al., 2017).

Tenor variations are homogenous along a sulfide vein, but distinctly heterogenous between different sulfide lenses, as depicted by deposit-scale studies of the Thompson 1D orebody from Lightfoot et al. (2017). However, from underground observations in this study of the Thompson 1D both barren and nickeliferous sulfide horizons occur along strike, neighbouring shear structures. Based on grab sample locations on plan maps **(Appendix 1)**, several gradations in Ni tenor are shown to exist within individual sulfide lenses on the scale of a stope. Possibly explained by remobilization of ore bearing fluids from one part of the sulfide body to another via shear zones in the 1D, as proposed by Liwanag et al. 2001 and discussed in **Section 8.5.2**. However, samples were plotted on plan maps based on ‘general’ locations; mine level, header, slot, cut ± northing **(Appendix 2)**. A lack of confidence in the exact sample locations (x,y,z coordinates) has hindered the ability to accurately plot samples locations, and ‘general’ locations were used. Therefore, it cannot be ruled out that the possibility of nickel tenor gradations along individual lenses may exist. However, this cannot be confidently proposed in this study.

Table 5-1: Twenty-six stopes and surrounding areas were mapped, dominantly from the Thompson 1D Lower zones [602, North Extension, South Extension), but also the Footwall Deep (FW Deep) and Midband zones. Note, 602 is a generic term that encompasses the whole of the 1D Lower zone (3700 to 4160 mine levels). Mapping spanned across eleven different mine levels (3590 – 4550) at T3 mine; a total of 78 underground sulfide samples were collected. The table also outlines key geological features, dominant mineralization styles [SH (shear-hosted); MASV (massive); SM (semi-massive); Conc (concordant); UMA (ultramafic associated)] and total # of samples collected from each mine level. Every sample is from a specific mine complex, from the 1D orebody, on a defined mine level, with sample locations listed. All sulfide samples have their respective mineralization styles and tenors shown (Ni, Cu, Co, Pt, Pd – normative sulfide method). The table also depicts where the sulfide ore is structurally located on every mine level (fold limbs or fold hinges), the grain size of every sample collected, presence of pegmatite porphyroclasts, and if the ore is inclusion-bearing. Pyrite ‘modal’ abundances (%) were determined visually via petrographic analysis. Grain-sizes; vfg (very fine-grained) <1.0 mm; fg (fine-grained) <2.0 mm; mg (medium-grained) <3.0 mm; cg (coarse-grained) 3.0-5.0 mm; vcg (very coarse-grained) >5.0 mm.

Mine level	Main min. style	# of samples	Key features	Structure	Mine complex	Stope (1-26)	Sample ID	Header	Slot (horiz.)	Cut (vert.)	Northing	Pt tenor (ppm)	Pd tenor (ppm)	Co tenor (ppm)	Cu tenor (wt%)	Ni tenor (wt %)	Ni tenor ranking	Min. style	Inclusion-bearing?	Peg clasts?	Grain-size	Pyrite %
3590	Shear-hosted	2	Vfg ore. Interlayered quartzites (setting frm.) with pelitic schists. Heavily sheared area, sulfides along fold limbs adjacent to shears. Many boudined pegs present. No cg Pn	Fold limbs	North Ext.	1	1045347				39050	2.57	3.08	1489	0.27	11.22	High	MASV	Yes	No	vfg	10
						2	1045343				39100	0.06	2.38	1434	0.21	11.06	High	SH	Yes	Yes	vfg	2
3700	Shear-hosted/ Concordant	11	Int-grained ore. Pelitic schists with boudined pegs and numerous peg swets. Presence of several ultramafic and amphibolite bodies. Moderately sheared area. Sulfide lenses forming concordant to pelitic schist foliation, in fold limbs adjacent to shear zones. Inclusion-bearing ore with numerous pegmatitic nodules.	Fold limbs	602	3	1045362	L21W	L slot	11		0.04	1.58	1405	0.43	10.13	High	UMA	Yes	No	ig	7
							1045382	23MN	L slot	11		0.08	2.60	1919	0.43	14.50	Very high	Conc	Yes	Yes	ig	10
							1045411	L23E	L slot	11		1.34	1.98	1851	0.12	13.08	Very high	SH	Yes	Yes	ig	20
							1045412	L23E	L slot	11		0.06	2.39	1353	0.12	12.26	Very high	SH	Yes	Yes	ig	8
							1045407	22HN	L slot	11		0.02	1.01	704	0.16	6.28	Moderate	Conc	Yes	Yes	fg	1
							1045402	J22W	L slot	11		0.20	3.05	1309	0.05	9.78	High	UMA	Yes	No	ig	5
						4	1045401	20GS	20	12		0.50	1.88	1427	0.92	9.47	High	Conc	Yes	Yes	fg	5
							1045408	20GS	20	12		0.04	2.49	1369	0.59	9.24	High	SH	Yes	Yes	ig	3
							1045379	20GS	20	12		0.07	1.04	1452	0.17	9.14	High	SM	Yes	No	ig	5
							1045383	20GS	20	12		0.04	1.21	1286	0.14	8.45	Moderate	UMA	Yes	Yes	ig	8
							1045441	20GS	20	12		0.02	1.02	1255	0.13	8.28	Moderate	Conc	Yes	Yes	ig	5
3770	Shear-hosted	3	Int- to cg-ore. Pelitic schists with interlayered, boudined pegmatites and numerous pegmatitic wisps and swets. Minor presence of amphibolites. Heavily sheared and faulted area. Sulfide lenses forming concordant to pelitic schist foliation, along fold limbs	Fold limbs	602	5	1045397		34			0.61	3.28	1255	0.15	11.50	High	Conc	Yes	Yes	cg	10
							1045410		34			0.13	4.17	1437	0.22	13.12	Very high	SH	Yes	Yes	ig	8
							1045415		34			0.23	3.43	1434	0.08	13.82	Very high	SH	Yes	Yes	cg	25
3800	Concordant / Shear-hosted	18	Int- to cg-ore. Pelitic schists with presence of pegmatitic swets and wisps. Heavily folded area, with moderate shearing. Presence of ultramfaic and amphibolite boudins with sulfides around them. Sulfides forming concordant lenses along fold limbs and within fold hinges of pegmatitic schists. Several lenses of sulfide adjacent to shears that schist foliation. Ore is very inclusion bearing, with presence of pyrite.	Fold limbs/ fold hinges	602	6	1045346	27.5LN	26	10		0.04	3.23	2083	0.24	13.73	Very high	SM	Yes	No	ig	12
							1045360	27.5LN	26	10		0.07	2.73	2154	0.13	12.37	Very high	Conc	Yes	No	ig	8
							1045361	M28E	26	10		0.02	1.45	1170	0.04	8.48	Moderate	UMA	No	No	cg	10
							1045365	26IN	26	10		0.01	1.18	1504	0.04	11.92	High	MASV	Yes	No	cg	25
							1045371	L27E (M27E)	26	10		0.11	4.89	1948	0.29	13.88	Very high	SH	Yes	Yes	ig	10
							1045372	M27.5E	26	10		0.10	2.52	2086	1.24	16.36	Very high	SH	Yes	No	ig	10
							1045373	28NN	26	10		11.02	2.24	1959	0.51	11.51	High	UMA	Yes	No	vcg	8
							1045376	L27.5E	26	10		0.27	3.99	2046	1.57	14.39	Very high	SH	Yes	Yes	ig	5
							1045377	M26.5W	26	10		0.73	3.73	1878	0.26	14.55	Very high	Conc	Yes	No	ig	20
							1045384	M28E	26	10		0.05	2.53	2358	0.38	12.31	Very high	UMA	Yes	Yes	ig	9
							1045395	28ON	26	10		14.55	2.73	1499	0.10	10.11	High	UMA	Yes	Yes	ig	15
							1045438	M26W Pillar	26	10		0.04	2.64	1905	0.34	14.08	Very high	SH	Yes	Yes	ig	6
							1045409	H34W	26	10		0.39	1.98	1599	0.35	10.01	High	Conc	Yes	Yes	fg	5
							1045413	L27.5E	26	10		5.93	2.68	1398	0.22	9.35	High	Conc	Yes	Yes	ig	8
							1045439	M26E Pillar	26	10		0.06	2.88	1880	0.13	13.86	Very high	SH	Yes	Yes	fg	8
							1045437	H34W	26	10		1.32	2.96	2166	0.61	12.44	Very high	Conc	Yes	Yes	ig	4
						7	1045396	20GS	20	12		0.02	1.09	1246	0.07	8.62	Moderate	Conc	Yes	Yes	cg	5
					South Ext.	8	1045416				36050	1.39	1.96	1723	0.17	11.57	High	Conc	Yes	Yes	ig	5
3890	Concordant	3	Fine- to Int-grained ore. Pelitic schists interlayered with dirty-quartzites - Setting frm. contact nearby. Numerous boudined pegmatites concordant to schist foliation. Sulfide lenses forming concordant along limbs of steeply dipping schists and within fold hinges.	Fold limbs	Midband	9	1045386				35800	0.01	1.58	1380	0.22	10.56	High	SM	Yes	Yes	ig	5
							1045403				35800	0.01	2.08	1342	0.43	10.21	High	Conc	Yes	Yes	fg	5
							1045417				35800	0.01	1.44	1296	0.35	10.18	High	Conc	Yes	Yes	ig	5

Mine level	Main min. style	# of samples	Key features	Structure	Mine complex	Stope (1-26)	Sample ID	Header	Slot (horiz.)	Cut (vert.)	Northing	Pt tenor (ppm)	Pd tenor (ppm)	Co tenor (ppm)	Cu tenor (wt%)	Ni tenor (wt %)	Ni tenor ranking	Min. style	Inclusion-bearing?	Peg clasts?	Grain-size	Pyrite %
4070	Concordant / Shear-hosted	19	Fine- to Int-grained ore. Pelitic schists with shear zones forming conformable to schist foliation. Heavily sheared area. Minor presence of ultramafic boudins, but numerous boudined pegmatites emplaced within schist foliation. Sulfide lenses forming concordant to steeply-dipping pelitic schists - emplaced along fold limbs adjacent to several shear structures developed on limbs. Ore is brecciated and inclusion-bearing - lots of pegmatitic inclusions.	Fold limbs/ fold hinges	602	10	1045351	H11W	8	10		3.13	4.92	1816	1.58	13.77	Very high	Conc	Yes	Yes	ig	5
							1045367	H11W	8	10		0.38	2.63	1521	0.66	11.91	High	SH	Yes	Yes	ig	5
							1045368	H11E	8	10		0.13	2.68	2053	1.61	10.88	High	SH	Yes	Yes	fg	5
							1045369	H11N	8	10		1.34	3.21	1059	0.37	10.38	High	SH	Yes	Yes	fg	2
							1045381	11IN	8	10		0.08	2.39	1296	0.50	9.29	High	Conc	Yes	Yes	ig	7
							1045406	8HN	8	10		0.20	3.01	1672	0.33	12.11	Very high	Conc	Yes	Yes	fg	5
							1045418	H14W	8	10		0.44	3.10	1800	0.24	13.82	Very high	Conc	Yes	Yes	fg	5
							1045419	8H Pillar	8	10		16.87	3.53	1534	0.39	12.42	Very high	Conc	Yes	Yes	ig	7
							1045442	11IS	8	10		0.07	0.93	1252	0.14	10.80	High	SM	Yes	Yes	ig	6
						11	1045344	15FS	13	10		0.02	1.86	1560	0.25	11.38	High	Conc	Yes	No	fg	10
							1045352	F13W	13	10		0.07	2.74	1688	0.12	11.00	High	Conc	Yes	No	ig	10
						12	1045339	C20E	19	10		0.01	2.10	513	0.41	6.88	Moderate	MASV	No	No	fg	0
							1045345	C22E	19	10		0.01	2.34	496	0.63	6.82	Moderate	Conc	Yes	No	ig	0
							1045353	20DN	19	10		0.01	1.07	611	0.45	7.53	Moderate	MASV	Yes	No	vfg	0
						13	1045338	H22E	30	8		0.02	1.80	1111	0.13	9.67	High	MASV	No	No	cg	3
							1045341	H22E	30	8		0.18	3.67	1184	1.26	9.47	High	SM	Yes	No	cg	5
							1045378	29IS	30	8		0.09	3.24	1482	0.25	12.56	Very high	Conc	Yes	No	ig	12
							1045436	25IS	30	8		14.47	4.34	3566	0.51	14.95	Very high	SH	Yes	Yes	ig	20
					Midband	14	1045370				35500	0.03	1.84	1328	0.24	9.95	High	MASV	Yes	No	ig	10
4160	N/A	1	Pelitic schists interlayerted with Setting frm. quartzites.	N/A	Midband	15	1045342				35700	1.04	2.34	1177	0.27	9.26	High	MASV	Yes	No	ig	4
4250	Shear-hosted	6	Fine- to Int-grained ore. Pegmatite-rich, pelitic schists with large presence of numerous amphibolite boudins. Heavily sheared area. Large pegmatite presence; pegmatites running conformable to schist foliation. Sulfide lenses emplaced adjacent to distinct shear zones that run conformable to schist fold limbs. Sulfide ore inclusion-bearing but generally very dull/brassy and fine-grained.	Fold limbs	FW Deep	16	1045440				37300	2.82	3.95	1609	0.17	15.94	Very high	SH	Yes	Yes	ig	5
						17	1045380				37500	0.02	3.90	997	0.20	9.94	High	SH	Yes	Yes	ig	8
						18	1045404				37550	0.01	0.20	237	0.08	1.74	Low	MASV	Yes	Yes	fg	0
							1045405				37550	0.01	0.15	209	0.05	1.71	Low	MASV	Yes	No	fg	0
						19	1045391				37600	0.15	2.08	1119	0.08	12.01	Very high	SH	Yes	Yes	fg	10
							1045392				37600	5.13	2.64	1499	0.12	12.67	Very high	SH	Yes	Yes	ig	8
4350	Concordant / Shear-hosted	6	Int- to cg-ore. Pelitic schists with dominant shears developed conformable to schist foliation. Several amphibolite boudins emplaced along schist foliation as well. Pegmatites emplaced along shears. Sulfide lenses also show a conformable nature, forming parallel to fold limbs, adjacent to shears.	Fold limbs	FW Deep	20	1045359				37300	0.89	2.55	1581	0.83	12.46	Very high	Conc	Yes	Yes	cg	4
							1045394				37300	0.98	0.90	1290	0.03	10.16	High	Conc	Yes	Yes	ig	15
						21	1045393				37550	0.21	2.09	1440	0.25	15.25	Very high	Conc	Yes	Yes	cg	0
						22	1045348				37600	0.02	2.58	1971	0.57	9.72	High	MASV	No	No	cg	35
							1045349				37600	3.63	2.21	1591	0.10	11.37	High	SH	Yes	No	ig	10
							1045374				37600	0.18	9.55	1683	0.97	12.47	Very high	SH	Yes	Yes	ig	7
4450	Massive	2	Fg-massive ore. Pelitic schists with numerous pegmatites forming along schist foliation, as well as cross-cutting sulfide lenses. Sulfides emplaced along fold limbs.	Fold limbs	FW Deep	23	1045387				37600	0.01	0.61	254	0.16	2.84	Low	MASV	No	No	fg	0
						24	1045399				37750	0.01	0.30	223	0.15	2.45	Low	MASV	No	Yes	vfg	1
4550	Massive	7	Fg- to cg-ore. Pelitic schists with interlayered setting frm. quartzites. High ultramafic and amphibolite presence. Heavily folded area. Pegmatite boudins forming along schist foliation. Not as many shears. Sulfide lenses along fold limbs of schist foliation.	Fold limbs	Midband	25	1045357		46	1		0.01	3.38	1633	0.64	11.42	High	MASV	Yes	No	cg	10
							1045363	46RS	46	1		0.02	2.79	1347	0.88	9.89	High	Conc	Yes	Yes	fg	5
							1045364	46RS	46	1		0.03	5.36	844	12.90	5.72	Low	MASV	Yes	No	cg	5
							1045389	46RN	46	1		0.02	1.50	1154	0.50	8.45	Moderate	UMA	Yes	Yes	vcg	10
							1045414	46PS	46	1		0.11	2.93	1132	1.03	9.57	High	SM	Yes	Yes	cg	0
					FW Deep	26	1045398				37800	0.01	0.34	215	0.25	2.61	Low	MASV	No	Yes	vfg	0
							1045390				37800	0.01	0.26	225	0.21	1.88	Low	MASV	Yes	No	fg	0

5.2 Structures and Timing Relationships

5.2.1 Shears

The Thompson 1D orebody is modified by large-scale shear structures (Bleeker, 1990; Layton-Matthews et al., 2007) that commonly are concordant to the steeply dipping P_2 foliation of the schist. These shears range from 0.5 – 5 metres in width and abundantly contain graphitic slickenside planes. An unidentified brittle, whitish-pink carbonate was observed to occur in sets of en echelon veins within shears, whereas larger en echelon quartz veins occur in the P_2 schist wall rocks that border shear zones. In both cases, the en echelon vein sets are closely spaced, sub parallel to each other, and are oblique to the overall structural trend. These en echelon veins also rarely consist of fine-grained pyrite. These extensional veins are kinematic indicators, and formed in response to late-tectonic stage, brittle-ductile deformation caused by dip-slip displacement along brittle faults and reactivated shears caused by D_4 deformation (Bleeker, 1990).

A common observation is that sulfide lenses in the Thompson 1D tend to occur continuously along large shears; sulfide bodies commonly exist along and in contact with these shear zones. Several shears are also mineralized (MSHR) and contain sulfide veinlets, a feature that Vale geologists commonly interpret from drill core. From the underground observations in this study, it is difficult to conclude whether sulfide lenses are pre-, syn-, or post-shearing. However, from literature it is widely accepted that sulfide mineralization was pre- to syn-D_1 deformation – as discussed in **Section 2.4**

(Heaman et al., 1986, 2009; Bleeker, 1990; Burnham et al., 2009; Hulbert et al., 2005; Machado et al., 2011; Lightfoot et al., 2017). Therefore, sulfide mineralization occurred before the onset of TNB deformation, with sulfides being remobilized during D_1 to D_4. It is also known that local shearing started with D_2, during tight to isoclinal F_2 fold development, but was mainly localized at the contact between basement TNB gneisses and adjacent supracrustal Ospwagan metasediments (Burnham et al., 2009; Layton-Matthews et al., 2007). However, most shearing occurred during the later stages of structural evolution of the TNB (Burnham et al., 2009). Shear zones were dominantly caused by high-strain deformation of the transpressive ductile regime D_3 to D_4, synchronous to Thompson Dome formation (Burnham et al., 2009). Shear zones are typically parallel to steeply dipping limbs of upright F_3 folds (Bleeker and Macek, 1996); the doubly-plunging F_3 folds are also the dominant ore controlling structures (Lightfoot et al., 2017). Therefore, from our evidence and literature, there seems to be a connection between late-shears and sulfide remobilization. Sulfides were remobilized along high-strain, steeply-dipping, retrogressed and young deformation zones (Burnham et al., 2009). Sulfide mineralization is pre- to syn-D_1 deformation, and pre-shearing (D_3). However, the remobilization of primary sulfide hosted by ultramafic boudins into the surrounding metasedimentary rocks is most likely synchronous with shear formation.

5.3 Key Underground Observations

5.3.1 Barren Massive Sulfide

The 1D orebody contains stopes with barren massive sulfide lenses, adjacent to other stopes on the same mine level with nickeliferous massive sulfide bodies. In both cases, the sulfides are fine to medium-grained, inclusion-poor, brassy in appearance. The two types of sulfide mineralization are sometimes not easily distinguished underground in cases where the pentlandite is fine-grained. Barren sulfide lenses have <1% Ni tenor, whereas nickeliferous sulfide lenses have >8% Ni tenor.

5.3.2 Pyrite-Biotite Association

Underground mapping completed for this study indicates that biotite is commonly associated with pyrite **(Figure 5-4)**, although this relationship is not associated with a specific mineralization style. Biotite laths are typically jet-black and tend to be surrounded by lenses of massive pyrite. Furthermore, pyrite is also present in rims around ultramafic bodies and on the outer margins of several sulfide lenses. These sulfide lenses are dominantly Po>Pn rich, with the Py concentrated in the outer margin that is in contact with the P_2 meta-sedimentary schists.

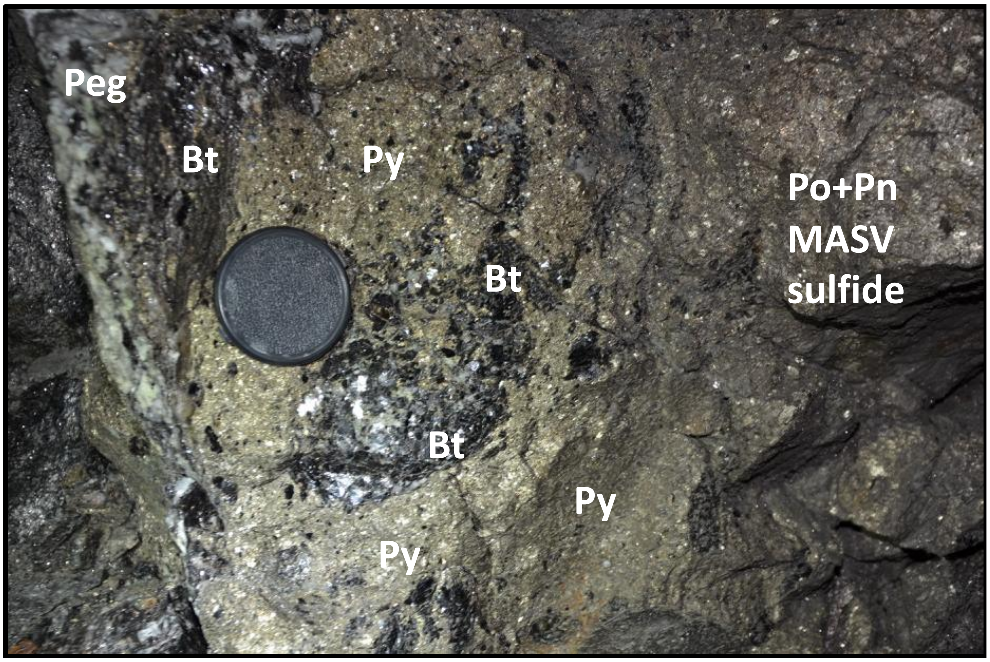

Figure 5-4: Underground photo in the 1D orebody showing jet-black biotite laths surrounded my massive pyrite. Pyrite in contact with massive Po+Pn sulfide. Note camera lens for scale (3" diameter). Abbreviation; Peg (pegmatite), Bt (biotite), Py (pyrite), Po+Pn MASV sulfide (pyrrhotite-pentlandite massive sulfide).

5.4 Underground Mapping

Sulfide-matrix breccia (SUMX) is a mine term used by Vale Canada Ltd. geologists to describe the presence of silicate rock fragments in a sulfide ore matrix. For example; if an ore lens is termed 'SUMX 70%', that means there is 70% sulfide-matrix with 30% lithic rock fragments. Although, sulfide-matrix breccia works as a common mine term to classify sulfide ores, it is too simple to classify ore types from an academic research perspective. Most of the sulfides in the Thompson 1D have been classified as sulfide-matrix breccia because they have high degree of brecciation and lithic fragment incorporation. **(Table 5-1).** Therefore, the terms 'sulfide-matrix breccia' or 'brecciated sulfide' were not used to describe mineralization types.

Net-textured (NT) and disseminated (DISS) are other common textural terms used to describe sulfide mineralization. However, the focus of the project was to study the economic sulfide bodies, as opposed to minor sulfide occurrences with the two aforementioned textures. However, mineralized schists (MSch) contain disseminated sulfides throughout. Disseminated sulfides have also been observed throughout ultramafic bodies (amphibolites & pyroxenites) in drill core. Disseminated and net textured sulfides are important, especially to PGE and Ni-sulfide exploration at Thompson. They are common sulfide textural terms used by Vale Canada Ltd. geologists to describe sulfide mineralization in exploration drill core, as seen in the summary sample log for drill hole #1365050 **(Table 5-2).** However, disseminated and net-textured sulfides are not currently being mined from Thompson, and therefore were not used to characterize the main sulfide mineralization styles in the Thompson 1D.

5.4.1 Mineralization Styles

Five main styles of mineralization were identified from underground mapping of dominantly the 1D Lower zone, as well as the FW Deep and Midband zones **(Table 5-1)**.

Massive (MASV) sulfide ores have >85% sulfide matrix by volume. MASV sulfide lenses consist of sulfide Po>Pn>Py>Ccp that can be fine- (<0.2 cm) to coarse-grained (>0.5 cm). MASV sulfides can also be inclusion-bearing, or inclusion-poor. In the case of the former, lithic fragments do not exceed 15% of the total sulfide body. MASV mineralization styles occur in fold hinges and along fold limbs, and are not associated with ultramafic boudins, however, massive sulfides may host brecciated ultramafic inclusions.

Semi-massive (SM) sulfide ores are similar to MASV sulfides but have greater abundances of lithic inclusions within the sulfide matrix. Semi-massive sulfide ores have between 50 and 85% sulfide matrix by volume, the rest comprised of silicate/lithic inclusions. Semi-massive sulfides can also be fine- (<0.2 cm) to medium- (<0.3 cm) and coarse-grained (>0.5 cm). Semi-massive mineralization styles also occur in fold hinges and fold limbs, and are not associated with ultramafic boudins, however, may host brecciated ultramafic inclusions.

Concordant (Conc) sulfide mineral zones are narrow, deformed lenses (<5 metres thick) of sulfide that typically are conformable to the foliation in the steeply-dipping P_2 schist in fold limbs. Concordant sulfides are predominantly MASV or SM in nature and can either be inclusion-bearing or inclusion-poor. For ore to be classified as a concordant sulfide in this study, multiple lenses of sulfide must be present.

Ultramafic associated (UMA) is a term used to describe sulfide bodies that are in contact with, or in very close proximity to ultramafic boudins. These sulfides have a direct link to the primary intrusions and have not been transported/remobilized long distances. UMA sulfides are usually brecciated and inclusion-bearing.

Shear-hosted (SH) sulfides are those that are in contact with, or near distinct shear zones. This style of mineralization is the most structurally controlled. Shear-hosted sulfides (Po>Pn>Py>Ccp) are commonly medium- (0.3 cm) to coarse-grained (>0.5 cm), but fine-grained (<0.3 cm) and dull-looking also occur. Sulfides are heavily brecciated and inclusion-bearing (P_2 schist wall rock, ultramafic and pegmatite porphyroclasts). The numerous inclusions within the shear-hosted sulfides are representative of a high degree of deformation that has acted on the sulfides and surrounding country rocks. The shear zones developed in high-strain zones, parallel to steeply-dipping limbs of upright F_3 folds (Bleeker and Macek, 1996). Dilation zones, parallel to high-strain shear zones, are host to shear-hosted mineralization (Burnham et al., 2009).

5.4.2 Relationships to Ni tenor

Along with characterizing the main underground mineralization styles, crucial relationships between mineralization style Ni, Pd and Pt tenor have been identified. **Figure 5-5** shows whole rock Ni tenor as a function of mineralization style. The shear-hosted mineralization style has an average Ni tenor of 12.8% Ni, followed by semi-massive, concordant and massive sulfide:10.6%,11.1% and 6.7% Ni, respectively. The latter also has tenors as low as 1.7 % Ni, which is attributed to the existence of barren massive sulfide lenses within the 1D orebody, as mentioned above in **Section 5.3.1**. Ultramafic associated (UMA) sulfides have slightly lower whole rock Ni tenors – on average 9.9%. This is consistent with previous studies done on the TNB, that primary ultramafic associated sulfides have lower Ni tenors than ore hosted by the adjacent meta-sedimentary rocks (House, 2009), with South Manasan being the exception (Franchuk et al., 2016). From **Figure 5-5**, it can be concluded that shear-hosted mineralization styles have the highest Ni tenors in the deposit. Massive sulfide ores have the lowest and most variable Ni tenors in the 1D orebody. See **Appendix 12** for excel spreadsheets and ioGas^{TM} workbooks containing data used to plot all graphs in this study.

Scatter plots of whole rock Ni vs. Pd, Ni vs. Co for all underground ore samples in the Thompson 1D are shown in **Figure 5-6 A** and **B**, respectfully. Regarding the latter, the Ni/Co data was also plotted as a histogram (not shown), with one definitive peak existing between 65-80 (see **Appendix 12 – Figure 5-6**). The average Ni/Co ratio of the Thompson 1D orebody is 79 (this study), which is consistent with the pentlandite-rich trend (70-100) outlined at the Thompson deposits by Lightfoot et al. (2017). Nickel versus copper (%) was also plotted (not shown), the amount of Cu was relatively constant over variable Ni contents, ranging between 0 and 0.75% Cu (see **Appendix 12 – Figure 5-6**). The Ni/Cu ratio of the Thompson 1D orebody is 56 (this study). Data from Lightfoot et al. (2017) shows an average Ni/Cu ratio of 16 from TNB ores from the Thompson Dome. The slightly higher Ni/Cu ratio (56) in the Thompson 1D could be due to the higher Ni tenors associated with the Thompson deposits, specifically the 1D orebody. Additionally, the plots of; Ni/Pd ratio vs. Ni tenor, Ni/Co vs. Ni tenor, and Ni/Pd vs. Ni/Co, all showed clustered data with no trends when plotted. These plots are not shown but can be found in the **Figure 5-6** IoGas^{TM} and excel files in **Appendix 12**. In conclusion, all these plots show that little to no fractionation of pentlandite occurred at Thompson. No evidence for fractional crystallization of a sulfide melt exists, and therefore some other processes are responsible for the variations in nickel tenor observed, not magmatic ones.

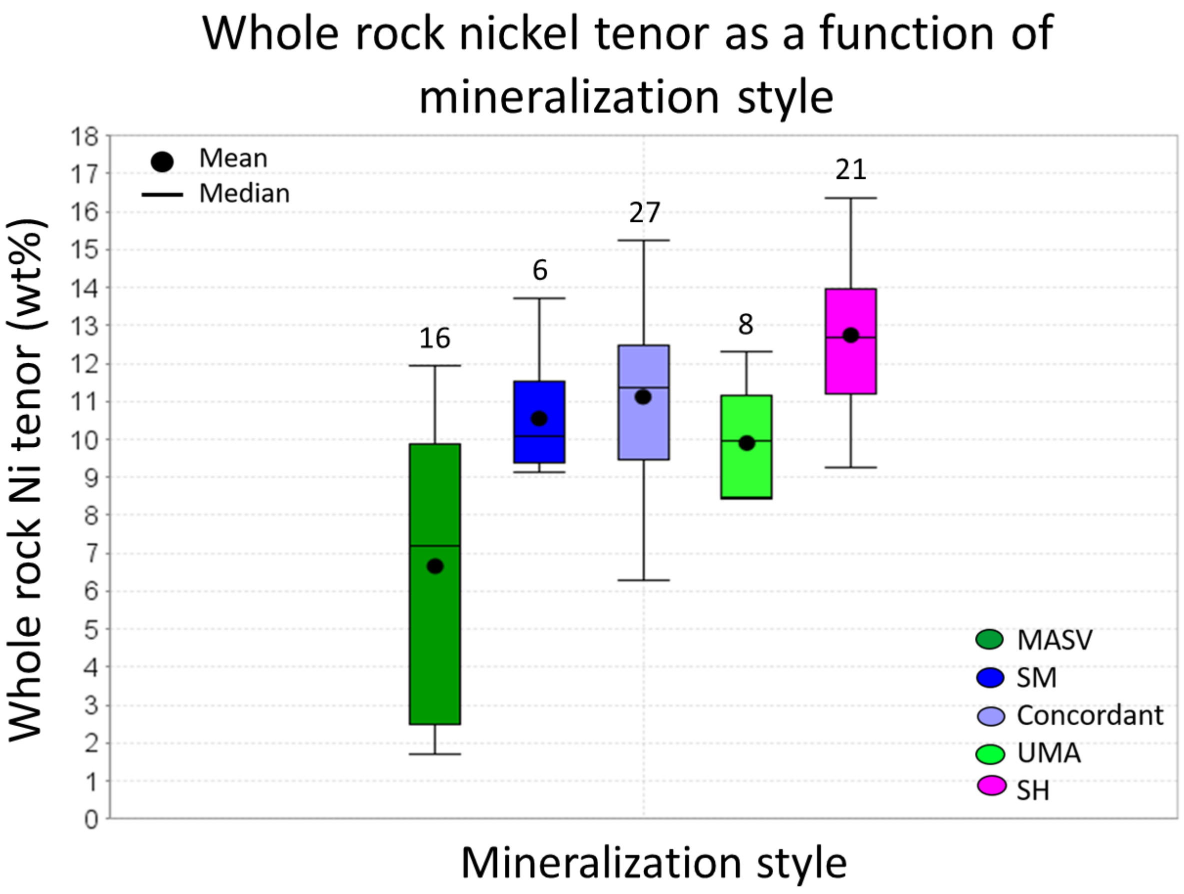

Figure 5-5: Shows how whole rock nickel tenor varies across the five underground mineralization styles. Shear-hosted (pink) styles have the highest nickel tenors, while massive styles (forest green) have the lowest and most variable nickel tenors. Data is based on 78 underground samples and their corresponding thin sections. The numbers on the box and whisker charts display the total number of underground samples represented by each mineralization style. MASV – massive sulfide; SM – semi-massive sulfide; Concordant sulfide; UMA – ultramafic associated sulfide; SH – shear-hosted sulfide. See Appendix 12 – Figure 5-5; for the excel spreadsheet of data used to make this plot.

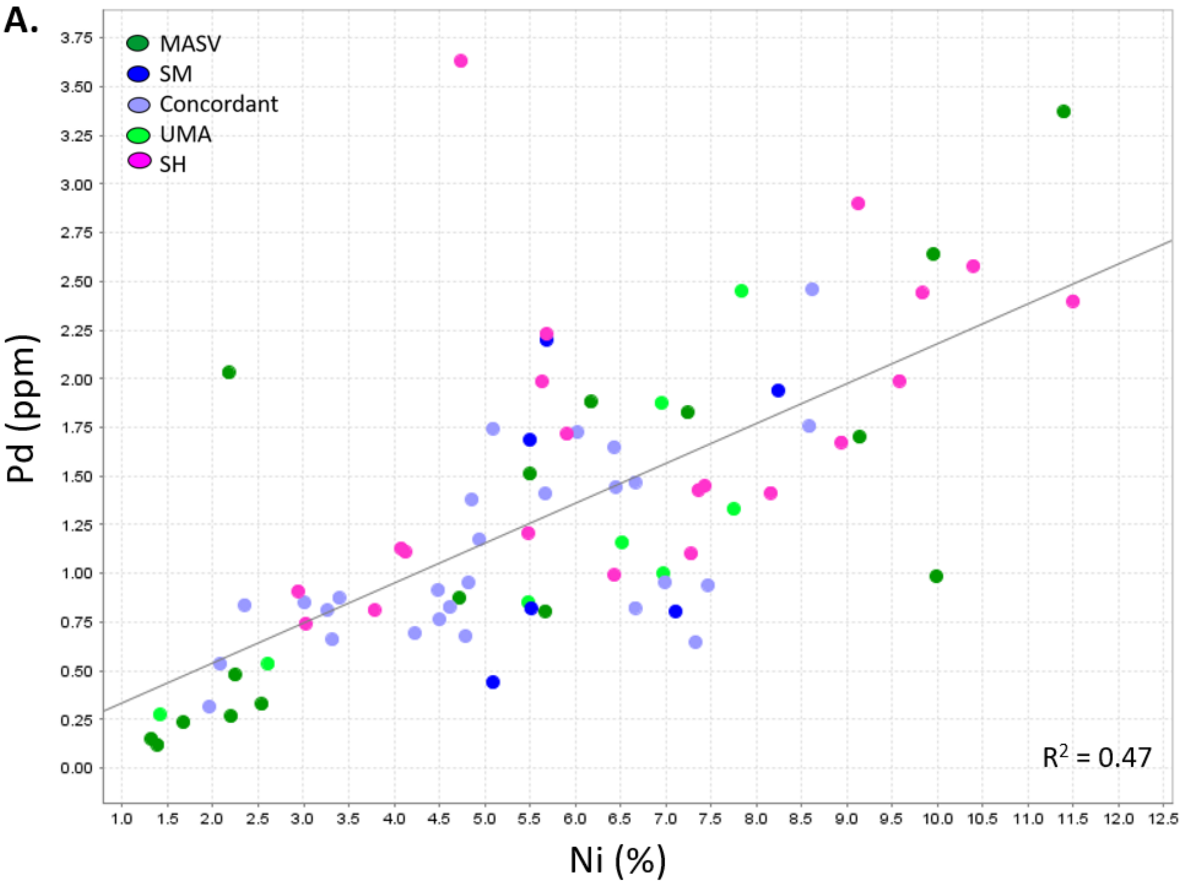
A.
MASV
SM
Concordant
UMA
SH
Pd (ppm)
3.75
3.50
3.25
3.00
2.75
2.50
2.25
2.00
1.75
1.50
1.25
1.00
0.75
0.50
0.25
0.00
1.0 1.5 2.0 2.5 3.0 3.5 4.0 4.5 5.0 5.5 6.0 6.5 7.0 7.5 8.0 8.5 9.0 9.5 10.0 10.5 11.0 11.5 12.0 12.5
Ni (%)
R² = 0.47

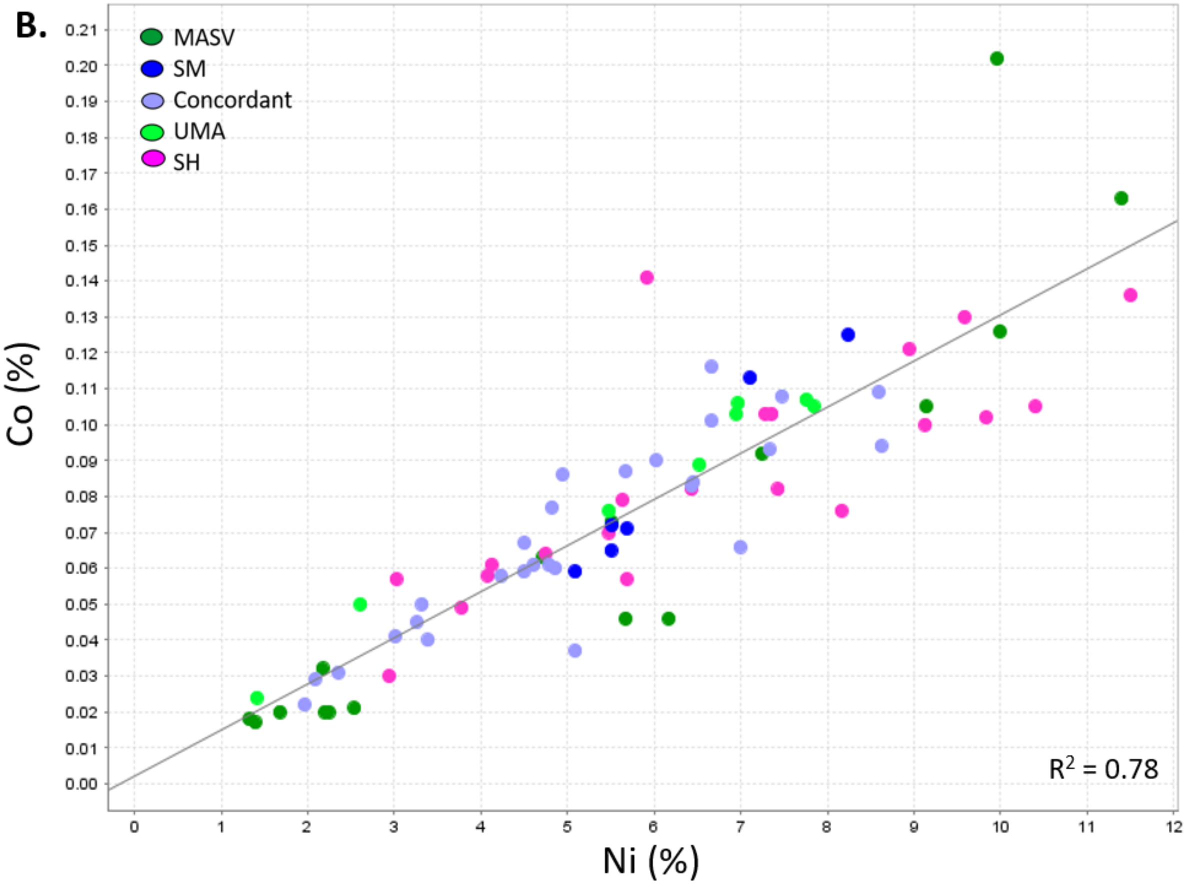
B.
MASV
SM
Concordant
UMA
SH
Co (%)
0.21
0.20
0.19
0.18
0.17
0.16
0.15
0.14
0.13
0.12
0.11
0.10
0.09
0.08
0.07
0.06
0.05
0.04
0.03
0.02
0.01
0.00
0 1 2 3 4 5 6 7 8 9 10 11 12
Ni (%)
R² = 0.78

Figure 5-6: A. Whole rock Ni (%) versus Pd (ppm) as a function of mineralization style for all underground ore samples in the Thompson 1D; $R^2 = 0.47$. Regression line shown. B. Whole rock Ni (%) versus Co (%) as a function of mineralization style for all underground ore samples in the Thompson 1D. Linear correlation with $R^2 = 0.78$. Regression line shown. Data from both plots is based on 78 underground ore samples. Abbreviation; MASV – massive sulfide; SM – semi-massive sulfide; Concordant sulfide; UMA – ultramafic associated sulfide; SH – shear-hosted sulfide. See Appendix 12 – Figure 5-6_revised; for the excel spreadsheet of data used to make these plots.

Platinum group metals (PGM) were not the focus of this study. However, we indicate mean Pd and Pt tenors in the Thompson 1D sulfide ores to be 2475 ppb and 1200 ppb, respectively, with a Pd/Pt ratio of 55 (**Appendix 3**). Shear-hosted mineralization styles have some of the highest whole rock Pd tenors (3375 ppb), while massive mineralization styles have some of the lowest Pd tenors (1660 ppb) (**Appendix 3**). It is acknowledged several very high-grade Pt samples have skewed the Pt average, although Pd values stay consistently high. The Thompson 1D ores also show elevated As contents; 141 ppm As on average with several samples containing up to 400 ppm As. Therefore, arsenic measurements are quite low in most ores, with locally higher concentrations possible. Whole rock data can be found in **Appendix 3.**

5.5 Drill Core Logging

Textural relationships between sulfides and host rocks were investigated to see whether a correlation exists between textural type and Ni tenor. Core logging was used to establish if a footprint (structural, mineralogical and chemical) exists around ore zones and whether exploration vectors can be developed; in particular, whether low and high-grade Ni zones could be distinguished from one another and whether the trace element content of biotite and garnet changes as a function of distance from sulfide mineralization.

5.5.1 Drill Hole #1365050

Detailed drill core investigation, K-feldspar staining and petrographic analysis of 36 drill core samples was completed. A summary sample log for DH#1365050 is shown in **Table 5-2**, which outlines sulfide lenses intersected, their respective mineralization styles and Ni tenors, sample descriptions, as well as the total metres and types of lithologies logged.

Barren to mineralized schist/pegmatite-schist units separate several sulfide ore lenses that were intersected in drill core. Schist units have a shallow core angle of ~20°, becoming steeply-dipping (60-70°) before the onset of a mineralized zone or an ultramafic contact. Schists are mica- and graphite-rich, consist of boudinaged pegmatite porphyroclasts that are oriented parallel to the strong schist fabric. The dominant mica making up the schist foliation is biotite - laths are a brown colour in hand sample and align parallel to schist foliation. Trace sillimanite wisps are also aligned parallel to the fabric of the schist.

Multiple pegmatite relationships are recorded in DH#1365050. These agree with observations of multiple generations of pegmatite emplacement at Thompson, as recorded by Machado et al. (2011) and discussed above in **Section 5.1.3**. Quartz and pegmatite veinlets are typically conformable to, but locally crosscut the schist foliation. Pegmatites are rich in quartz + feldspar and have jet-black coloured biotite that is concentrated at or near the margins. Trace fuchsite (chromium mica) also occurs late in the pegmatites (pale apple-green colour). Pegmatites are present along margins of sulfide lenses but were also observed to cut several sulfide ore horizons at two locations in **Table 5-2**: sample 2 (19.7 – 25.3 metres) and sample 25 (148.9 – 151.8 metres). Several smaller pegmatitic veinlets also crosscut sulfide horizons throughout the drill core. The mineralized sulfide zones are either mineralized schist, massive, semi-massive, net-textured, or disseminated in nature. However, sulfide-matrix ore (SUMX) is commonly used to describe massive or semi-massive lenses that are brecciated and lithic fragment bearing. Mineralized shears are also evident. However, the true style of mineralization of the sulfide lenses is difficult to establish in drill core samples. The main sulfide minerals are Po>Pn>Py, with trace Ccp as stringers within/around main ore zones. Coarse-grained pentlandite eyes (>2 cm) are disseminated in the pyrrhotite-dominant sulfide matrix. The massive and semi-massive sulfide zones are brecciated; host semi-rounded inclusions of ultramafic, foliated P_2 schist wall rock, pegmatitic porphyroclasts and solo laths of jet-black coloured biotite. Pegmatitic porphyroclasts consist of quartz- and feldspar-rich assemblages, commonly with biotite + muscovite + sillimanite rims. Electron probe micro analysis (EPMA) and K-feldspar staining has determined that the pegmatitic porphyroclasts are dominantly plagioclase + quartz with trace K-feldspar (**Section 4.4**). Mineralized schist units consist of sulfide stringers that are conformable to semi-conformable to the schist foliation. The drill hole cuts multiple thin ultramafic lenses, including multiple metre scale amphibolite/pyroxenite dykes, which have abundant garnet. Disseminated mineralization occurs within several ultramafic dykes. The timing relationships in DH#1365050 between the P_2 member schist host-rocks, shears, sulfide mineralization, ultramafic and pegmatite occurrences agree with relationships stated above in **Sections 5.1** and **5.2**.

As alluded to earlier, it was difficult to establish true mineralization styles; although disseminated, net-textured, mineralized schist, semi-massive, and massive sulfide styles were identified. Several key signals to high Ni tenor sulfide mineralization are documented. Drill hole #1365050 cut through structurally complex and shear-prominent zones with abundant pegmatites neighbouring/cutting sulfide lenses. It was commonly observed that mineralized schist usually occurred before the onset of a massive sulfide lens. Also, schist and pegmatite-schist foliation steepened (50-70˚) before the onset of a mineralized sulfide lens. Abundance of coarse-grained pentlandite eyes (cm-scale), pegmatite nodules, garnet grains and biotite laths within sulfide ore tends to be characteristic of high Ni tenor sulfide lenses in DH#1365050. The importance of pyrite abundance was not known at this time, therefore drill logs lack detail pertaining to mention of pyrite.

Table 5-2: Summary Sample Log of DH#1365050. Table shows sulfide lenses intersected, their respective mineralization styles and Ni tenors (normative sulfide method). The table also outlines the total # of samples taken (36), total metres logged, and types of lithologies logged. Sample 1045225 was a 'Quality Control Standard' – TH-1. Lithology abbreviations; PSCH (pegmatite schist); SUMX (sulfide-matrix ore); MSCH (mineralized schist); SCH (schist); MASV (massive ore); SM (semi-massive ore); NT (net-textured ore); MIF (mineralized iron-formation); MSCHR (mineralized shear); DISS (disseminated mineralization). Other abbreviations: FG (fine-grained); MG (medium- or intermediate-gained); CG (coarse-grained); PEG (pegmatite).

SUMMARY SAMPLE LOG FOR DH#1365050							Ni tenor	Sample Descriptions
Sample ID	Thin-sxn. ID	Sample	From (m)	To (m)	Length (m)	Lithology	wt %	
1045201	D103	1	18.5	19.7	1.2	PSCH	1.19	FG-MG PSCH BUFFER BEFORE ONSET OF MINERALIZATION. QTZ RICH PEG VEIN CUTS PSCH
1045202	D104	2	19.7	25.3	5.6	SUMX	11.65	MG-CG SEMI-MASSIVE SULPH. SEMI-CONC TXT SEEN AS WELL. PO, PN, CP EVIDENT. SHARP CONTACT W/ PSCH BUFFER. PEG (~5CM) CUTS SULPH LENS.
1045203	D105	3	25.3	29.5	4.2	MSCH	10.80	FG-MG MSCH INTERCHANGING WITH PEG VEINS. MINERALIZATION TENDS TO FOLLOW SCH BEDDING. OCCURS AS STRINGERS
1045204	D106	4	37.3	39.4	2.1	SCH	0.22	FG-MG SCH WITH CM SCALE NODES OF PEG. STEEPLY DIPPING BEDS ~70 DIP
1045205	D107	5	39.4	43.5	4.1	SCH	1.29	FG SCH BEDS DIPPING AT A SHALLOWER ANGLE ~40 DIP. FOLDED PEG? NODES WITHIN BEDS
1045206	D108	6	43.5	44.5	1.0	MSCH	13.33	MG-CG MSCH BUFFER BEFORE THE ONSET OF MASV SULPH BAND. PO, PN + LOTS OF CPY EVIDENT.SULPH SEMI-CONC TO FOLDED SCH
1045207	D109	7	44.5	46.2	1.7	MASV	9.54	CG SM-MASV SULPH. PO+PN 'EYES' + CPY EVIDENT.INCLUSION BEARING (PEG OR KFELD CLASTS? + SCH WALLROCK).
1045208	D110	8	46.2	48.9	2.7	SCH	0.61	FG SCH BEDS DIPPING ~40 DEGREES. PEG BANDS (CM SCALE) INCREASING TOWARDS UM CONTACT (PXT).
1045209	D111	8a	60.6	63.2	2.6	SCH	0.08	FG-MG SCH. BEDS STEEPLY DIPPING ~ 70 DEGREES. BT LOOKS BROWN (PHLG?). FOLDED PEG NODES WITHIN BEDS
1045210	D112	9	63.2	65.7	2.5	SCH	11.18	FG-MG SCH RIGHT BEFORE A SM SULPHIDE BAND. BEDS STILL STEEPLY DIPPING ~70 DEGREES. THOUGH MORE PEG NODES (CM SCALE) VISIBLE.
1045211	D113	10	65.7	66.9	1.2	SM	9.65	CG SM SULPH. BRECCIATED CLASTS WITHIN SULPH (PEG SWEATS/NOEDS, SCH WALL ROCK, K-FELD NODES?). CM SCALE CLASTS IN SULPH.
1045212	D114	11	66.9	68.9	2.0	SCH	5.22	FG SCH STEEPLY DIPPING ~50 DEGREES AFTER A SM SULPH BAND. LESS PEG NODES SEEN IN SCH. SOME PEG LAYERS (<CM) CONC TO SCH BEDDING.
1045213	D115	12	82.7	84.7	2.0	PSCH	1.08	STEEP (~80) TO SHALLOW (~30) DIPPING SCH BEDS. SCH BEDS CRENULATED AND PEGS SEMI-CONC. BUFFER BEFORE THE ONSET OF AMPT BAND.
1045214	D116	13	93.5	96.5	3.0	MSCH	19.23	HIGHLY FOLDED SCH BEDS WITH PEG SWEATS EVERYWHERE. SULPH STRINGERS WITHIN SCH BEDS. PO, PN AND CPY EVIDENT
1045215	D117	14	96.5	97.2	0.7	SM	13.59	SM, CG SULPH WITH CM SCALE BRECCIATED CLASTS WITHIN IT. PN 'EYES' SEEN. SULPH LOOKS INFUSED INTO WALLROCK WITH WALLROCK CLASTS IN IT
1045216	D118	15	97.2	98.4	1.2	PSCH	12.51	FG-MG PSCH VARYING IN DIP. LOTS OF PEGS VEINS AND STRINGERS SEEN. FAINT GREEN MINERAL SEEN - FUCHSITE?
1045217	D119	16	115.4	118.1	2.7	MSCH	4.03	MG SCH BEDS WITH CONC (<CM SCALE) SULPH STRINGERS WITHIN SCH BEDDING. SCH BEDS DIPPING ~ 50 DEGREES.
1045218	D120	17	121.2	123.3	2.1	MSCH	14.20	SCH BEDS SHALLOWLY DIPPING ~35 DEGREES. MULTIPLE INFLUXES OF SULPH STRINGERS (BRECCIATED). LOOKS HEAVILY FOLDED AREA MOVING INTO ~70 DIP
1045219	D121	18	123.3	127.1	3.8	NT	14.78	MG, NET-TEXTURED ORE. ALSO AREAS OF DISSEMINATED STRINGERS. SULPH WRAPPING ITSELF AROUND PEG CLASTS. BRECCIATED LOOKING. PO, PN AND CPY
1045220	D122	19	127.1	129.0	1.9	PSCH	17.39	FG, SHALLOWLY DIPPING (~25 DEGREES) SCH BEDS WITH PEG VEINS (CM SCALE) AND NODES. GRN'S EVIDENT. BT LOOKS BROWNISH (PHLG?)
1045221	D123	20	135.3	138.3	3.0	MSCH	16.63	FG CRENULATED SCH BEDS W/ RANDOM PEG NODES. SULPH CONC TO CRENUALTED SCH BEDS.LARGER STRINGERS OF SULPH EVIDENT (MM SCALE)
1045222	D124	21	143	145.1	2.1	MSCH	13.65	DISSEMINATED AND STRINGERED SULPH AMONGST PSCH BEDS. NO ORIENTATIONS (A BIG MESS). K-FLED OR PEG NODES? BUFFER BEFORE MASV SULPH LENS
1045223	D125	22	145.1	145.8	0.7	MASV	12.77	MASV, CG SULPH BAND. PO, PN AND CPY EVIDENT. SOME CM SCALE BRECCIATED CLASTS EVIDENT.
1045224	D126	23	145.8	147.6	1.8	PSCH	17.79	FG - MG PSCH WITH LOTS OF PEG NODES. SOME STRINGERS OF SULPH SEEN (CM SCALE). LOTS OF PEG CLASTS/K-FELD NODES? DIPS B/W 50-70 DEGREES.
1045225	TH-1 (QUALITY CONTROL SAMPLE)						N/A	
1045226	D127	24	147.6	148.9	1.3	PSCH	15.12	FG SCH BEDS DIPPING ~40 DEGREES. LRG PEG VEINS (MULTIPLE CM'S), PEG NODES AND K0FELD NODES? LITTLE SULPH STRINGERS FOLLOWING FOLDED SCH BEDS
1045227	D128	25	148.9	151.8	2.9	SM	13.60	CG, SM SULPH WITH DISTINCT ROUNDED, BRECCIATED CLASTS WITHIN MATRIX. PEGS? K-FELD NODES? PEG VEIN (~10CM) CUTS SULPH LENS.
1045228	D129	26	151.8	152.8	1.0	MIF	13.82	MINERALIZED IF. SULPH OCCURING AS MINIMAL STRINGS CONC TO SCH BEDDING. SCH BEDS DIPPING ~40 DEGREES
1045229	D130	27	152.8	156.5	3.7	SM	16.46	CG, SM SULPH OCCURING IN MORE MASSIVE LENSES AND THEN DISSEMINATED LENSES THAT ARE CONC TO SCH BEDS. CRS GRAINED PEG NODES SEEN.
1045230	D131	28	157.5	159.5	2.0	SM	13.04	LENS OF SM, CG SULPH WITH EVIDENT PN 'EYES'. SAMPLED A NT/DISSEMINATED SCH AREA. PO, PN AND MINOR CPY SEEN.
1045231	D132	29	159.5	160.9	1.4	NT	14.58	MG-CG, NT SULPH OCCURING AS STRINGERS SEMI-CONC TO SCH BEDDING. LENSES OF CPY SEEN TOO. (<CM) BRECCIATED CLASTS IN MATRIX SEEN. PEG NODES
1045232	D133	30	160.9	162.9	2.0	MIF	17.79	FG MIF WITH ABUNDANT GRN'S (CM SCALE) PRESENT. SULPH OCCURING AS STRINGERS SEMI-CONC TO BEDS. BEDS DIPPING ~30 DEGREES.
1045233	D134	31	168.8	172.8	4.0	SCH	5.30	FG-MG SCH BEDS DIPPING STEEPLY (~60) THAN TO MORE SHALLOW DIPS (~20). BLACK BT. FOLDED PEG NODES SEEN
1045234	D135	32	238.3	243.3	5.0	PSCH	12.37	CG, SCH BEDS WITH INTERCHANGING PEGS. LOTS OF PEGS PRESENT. MINIMAL SCH ACTUALLY. SAMPLED BLACK BT AREA.
1045235	D136	33	243.3	244.3	1.0	SM	12.20	VERY CG, SM-NT SULPH. CM SCALE PN 'EYES' SEEN. SULPH MATRIX LOOKS BRECCIATED. BLACK BT. PEG NODES OR K-FELD NODES IN SULPH MATRIX AS WELL.
1045236	D137	34	244.3	246.1	1.8	PSCH	12.65	MG-CG PSCH AFTER A DISTINCT SULPH LENS. BEDS STEEPLY DIPPING ~70 DEGREES. NODULES OF PEG OR KFELD SEEN WITHIN SCH.
1045237	D138	35	248.1	249.0	0.9	SCH	8.07	FG, SCH BEDS FORMING STEEP FOLD. STEEPLY DIPPING ~70 DEGREES. SURROUNDED BY PEG VEINS AND PSCH. PEG NODES SEEN VERY CLOSE BY.

Chapter 6: Silicate Mineralogy and Mineral Chemistry

6.1 Biotite

Whole rock geochemical analyses were conducted on various biotite-types (4) to classify the dominant biotite end members present in silicate-hosted versus sulfide-hosted biotite grains in the Thompson 1D. Relationships were investigated, following stoichiometric equations by Munoz (1984), to show the range of compositions of three principal biotite end members in the Thompson 1D deposit; annite (Fe-rich), phlogopite (Mg-rich) and siderophyllite (Al-rich).

6.1.1 Mineralogy

Biotite is a major silicate phase within the 1D ores at the T3 mine. It is closely associated with pyrite (**Section 5.3.2**), which is intimately linked with the highest Ni tenor sulfide mineralization in the deposit. Therefore, further investigations on the petrography and mineral chemistry of biotite in the 1D orebody are justified.

Biotite is largely a pro-grade metamorphic mineral however, it is possible that biotite is also produced via hydrous fluids during silicate-sulfide (pyrrhotite) interaction, as expressed in **Reaction 1:**

$$\mathbf{KAlSi_3O_8 + 3\ Fe_{(1-x)}S + H_2O + 1.5\ O_2 \rightarrow KFe_3^{2+}AlSi_3O_{10}(OH)_2 + 1.5\ S_2} \tag{1}$$

K-feldspar + Pyrrhotite + Water + Oxygen → Fe-biotite (annite) + Sulfur degassing

Reaction 1 will be further discussed in **Section 8.7.2**. This chapter characterizes biotite grains from both silicate rocks (i.e., pelitic schists) and sulfide-rich rocks that have been classified into four types as shown in **Figure 6-1.** Biotite grains from silicate rocks are classified into two-types (1, 2) and biotite grains from sulfide-rich rocks are classified into two-types (3, 4):

1) Biotite grains in P_2 pelitic schist (BT_P2_SCHIST), biotite grains coexist with other silicate minerals and define a distinct foliation in the P_2 pelitic schist unit **(Figure 6-1A).**
2) Metasomatic biotite (METASOMATIC), biotite grains are also within the P_2 pelitic schist unit but have replaced feldspar grains and thus are hydrothermal in origin **(Figures 6-1 B; 6-2).**
3) Biotite grains that were incorporated in sulfide as a result of brecciation (BT_SULF) **(Figure 6-1C),** and grains are in contact with pyrrhotite, pentlandite and pyrite.
4) Biotite grains that were incorporated in sulfide as individual laths entrained within the sulfide matrix (SOLO_SULF) **(Figure 6-1D).** These biotite grains occur as laths within dominantly pyrrhotite, but also pentlandite ± pyrite assemblages.

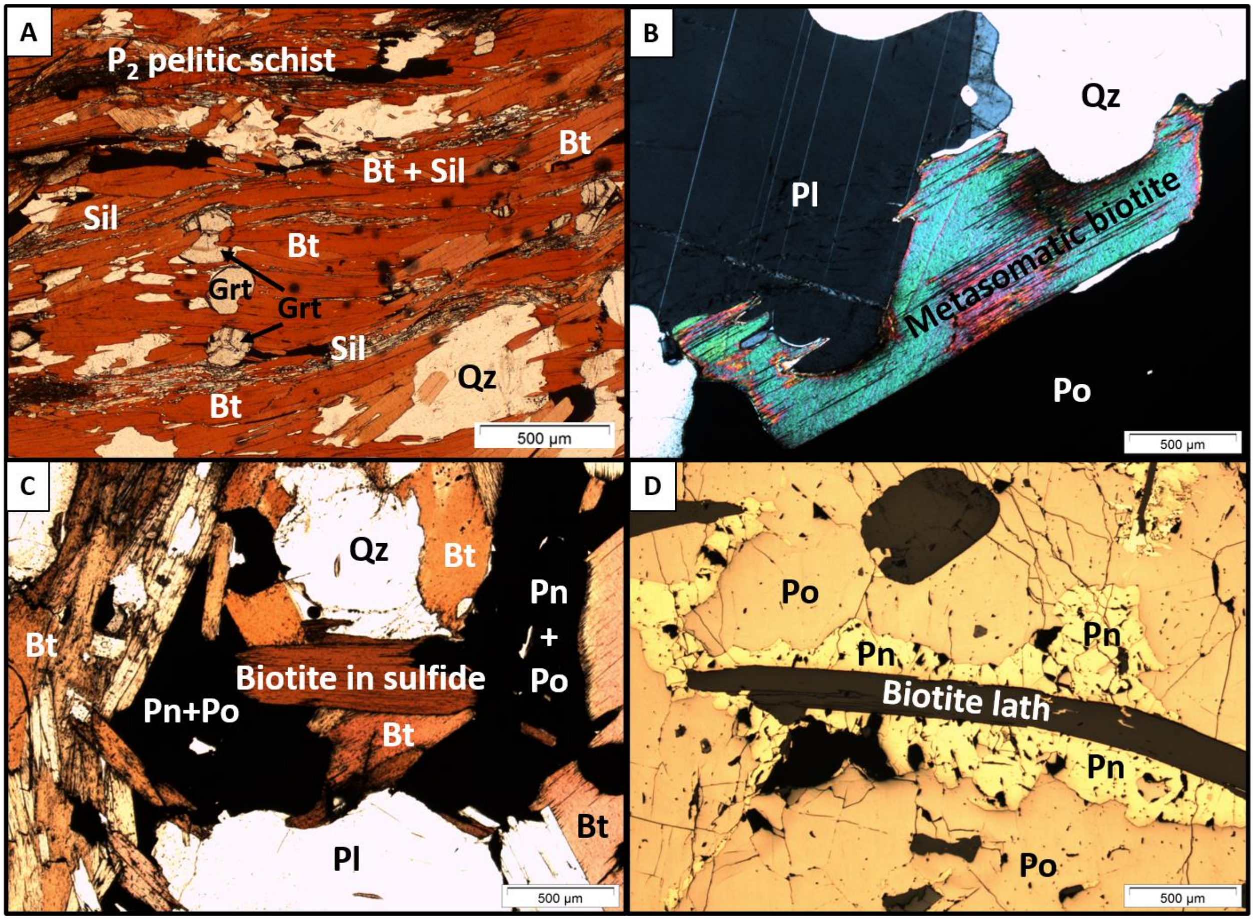

Figure 6-1: shows petrographic relationships of silicate- and sulfide-hosted biotite. The two main biotite groups are further classified into four types. A: Plane polarized light photomicrograph from thin section 1045327 (sample Bt1) showing biotite grains in P_2 pelitic schist (BT_P2_SCHIST). Biotite grains define foliation and are usually interlocked with; micas, quartz, feldspar, garnet and are overprinted by late-sillimanite. B: Transmitted light photomicrograph in XPL from thin section 1045359 (Bt2) shows biotite replacement of plagioclase (METASOMATIC). C: Plane polarized light photomicrograph from thin section 1045359 that shows biotite fragments incorporated within sulfide matrix (BT_SULF). D: Reflected light photomicrograph from thin section 1045342 (sample Bt2) showing an isolated lath of biotite entrained within the sulfide matrix (SOLO_SULF). This biotite lath is dominantly surrounded by pentlandite. Biotite laths are also commonly surrounded by pyrrhotite and pyrite (not pictured). Abbreviations; Bt (biotite), Sill (sillimanite), Qz (quartz), Grt (garnet), Pl (plagioclase), Po (pyrrhotite), Pn (pentlandite).

The strength and colour of pleochroism does not vary to a great degree across the four-biotite groups; a strong pleochroism from light orange to dark orange/red is a common property throughout most biotite grains. However, isolated biotite laths (SOLO_SULF) do show some variations in strength and colour of pleochroism, as will be discussed below. A correlation between strength and colour of pleochroism and Ni tenor was not established based on a descriptive review of the colour and pleochroism of biotite in samples with different sulfide metal tenor.

Hand specimen observations between silicate and sulfide-hosted biotite grains are quite distinct. All biotite grains generally occur as tabular laths that can range in size from 10μm to several centimeters in length. Pleochroic halos around minute inclusions of zircon and less commonly titanite, are present in biotite grains, however this is more common in silicate-hosted biotite grains. Most biotite laths are pristine, however replacement by sericite and chlorite does occur, the former being more common. Several biotite grains and pelitic schist fragments in sulfides are 'kinked' and 'warped', which is indicative of deformation that pre-dated late-stage brecciation. Descriptions of all four biotite types are discussed below:

1) Biotite grains in P_2 pelitic schist (BT_P2_SCHIST) are brown in hand sample and have a strong pleochroism from light orange to dark orange/red-brown in PPL. This group of biotite grains make up a major component of the P_2 schist wall rock, interlocked with other silicate minerals (feldspar, garnet, muscovite, sillimanite, quartz) distal from sulfide mineralization.
2) Metasomatic biotite grains (METASOMATIC) are also a deep brown in hand sample and have a strong pleochroism from light orange to dark brown/orange in PPL. They also occur in P_2 pelitic schist however, they are more closely associated with K--feldspar and plagioclase. As the name suggests, these biotite grains occur as tabular laths (commonly with sericite) that have replaced K-feldspar **(Figure 6-2)** and plagioclase grains. Biotite laths are also common as overgrowths on embayments and rims of feldspar

grains **(Figure 6-2)**. The replacement of feldspars is evidence for potassic metasomatism.

3) Biotite grains concentrated within sulfide (BT_SULF) are jet-black in hand specimen and have a strong pleochroism from light orange to dark orange in PPL. These biotite grains occur amongst fragments of P_2 pelitic schist that have been entrained within the sulfide matrix. Biotite grains are commonly surrounded by the main sulfide minerals; pyrrhotite, pentlandite and pyrite.
4) Individual laths of biotite entrained in sulfide (SOLO_SULF) do show some variations in strength and colour of pleochroism. These biotite laths are jet-black in hand sample, and pleochroism ranges from weak to strong. Pleochroic colors can range from light orange to dark orange/brown, similar to other types of biotite. However, biotite laths that show weak to moderate pleochroism tend to have colors that range from light yellow to brown/green.

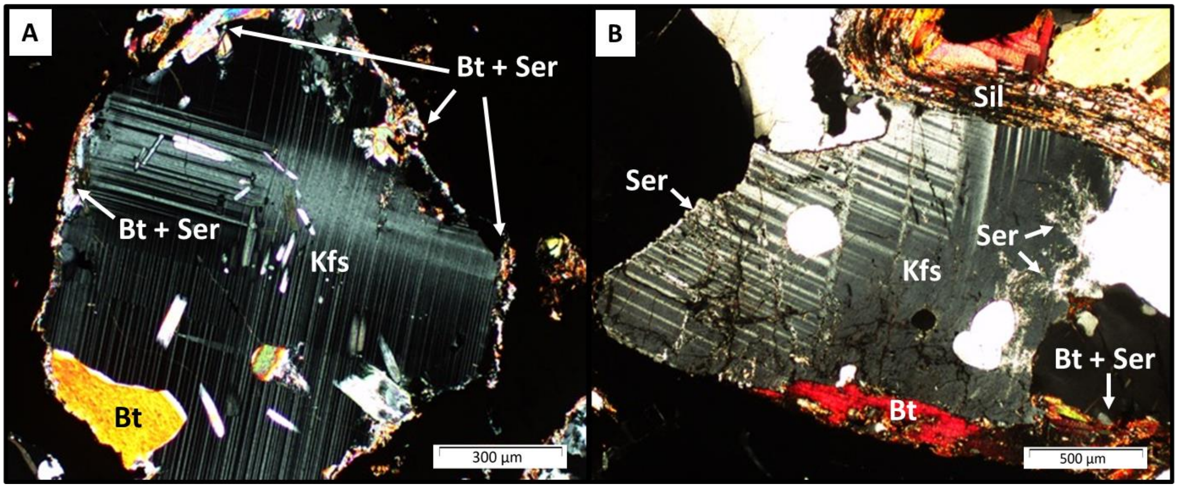

Figure 6-2 A): Transmitted light image in XPL of thin section 1045374, biotite laths and fine-grained sericite are replacing a tartan twinned K-feldspar grain. Note, biotite + sericite assemblages rimming the outer margins of the K-feldspar grain. B) Transmitted light image in XPL of thin section 1045383, biotite laths + fine-grained sericite replacing a tartan twinned, corroded K-feldspar grain. Note, late-sillimanite foliation (upper right of image) overprints silicate assemblages. Both A) and B) are evidence for potassic metasomatism. Abbreviations; Bt (biotite), Kfs (K-feldspar), Sil (sillimanite) Ser (sericite).

6.1.2 Mineral Chemistry

The SiO_2, Al_2O_3, FeO, MgO, F, Cr_2O_3, CoO, NiO, TiO_2, K_2O, Na_2O, F and Cl compositions in biotite were determined by EPMA. A total of 237 spots were analyzed from 59 grains and 20 different polished thin sections. Weight percent totals of >94% were acceptable and the stoichiometries for all 237 biotite spot analyses are presented in **Appendix 13**, along with a calculation spreadsheet' for determining stoichiometries. **Table 6-1** lists representative EPMA data, stoichiometries and the mole fractions of end-members annite (Fe-rich), phlogopite (Mg-rich) and siderophyllite (Al-rich).

Table 6-1 shows four representative analyses of biotite types in terms of EPMA weight % data, stoichiometry and mole fraction of end-members; annite (Fe-rich), phlogopite (Mg-rich) and siderophyllite (Al-rich). End-member mole fractions are calculated using equations from Munoz (1984): ***Xphl*** *= Mg(VI)/ Σoct;* ***Xsid*** *= [(3-Si)/Al]/1.75*[1-Xphl];* ***Xann*** *= 1-(Xphl+Xsid). Abbreviations; biotite grains in* P_2 *pelitic schist (BT_P2_SCHIST); metasomatic biotite (METASOMATIC); biotite grains concentrated within sulfide (BT_SULF); individual laths of biotite entrained in sulfide (SOLO_SULF).*

Sample	1045237	1045201	1045359	1045235
Analysis code	Bt1_03	Bt1_01	Bt3_02	Bt3_01
Biotite type	BT_P2_SCHIST	METASOMATIC	BT_SULF	SOLO_SULF
	EPMA data (wt%)			
SiO2	34.5	35.0	35.2	34.0
Al2O3	19.7	20.0	19.8	19.7
Na2O	0.14	0.12	0.16	0.21
MgO	8.42	8.39	8.10	7.40
F	0.24	0.13	0.25	0.13
F Oxy. Eq.	-0.10	-0.06	-0.11	-0.05
FeO	19.6	18.3	18.8	20.9
Cr2O3	0.05	0.08	0.68	0.76
CoO	0.03	0.02	0.02	0.03
NiO	0.10	0.12	0.21	0.20
TiO2	2.84	2.88	2.66	2.48
K2O	9.66	9.67	9.68	9.20
Cl	0.03	0.03	0.05	0.05
Cl Oxy. Eq.	-0.01	-0.01	-0.01	-0.01
Total wt%	95.2	94.6	95.6	95.0
	Atom units based on 11(O)			
Si	2.64	2.67	2.68	2.63
Al	1.78	1.80	1.78	1.80
Na	0.02	0.02	0.02	0.03
Mg	0.96	0.96	0.92	0.86
Fe	1.26	1.17	1.20	1.35
Cr	0.00	0.01	0.04	0.05
Co	0.00	0.00	0.00	0.00
Ni	0.01	0.01	0.01	0.01
Ti	0.16	0.17	0.15	0.14
K	0.94	0.94	0.94	0.91
	Tetrahedral site			
Si(IV)	2.64	2.67	2.68	2.63
Al(IV)	1.36	1.33	1.32	1.37
Σtetr	4.00	4.00	4.00	4.00
	Octahedral site			
Al(VI)	0.42	0.47	0.46	0.42
Fe(VI)	1.26	1.17	1.20	1.35
Mg(VI)	0.96	0.96	0.92	0.86
Ti(VI)	0.16	0.17	0.15	0.14
Σoct	2.81	2.77	2.73	2.78
	Interlayer site			
K(inter)	0.94	0.94	0.94	0.91
Na(inter)	0.02	0.02	0.02	0.03
Σinter	0.96	0.96	0.96	0.94
	Mole fractions of different biotite solid solution endmembers			
Xphl	0.34	0.35	0.34	0.31
Xsid	0.08	0.07	0.07	0.08
Xann	0.58	0.59	0.59	0.61

Mole fraction values for siderophyllite (Xsid) of all 237 biotite is consistent and ranges between 0.07 and 0.09. However, mole fraction values of the Fe- and Mg-end members do vary. Biotite analyzed as part of this study shows two strong signatures **Figure 6-3**; silicate-hosted biotite-types are more Mg-rich versus sulfide-hosted biotite-types which are more ferrous-rich, although there is also an overlap in compositions. The sulfide-hosted biotite types were further investigated in **Figure 6-4** where the mole fractions of annite were plotted against phlogopite, including the sulfide mineral with which the biotite is intergrown with. Biotite laths dominantly in contact with pyrite are relatively Mg-rich, whereas those in contact with pentlandite are Fe-rich and those in contact with pyrrhotite have an intermediate composition. This suggests that biotite compositions may be controlled by local biotite-sulfide mineral equilibrium.

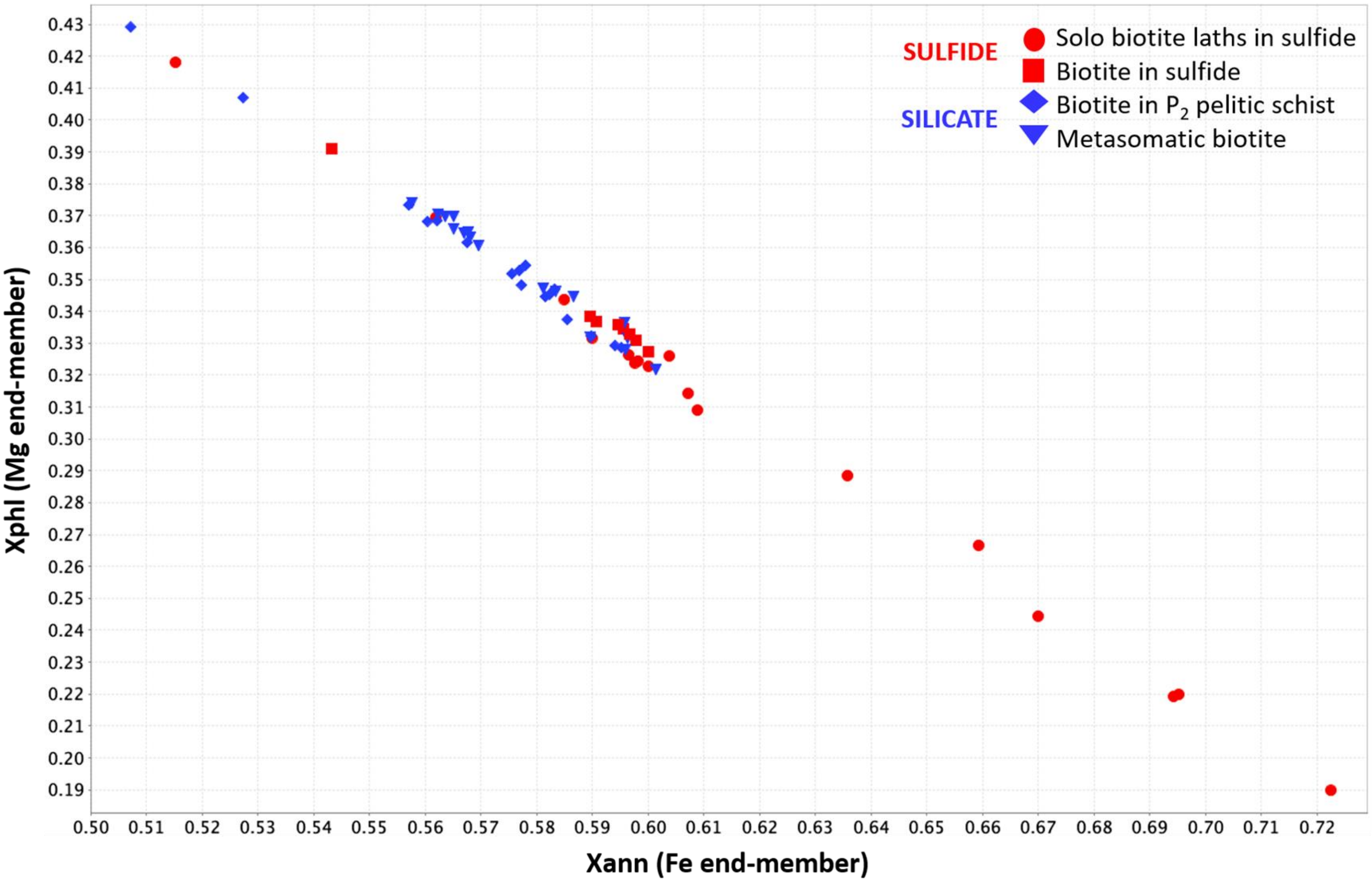

Figure 6-3: Mole fraction of annite (Xann) as a function of phlogopite (Xphl) for biotite grains in sulfide- (red) and silicate- (blue) hosted rocks for the four-biotite types. Data is based on mean probe values calculated for 59 biotite grains across 20 different thin sections. A correlation between silicate-hosted biotite types and high Xphl values exists, as well as sulfide-hosted biotite types and high Xann values.

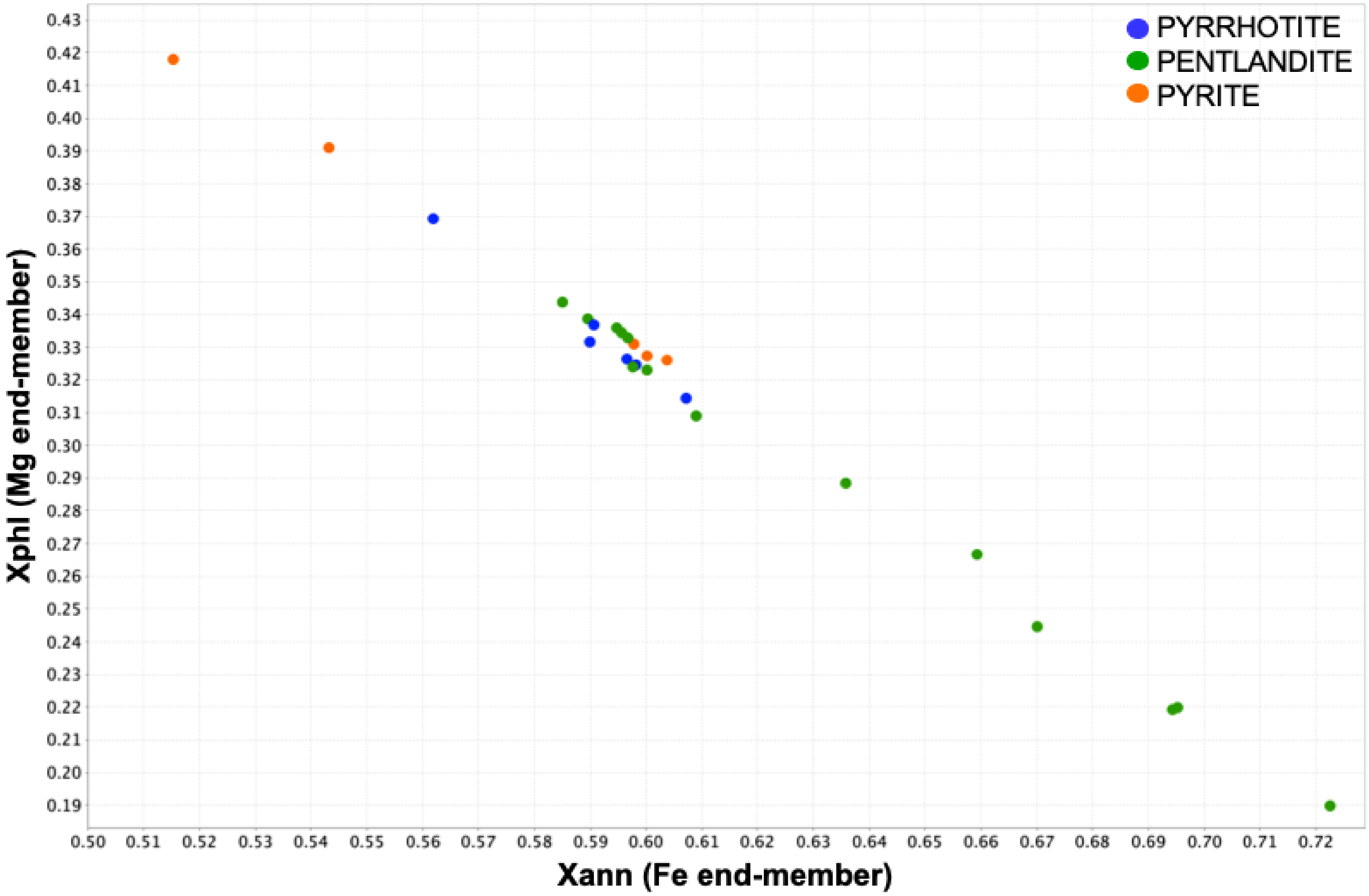

Figure 6-4: Mole fraction of annite (Xann) as a function of phlogopite (Xphl) for sulfide-hosted biotite grains dominantly surrounded by pyrrhotite (blue), pentlandite (green) and pyrite (orange). Only biotite grains from the sulfide-hosted groups; BT_SULF and SOLO_SULF, were considered. Data is based on mean probe values calculated for 25 sulfide-hosted biotite grains across 9 different thin sections. Biotite laths dominantly in contact with pyrite have the highest Xphl, and lowest Xann concentrations; averages of 0.359 and 0.572, respectively. Biotite laths dominantly in contact with pentlandite have the lowest Xphl and highest Xann concentrations; averages of 0.291 and 0.632, respectively. Biotite laths dominantly in contact with pyrrhotite take up an intermediate composition between the two, 0.334 Xphl and 0.592 Xann.

The FeO, MgO, NiO, Cr_2O_3, CoO and TiO_2, concentrations in biotite grains within pelitic schists were also examined as a function of the distance from sulfide mineralization in order to test if a possible elemental envelope could be detected.

The compositions of biotite from the horizonal drill hole DH#1365050 were examined from the contact with sulfide mineralization to 4.0 metres in the neighbouring pelitic schists **(Figure 6-5).** The mole fractions of annite, phlogopite and siderophyllite values did not vary with distance.

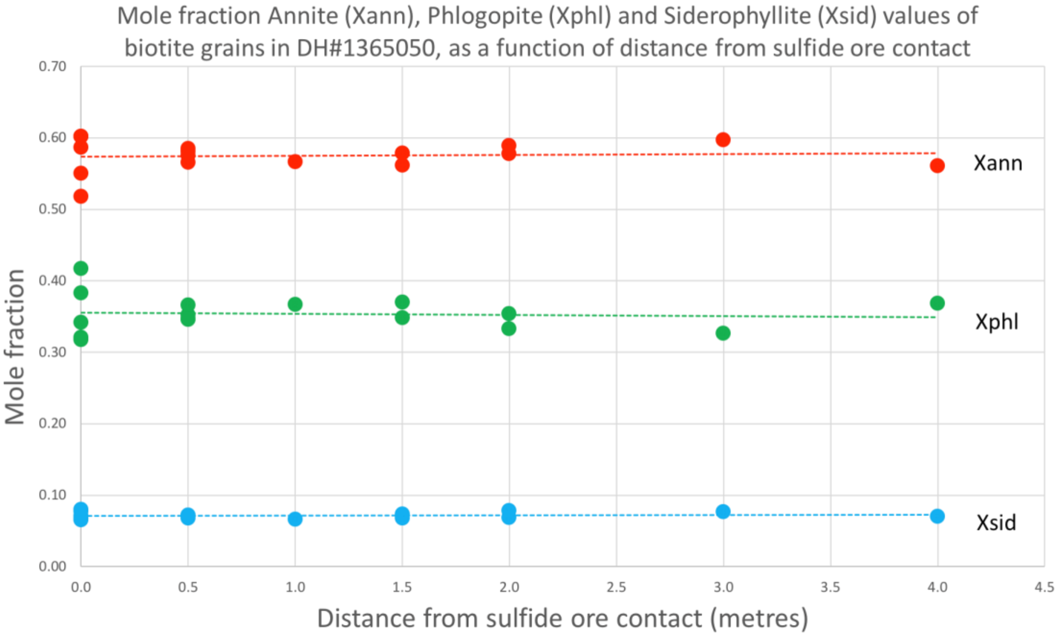

Figure 6-5: Mole fraction Annite (Xann), Phlogopite (Xphl) and Siderophyllite (Xsid) values of biotite grains hosted within sulfide (denoted at 0.0 metres on the X-axis) and in neighbouring pelitic schists (denoted from 0.5 – 4.5 metres). Mole fraction values of end-members are constant in biotite grains within sulfide and in neighbouring pelitic schists up to 4.0 metres away.

The nickel (NiO) and chromium (Cr_2O_3) concentrations were evaluated in biotite laths from drill hole #1365050. Biotite grains in sulfide have enriched nickel and chromium contents, on average 0.236 wt% and 0.482 wt %, respectively **(Figure 6-6).** Biotite grains in neighbouring pelitic schists (0.5 – 4.0 metres away from a sulfide horizon) have averages of 0.059 wt% nickel and 0.049 wt% chromium contents **(Figure**

6-6). Chromium contents fall off strongly beyond 0.5 metres (<500 ppm Cr) from the sulfide ore contact, but the nickel contents in biotite grains are elevated within 2.0 metres of the sulfide ore contact but fall off beyond 2.0 metres (<150 ppm Ni) **(Figure 6-6).** Additionally, biotite grains from underground ore samples in the 1D were also probed and a mean of 0.238 wt% Ni in biotite is consistently shown **(Appendix 9)**. Therefore, significant evidence for nickel in mica is supported by EPMA probe analyses on biotite grains in sulfide from both drill hole and underground ore samples in the 1D orebody.

During proposed formation of biotite **(Reaction 1),** if any nickel were present in pyrrhotite during silicate-sulfide (pyrrhotite) interactions, it would be expected that the nickel would end up in the biotite. This agrees with our observations of elevated Cr- and Ni- in micas in the 1D. Further discussions on the significant concentrations of Ni and Cr in mica are presented in **Sections 8.3.1** and **9.2**.

Cobalt (CoO) and titanium (TiO_2) values of biotite grains were also analyzed. Ranges from 200 to 300 ppm Co and 2.22 to 2.95 weight % TiO_2 were recorded but did not vary as a function of distance from the sulfide contact.

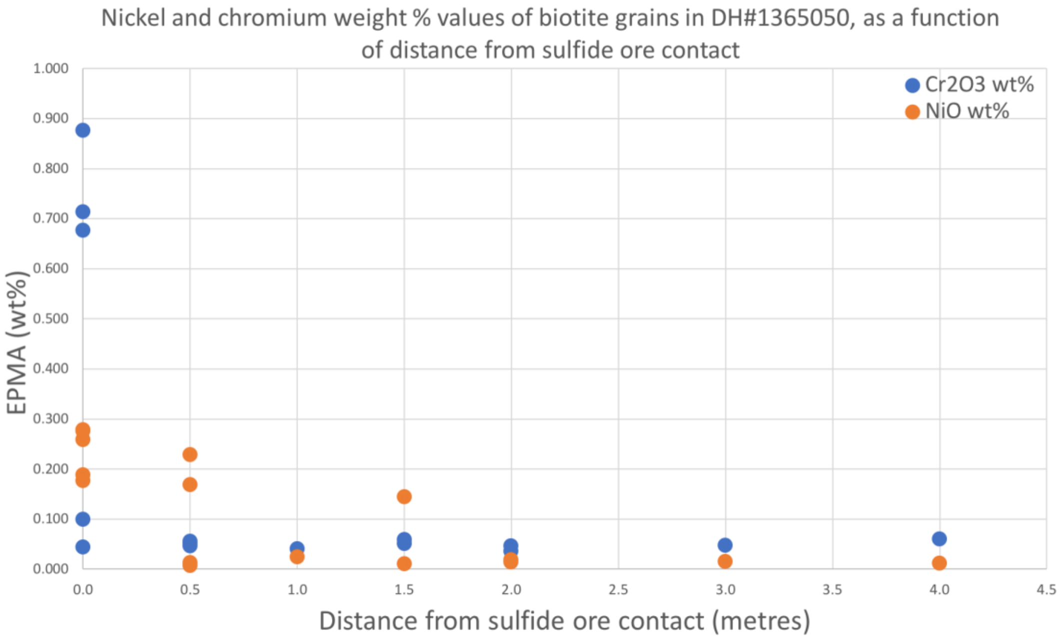

Figure 6-6: Nickel and chromium values of biotite grains hosted within sulfide (denoted at 0.0 metres on the X-axis) and in neighbouring pelitic schists (denoted from 0.5 – 4.5 metres). Biotite grains in sulfide have enriched nickel (orange) and chromium (blue) contents, on average 0.236 and 0.482 wt %, respectively. Biotite grains in neighbouring pelitic schists (0.5 – 4.0 metres away from a sulfide horizon) have averages of 0.059 wt% nickel and 0.049 wt% chromium contents. Chromium contents fall off strongly beyond 0.5 metres from the sulfide ore contact. Nickel contents in biotite grains stay elevated within 2.0 metres of the ore contact, then fall off sharply >2.0 metres.

6.2 Garnet

Whole rock geochemical analyses were compared between sulfide- and silicate-hosted garnet grains in the Thompson 1D orebody. Stoichiometric relationships were investigated and compositions of four principal end members were determined: almandine (Alm), grossular (Grs), pyrope (Pyr), and spessartine (Sps). The dominant end members present in both cores and rims of garnet grains were determined. Furthermore, sulfide samples with modal abundances of >5% garnet in thin sections, coincide with samples that have a Ni tenor of >8%. High nickel tenor sulfide samples were observed to have high garnet modal abundances in this study. Therefore, it is worthwhile to determine the trace element compositions of garnet, specifically Ni, Co and Cr distributions, and how they vary between silicate- and sulfide-hosted garnet types.

6.2.1 Mineralogy

Garnet is a common silicate phase within the 1D ores at the T3 mine. It commonly occurs in the P_2 metasediments, dominantly within biotite-rich portions of the schist, but is also present in sulfide lenses and ultramafic intrusions (amphibolite/pyroxenite). Garnet dominantly occurs as euhedral grains that range in size from 50µm to several centimeters in diameter. Garnet grains are poikilitic in nature, and host biotite laths, quartz and feldspar grains in their cores. Garnet grains also contain anhedral sulfide and polymetallic sulfide melt inclusions; the difference between sulfide melt and mineral inclusions is discussed in **Section 7.6**. However, garnet grains can also be clear and inclusion-free, particularly at the rims of grains, which represents homogenization and late-growth (Bleeker, 1990).

Garnet can be characterized into two-main types: hosted within sulfide-rich rocks (Grt_sulf) or within the neighbouring P_2 pelitic schist (Grt_P2_schist). In the case of the former, garnet is present as sub- to euhedral porphyroclasts that are heavily fractured and contain abundant sulfide and silicate mineral inclusions. Garnet is predominantly entrained within a sulfide-rich matrix (Po>Pn>Py) as isolated porphyroclasts **(Figure 6-7)** or hosted within ripped up schist wall rock entrained in sulfide.

The second-type of garnet that occurs in schists is locally fractured and forms an- to subhedral porphyroclasts interlayered within the strong pelitic schist fabric **(Figure 6-8 A).** Garnet hosted within the pelitic schists is also inclusion-bearing, however inclusions are concentrated within the cores of grains.

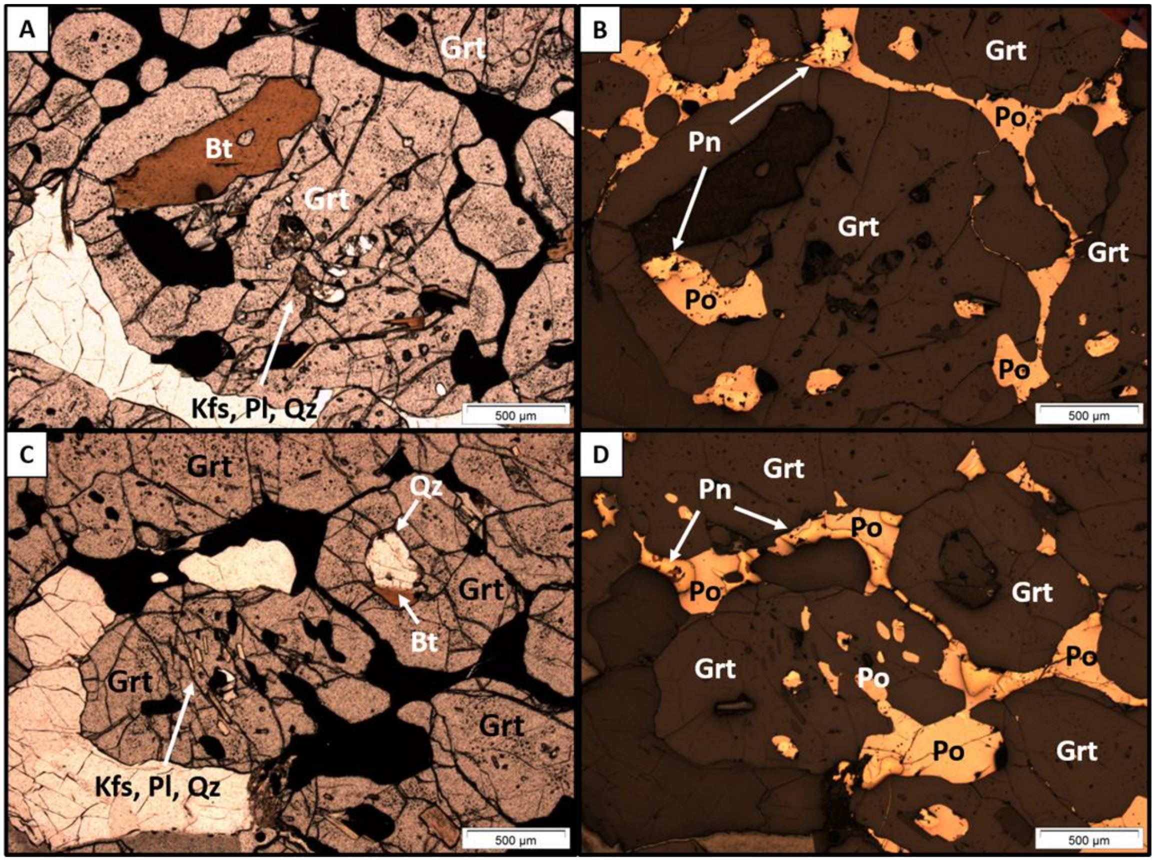

Figure 6-7 A) Transmitted light image in PPL of thin section 1045364, showing numerous silicate (Qz, Kfs, Pl, Bt) and sulfide inclusions trapped within two sulfide-hosted garnet grains (Grt_sulf). B) Reflected light image of the same grain in A. Dominantly anhedral pyrrhotite and pentlandite inclusions within the garnet. Note, these do not classify as 'sulfide melt inclusions'. C) Transmitted light image in PPL of thin section 1045364, showing numerous silicate (Qz, Kfs, Pl, Bt) and sulfide inclusions trapped within garnet grains. D) Reflected light image of the same image as C. Dominantly anhedral pyrrhotite and pentlandite inclusions within the garnet. Note, these do not classify as 'sulfide melt inclusions'. Abbreviations; Bt (biotite), Qz (quartz), Grt (garnet), Kfs (K-feldspar), Pl (plagioclase), Po (pyrrhotite), Pn (pentlandite).

6.2.2 Mineral Chemistry

In total, 46 spots were analyzed for SiO_2, Al_2O_3, MgO, FeO, MnO, Cr_2O_3, NiO, CaO and CoO. by EPMA from 8 grains and from 4 different polished thin sections. Total weight percent values of >98.5% were acceptable in this study. The stoichiometries for all 46 garnet spot analyses are presented in **Appendix 13** along with a calculation spreadsheet for determining stoichiometries that shows the mole fractions of the almandine (Alm), grossular (Grs), pyrope (Pyr), and spessartine (Sps) end-members. **Table 6-2** gives representative spot data and stoichiometries of core-rim values for the two main garnet-types.

Table 6-2 shows four representative analyses of the two main garnet types; sulfide-hosted (Grt_sulf) versus silicate-hosted (Grt_P2_schist) along with core and rim values. Data is presented in EPMA weight %, stoichiometry and mole fraction of garnet end-members; Almandine (Alm), Grossular (Grs), Pyrope (Pyr), Spessartine (Sps). End-member mole fractions are calculated in reference to Zeh (2006): Alm = (Fe2+/Σ X); Grs = (Ca/Σ X); Pyr = (Mg/Σ X); Sps = (Mn/Σ X). Abbreviations; n.d. (not detected by probe; below detection limits), N/A (not available).

Sample	1045364	1045364	1045351	1045351
Analysis code	Grt1_04	Grt2_04	Grt2_03	Grt3_05
Garnet type	Grt_sulf	Grt_sulf	Grt_p2_schist	Grt_p2_schist
Core/Rim	Core	Rim	Core	Rim
	EPMA data (wt%)			
SiO2	37.4	37.4	36.7	36.4
Al2O3	21.6	21.9	21.5	21.2
MgO	5.73	5.96	3.76	2.37
FeO	28.3	27.3	31.2	32.0
MnO	4.38	4.96	4.26	5.37
Cr2O3	0.04	0.05	0.02	0.02
NiO	n.d.	n.d.	n.d.	n.d.
CaO	1.88	1.72	1.57	1.89
CoO	n.d.	n.d.	n.d.	n.d.
Total wt%	99.3	99.3	99.0	99.3
	Atom units based on 12(O)			
Si	2.97	2.96	2.97	2.97
Al	2.03	2.05	2.05	2.04
Mg	0.68	0.70	0.45	0.29
Fe	1.88	1.81	2.11	2.18
MnO	0.30	0.33	0.29	0.37
Cr2O3	0.00	0.00	0.00	0.00
Ni	N/A	N/A	N/A	N/A
CaO	0.16	0.15	0.14	0.16
Co	N/A	N/A	N/A	N/A
	Tetrahedral site			
Si(IV)	2.97	2.96	2.97	2.97
Al(IV)	0.03	0.04	0.03	0.03
Σtetr	3.00	3.00	3.00	3.00
	Octahedral site			
Al(VI)	2.00	2.01	2.02	2.01
Ti	0.00	0.00	0.00	0.00
Σ Y	2.00	2.01	2.02	2.01
Fe2+	1.88	1.81	2.11	2.18
Ca	0.16	0.15	0.14	0.16
Mn	0.30	0.33	0.29	0.37
Mg	0.68	0.70	0.45	0.29
Σ X	3.02	2.99	2.99	3.00
	Mole fractions of garnet endmembers			
Alm	0.62	0.60	0.71	0.73
Grs	0.05	0.05	0.05	0.05
Pyr	0.23	0.23	0.15	0.10
Sps	0.10	0.11	0.10	0.12
Fe/(Mg+Fe)	0.73	0.72	0.82	0.88

Mole fraction values for grossular and spessartine compositions are nearly constant and range ~0.05 grossular and 0.10 to 0.12 spessartine. However, spessartine mole fraction values are slightly elevated in the rims of grains, compared to their cores.

Sulfide-hosted garnet grains have mole fraction values of 0.60 to 0.63 almandine and 0.22 to 0.24 pyrope. Silicate-hosted garnet grains have mole fraction values of 0.70 to 0.73 almandine and 0.10 to 0.15 pyrope. Therefore, sulfide-hosted garnet types have slightly lower Fe- and higher Mg-compositions, compared to silicate-hosted garnet types which are slightly more Fe-rich. However, the dominant garnet end member in the Thompson 1D orebody is almandine (Fe-rich) as outlined by **Table 6-2.**

6.2.3 EDS/WDS X-Ray Mapping

EDS X-ray maps of Al, Ca, Mn, Si, Ti and WDS X-ray maps of elements Co, Cr, Fe, Mg, Ni were completed to establish whether the garnets are zoned. The EDS-Mn and WDS-Mg maps show very slight zoning of Mn and Mg in garnet **(Figure 6-8).** In the case of the former, the outer margins of silicate-hosted garnet grains are slightly more enriched in Mn, compared to the cores of the grain **(Figure 6-8 B).** Whereas the cores of silicate-hosted garnet grains are slightly more enriched in Mg, compared to the outer margins of the grains **(Figure 6-8 C).** These EDS/WDS observations are consistent with core/rim data presented in **Table 6-2** for silicate-hosted garnet grains. In both cases, Mn and Mg zoning is very subtle. All other element maps apart from Mn and Mg were homogenous and did not show zoning.

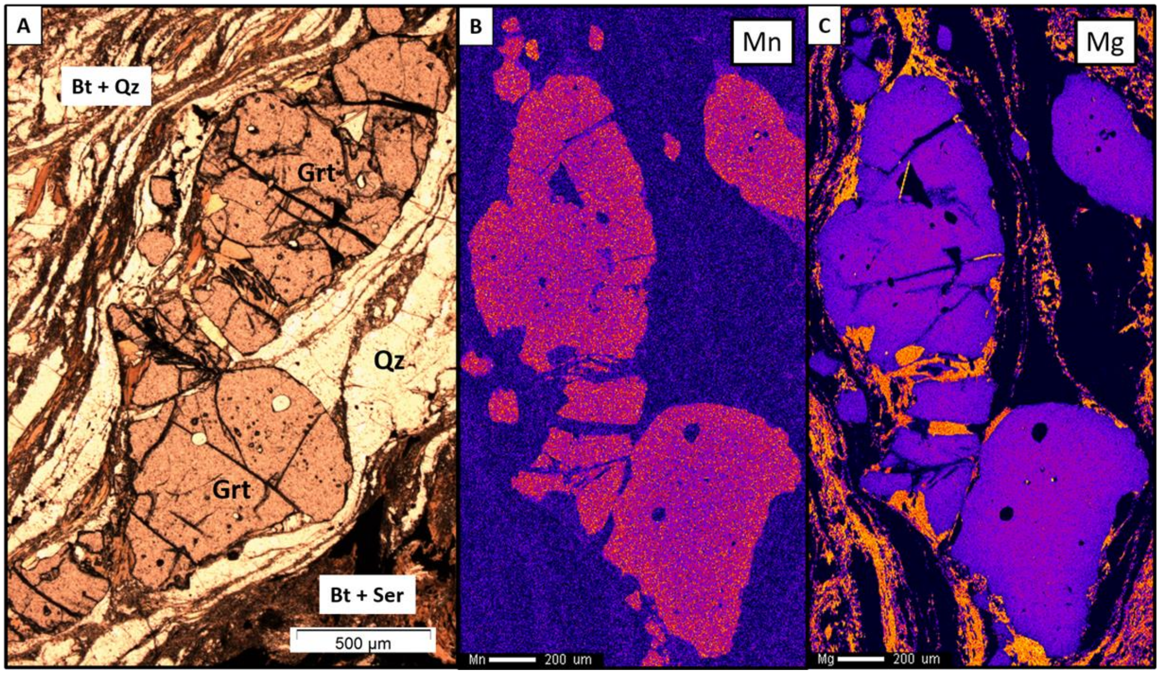

Figure 6-8 A) Transmitted light image in PPL of thin section 1045351, showing numerous silicate (Qz, Kfs, Pl, Bt) and sulfide inclusions trapped within a silicate-hosted garnet grain (Grt_P2_schist). The garnet grain has been fractured, squished and rotated parallel to the Bt + Qz schist foliation. B) Shows a EDS-Mn map of the same garnet grain in A. Notice the slight enrichment of Mn towards the outer margins of the grain. C) Shows a WDS-Mg map of the same grain in A. Notice the slight enrichment of Mg towards the core of the garnet grain. Abbreviations; Bt (biotite), Qz (quartz), Grt (garnet), Ser (sericite).

Chromium contents are higher in sulfide-hosted garnets (350 – 550 ppm Cr) compared to silicate-hosted garnets (130 – 200 ppm Cr). Interestingly, cobalt and nickel values in both types of garnet were consistently below detection limits of the probe. Therefore, there is <280 ppm Ni and <215 ppm Co in sulfide- and silicate-hosted garnet grains in the 1D ore zone.

6.3 Quartz

6.3.1 Cathodoluminescence Maps

Several metamorphic quartz grains were analyzed by cathodoluminescence (CL) to determine whether there are multiple generations of quartz. Three backscatter and ‘false colour’ Cathodoluminescence maps of metamorphic quartz grains from thin section 1045386 are shown in **Figure 6-9.** ‘False colour’ imaging was used to better contrast the different generations of quartz. Subrounded, polymetallic (Po-Pn-Py-Ccp) sulfide melt inclusions occur in the orange quartz, which is surrounded by purple quartz that lacks sulfide melt inclusions. The latter is intergrown with biotite and metamorphic graphite laths. Quartz grains are recrystallized (grain-size reduced) around primary sulfide melt inclusions. Several sulfide melt inclusions also occur along some, but not all, fractures in the purple quartz that cut the orange quartz. From the Cathodoluminescence maps it is evident that two generations of metamorphic quartz exist; orange (early-quartz) versus purple (late-quartz) and that sulfide melt inclusions are associated with the early quartz. Further analysis on mineralogy and mineral chemistry of sulfide melt inclusions are reported in **Section 7.6**, along with detailed discussions in **Section 8.2.5**.

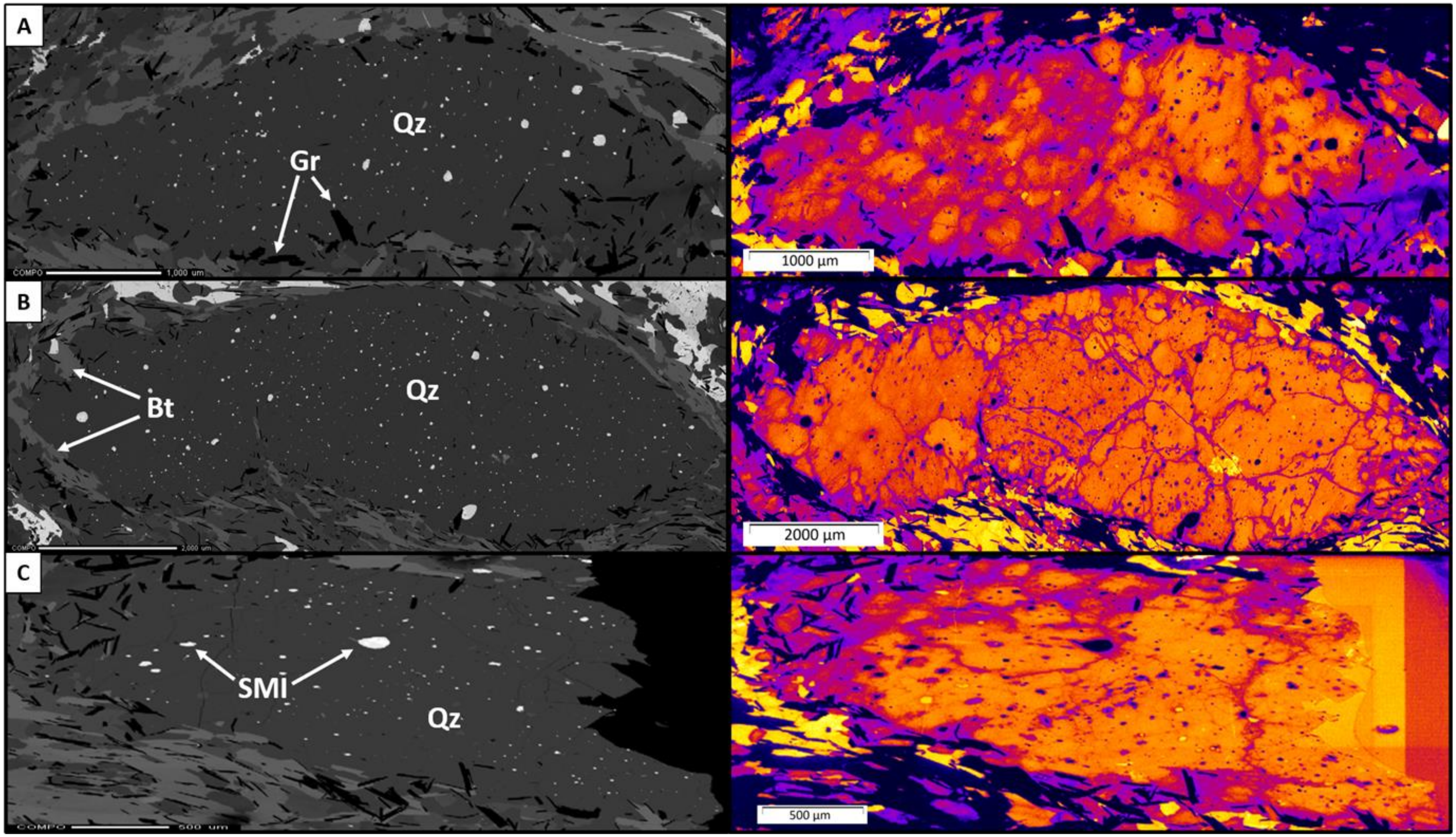

Figure 6-9: Three backscatter images of several metamorphic quartz grains (A, B, C) from thin section 1045386. In the backscatter images, graphite laths are black; sulfide melt inclusions (SMI) are white; biotite laths are a lighter grey; quartz grains are a darker grey. The SMI are dominantly made up of Po-Pn-Py-Ccp. All three metamorphic quartz grains have accompanying 'false-colour' cathodoluminescence (CL) maps. In the CL maps, two generations of quartz exist: orange (early-quartz) versus purple (late-quartz). The SMIs are concentrated in the early generation of quartz (orange) being surrounded by a later generation of quartz (purple) that is intergrown with biotite and graphite laths. Many SMIs occur along fractures in quartz grains, however many are not associated with fractures at all. Abbreviations; Bt (biotite), Gr (graphite), Qz (quartz), SMI (sulfide melt inclusion).

Chapter 7: Sulfide Mineralogy and Mineral Chemistry

Petrographic analysis of 103 underground grab samples and 51 drill-core samples, has led to the textural classification of 5 types of pyrrhotite, 6 types of pentlandite and 7 types of pyrite. The following chapter will outline the mineralogy, textural variations, mineral chemistry and EPMA X-ray maps of the main sulfide assemblages (Po-Pn-Py-Ccp-Gdf) observed in this study in the 1D orebody at Thompson.

7.1 Pyrrhotite

7.1.1 Mineralogy

Pyrrhotite (Po) is the most abundant sulfide mineral in the Thompson Nickel Belt (TNB) and within the 1D orebody at Thompson mine. All other sulfide minerals (Pn>Py>Ccp>Gdf) are related to pyrrhotite. Detailed reflected light petrographic analysis has led to the identification of 5 different textural types of pyrrhotite: polygonal grain boundary texture (PGBT), homogenous Po matrix (homPo), subhedral inclusions within silicates (SI-X), Po infill (Po-INF) and an elongated pyrrhotite texture (EPT).

Polygonal grain boundary texture (PGBT)

This is a common texture in which pyrrhotite (up to 500µm across) shows distinct, recrystallized polygonal grain boundaries with sub-grains that become extinct at different positions under cross-polarized light **(Figure 7-1 A).** Pyrrhotite grains are commonly fractured and pitted. Pentlandite and pyrite commonly occur along pyrrhotite grain boundaries and/or at triple junctions.

Homogenous pyrrhotite matrix (homPo)

This is the most common pyrrhotite textural type. The sulfide matrix consists of a homogenous mass of pyrrhotite with no visible grain boundaries **(Figure 7-1 B)**, therefore determining a grain size for the pyrrhotite is difficult. This textural type commonly shows pits and fractures.

Subhedral inclusions within silicates (SI-X)

Subrounded pyrrhotite grains (up to 500µm) are present as inclusions in silicate grains **(Figure 7-1 C).** Traces of pentlandite and minor amounts of pyrite, chalcopyrite, and gersdorffite can also occur with pyrrhotite in these inclusions. Silicate grains consist dominantly of garnet, as well as plagioclase, K-feldspar, and grain-size reduced quartz grains.

Pyrrhotite infill (Po-INF)

This is a common texture where pyrrhotite has infilled open space and fractures between interlocked silicate grains, commonly biotite laths making up the host P_2 schist unit **(Figure 7-1 D).** Pyrrhotite also infills micro-fractures in silicates (garnet, biotite, quartz), and commonly occurs at pressure shadow zones and triple junctions.

Elongated pyrrhotite texture (EPT)

This pyrrhotite texture is less common but the most interesting. Pyrrhotite grains occur as ribbons that are up to 600µm long and 300µm across. These ribbons are defined by variable extinction within the interlayered bands in cross-polarized light **(Figure 7-1 E)**. Monteiro and Krstic (2006) describe this texture as ‘kink bands’ that they interpret to be the result of ductile deformation. Elongated pyrrhotite lacks polygonal grain boundaries, however, both pyrrhotite textures commonly occur together.

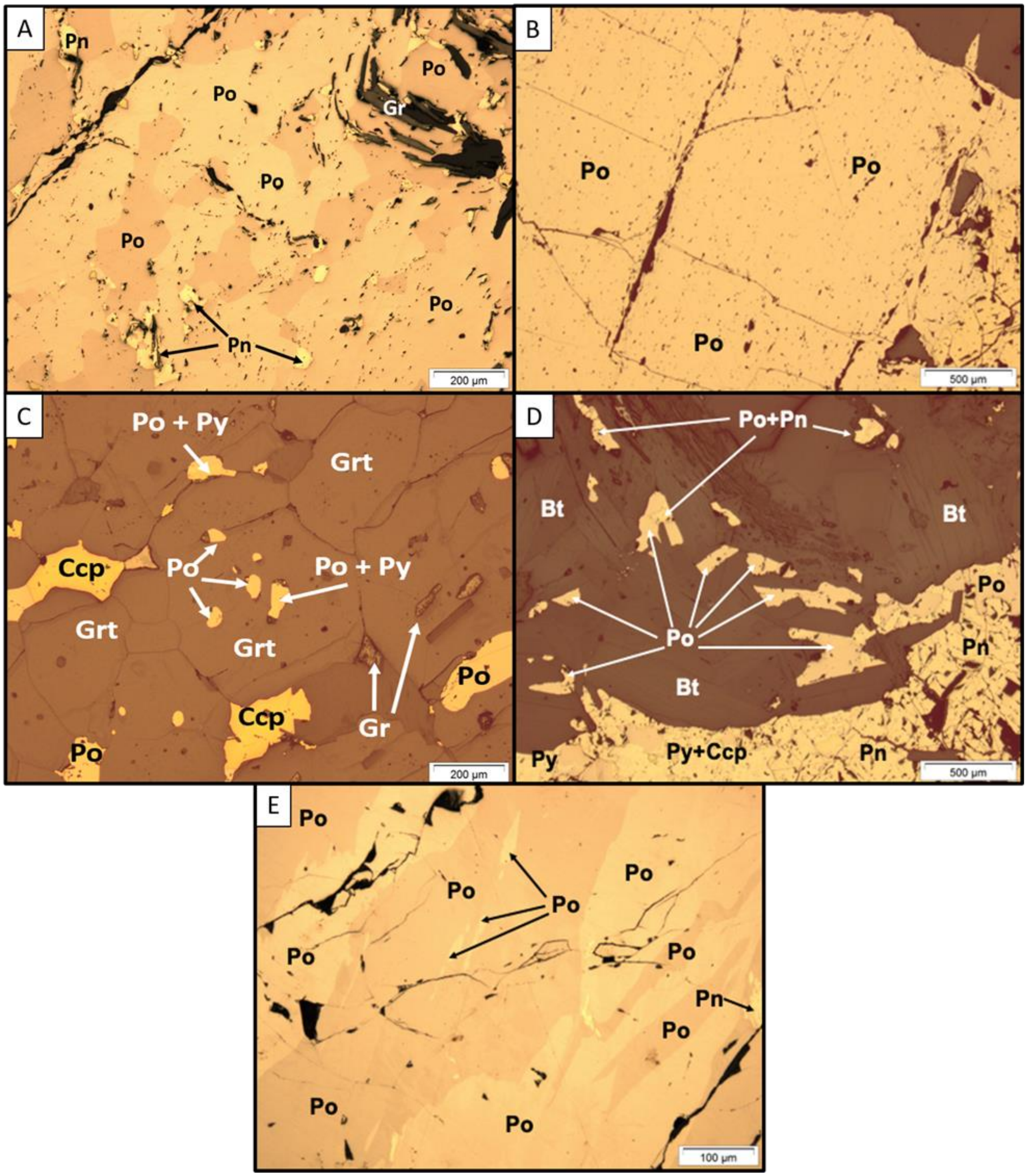

Figure 7-1: Reflected light photomicrographs in PPL of the different pyrrhotite textures in the 1D orebody. (A) Polygonal grain boundary texture (PGBT) from thin section 1045398. (B) Homogenous pyrrhotite (homPo) in thin section 1045359. (C) Subhedral inclusions within silicates (SI-X) from thin section 1045364. In this case, the sulfide inclusions are entrained within fractured garnet grains. (D) Pyrrhotite infill (Po-INF) from thin section 1045397. Pyrrhotite is interstitial between interlocked biotite grains. (E) Elongated pyrrhotite texture (EPT) from thin section 1045357. In EPT, the pyrrhotite is described as the light and dark ribbons that show different extinction orientation as the stage is rotated. Abbreviations; Pn (pentlandite), Po (pyrrhotite), Py (pyrite), Ccp (chalcopyrite), Gr (graphite), Grt (garnet), Bt (biotite).

7.1.2 Textural Variations

Four of the five pyrrhotite textural types are present in all ore mineralization styles **(Figure 7-2).** Their distribution does not change with ore type. However, the elongated pyrrhotite texture does show some variation amongst mineralization styles; it is absent from the semi-massive style of mineralization, not common in concordant style of mineralization, but largely abundant in the massive style of mineralization. In general, there is a lack of correlation between pyrrhotite textural type and mineralization style.

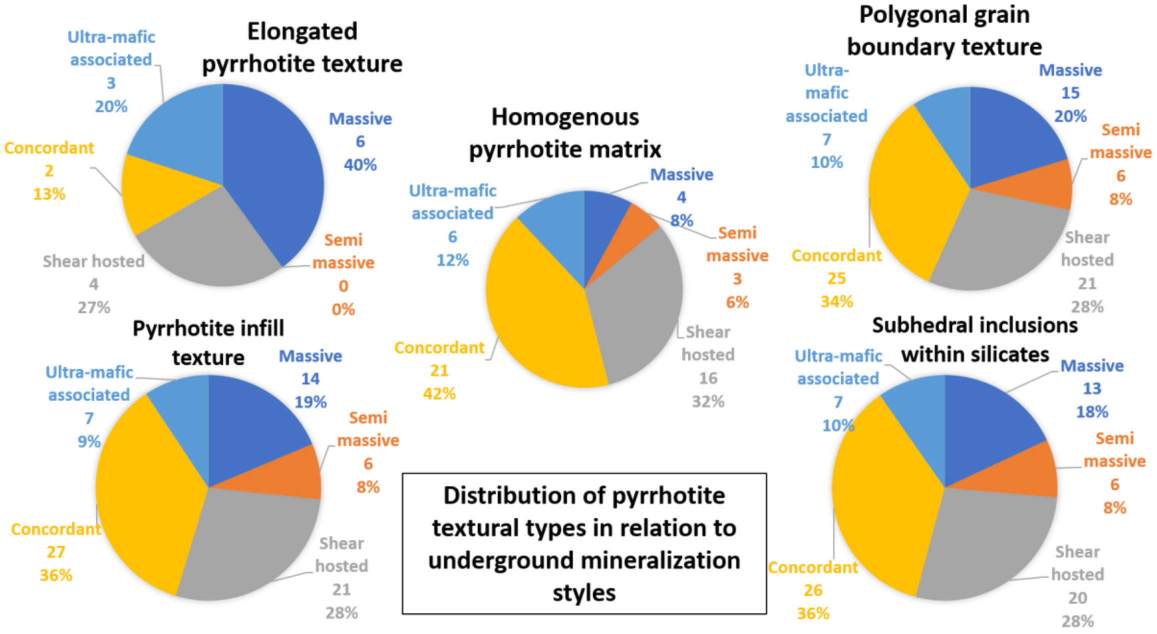

Figure 7-2: Distribution of pyrrhotite textural types across the major mineralization styles. All pie charts show similar abundances, elongated pyrrhotite texture being the exception. Elongated pyrrhotite texture is absent from semi-massive ore and largely concentrated in massive sulfide. Data is based on 78 underground ore samples.

7.1.3 Mineral Chemistry

The iron, sulfur and nickel compositions in pyrrhotite were determined by electron microprobe analysis. A total of 189 spots from 44 pyrrhotite grains from 15 different thin sections were analyzed in order to determine whether different textural types of pyrrhotite are compositionally different. Weight percent totals of >98% and <101.5% were acceptable and the stoichiometries for all 189 pyrrhotite spot analyses are presented in **Appendix 13**. **Table 7-1** lists EPMA weight percent data and atomic Fe (1-x) and ‘x’ values for the five representative pyrrhotite textural types, with the elongated pyrrhotite texture (EPT) having two representative analyses; EPT_1 characteristically has a higher atomic Fe (1-x) value and thus a higher Ni content compared to EPT_2. Apart from the EPT texture, there is no correlation between nickel and stoichiometry (1-x) across pyrrhotite textural types. Pyrrhotite stoichiometry was calculated by normalizing to an atomic S of 1.0 by multiplying by the ‘normalization value’. The concentrations of Fe, S and Ni are well above the EPMA detection limits of 200, 90 and 100 ppm, respectively.

Arsenic, Platinum, Palladium, Cobalt, Bismuth and Selenium were also analyzed in pyrrhotite by EPMA. However, all determinations were below their detection limits: As <160ppm, Pt <260ppm, Pd <100ppm, Co <100ppm, Bi <210ppm, and Se <410ppm. Additional LA-ICPMS analyses are needed to characterize the trace element compositions of pyrrhotite, but this is outside of the scope of this study.

Table 7-1: Six representative analyses for each pyrrhotite textural type; polygonal grain boundary texture (PGBT), homogenous pyrrhotite (homPo), subhedral inclusions within silicates (SI-X), pyrrhotite infill texture (Po-INF), elongated pyrrhotite texture one (EPT_1) and elongated pyrrhotite texture two (EPT_2). Two representative analyses of elongated pyrrhotite texture (EPT) are presented to show the Ni wt% variations that were observed between different anisotropic sections. Data is presented in EPMA weight % and atomic units normalized to 1.0 sulfur (Fe_{1-x} *S). The 'normalization value' along with the molecular weight for each element is used to calculate both Atomic S and Atomic Fe (1-x).*

Sample	1045410	1045410	1045365	1045397	1045361	1045361
Analysis code	P2_MUE_02	P1_HOM_02	P3_SI_05	P3_INF_06	pyrr01_01	pyrr01_06
Pyrrhotite type	PGBT	homPo	SI-X	Po-INF	EPT_1	EPT_2
	EPMA data (wt%)					
Fe	59.2	59.5	59.6	59.5	59.4	59.3
S	38.6	39.1	39.3	39.1	38.9	39.4
Ni	0.54	0.60	0.43	0.47	0.65	0.43
Total wt%	98.3	99.3	99.4	99.1	98.9	99.1
	Atomic Units					
Atomic S	1.000	1.000	1.000	1.000	1.000	1.000
Atomic Ni	0.008	0.008	0.006	0.007	0.009	0.006
Atomic Fe (1-x)	0.880	0.873	0.871	0.876	0.876	0.864
x	0.120	0.127	0.129	0.124	0.124	0.136

The average nickel content in pyrrhotite grains across all textural types is 0.48 wt% Ni with a standard deviation of 0.13 reported in 1σ. The amount of nickel in pyrrhotite is negligible and will not affect the stoichiometry calculations. Therefore, Fe+Ni values were not calculated. **Figure 7-3** shows nickel content in pyrrhotite as a function of whole rock nickel tenor. Whole rock nickel tenor groups are broken up into four categories: very high, high, moderate and low. Pyrrhotite grains in the very high and high whole rock nickel tenor groups have averages of 0.45 wt% Ni. Whereas the moderate and low nickel tenor groups have slightly higher values at 0.55 wt% Ni. It is important to note that the low nickel tenor group has a smaller sample group. Additionally, the data in **Figure 7-3** was plotted as a histogram (not shown) and two major peaks centered around 0.35 wt% Ni and 0.50 wt % Ni, with a smaller third peak around 0.75 wt% Ni was shown. The nickel variations between the groups could be related to monoclinic versus hexagonal pyrrhotite but there are not enough data (especially in the low tenor group) to make this conclusion.

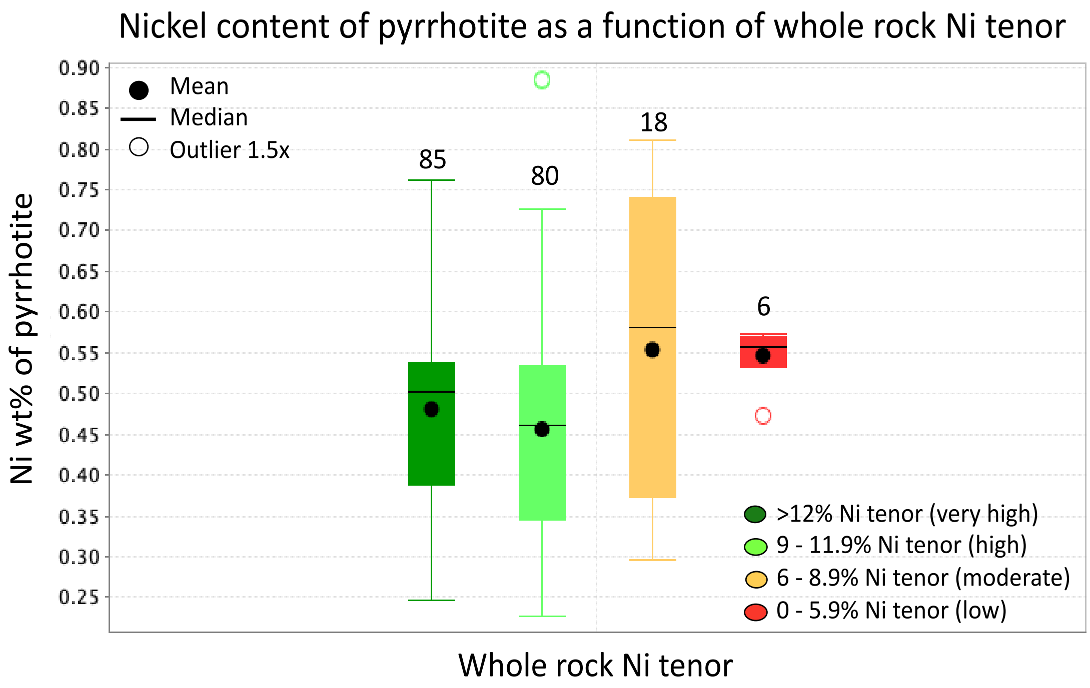

Figure 7-3: Nickel content of pyrrhotite versus different brackets of whole rock Ni tenor (low, moderate, high, very high). There is a lack of an apparent relationship between the nickel contents of the pyrrhotite and the whole rock nickel tenor of the sample. The numbers above the box and whisker plots represent the total number of pyrrhotite data points. Data is based on 189-point analyses from 15 different thin sections.

An additional question is whether the nickel content of pyrrhotite changes with textural type (**Figure 7-4**):

Mean nickel weight percent values (Ni wt. %) for each pyrrhotite textural type reported to 2σ are as follows; elongated pyrrhotite texture (0.52 ± 0.27), pyrrhotite infill texture (0.45 ± 0.21), subhedral inclusions within silicates (0.43 ± 0.30), homogenous pyrrhotite matrix (0.57 ± 0.20), polygonal grain boundary texture (0.47 ± 0.18).

Mean sulfur weight percent values (S wt. %) for each pyrrhotite textural type reported to 2σ are as follows; elongated pyrrhotite texture (38.8 ± 0.82), pyrrhotite infill texture (39.0 ± 0.73), subhedral inclusions within silicates (39.1 ± 0.71), homogenous pyrrhotite matrix (39.0 ± 0.69), polygonal grain boundary texture (39.0 ± 0.83).

Mean iron weight percent values (Fe wt. %) for each pyrrhotite textural type reported to 2σ are as follows; elongated pyrrhotite texture (59.7 ± 0.74), pyrrhotite infill texture (59.5 ± 0.47), subhedral inclusions within silicates (59.5 ± 0.48), homogenous pyrrhotite matrix (59.3 ± 0.62), polygonal grain boundary texture (59.6 ± 0.62).

Although there is slight variation between the different textural types (**Figure 7-4**); the nickel, sulfur and iron values overlap within 2σ, and conclude that there are no significant statistical differences.

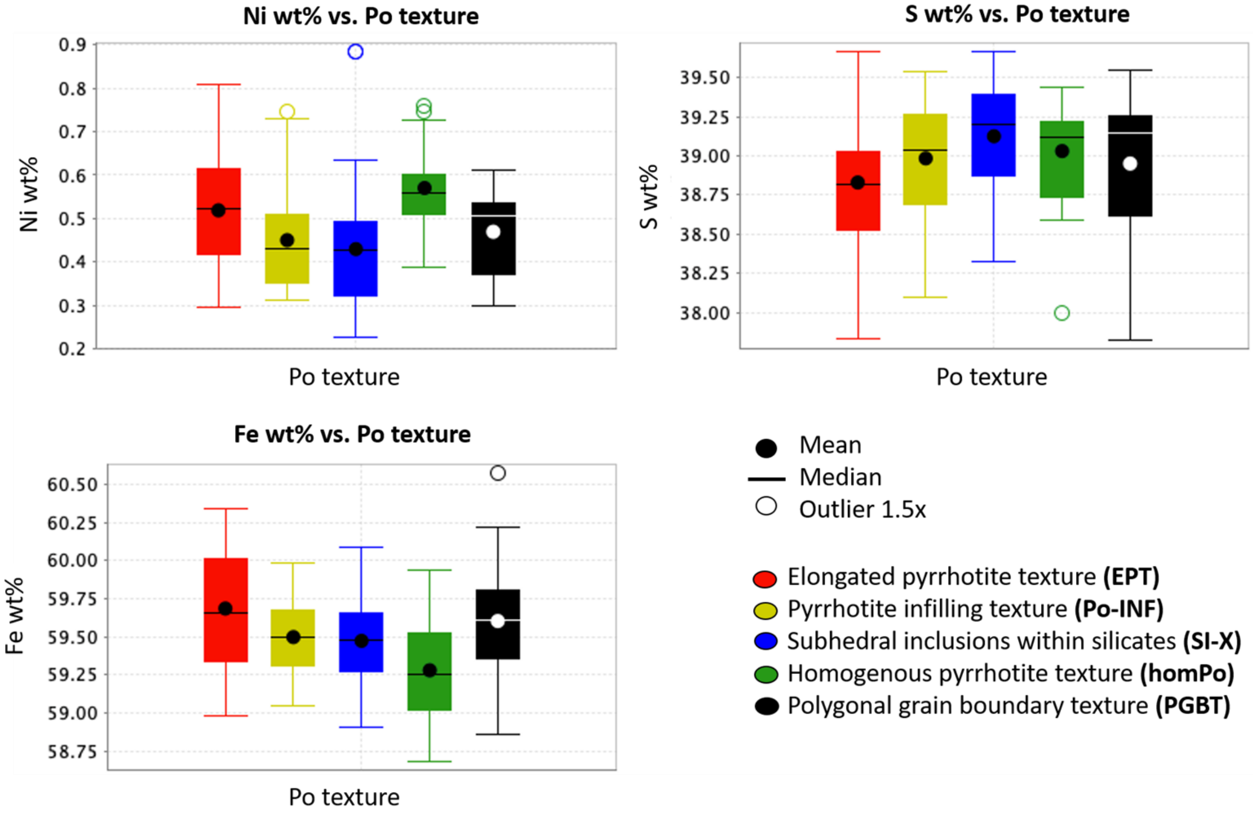

Figure 7-4: Box and whisker plots of Ni, S, Fe weight % values versus pyrrhotite texture. Data is based on 189-point analyses from 15 different thin sections. Colours represent the five different pyrrhotite textural types. The nickel, sulfur and iron values overlap within 2σ, and conclude that there are no significant statistical differences.

Binary plots of atomic Fe (1-x) as a function of nickel weight percent were plotted for 4/5 different types of pyrrhotite in **Figure 7-5.** There is no apparent correlation between atomic iron and nickel in these textures. Data indicates that pyrrhotite could have equilibrated at relatively constant temperatures. By contrast, atomic iron as a function of nickel weight percent for the elongated pyrrhotite texture was plotted separately in **Figure 7-6.** There is an apparent positive correlation between atomic iron and nickel within some samples (1045361,1045439,1045365), but this is not consistent for all samples. The lack of consistent variation precludes any further interpretation.

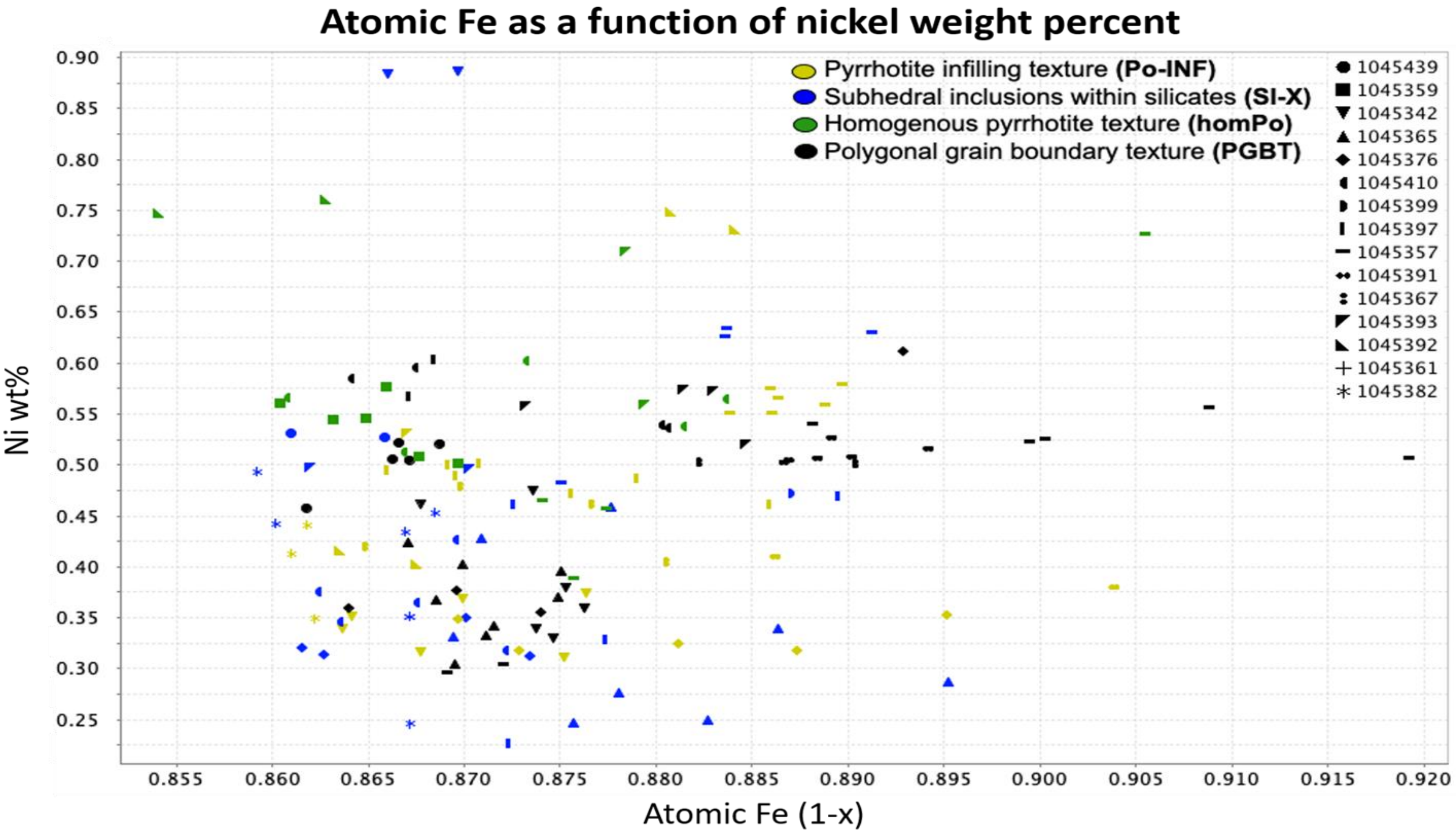

Figure 7-5: Atomic Fe (1-x) as a function of nickel weight percent for four pyrrhotite textural types; PGBT, homPo, SI-X, and Po-INF. No correlation between atomic Fe and Ni. Data indicates that pyrrhotite equilibrated at relatively constant temperatures. EPT (elongated pyrrhotite texture) has been omitted. Colours refer to the pyrrhotite texture, shapes refer to the various thin section samples. Data based on 143-point analyses from EPMA.

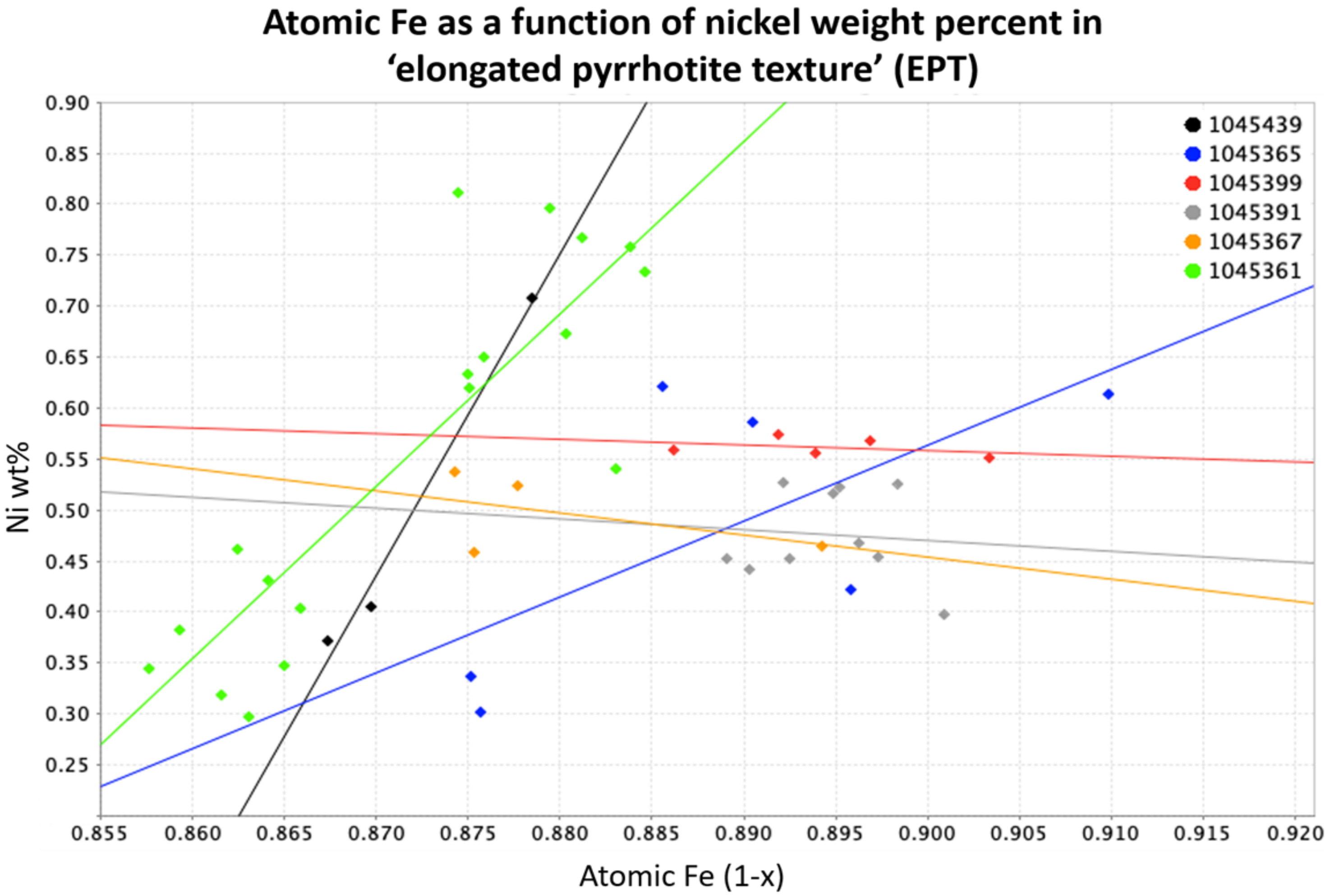

Figure 7-6: Atomic Fe (1-x) as a function of nickel weight percent for elongated pyrrhotite texture (EPT). There is a correlation between atomic Fe and Ni in several thin sections, but this is not consistent for all samples. Colours refer to a particular thin section. Data is based on 46-point analyses of EPT-type pyrrhotite across 6 thin sections.

7.1.4 EDS/WDS X-Ray Mapping

The energy dispersive spectrometer (EDS) X ray maps of Al, Bi, Ca, Cu, Fe, Na, Pb, Si and wavelength dispersive spectrometer (WDS) X-ray maps of elements As, Co, Mg, Ni, S were examined for the five different pyrrhotite textures. Pyrrhotite was very homogenous and did not show zoning of any elements. All pyrrhotite textures except for elongated pyrrhotite texture, were monotonous under EDS/WDS X ray maps. The elongated pyrrhotite texture locally showed heterogeneity in nickel content, as shown in the WDS-Ni map and table in **Figure 7-7.** Higher atomic iron values correlate with higher nickel concentrations, which could be attributed to exsolution of hexagonal pyrrhotite (S-poor) from the dominant monoclinic pyrrhotite (S-rich) via metamorphism and deformation of sulfides. However, this observation was not consistent in all samples where elongated pyrrhotite texture occurred.

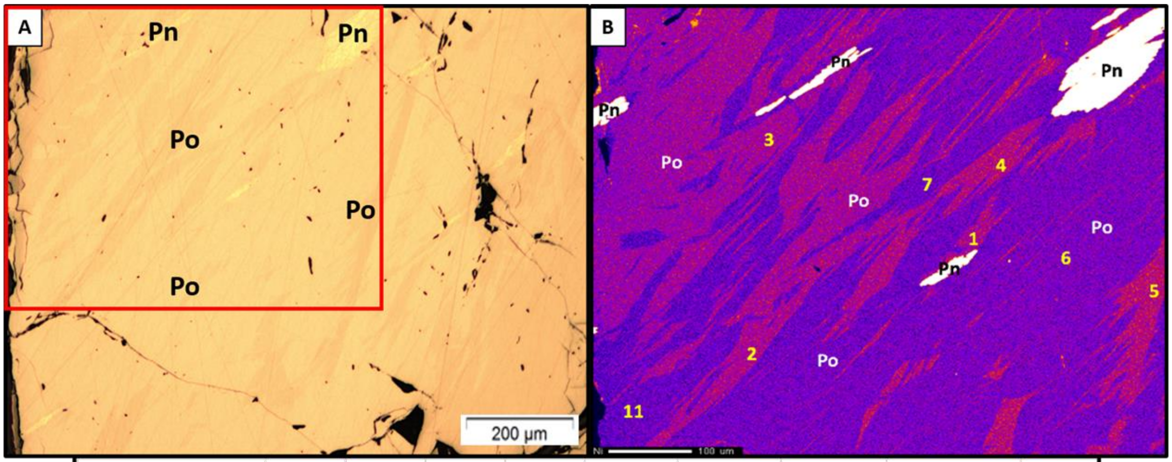

Po ID	Spot	Fe wt%	S wt%	Ni wt%	Total wt %	Atomic S	Norm. value	Atomic Fe (1-x)	x
1045361_pyrr01	1	59.4	38.9	0.65	98.9	1.00	0.824	0.876	0.124
1045361_pyrr01	2	59.6	38.8	0.67	99.1	1.00	0.825	0.880	0.120
1045361_pyrr01	3	59.5	39.0	0.63	99.2	1.00	0.821	0.875	0.125
1045361_pyrr01	4	59.7	38.7	0.73	99.1	1.00	0.828	0.885	0.115
1045361_pyrr01	5	59.6	38.8	0.77	99.1	1.00	0.826	0.881	0.119
1045361_pyrr01	6	59.3	39.4	0.43	99.1	1.00	0.814	0.864	0.136
1045361_pyrr01	7	59.3	39.6	0.38	99.3	1.00	0.809	0.859	0.141
1045361_pyrr01	11	59.3	39.7	0.35	99.3	1.00	0.808	0.858	0.142

Figure 7-7 A: Shows a reflected light photomicrograph of thin section 1045361, showing elongated pyrrhotite texture (EPT). This texture occurs as ribbons with varying anisotropism as the stage is rotated, giving the appearance of alternating light and dark bands. Pentlandite lamellae are a cream yellow colour sitting in a pyrrhotite matrix (pink coloured). Fractures and/or pits are a black colour. B: Shows the same area as in A (outlined by a red rectangle), but seen as a WDS Ni map. There is a correlation between areas of high atomic Fe and high Ni content, hexagonal pyrrhotite (pink) and areas of low atomic Fe and lower Ni content, monoclinic pyrrhotite (purple). Probed pyrrhotite spots and colours (pink and purple) correlate with areas on the WDS Ni map.

7.2 Pentlandite

7.2.1 Mineralogy

Pentlandite (Pn) is the dominant host of nickel in the 1D orebody, where it is associated with pyrrhotite-rich sulfide. Detailed reflected light petrographic analysis has led to the identification of six different types of pentlandite: granular pentlandite eyes (GPnE), pentlandite trails (PnT), grain boundary texture (Gb-Pn), subhedral inclusions within silicates (SI-X), pentlandite flames (FL), and rims around silicates (RIMS-X). Pentlandite grains are typically heavily pitted and fractured under reflected light.

Granular pentlandite eyes (GPnE)

This is a very common pentlandite texture in the 1D orebody that occurs in all nickel tenor groups **(Figure 7-9).** However, the coarser-grained ‘eyes’ are concentrated in the high and very high nickel tenor samples, whereas the finer-grained eyes dominantly occur in lower nickel tenor samples. Pentlandite has a distinct cream-yellow colour under plane-polarized reflected light, subhedral in nature and occurs as granular eyes (>500μm) dominantly within pyrrhotite **(Figure 7-8 A).** Locally, granular pentlandite grains are annealed, and commonly contain inclusions of euhedral pyrite (<350μm), anhedral chalcopyrite (<200μm) or anhedral to subhedral gersdorffite (<250μm). Less-commonly, pentlandite eyes are fine-grained, <500μm, and lack inclusions of other sulfide minerals.

Pentlandite trails (PnT)

This pentlandite texture is also common to all nickel tenor groups (**Figure 7-9**)**.** Fine- to coarse-grained trails of pentlandite (PnT) occur between pyrrhotite grains in the sulfide matrix (**Figure 7-8 B**) or have filled fractures in the pyrrhotite matrix or fractures in quartz, plagioclase and K-feldspar grains**.** The trails can be as long and wide as 3000 μm and 1000 μm, respectively, and pentlandite grains are locally annealed within these trails.

Grain boundary pentlandite (Gb-Pn)

This pentlandite texture occurs throughout all tenor groups but is more common in low and moderate nickel tenor samples **(Figure 7-9).** It consists of fine-grained pentlandite, <25 µm across, but it has been observed along the length of a pyrrhotite grain, up to 250 µm in length. Grain boundary pentlandite texture occurs along pyrrhotite grain boundaries or at triple junctions **(Figure 7-8 C)**, and commonly occurs where pyrrhotite exhibits a polygonal grain boundary texture.

Subhedral inclusions within silicates (SI-X)

This texture is common in all tenor groups but is rare in low nickel tenor samples **(Figure 7-9).** Sub-euhedral inclusions of pentlandite (up to 500µm across) are commonly present within larger, anhedral pyrrhotite inclusions that are hosted within silicate grains **(Figure 7-8 D).** However, subhedral inclusions of monomineralic pentlandite also occur (but it is also recognized that this is a 2-dimensional cut through a sulfide grain). These sulfide inclusions are commonly hosted by garnet, plagioclase, K-feldspar and quartz grains that have developed subgrains (undergone grain-size reduction).

Pentlandite flames (FL)

This is a very common pentlandite texture that is present in all nickel tenor groups **(Figure 7-9).** Fine-grained pentlandite flames are typically <50µm wide and <75µm long, and always occur exsolved from matrix pyrrhotite **(Figure 7-8 E).** Flames occur in polygonal grain boundary and homogenous matrix pyrrhotite textures. Flames also occur perpendicular to fractures or at contacts between pyrrhotite and silicate grains. Flames related to fractures or silicates are generally more course-grained, <50µm wide and up to 200µm long.

Rims around silicates (RIMS-X).

This is a rare pentlandite texture that only occurs in high nickel tenor samples **(Figure 7-9).** Fine- to coarse-grained rims of pentlandite up to 500µm across surround predominantly sericitized quartz and plagioclase grains. However, pentlandite rims also occur around biotite and muscovite laths **(Figure 7-8 F).** Rims can also be made up of granular pentlandite eyes, up to 500µm across, that are annealed and preferentially surround silicate grains.

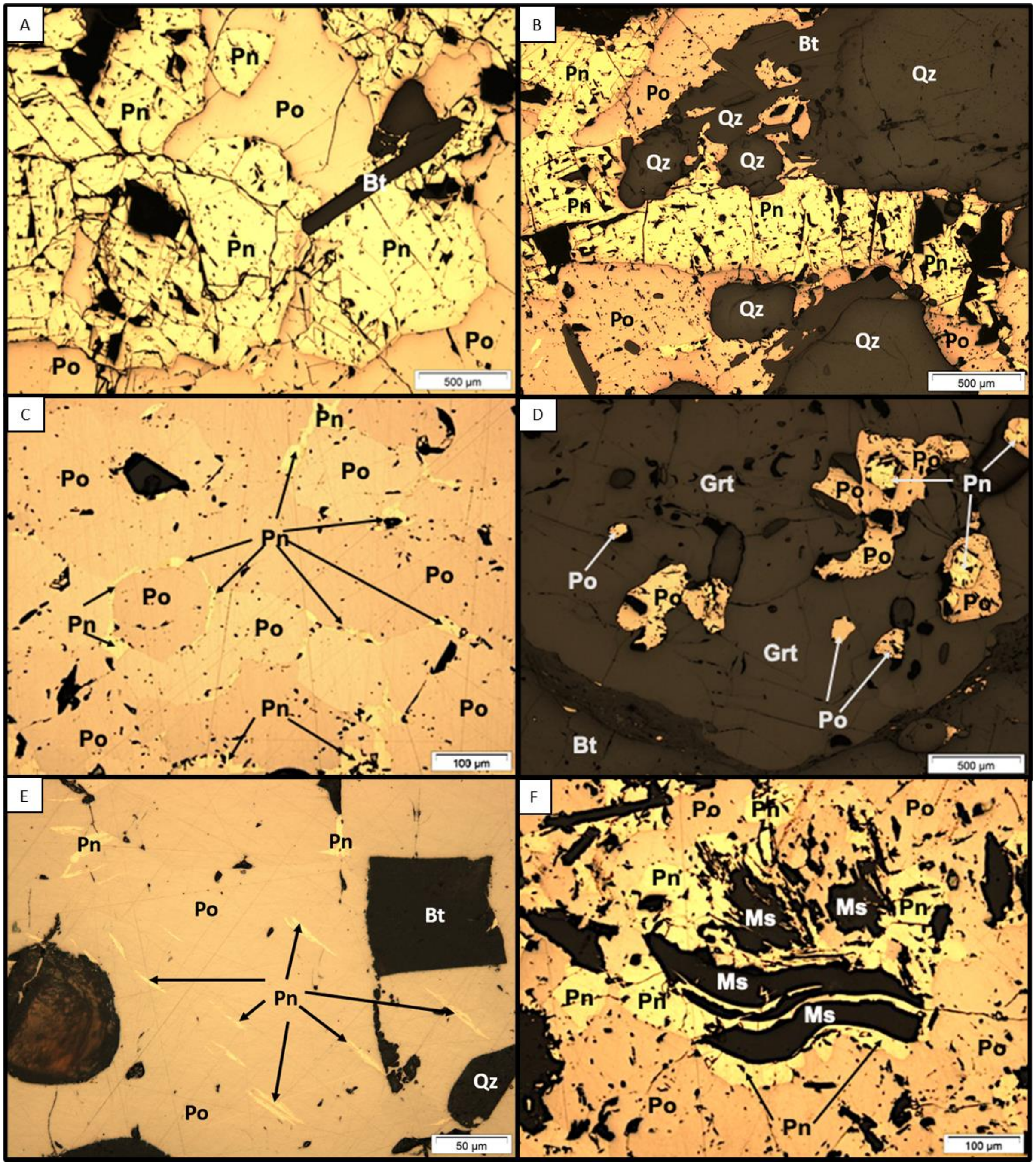

Figure 7-8: Reflected light photomicrographs in PPL of the six different pentlandite textures in the 1D orebody. Pentlandite grains are generally heavily pitted and fractured. (A) Granular pentlandite eyes (GPnE) from thin section 1045365. (B) Pentlandite trails (PnT) from thin section 1045356. (C) Grain boundary pentlandite (Gb-Pn) from thin section 1045353. (D) Subhedral inclusions within silicates (SI-X). In this case, the pentlandite inclusions are hosted within larger pyrrhotite inclusions within a garnet grain from thin section 1045363. (E) Pentlandite flames (FL) from thin section 1045346. Here, pentlandite flames occur in a planar orientation, exsolved from a pyrrhotite matrix. (F) Rims around silicates (RIMS-X) from thin section 1045347. In this case, pentlandite rims are surrounding muscovite laths. Abbreviations; Pn (pentlandite), Po (pyrrhotite), Py (pyrite), Ccp (chalcopyrite), Grt (garnet), Qz (quartz), Bt (biotite), Ms (muscovite).

7.2.2 Textural Variations

Figure 7-9 shows the relative abundance of pentlandite textural types in low, moderate, high and very high nickel tenor samples. The data is based on 80 thin sections from underground ore samples. If a pentlandite texture was present in a specific thin section, it was recorded in the pie charts **(Figures 7-10 and 7-11).** These pie charts do not necessarily reflect the dominant pentlandite textural type for a specific thin section, only whether a texture is present or absent and multiple textures are typically observed in each thin section. **Figure 7-9** shows that there is no apparent correlation between pentlandite textures and various nickel tenor groups. But in some instances, it does provide information on which textures are common, rare or absent from certain tenor groups. In addition, **Figure 7-10** shows that pentlandite textures do not change as a function of underground mineralization styles.

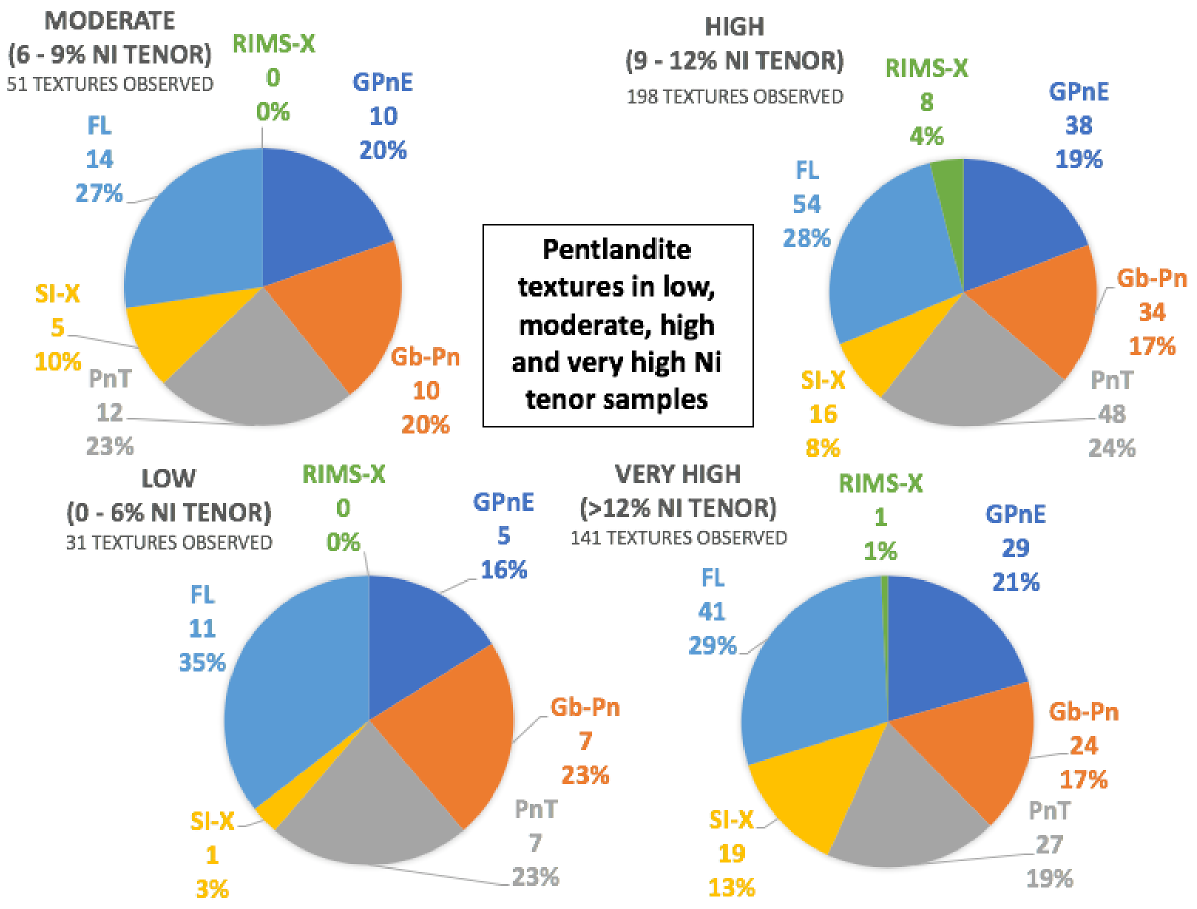

Figure 7-9: Pie charts showing the abundance of pentlandite textures in low, moderate, high and very-high Ni tenor groups. (SI-X) – subhedral inclusions, (FL) – flames, (RIMS-X) – rims around silicates, (GPnE) – granular pentlandite eyes, (Gb-Pn) – grain boundary pentlandite, (PnT) – pentlandite trails. All pentlandite textures that occur in a specific thin section were considered and recorded in the pie charts. Data is based on 80 thin sections from underground ore samples.

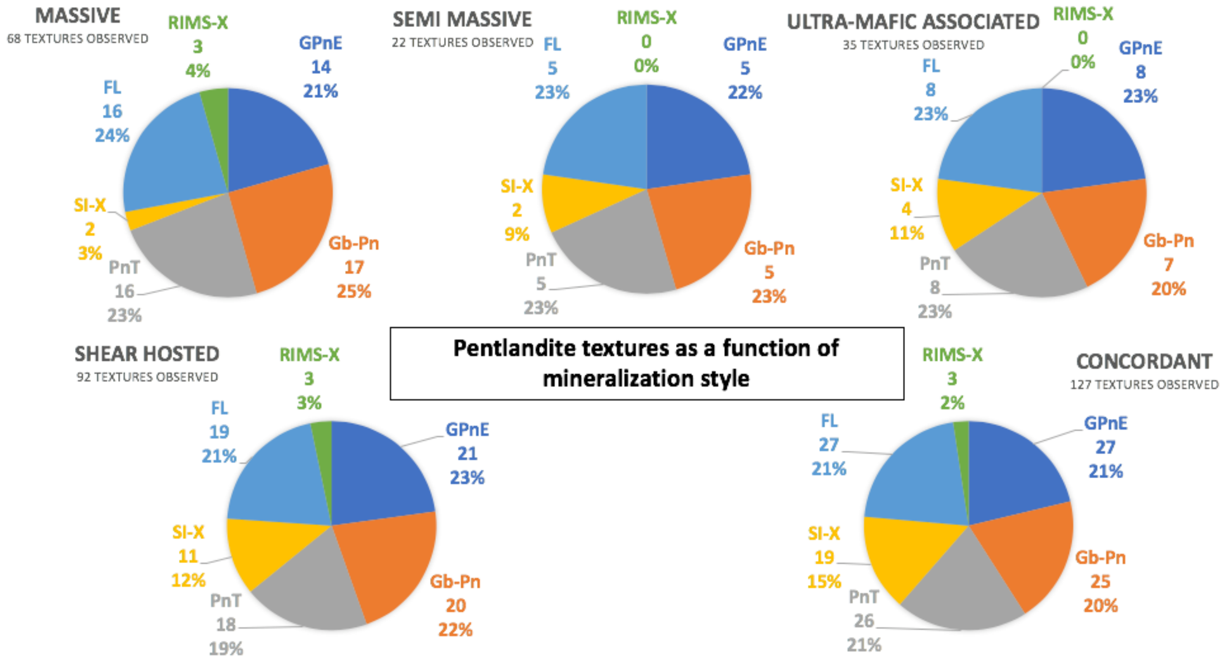

Figure 7-10: Pie charts show the abundance of pentlandite textures per underground mineralization styles. (SI-X) – subhedral inclusions, (FL) – flames, (RIMS-X) – rims around silicates, (GPnE) – granular pentlandite eyes, (Gb-Pn) – grain boundary pentlandite, (PnT) – pentlandite trails. All pentlandite textures that occur in a specific thin section were considered and recorded in the pie charts. Data is based on 78 thin sections from underground ore samples.

7.2.3 Mineral Chemistry

The iron, nickel, sulfur, and cobalt compositions in pentlandite were determined by electron microprobe analysis. A total of 88 spots from 46 pentlandite grains from 14 different thin sections were analyzed in order to determine whether different textural types of pentlandite are compositionally different. The stoichiometries for all 88 pentlandite spot analyses are presented in **Appendix 13**. Weight percent totals of >98.5% and <101.5% were acceptable. **Table 7-2** lists electron microprobe analysis weight percent and atomic unit data for the four of six representative pentlandite textural types. Subhedral inclusions within silicates and grain boundary pentlandite textures were omitted due to time constraints. Of the four mineralization styles; 44 spot analyses are from granular pentlandite, 13 spots from pentlandite trails, 6 spots from pentlandite rims around silicates, and 25 spots from pentlandite flames. Pentlandite stoichiometry was calculated by normalizing to an atomic S of 8.0. Arsenic, Silver, Palladium, Platinum and Bismuth were analyzed in the pentlandite grains using electron microprobe analysis. All probe data collected on these elements were below their detection limits of <200ppm, <100ppm, <100ppm, <250ppm, and <570ppm, respectively.

Table 7-2: Four representative analyses for pentlandite textural type; RIMS-X (rims around silicates), PnT (pentlandite trails), GPnE (granular pentlandite eyes), and FL (flames). Note, only four of six pentlandite textural types are displayed here; SI-X (subhedral inclusions within silicates) and Gb-Pn (grain boundary pentlandite) are omitted. Due to the relative similar mineral chemistry between pentlandite textural types, further data collection was deemed unnecessary. The following data is presented in EPMA weight % and atomic units normalized to 8.0 sulfur ($Fe_{4.5}$ $Ni_{4.5}$ S_8). The 'normalization value' along with the molecular weight for each element was used to calculate atomic units.

Sample	1045394	1045369	1045387	1045353
Analysis code	Pn1_1	Pn2_3	Pn2_1	fl2
Pentlandite type	RIMS-X	PnT	GPnE	FL
	EPMA data (wt%)			
Fe	30.2	31.6	31.1	31.1
Ni	36.5	35.1	35.3	35.6
S	33.0	33.1	32.9	33.0
Co	0.45	0.30	0.36	0.25
Total wt%	100.1	100.2	99.7	100.0
	Atomic Units			
Atomic S	8.00	8.00	8.00	8.00
Atomic Fe	4.20	4.38	4.35	4.32
Atomic Ni	4.82	4.63	4.69	4.71
Atomic Co	0.06	0.04	0.05	0.03

Figure 7-11 shows the nickel content of pentlandite as a function of whole rock nickel tenor. Pentlandite has an average of 35.0 wt% Ni in the low tenor group, through to an average of 35.5 wt% Ni in the moderate tenor group, with a probe error of 0.5% Ni reported in 1σ. The concentration of Ni in pentlandite is consistent across the four nickel

tenor groups. Outlier data have good analysis totals (near 100%), therefore cannot be excluded. It is important to note that, all outlier points **(Figure 7-11)** are pentlandite flame analyses. The flame outliers tend to have slightly elevated iron concentrations (33.0 - 35.5 wt% Fe) compared to an average value of 31.5 wt% Fe for all pentlandite textures.

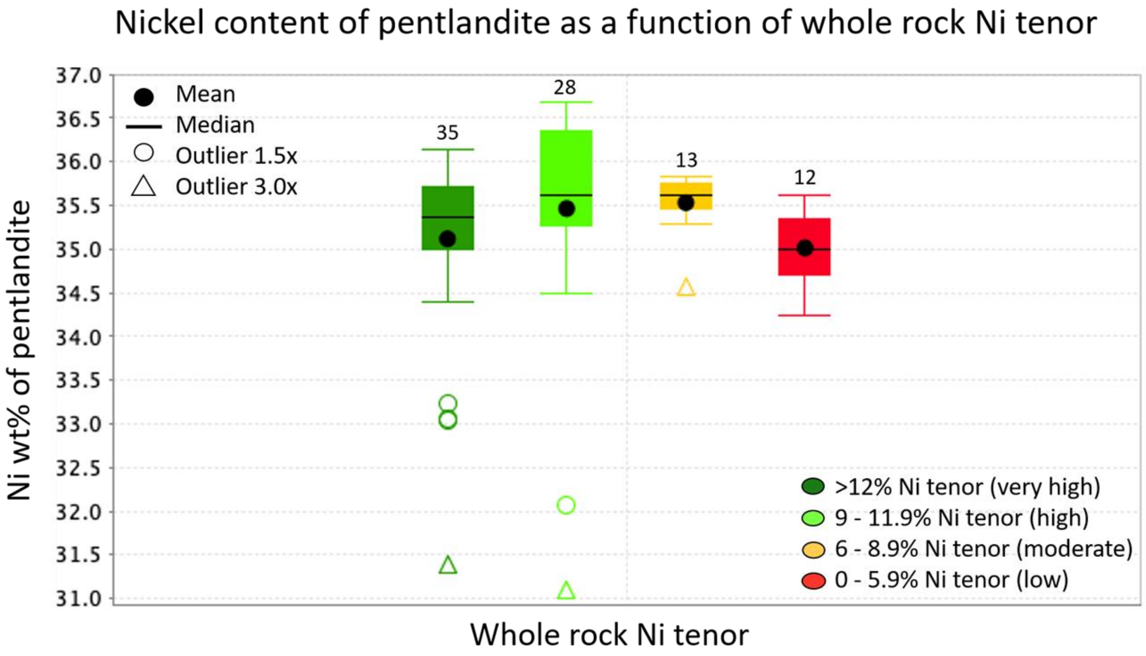

Figure 7-11: Nickel content in pentlandite versus different brackets of whole rock Ni tenor (very high, high, moderate, low). Nickel contents of the pentlandite do not seem to change with varying whole rock Ni tenor. The numbers above the box and whisker plots represent the total number of pentlandite point analyses. Data is based off 88-point analyses across 14 different thin sections. All outlier points (very high and high whole rock Ni) are pentlandite flame analyses. The outliers tend to have slightly elevated Fe values (33.0 - 35.5 wt% Fe) compared to average values of 31.50 wt% Fe.

Pentlandite has an average S content of 32.9 wt.% S with 1σ standard deviation of 0.22 wt%, independent of textural type **(Figure 7-12 D).** By contrast, Fe contents are variable and as the Fe content is progressively higher, the concentrations of Ni and Co are progressively lower.

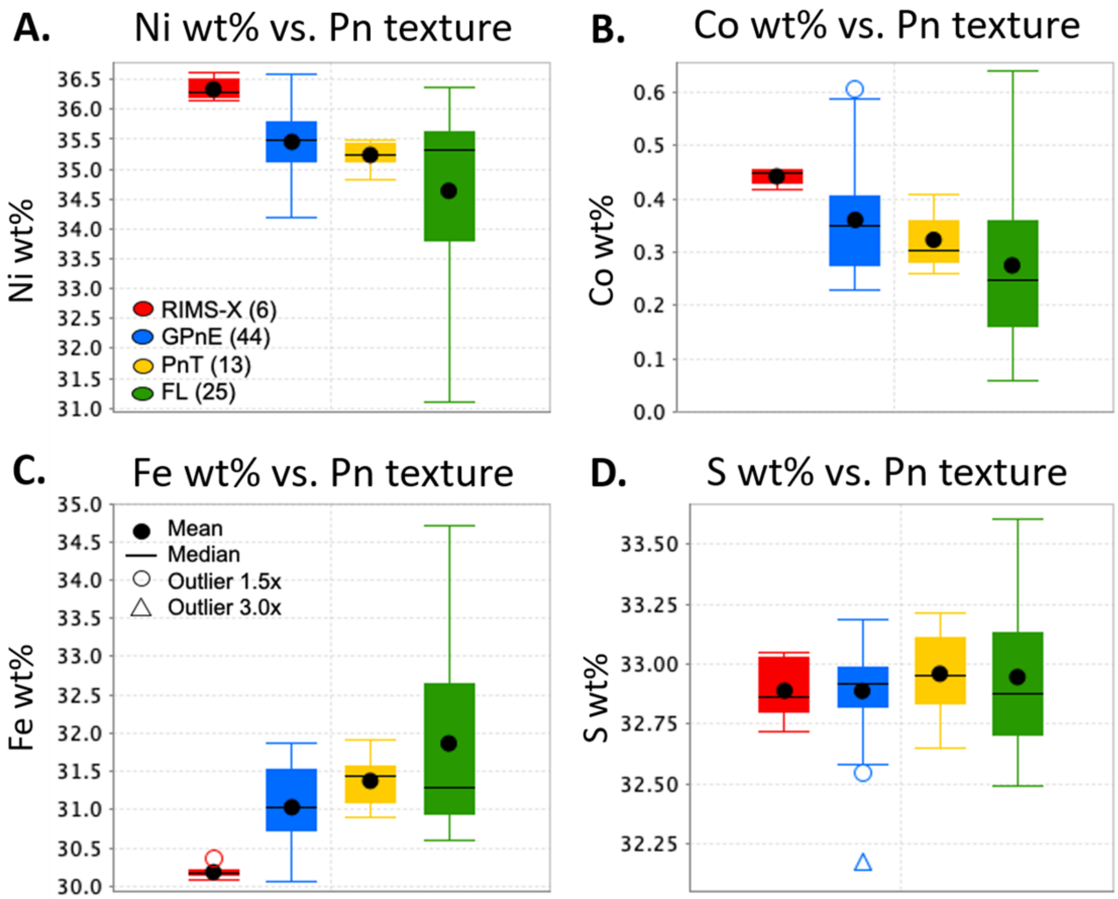

Figure 7-12: Box and whisker plots of the following; (A) Ni wt% vs. Pn texture, (B) Co wt% vs. Pn texture, (C) Fe wt% vs. Pn texture, (D) S wt% vs. Pn texture. Colours represent four of six pentlandite textural styles, numbers in brackets represent number of analyses per textural type taken, see legend in Figure (A). Data is based off a total of 88-point analyses from 14 different thin sections. Rims around silicates - (RIMS-X), granular pentlandite eyes (GPnE), pentlandite trails (PnT) and pentlandite flames (FL). In general; nickel, cobalt, iron and sulfur values don't seem to vary with different pentlandite textures. Weight % averages for Ni, Co and Fe for the various pentlandite textures are all within 2%. However, pentlandite flames (green), have the largest spread of data for all elements – Ni, Co, Fe, and S. No significant correlations can be made.

The negative correlation between Fe and Ni+Co (R^2 0.80) is evident in the plot of pentlandite stoichiometry in **Figure 7-13**. Pentlandite rims around silicates have the highest atomic Ni+Co concentrations, pentlandite flames the lowest, and granular pentlandite eyes and pentlandite trails have intermediate compositions.

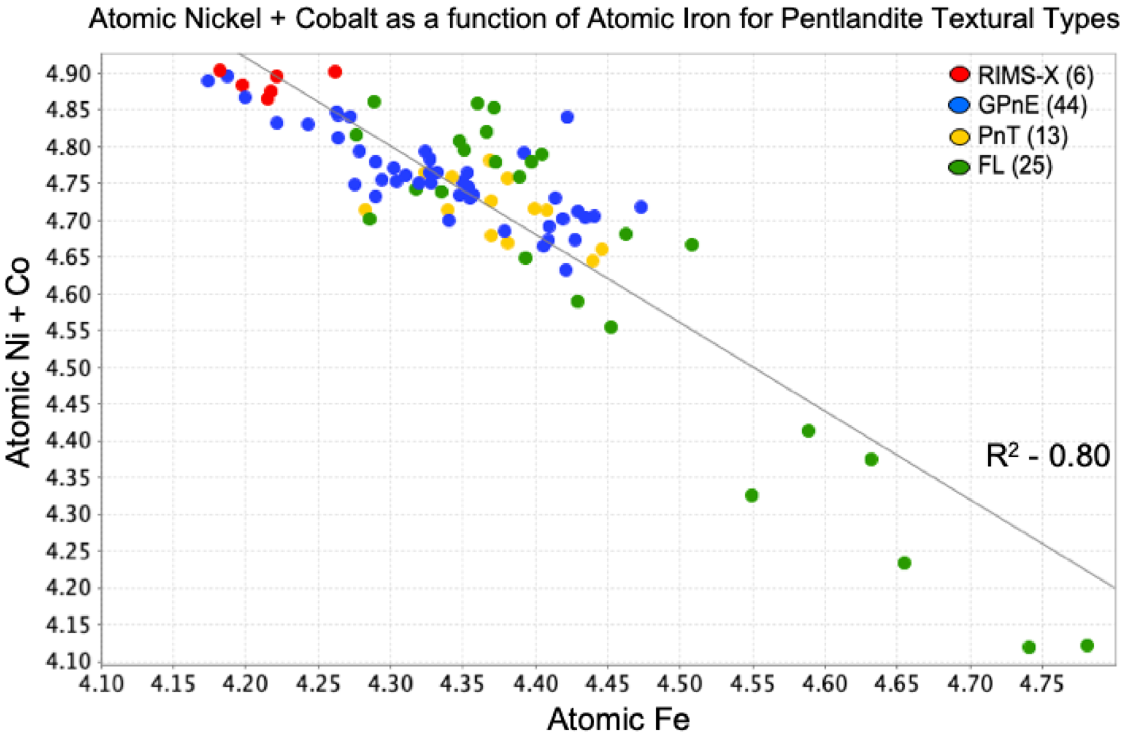

Figure 7-13: Atomic nickel + cobalt as a function of atomic iron was plotted for four pentlandite textural types. Colours represent the pentlandite textural types; RIMS-X (rims around silicates), GPnE (granular pentlandite eyes), PnT (pentlandite trails), FL (flames). Note, SI-X (subhedral inclusions within silicates) and Gb-Pn (grain boundary pentlandite) textures are not shown. The total number of pentlandite analyses per textural type are shown by the number in the brackets. Atomic Ni+Co versus Atomic Fe produces a negatively trending X-Y plot with an R^2 value of negative 0.80.

The cobalt contents of pentlandite are compared to whole rock nickel tenor values in **Figure 7-14.** The highest cobalt abundances occur in pentlandite grains from low tenor samples, with an average of 0.46 ± 0.10 wt.% Co reported to 1σ. Very high, high and moderate tenor groups have averages of; 0.29 ± 0.10, 0.37 ± 0.12 and 0.27 ± 0.05 wt.% Co reported to 1σ, respectively. Apart from a slight elevation in cobalt in pentlandite grains from low tenor samples, the cobalt contents of pentlandite do not seem to be related to whole rock nickel tenor.

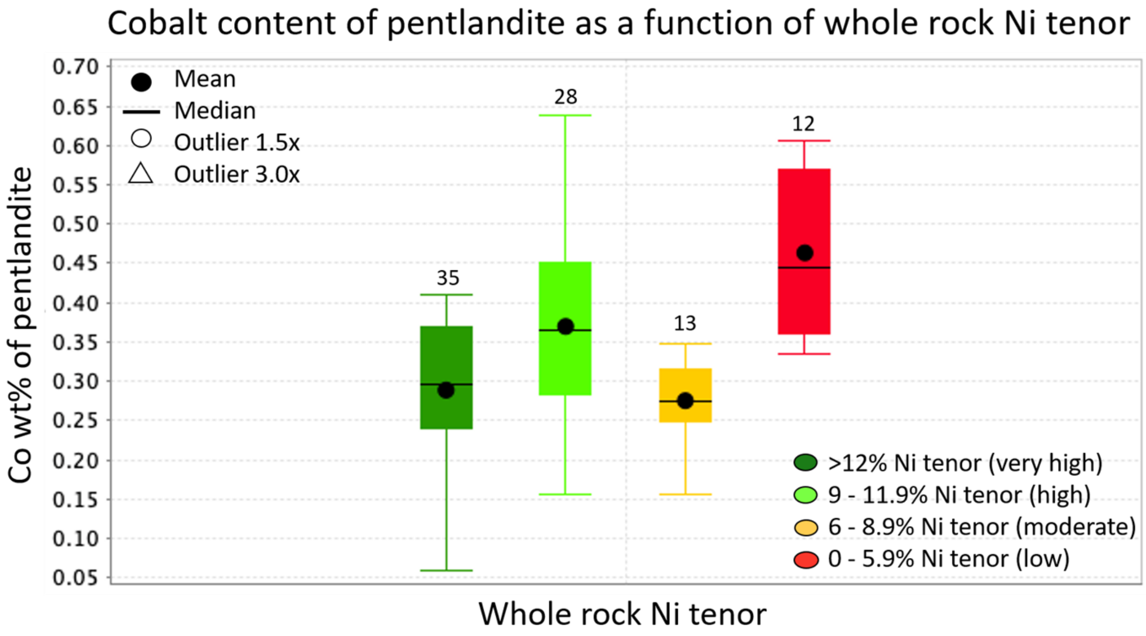

Figure 7-14: Cobalt content in pentlandite grains from different ranges of whole rock Ni tenor (very high, high, moderate, low). Pentlandite from low tenor samples have the largest Co averages (0.46 wt% Co) compared to very high (0.29 wt% Co), high (0.37 wt% Co) and moderate (0.27 wt% Co) tenors. Co contents of the pentlandite are independent of whole rock Ni tenor. The numbers above the box and whisker plots represent the total number of pentlandite point analyses. Data is based off 88-point analyses across 14 different thin sections.

The cobalt content (ppm) of pentlandite as a function of whole rock cobalt tenor is shown in **Figure 7-15** with cobalt tenor groups broken down into brackets of 500 ppm intervals. The highest mean cobalt values (~4700 ppm) occur in pentlandite grains belonging to the lowest whole rock cobalt tenor bracket (<500 ppm) **(Figure 7-15).** As shown in **Figure 7-14,** the highest mean cobalt values occur in pentlandite grains from the lowest whole rock nickel tenor bracket. This suggests that cobalt is controlled by a different sulfide phase, very likely pyrite, see below.

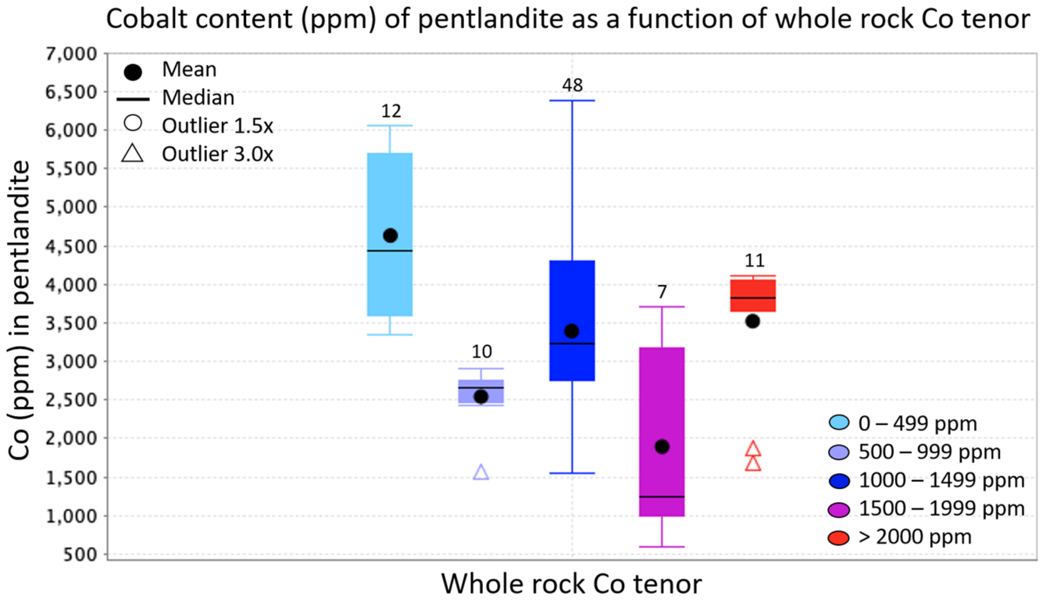

Figure 7-15: Cobalt content (ppm) of pentlandite grains as a function of whole rock Co tenor. Co tenor groups are broken down into brackets of 500 ppm intervals. The highest mean Co values (~4700 ppm) occur in pentlandite grains belonging to the lowest whole rock Co bracket (<500 ppm). The numbers above the box and whisker plots represent the total number of pentlandite point analyses. Data is based off 88-point analyses across 14 different thin sections.

7.2.4 EDS/WDS X-Ray Mapping

The EDS X-ray maps of Bi, Fe, S and WDS X-ray maps of Ni, Co, Pt, Pd, and As were acquired for various pentlandite textural types and all types are homogenous. **Figure 7-16** shows a reflected light photomicrograph in plane polarized light, a backscatter image and WDS-Ni and Co X-ray maps of a pentlandite trail texture. The EDS/WDS spectra of the pentlandite grain are homogenous. **Figure 7-16** also shows cobalt-rich pyrite on the margins of pentlandite grain. **Table 7-3** presents the electron microprobe analysis data corresponding to the spots on the pentlandite grain in **Figure 7-16** and indicate that the nickel and cobalt values are consistent.

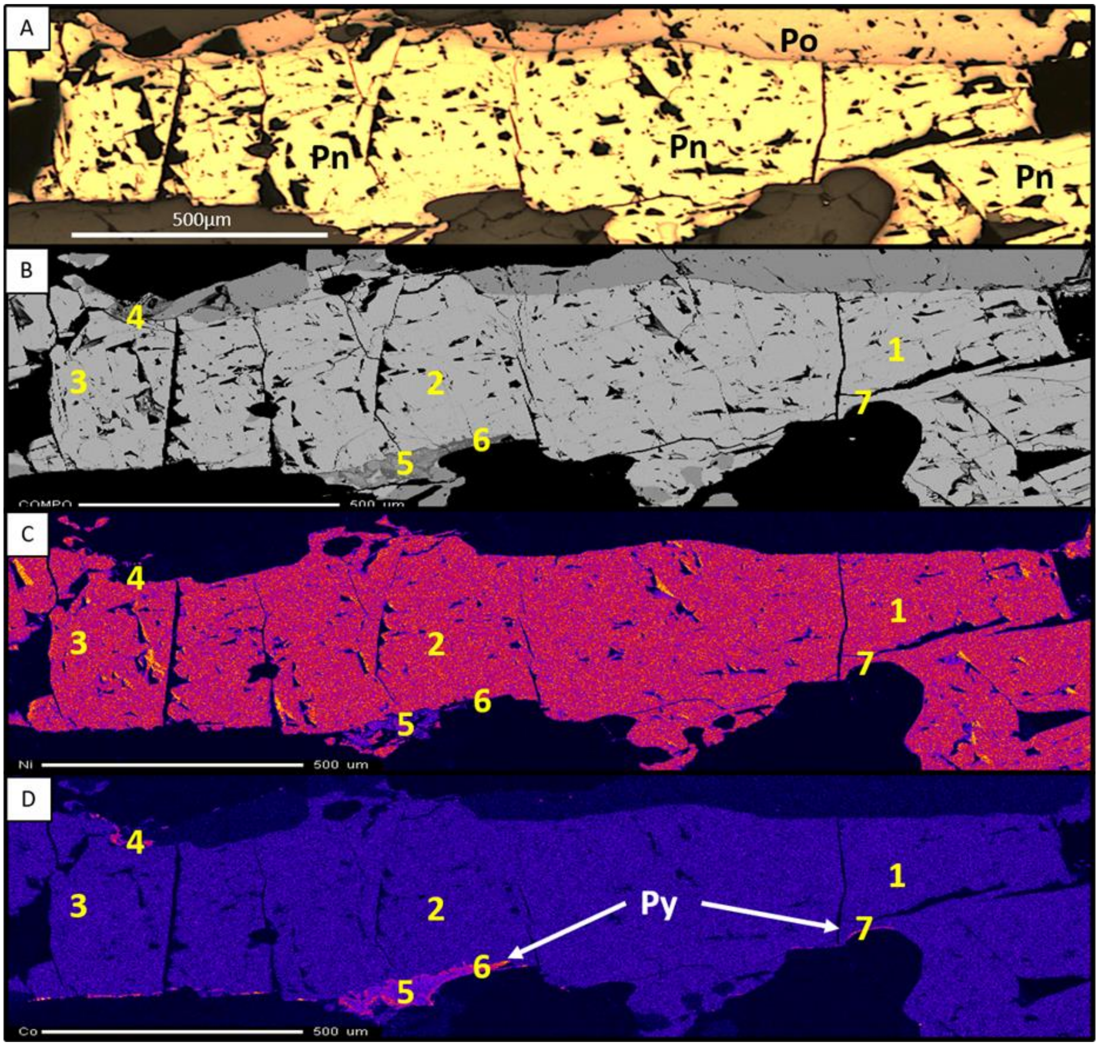

Figure 7-16: (A) Reflected light photomicrograph in PPL of a pentlandite trail (PnT) texture. (B) Backscatter image from EPMA analysis. (C) WDS-Ni X-ray map. (D) WDS-Co X-ray map. No zoning of nickel or cobalt evident in the pentlandite grain. Note, numbers 1 through 7 are individual EPMA spot analyses that correspond to Table 7-3. Points 1-3 are pentlandite, points 4-7 are pyrite. Abbreviations; Pn (pentlandite), Po (pyrrhotite), Py (pyrite).

Table 7-3: EPMA spot analysis data. Analysis ID numbers correlate to spots on the WDS Ni/Co maps in Figure 7-16. Pentlandite (1 to 3) and pyrite (4 to 7) data within normal elemental averages. Pyrite has elevated As, Co and Bi abundances. Detection limits in ppm; As (220), Ni (240), Fe (190), S (90), Co (110), Bi (570). Abbreviations; nd (not detected with the accuracy of the probe), As (arsenic), Ni (nickel), Fe (iron), S (sulfur), Co (cobalt), Bi (bismuth).

Analysis ID	As ppm	Ni wt%	Fe wt%	S wt%	Co wt%	Bi ppm	Total wt%
1045372_Pn3_1	nd	35.5	31.1	32.9	0.39	470	100.0
1045372_Pn3_2	nd	35.3	31.3	33.1	0.37	1020	100.1
1045372_Pn3_3	10	35.4	31.0	33.2	0.41	430	100.2
1045372_Py3_4	190	0.62	45.4	53.8	1.69	880	101.6
1045372_Py3_5	nd	20.8	37.6	41.1	0.57	1700	100.2
1045372_Py3_6	nd	0.42	45.5	53.7	1.56	650	101.2
1045372_Py3_7	100	0.69	45.6	53.9	1.23	580	101.4

7.3 Pyrite

Although pyrite (Py) is considered a gangue mineral at Thompson, it was examined in detail in this study, due to the intricate link between pyrite abundance and high tenors. Pyrite commonly occurs within granular pentlandite and annealed pyrrhotite grains. Detailed reflected light petrographic analysis has led to the identification of seven different textural types of pyrite: euhedral pyrite grains (EuG), subhedral inclusions (SI-X), exsolution textures (ET), pyrite-chalcopyrite intergrowth textures (Py-Ccp-INT), pyrite trails (PyT), grain-boundary texture (Gb-Py), rims around silicates (RIMS-X).

7.3.1 Mineralogy

Euhedral pyrite grains (EuG)

Euhedral grains are the most common pyrite textural type in the Thompson 1D ores. They are absent from low tenor samples, but are common in moderate, high, and very high nickel tenor samples **(Figure 7-19).** Euhedral pyrite grains occur as overgrowths on granular pentlandite grains, pentlandite trails, polygonal grain boundary and homogenous pyrrhotite textures. Single euhedral grains of pyrite are up to 500µm across and are commonly surrounded by or have chalcopyrite and/or pentlandite inclusions within their cores (**Figure 7-17 A; Figure 7-25 A**). Polycrystalline masses of euhedral pyrite (>500µm) are dominantly made up of smaller euhedral pyrite grains

(<250μm) that show annealed grain boundaries with triple joint junctions between 110° to 130°, like those described by Lawrence (1972). Chalcopyrite and/or pentlandite is locally present in these triple junctions. Euhedral pyrite rarely occurs in silicate grains but is locally present in quartz, and commonly contains anhedral chalcopyrite inclusions. Pyrite grains either have a clean polish or are pitted and have corroded grain boundaries. The corroded pyrite grains are porous and are cut by microfractures that are filled with chalcopyrite.

Subhedral inclusions within silicates (SI-X)

This is a rare pyrite texture, as most subhedral inclusions within silicates are dominantly Po>Pn>Ccp. It was not observed in low and moderate tenor but subhedral inclusions of pyrite were observed in high and very high nickel tenor samples **(Figure 7-19).** Subhedral inclusions (up to 800μm across) are present within larger, anhedral pyrrhotite blebs that are hosted dominantly within garnet cores **(Figure 7-17 B)** and less-commonly within quartz grains that have experienced subgrain development. Subhedral inclusions have not been observed to occur in garnet rims. Pyrite inclusions are commonly pitted and fractured, with chalcopyrite infilling microfractures and surrounding grains. Very rarely, subhedral inclusions of pyrite occur in plagioclase and K-feldspar grains.

Exsolution textures (ET)

Exsolution textures are common to all tenor groups **(Figure 7-19).** There are two-types of exsolution textures, flames and lamellae.

Flames

Pyrite flames are typically elliptical and <30µm, but locally up to 50µm long. Flames dominantly occur in a pyrrhotite homogenous matrix, as well as where pyrrhotite shows polygonal grain boundary texture (**Figure 7-17 C**)**.** Flames are commonly near larger pyrite grains, but locally are distal from pyrite. Several flames generally occur in the same area, and isolated pyrite flames are rare. Pyrite flames tend to be randomly distributed across the pyrrhotite matrix with no distinct orientation.

Lamellae

Exsolution lamellae dominantly occur in a homogenous pyrrhotite matrix, as well as when pyrrhotite shows an elongated pyrrhotite texture. Lamellae have disk shapes, are much larger than pyrite flames and range from 100µm to upwards of 1000µm in length, and up to 30µm wide. It is common that the lamellae are aligned into a preferred orientation. Exsolution lamellae are more abundant in high and very-high nickel tenor samples, as opposed to flames which are abundant throughout all groups. Therefore, exsolution is more coarse-grained at higher tenor.

Pyrite trails (PyT)

This is a less-common texture. Pyrite trails are absent from low and moderate tenors and have only been observed in high and very high nickel tenor samples **(Figure 7-19).** There are two types of pyrite trails; 1. coarse-grained in size, annealed euhedral pyrite that form a distinct pyrite trail **(Figure 7-17 D).** Here grain boundaries between pyrite grains are distinguishable. 2. coarse-grained pyrite, as thick as 500μm and as long as 3500μm, that occur in lenses, have a preferred orientation, are tapered at the margins and are commonly fractured. Grain boundaries are indistinguishable, and it appears that the lenses are made up of a single crystal. Pyrite trails dominantly occur in granular pentlandite grains, pentlandite trails, but also occur in a homogenous pyrrhotite matrix and when pyrrhotite shows an elongated pyrrhotite texture. There is a transition between coarser-grained pyrite trails and finer-grained pyrite exsolution lamellae.

Grain boundary texture (Gb-Py)

Grain boundary pyrite is a common texture that is observed in all nickel tenor groups **(Figure 7-19).** It consists of fine-grained pyrite along pyrrhotite grain boundaries and at triple junctions **(Figure 7-17 E).** Pyrite is up to 50μm wide and 400μm long. Grain boundary pyrite occurs where pyrrhotite grains exhibit a polygonal grain boundary texture and rarely within fractures in a homogenous pyrrhotite matrix. Grain boundary pyrite is commonly intergrown with grain boundary pentlandite.

Rims around silicates (RIMS-X)

This pyrite rim texture is absent from low tenor samples and dominantly occurs in high and very high nickel tenor samples **(Figure 7-19).** Fine or coarse-grained rims of pyrite dominantly surround quartz grains that have developed subgrain boundaries, and rarely around plagioclase grains. Rims are dominantly coarse-grained but occur as two distinct types. They are either annealed, euhedral pyrite grains that have a clean polish and surround a silicate grain. Or resemble a corroded homogenous mass where pyrite grains are pitted, and grain boundaries are non-distinguishable but are surrounding a silicate grain **(Figure 7-17 F).** Rims are up to 800μm thick and locally encapsulate the whole silicate grain.

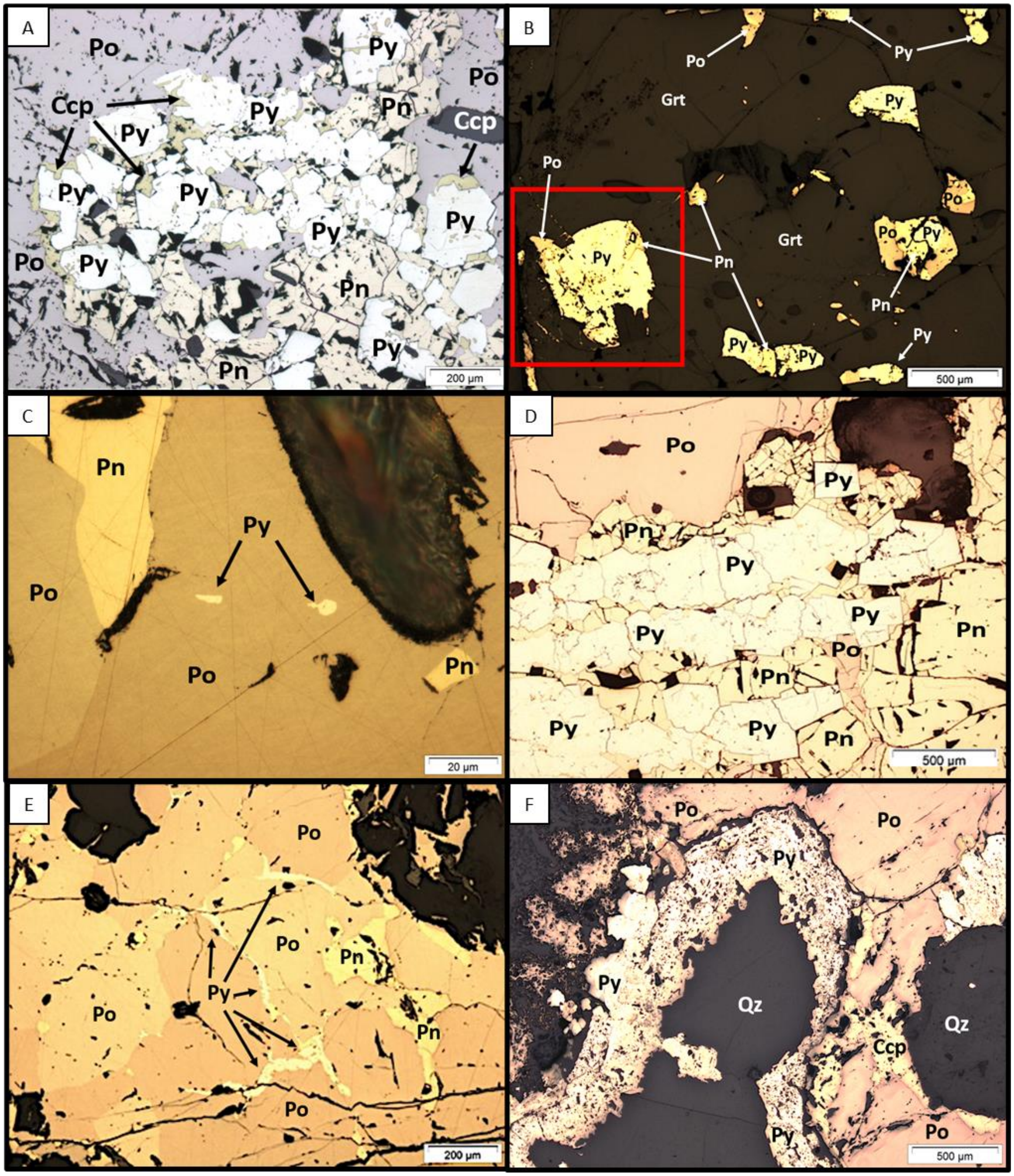

Figure 7-17: Reflected light photomicrographs in PPL of different pyrite textures in the 1D orebody. (A) Euhedral pyrite grains (EuG) hosted within granular pentlandite (GPnE) amongst a homogenous pyrrhotite matrix (homPo, from thin section 1045377. Chalcopyrite commonly surrounds or occurs as inclusions within euhedral pyrite grains. (B) Subhedral inclusions (SI-X) of dominantly pyrite, chalcopyrite and pyrrhotite within a garnet grain, from thin section 1045351. The grain with the 'red box' surrounding it is the same grain from Figure 7-25 B but oriented 90˚ counter-clockwise, where a WDS-Ni map is shown. (C) Pyrite flames (exsolution texture) within a pyrrhotite matrix exhibiting a polygonal grain boundary texture (PGBT), from thin section 1045406. (D) Euhedral pyrite grains annealing with one another into a pyrite trail texture (PyT) hosted within granular pentlandite (GPnE), from thin section 1045365. (E) Fine-grained pyrite exhibiting a grain boundary texture (Gb-Py) around grains of pyrrhotite showing a polygonal grain boundary texture (PGBT), from thin 1045386. (F) A corroded, homogenous mass of pyrite exemplifying a rim texture around a quartz grain (RIMS-X). Pyrite grain boundaries are not distinguishable, and pyrite is corroded and pitted. Abbreviations; Pn (pentlandite), Po (pyrrhotite), Py (pyrite), Ccp (chalcopyrite), Grt (garnet), Qz (quartz).

Pyrite-chalcopyrite intergrowth textures (Py-Ccp-INT)

Pyrite-chalcopyrite intergrowth textures are observed in all nickel tenor groups (**Figure 7-19**) and consist of four-types of textures: symplectic intergrowth textures (SIT), anhedral blebs of pyrite (Ab-Py), corroded pyrite enveloped by chalcopyrite (CP-envCcp) and massive pyrite (MASV-Py).

Symplectic intergrowth texture (SIT)

The texture consists of wormy pyrite intergrown with either chalcopyrite (**Figure 7-18 A**), or less commonly pentlandite. The symplectic masses also show evidence of pre-existing, annealed, euhedral pyrite grains that were overgrown by wormy, symplectic intergrowths at the margins or within granular pentlandite grains. Remnant pentlandite commonly occurs within the cores of several symplectic intergrowth masses.

Anhedral blebs (Ab-Py)

Pyrite and chalcopyrite are intergrown in anhedral blebs (up to 1500μm across) that commonly have cores with remnant pentlandite. These pyrite-chalcopyrite anhedral blebs form augen-shaped grains, that are dominantly hosted in a homogenous pyrrhotite matrix (**Figure 7-18 B**) or a pyrrhotite polygonal grain boundary texture. Anhedral blebs differ from symplectic intergrowth textures because pyrite-chalcopyrite do not occur as wormy intergrowths. Anhedral blebs have a pyrite-chalcopyrite assemblage in the core and are pyrite-rich towards the grain margins. They resemble ‘augen-like’ grains, where the pyrite-rich margins thin outwards. Remnant pentlandite is commonly seen in cores of anhedral blebs.

Corroded pyrite enveloped by chalcopyrite (CP-envCcp)

Coarse-grained, corroded subhedral grains of pyrite (up to 1000µm across) are enveloped by chalcopyrite. Pyrite grains are pitted, anhedral grains with deteriorated grain margins that have been replaced by chalcopyrite (**Figure 7-18 C**) or rarely, are euhedral**.** These corroded pyrite grains are enveloped by chalcopyrite and occur in a homogenous pyrrhotite matrix and a pyrrhotite polygonal grain boundary texture, but are not associated with pentlandite.

Massive pyrite (MASV-Py)

Massive pyrite is defined as a homogenous mass of pyrite that is composed of smaller euhedral pyrite grains that show annealing characteristics (**Figure 7-18 D**). Abundant chalcopyrite inclusions fill the triple junctions between annealed pyrite grains. Microfractures are also filled with chalcopyrite. However, chalcopyrite is also locally present as overgrowths on the homogenous pyrite mass. Massive pyrite is commonly pitted and fractured. Massive pyrite also occurs within/around silicate grains as an anhedral mass.

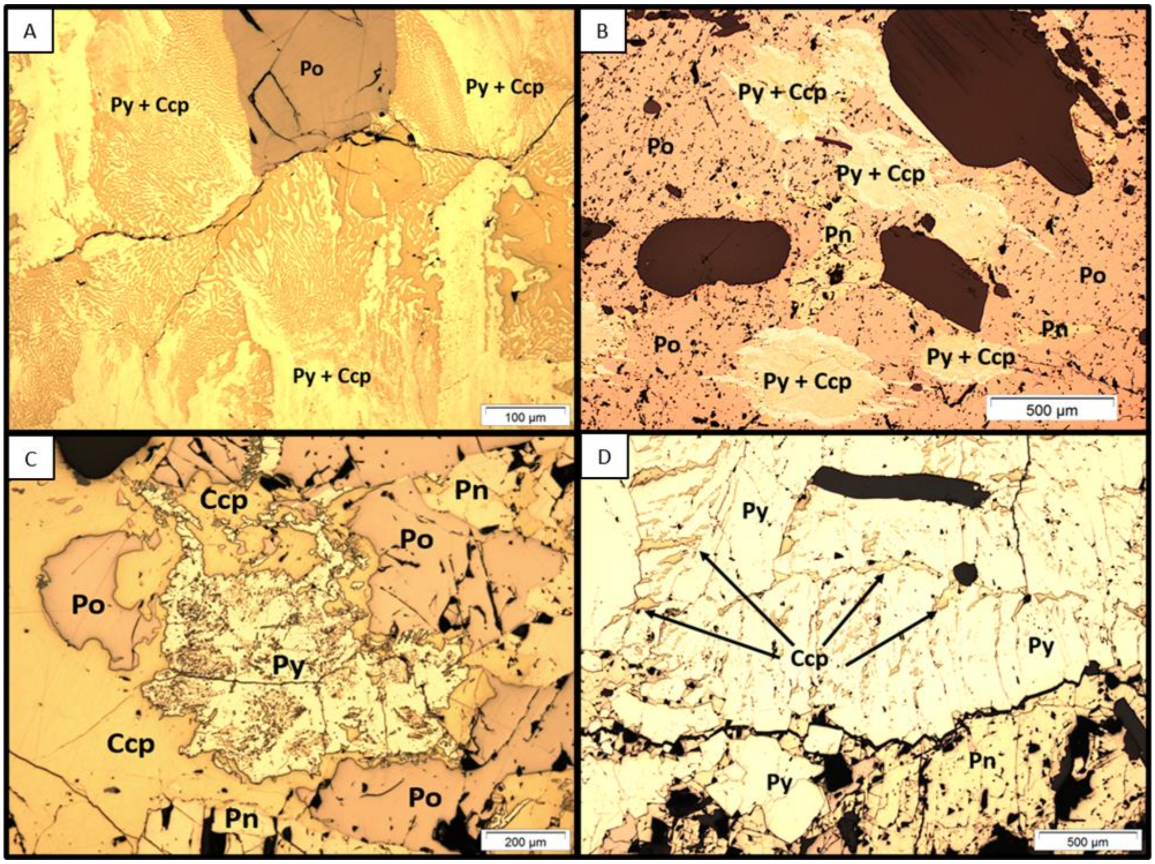

Figure 7-18: Reflected light photomicrographs in PPL of pyrite-chalcopyrite intergrowth textures (Py-Ccp-INT) in the 1D orebody. (A) A symplectic intergrowth texture (SIT) between pyrite-chalcopyrite, from thin section 1045357. (B) Pyrite-chalcopyrite anhedral blebs (AB-Py) hosted within a homogenous pyrrhotite matrix (homPo), from thin section 1045372. AB-Py grains commonly exhibit remnant pentlandite at cores. (C) A corroded, subhedral grain of pyrite enveloped and being replaced by chalcopyrite (CP-envCcp), from thin section 1045364. (D) Massive pyrite texture (MASV-Py) with abundant chalcopyrite inclusions. Annealed, euhedral pyrite grains occur on the contact between massive pyrite and granular pentlandite. The massive pyrite is pitted and fractured, from thin section 1045348. Abbreviations; Pn (pentlandite), Po (pyrrhotite), Py (pyrite), Ccp (chalcopyrite).

7.3.2 Textural Variations

Figure 7-19 shows the relative abundance of pyrite textures observed in low, moderate, high and very high nickel tenor samples. Pyrite textures in **Figure 7-19** do not necessarily represent the dominant-type per thin section. Instead, all pyrite textures that occurred in a specific thin section were considered in the pie charts, i.e., multiple textures per thin section were recorded. The data is based on 78 thin sections from underground ore samples. **Figure 7-19** shows that there is some correlation between pyrite textures and various nickel tenor groups (as discussed above in mineralogy). It is important to note that pyrite contents in the low nickel tenor samples are very low. Consequently, this provides a small sample group that constitutes for <2% of samples. Therefore, caution must be taken when comparing between low, moderate, high and very-high nickel tenor groups in the pie charts below.

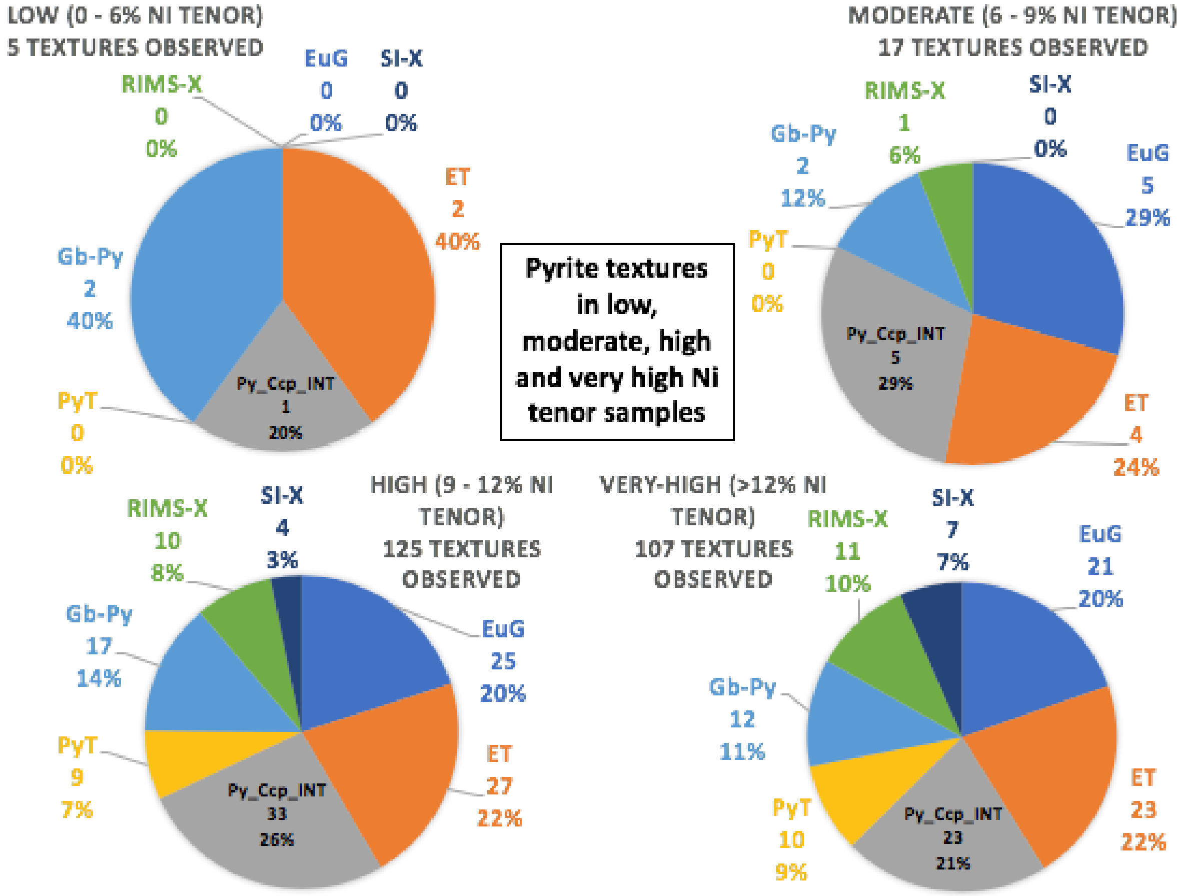

Figure 7-19: Pie charts showing the relative abundance of pyrite textures in low, moderate, high and very high Ni tenor groups. All pyrite textures that occur in a specific thin section were considered and recorded in the pie charts: (SI-X) – subhedral inclusions, (EuG) – euhedral grains, (EL) exsolution textures, (Py-Ccp-INT) pyrite-chalcopyrite intergrowth textures, (PyT) pyrite trails, (Gb-Py) grain boundary pyrite, (RIMS-X) – rims around silicates. Data is based on 78 thin sections from underground ore samples.

7.3.3 Mineral Chemistry

A total of 63 spot analyses on 13 different pyrite grains over 6 thin sections were analyzed for Fe, S, Ni, Co and As by electron microprobe analysis with detection limits of 230, 110, 90, 90 and 170 ppm, respectively. Over 100 pyrite spot analyses were initially collected from various pyrite textures, however due to low probe totals (<98.5%) a great majority of them were omitted from data representation. Therefore only 63 pyrite spot analyses were collected and ~60% of these analyses were of euhedral pyrite grains. Due to a small dataset of pyrite analyses, we were not able to compare elemental compositions across the various pyrite textures. The electron microprobe analysis weight percent and atomic unit data in **Table 7-4,** show representative stoichiometric values for two groups; euhedral pyrite grains and all other pyrite textures. Euhedral pyrite grains are the most common pyrite texture in the Thompson 1D orebody. Pyrite stoichiometry was calculated by normalizing to an atomic sulfur of 2.0 and the stoichiometries for all 63 pyrite spot analyses are presented in **Appendix 13.**

Table 7-4: Representative analyses for euhedral pyrite grains (EuG) and all other pyrite textures combined. Due to a small dataset of pyrite analyses, all textural analyses apart from EuG were combined into one group. The following data is presented in EPMA weight % and atomic units normalized to 2.0 sulfur (FeS_2). The 'normalization value' along with the molecular weight for each element was used to calculate atomic units. Arsenic values were not detected (n.d.) and are therefore below the accuracy of the electron microprobe (<170ppm As).

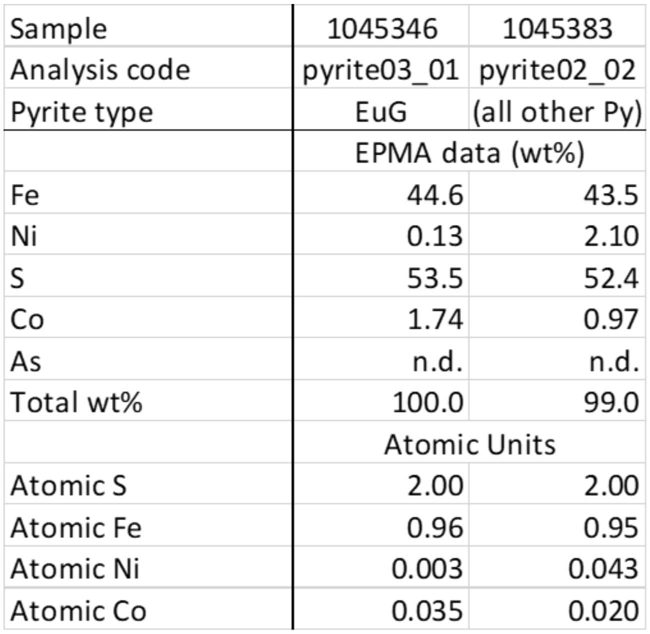

Sample	1045346	1045383
Analysis code	pyrite03_01	pyrite02_02
Pyrite type	EuG	(all other Py)
	EPMA data (wt%)	
Fe	44.6	43.5
Ni	0.13	2.10
S	53.5	52.4
Co	1.74	0.97
As	n.d.	n.d.
Total wt%	100.0	99.0
	Atomic Units	
Atomic S	2.00	2.00
Atomic Fe	0.96	0.95
Atomic Ni	0.003	0.043
Atomic Co	0.035	0.020

Pyrite has an average sulfur composition of 53.4 ± 0.6 wt.% S and iron composition of 44.1 ± 1.5 wt.% Fe, both reported to 1σ. Nickel concentrations are highly variable, pyrite has an average nickel composition of 1.10 ± 3.8 wt.% Ni reported to 2σ. **Figure 7-20** shows the nickel content of pyrite as a function of whole rock nickel tenor. Pyrite from very high nickel tenor samples (>12% Ni) have a mean of 1.24 ± 4.17 wt.% Ni reported to 2σ. Pyrite in high nickel tenor samples (9-12% Ni) has a mean concentration of 0.33 ± 0.71 wt.% Ni reported to 2σ. Pyrite in moderate nickel tenor samples (6-9% Ni) have the largest spread of data, with a mean of 1.36 ± 3.29 wt.% Ni reported to 2σ. Very little probe data was collected on pyrite from low tenor groups because pyrite does not commonly occur in low nickel tenor samples. However, of those analyzed, pyrite in low nickel tenor samples have a mean of 0.14 ± 0.11 wt.% Ni reported to 2σ.

Pyrite mean Ni wt.% values across various tenor groups overlap within 2σ, therefore no significant statistical differences occur.

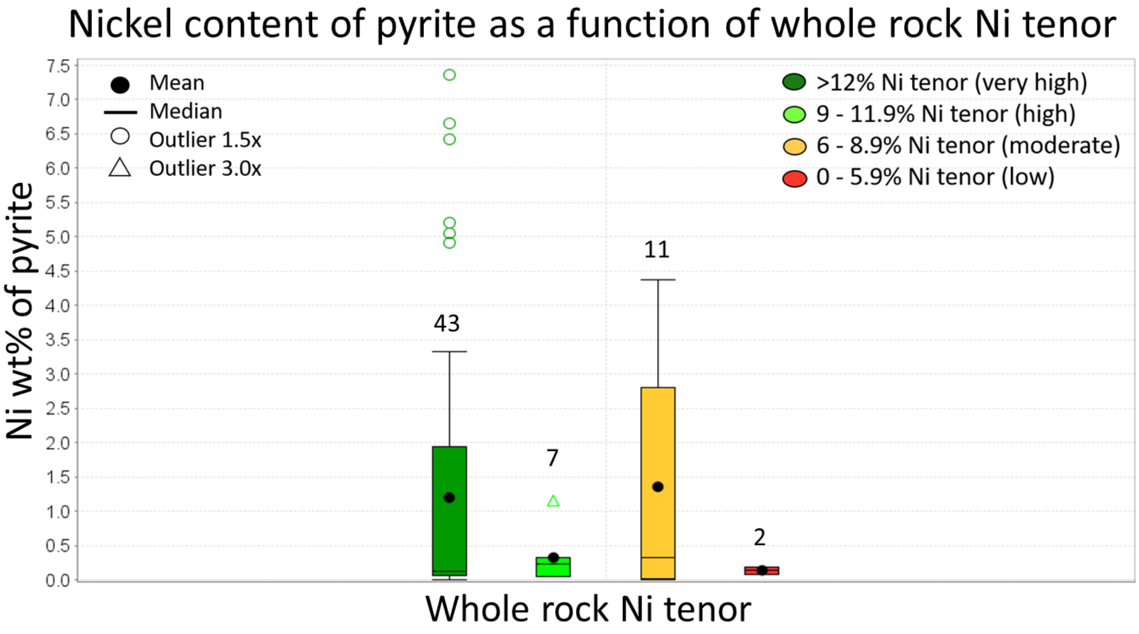

Figure 7-20: Box & whisker plots showing nickel content of pyrite as a function of whole rock nickel tenor (very high, high, moderate, low). The numbers above the box and whisker plots represent the total number of pyrite point analyses. Data is based on 63 probe points taken on 13 pyrite grains from 6 different thin sections.

Pyrite has an average cobalt composition of 1.30 ± 1.93 wt.% Co reported to 2σ. The atomic concentration of Co was compared to atomic Co/Ni values, but there is a lack of correlation between these parameters, consequently the graph is omitted here. However, the mean atomic Co/Ni value is 40 with a 2σ standard deviation of 296 (outliers included), and 17 with a 2σ standard deviation of 50 (outliers excluded). The atomic Co/Ni ratio for pyrite has no apparent relationship to tenor, but these data, including atomic Co/Ni ratios are presented in **Appendix 13.**

Modal abundance

The analysis of pyrite modal abundances in **Table 4-1**. indicate that the visual estimates provide an overestimate of pyrite percentage. However, it was also shown that the relative abundance of pyrite was accurately determined by visual estimates and therefore can be used to compare with other variables such as tenor and mineral composition.

Pyrite modal abundance was plotted as a function of whole rock nickel and cobalt tenor in **Figure 7-21** and **Figure 7-22**, respectively. The highest nickel and cobalt tenor samples have the highest pyrite modal abundances, >10%.

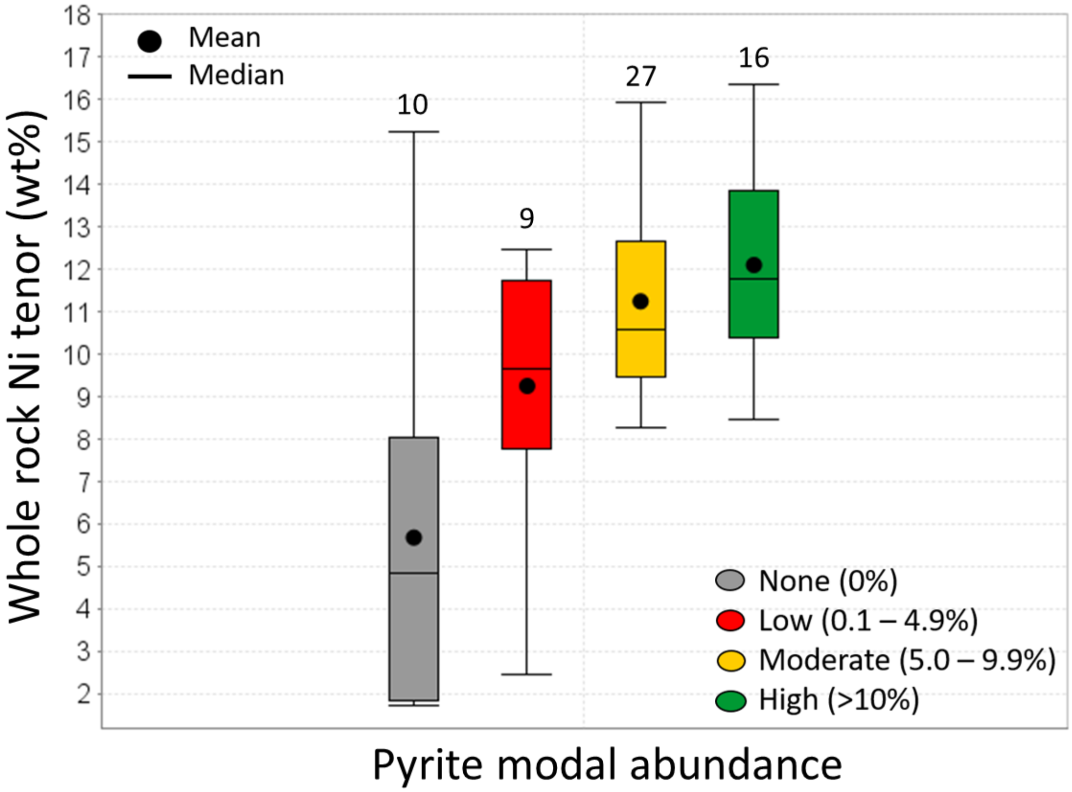

Figure 7-21: Box and whisker plots showing whole rock nickel tenor as a function of pyrite modal abundance. Pyrite modal abundances were estimated visually. Data is based on 62 representative underground samples and their corresponding thin sections. If no pyrite was recorded in the thin section (0%), a value of 0.5% modal was assigned in order to construct the box & whisker plot.

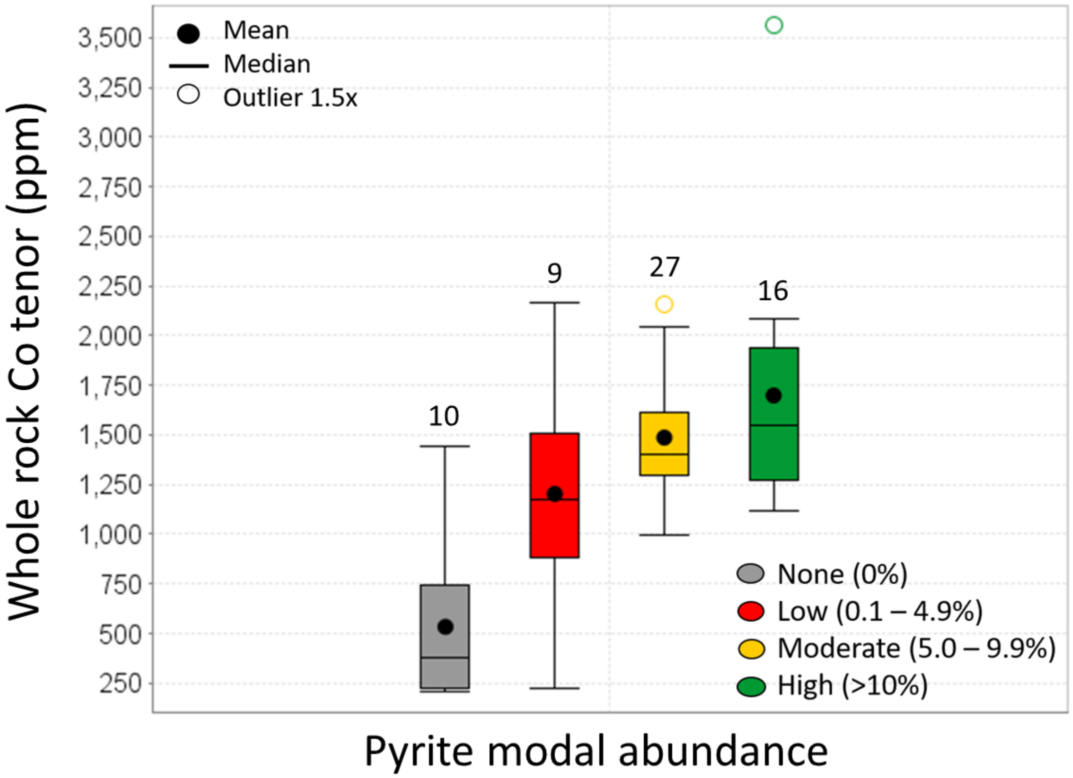

Figure 7-22: Box and whisker plots showing a positive trend between whole rock cobalt tenor (ppm) as a function of pyrite modal abundance. Pyrite modal abundances were estimated visually. Data is based on 62 representative underground samples and their corresponding thin sections. If no pyrite was recorded in the thin section (0%), a value of 0.5% modal was assigned in order to construct the box & whisker plot.

The correlation between pyrite modal abundance and nickel and cobalt tenor can be further investigated by examining the relationship of pyrite modal abundance with sulfide mineralization styles. **Figure 7-23** shows that shear-hosted mineralization styles have the highest pyrite modal abundances of 8.5%. Ultramafic associated samples have the second highest pyrite modal abundances of 8.0% and samples from concordant styles of mineralization show the third largest pyrite modal abundances of 6.4%. Concordant styles also show the largest spread of data. Semi-massive styles have the smallest spread of data, with pyrite modal abundances of 6.0%. Massive styles of mineralization have lower pyrite modal abundances of 3.2%. Thus, the pyrite modal abundance between the five main styles of underground mineralization is variable.

Plots of pyrite modal abundance versus the nickel tenor of individual samples were plotted for each of the different styles of mineralization and an R^2 value of 0.65 was generated for all samples. This data is omitted because not enough data was available to evaluate whether pyrite modal abundances changed with style of mineralization. Although, ultramafic associated sulfides did show a negative correlation, with the lowest pyrite abundances having some of the highest nickel tenors. The rest of the mineralization styles showed a positive correlation, albeit the R^2 values were poor.

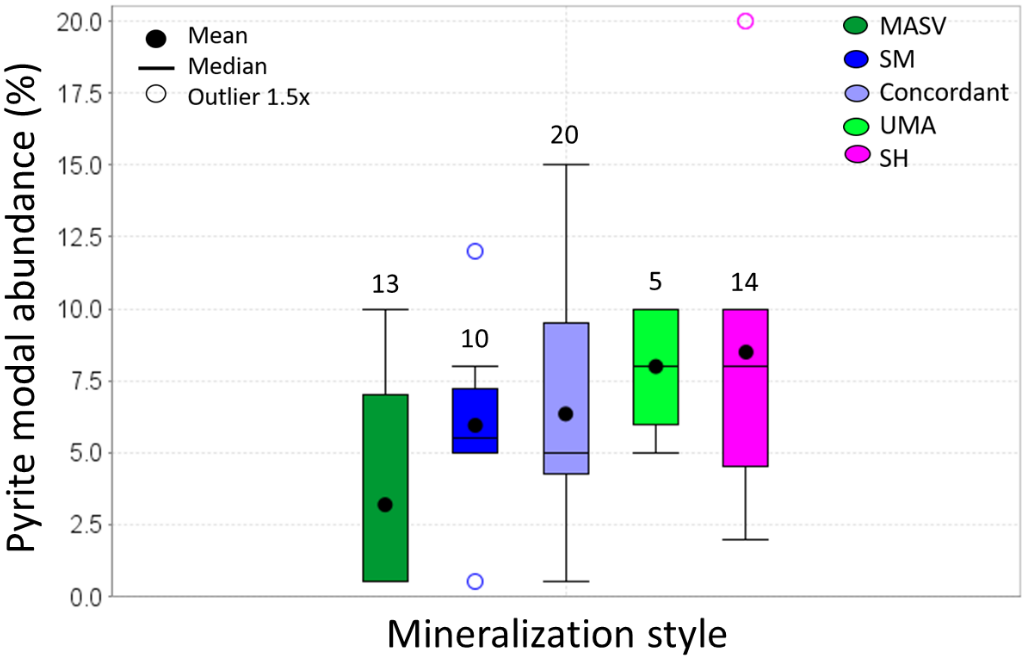

Figure 7-23: Shows mineralization style as a function of pyrite modal abundance between the five underground mineralization styles. Data is based on 62 representative underground samples and their corresponding thin sections. The numbers on the box and whisker charts display the number of underground samples for that specific mineralization style. If no pyrite was recorded in the thin section (0%), a value of 0.5% modal was assigned in order to construct the box & whisker plot.

Whole rock nickel tenor as a function of mineralization style showed that shear-hosted sulfides had the highest whole rock nickel tenors (12.8% Ni), and massive sulfides had the lowest and most variable nickel tenors (6.7% Ni) (**Figure 5-5, Ch.5**)**.** It is clear from **Figure 7-23** that shear-hosted ores also have the highest average pyrite modal abundances (8.5% pyrite), and massive ores had the lowest average pyrite modal abundances (3.2% pyrite).

Figure 7-24 summarizes the findings in **Figure 5-5** and **Figures 7-22 to 7-24,** and shows that there is a positive correlation between whole rock nickel and cobalt tenor, and that samples with the highest pyrite modal abundances (large circles) have the highest nickel and cobalt tenors. It is also evident from **Figure 7-24** that the shear-hosted mineralization style (pink) generally has the highest nickel and cobalt tenors, and samples from the massive mineralization style (forest green) have some of the lowest and most variable nickel and cobalt tenors. The mean Ni/Co ratio of all sulfide ore samples in **Figure 7-24** is 79.

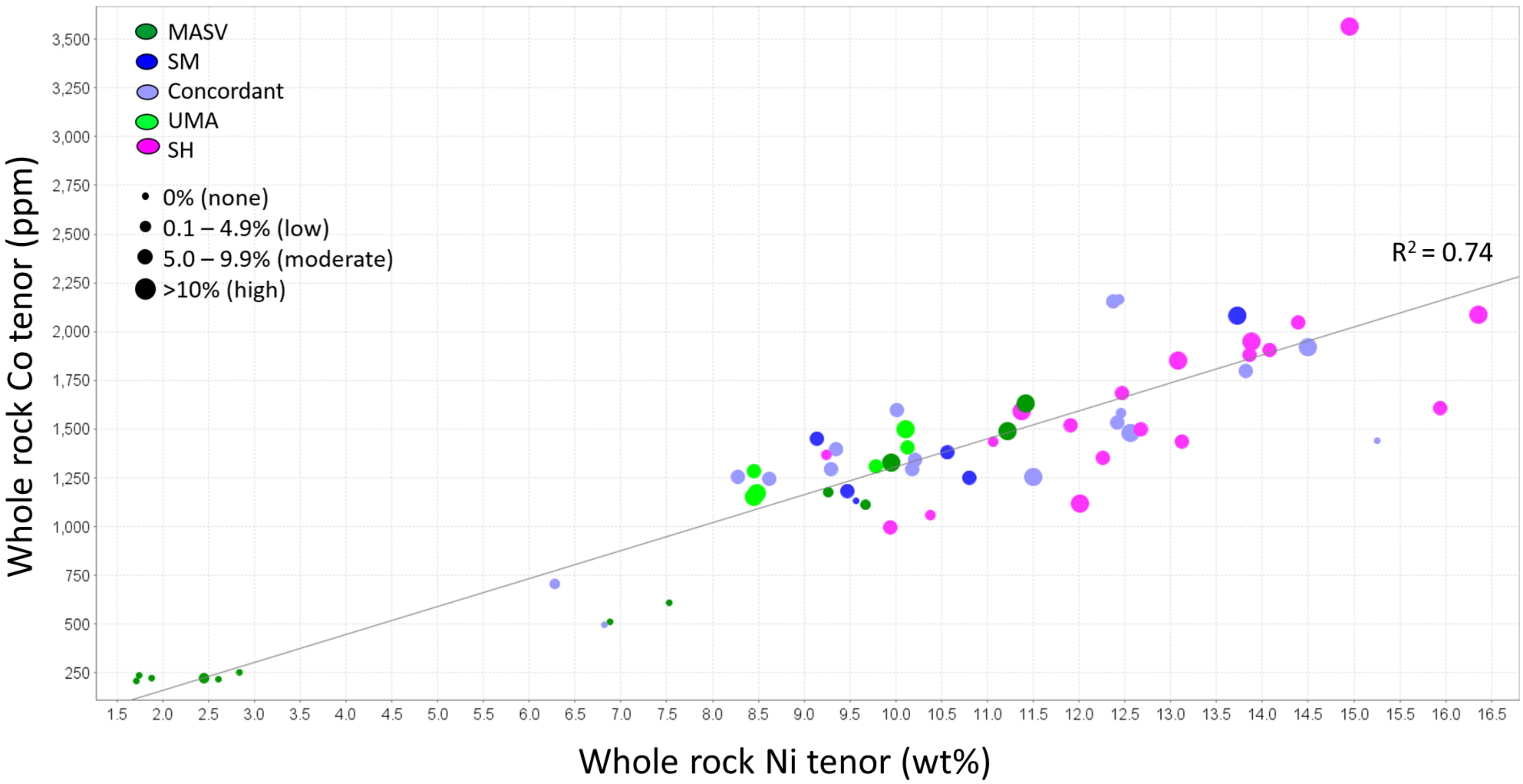

Figure 7-24: Whole rock Ni/Co tenor as a function of mineralization style (colour) and pyrite modal abundance (size). Linear correlation between whole rock nickel and cobalt (R^2 = 0.74). Modal abundances were recorded by visual interpretation of thin sections via petrographic analysis. Non-representative thin-section samples were discarded from dataset to avoid a sampling bias. The mean Ni/Co ratio of all sulfide ore samples in Figure 7-24 is 79. MASV (massive), SM (semi-massive), Concordant (Concordant), UMA (ultramafic associated), SH (shear-hosted). Data is based on 62 representative thin sections from underground ore samples.

7.3.4 EDS/WDS X-Ray Mapping

The EDS X ray maps of Al, Bi, Ca, Cu, Fe, Na, Pb, Si and WDS X ray maps of elements As, Co, Mg, Ni, S were examined for 13 different pyrite grains and show that pyrite are homogenous for all elements except for nickel and cobalt. Strong cobalt zoning **(Figure 7-25 A)** and to a lesser extent nickel, was evident in several euhedral pyrite grains. There is evidence for nickel zoning in some corroded pyrite grains but is variable from grain to grain. Where it does occur, nickel zoning is patchy and irregular (**Figure 7-25 B**).

The cores of euhedral pyrite grains generally lack cobalt zoning, but cobalt-rich rims are typically present **(Figure 7-25 C)**. The same euhedral pyrite grain is pictured in **Figure 7-25 D**, where the WDS-Ni maps shows a primary core enriched in nickel and depleted in cobalt. Nickel-rich cores occur in some pyrite grains and are absent in others, however anhedral pyrite grains consistently have nickel-poor cores, surrounded by an enriched nickel outer core **(Figure 7-25 E)** and cobalt-rich rims.

A corroded, subhedral grains of pyrite enveloped by chalcopyrite texture, shows that cobalt has been mobilized along fractures and grain boundaries in the pyrite **(Figure 7-25 F).** Nickel-rich pyrite is also present along fractures, but to a lesser extent than cobalt-rich pyrite. The cobalt distribution in this figure also outlines the subgrain boundaries of the annealed, polycrystalline mass of euhedral pyrite. **Figure 7-25 G** shows another corroded pyrite grain enveloped by chalcopyrite texture. This is different from **Figures 7-26 C** and **D**, as the inner core has low concentrations of nickel and cobalt, surrounded by an outer core that is more nickel-rich, and encompassed by cobalt-rich outer margins of the grain (cobalt-map not pictured). Remnant pentlandite at the core of symplectic pyrite-chalcopyrite grains and anhedral pyrite blebs is a common occurrence. White blotches on the WDS-Ni map show corroded pentlandite surrounded by pyrite **(Figure 7-25 H)**. The textural nickel and cobalt concentration may vary across pyrite textures, however consistent across all WDS-Co maps is a cobalt-rich outer grain margin.

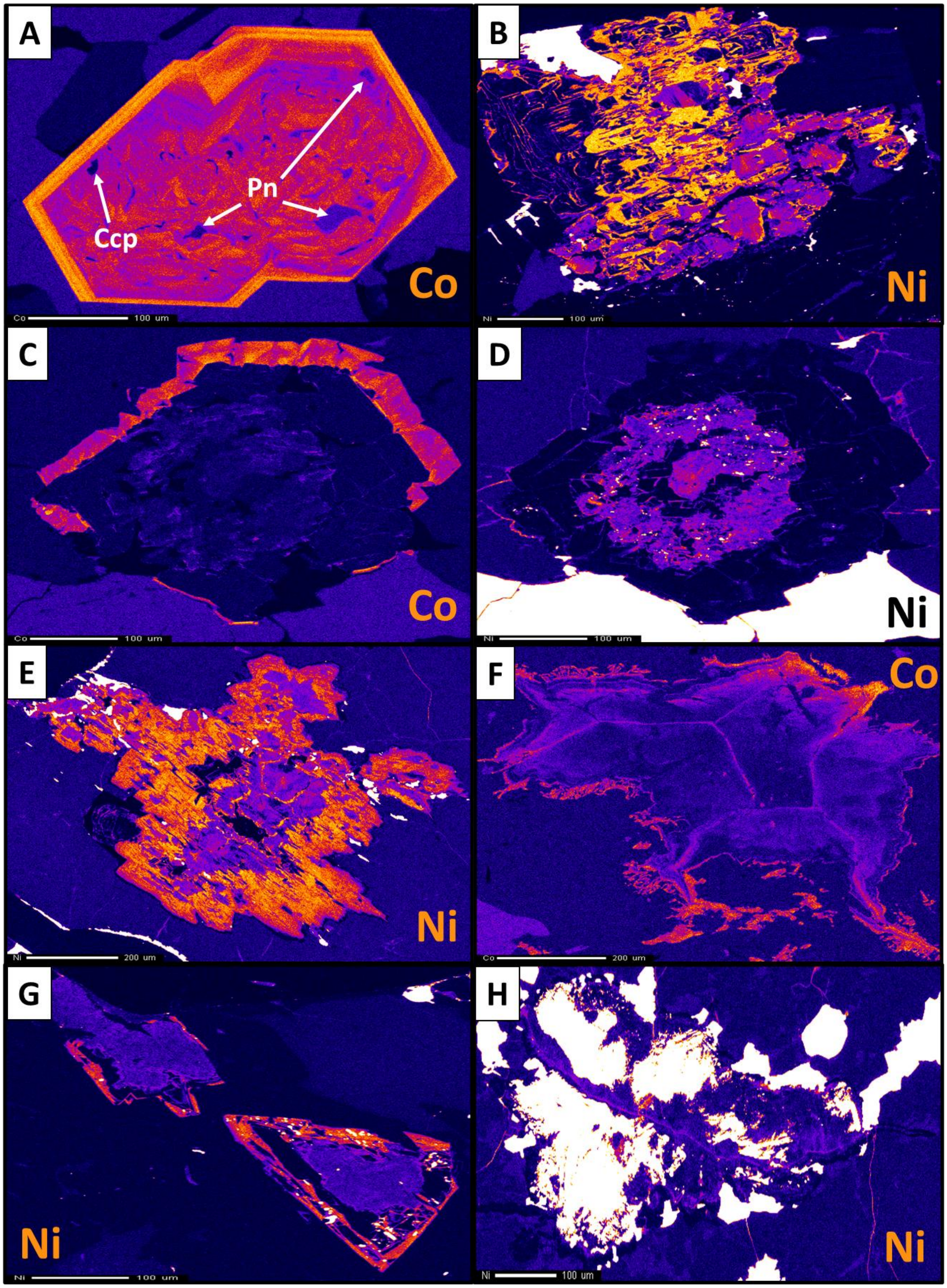

Figure 7-25 A: A WDS-Co map of a euhedral pyrite grain (EuG) showing strong cobalt zoning, from thin section 1045365. Notice the pentlandite and chalcopyrite inclusions within the pyrite grain. B: A WDS-Ni map showing patchy and irregular nickel zoning of a subhedral inclusion of pyrite (SI-X) in garnet, the white areas are pentlandite. From thin section 1045351, see Figure 7-17 B

for the reflected light photomicrograph (PPL) of this grain (oriented 90˚ clockwise). C: A WDS-Co map of a euhedral pyrite grain (EuG) showing a cobalt-rich outer rim, from thin section 1045383. Cobalt-rich outer grain margins are common across all pyrite grains. D: A WDS-Ni map of the same grain in C, showing a primary core enriched in nickel and depleted in cobalt (not seen). White areas and specks in the core of the grain are pentlandite. E: A WDS-Ni map of an anhedral bleb of pyrite (AB-Py) showing a nickel-poor core surrounded by an enriched nickel outer core, from thin section 1045383. Note, white specks are pentlandite. F: A WDS-Co map of a corroded, subhedral grain of pyrite enveloped by chalcopyrite (CP-envCcp) showing mobilization of cobalt along fractures and grain boundaries in pyrite. Notice the annealed, euhedral pyrite subgrains in the background forming the polycrystalline mass of pyrite. From thin section 1045364. G: A corroded, pyrite grain enveloped by chalcopyrite (CP-envCcp) showing a nickel-poor core, and nickel-rich outer core. The grain also has a cobalt-rich outer margin (not seen). The white specks are remnant pentlandite. From thin section 1045264. H: A WDS-Ni map of an anhedral bleb of pyrite (AB-Py) with remnant pentlandite (white blotches) at the core of the grain, from thin section 1045365. The grain also has a cobalt-rich outer margin (not shown).

Pyrite flames are an unusual texture. Consequently, spot analyses were taken and analyzed by electron microprobe analysis. After confirmation that the flames are pyrite, EDS-WDS elemental maps of the pyrite flames were acquired in order to determine if they are compositionally similar or different to other pyrite grain textures. The EDS X-ray maps of Cu, Fe, S, and WDS X ray maps of As, Co, Mn, Ni were examined for 14 different pyrite flames from 5 different thin section samples.

The EDS/WDS elemental maps of flame pyrite were homogenous for all elements except for cobalt and to a lesser extent, nickel. Reflected light photomicrographs along with accompanying WDS cobalt maps of several pyrite flames (<25μm) are shown in **Figure 7-26 A** and **B**. Pyrite flames all have a strong cobalt signature. **Figure 7-26 C** shows a reflected light photomicrograph (plane polarized light) of a 30μm pyrite flame hosted within an elongated pyrrhotite texture along with the WDS-Ni and Co maps (**Figure 7-26 D** and **E**). Note the nickel-rich sliver along the fracture in the pyrite flame. The flame is made up of a cobalt-rich composition, similar to **A** and **B**.

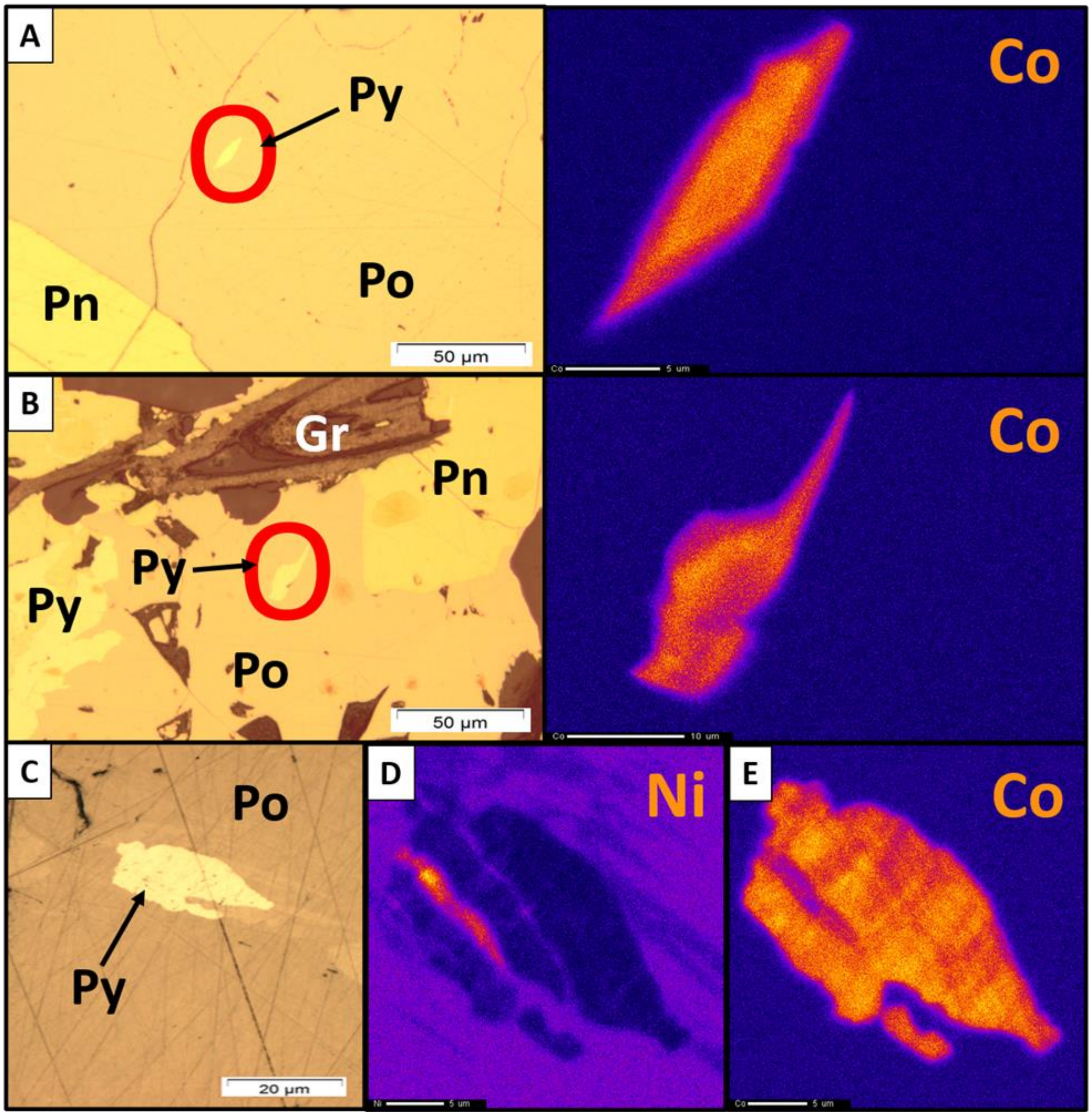

Figure 7-26 A: Reflected light photomicrograph in PPL and accompanying WDS-Co map for a single 20µm pyrite flame (FL) within a pyrrhotite matrix, distal from any other pyrite occurrences. Taken from thin section 1045386. B: Reflected light photomicrograph in PPL and accompanying WDS-Co map for a 25µm pyrite flame (FL) within a pyrrhotite matrix near a pyrite grain. Taken from thin section 1045386. C: Reflected light photomicrograph in PPL of a 30µm pyrite flame (FL) within an elongated pyrrhotite matrix (EPT), from thin section 1045399. D: WDS-Ni map of the same grain in C. Nickel-rich sliver within a cobalt-rich pyrite grain. E: WDS-Co map of the same grain in C and D showing a strong cobalt composition for the pyrite flame.

A reflected light photomicrograph along with the EDS/WDS maps of a symplectic intergrowth texture between pyrite-chalcopyrite are shown in **Figure 7-27**. In **A**, the reflected light photomicrograph shows the symplectic intergrowth grain overgrowing on the margins of a granular pentlandite grain. The WDS-Co map in **B** shows that the pyrite is concentrated in cobalt. More massive pyrite (higher cobalt concentrations) near the bottom of the grain, and intergrown with chalcopyrite near the top of the grain. The EDS-Cu map in **C** shows that chalcopyrite makes up the wormy intergrowth texture with pyrite near the top of the grain. The WDS-Ni map in **D** shows minimal nickel concentrations in the symplectic intergrowth grain. However, remnant pentlandite (white blotches) occur within the symplectic pyrite-chalcopyrite grain. Also, in **D** there are faintly visible subgrain boundaries in the background of the symplectic mass of pyrite-chalcopyrite. These are pyrite grains that have annealed to form a polycrystalline mass of pyrite on the margins of preexisting pentlandite grains, with the former having been replaced by wormy, symplectic intergrowths of pyrite-chalcopyrite.

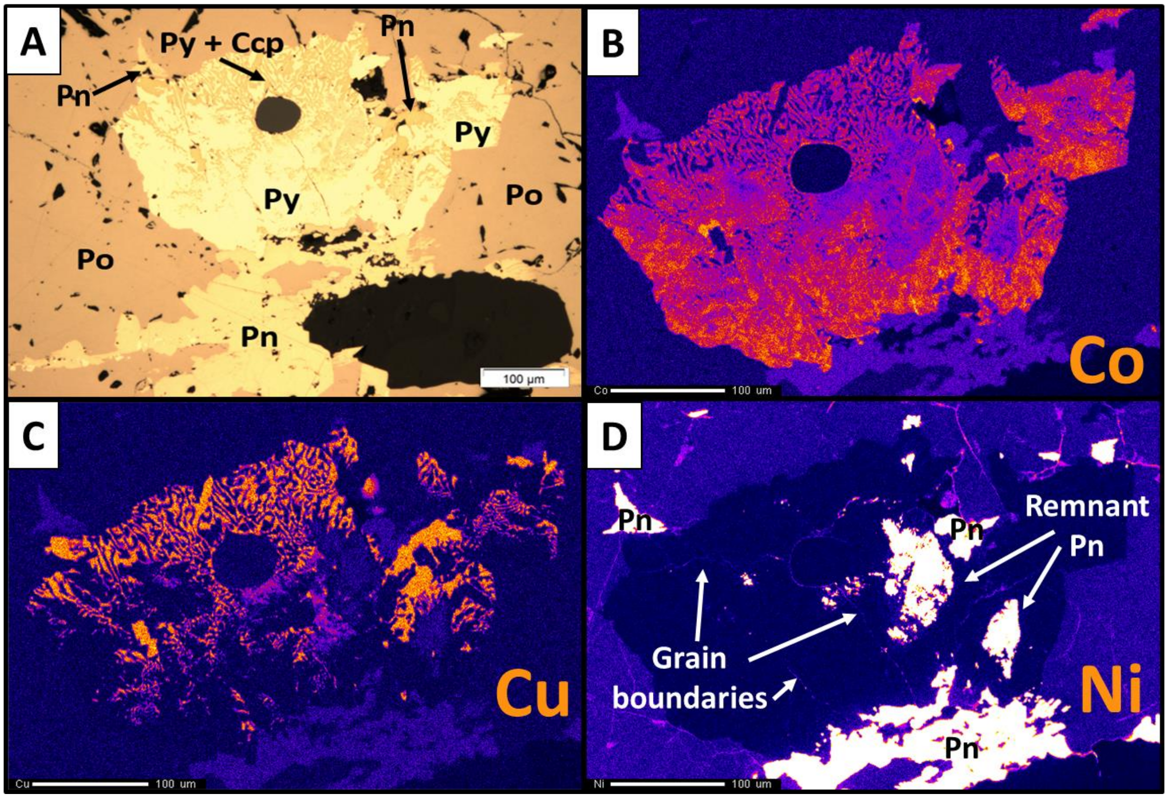

Figure 7-27 A: Reflected light photomicrograph of thin section 1045383 showing a grain with a symplectic intergrowth texture (SIT) between pyrite-chalcopyrite. The SIT grain occurs on the margin of granular pentlandite (GPnE), with remnant pentlandite hosted within the grain. B: The WDS-Co map of the same SIT grain showing the cobalt-rich pyrite. The pyrite is more massive (more cobalt-rich) towards the bottom of the grain, becoming intergrown with chalcopyrite towards the top of the grain. C: The EDS-Cu map of the same grain showing the chalcopyrite (higher copper concentrations) intergrown with pyrite near the top of the grain, hence the wormy intergrowths. D: The WDS-Ni map showing minimal nickel concentrations throughout the grain. However, remnant pentlandite (white blotches) occurs within the SIT pyrite-chalcopyrite grain. Also, in the background, one can faintly witness the annealed subgrain boundaries of pyrite, congealing into a polycrystalline pyrite mass that has since been replaced by wormy, symplectic intergrowths of pyrite-chalcopyrite.

It is evident from the EDS/WDS X-ray maps that the cobalt and nickel contents of the various pyrite types show different textures. Cobalt-rich rims and the absence of nickel zoning is evident in several euhedral pyrite grains (**Figure 7-25 A**). Elsewhere, patchy nickel zoning is present, whereas cobalt zoning is absent (**Figure 7-25 B, E**). Other grains have both patchy nickel zoning and a late-stage cobalt-rich overgrowth (**Figure 7-25 C, D**). Many euhedral pyrite grains and anhedral blebs of pyrite, have nickel- and cobalt-poor inner cores, surrounded by nickel-rich outer cores and cobalt-rich outer grains margins (**Figure 7-25 E, G**). By contrast, some euhedral pyrite grains have nickel-rich inner cores, nickel- and cobalt-poor outer cores, surrounded by cobalt-rich outer grain margins (**Figure 7-25 C, D**). Annealed, euhedral pyrite subgrains form polycrystalline pyrite masses that have since undergone textural changes that have overprinted the original texture. Amongst these masses, cobalt mobilization along subgrain boundaries and fractures (**Figure 7-25 F**), and to a lesser extent nickel mobilization (**Figure 7-27 D**) is evident.

Pyrite flames have been identified to occur within; a homogenous pyrrhotite texture, polygonal grain boundary- and elongated pyrrhotite textures. All pyrite flames are consistently cobalt-rich and nickel-poor (**Figure 7-26 A, B).** However, nickel-rich remnants have been observed in several grains (**Figure 7-26 C**). Electron microprobe analysis of a small sample of pyrite flames indicate compositions of <0.2 wt.% Ni and a mean of 1.9 ± 0.1 wt.% Co, reported to 1σ (or a range of 1.5 – 2.0 wt% Co).

Interestingly, the symplectic intergrowth textures between pyrite-chalcopyrite show intricate, wormy intergrowths between the two minerals (**Figure 7-27 B, C**). These symplectic intergrowth grains occur on annealed, polycrystalline pyrite masses that have themselves grown on the margins of granular pentlandite grains (**Figure 7-27 A**). The symplectic intergrowth grains host remnant pentlandite within their cores (**Figure 7-27 D**). In addition to the seven textural types of pyrite described in **Section 7.3.1**. Our geochemical analyses can be summarized by the following four key geochemical observations when describing the growth of pyrite grains: 1) an early stage growth with the absence of cobalt, but presence of ± nickel at the cores of grains, and with cobalt-rich overgrowths (**Figure 7-25 B, C, D, H**); 2) pyrite grains with cobalt and nickel poor cores, but nickel-rich outer cores and cobalt-rich overgrowths (**Figure 7-25 E, F, G**); 3) a dominant late-stage pyrite growth formed homogeneously from a cobalt-rich fluid (**Figure 7-25 A**), which also includes generation of all pyrite flames (**Figure 7-26**); and 4) a late-stage, low temperature pyrite growth forming symplectic intergrowths with chalcopyrite and pentlandite (**Figure 7-27**). In conclusion, pyrite paragenesis in the 1D ores is complex, but a commonality between all seven textural types, is cobalt enrichment of grains (**Table 7-4**) and a late-stage, cobalt-rich overgrowth on all seven pyrite textural types. Further textural and geochemical investigations would need to be done on the pyrite to understand the variability between textures.

7.4 Chalcopyrite

7.4.1 Mineralogy

Chalcopyrite (Ccp) is a minor sulfide mineral in the Thompson Nickel Belt and within the Thompson 1D orebody. Chalcopyrite modal abundance is rarely greater than 5% (visual estimate) in the thin sections of this study. Chalcopyrite occurs in three different assemblages. The most abundant is a pyrite-chalcopyrite assemblage. Pyrrhotite-chalcopyrite assemblages are less common, whereas pentlandite-chalcopyrite assemblages are the least abundant. A minor amount of chalcopyrite also occurs along fractures in silicate and sulfide grains.

Pyrite-Chalcopyrite Assemblage

Chalcopyrite commonly occurs as inclusions (up to 75μm) within sub-euhedral pyrite grains (**Figures 7-18 A** and **7-26 A**), forms symplectic intergrowth textures with pyrite (**Figures 7-19 A** and **7-28**), forms pyrite-chalcopyrite anhedral blebs (**Figure 7-18 B**) and envelops corroded pyrite grains (**Figure 7-18 C**). Anhedral blebs of chalcopyrite (<1000μm) also commonly occur as overgrowths on massive pyrite (**Figures 7-19 D** and **7-29 A**).

Pyrrhotite-Chalcopyrite Assemblage

Within pyrrhotite, chalcopyrite occurs dominantly as irregularly dispersed anhedral blebs (<500μm) dominantly within a homogenous pyrrhotite matrix **(Figure 7-28 B).** Chalcopyrite also occurs at triple junctions between pyrrhotite grains showing a polygonal grain boundary texture.

Pentlandite-Chalcopyrite Assemblage

A pentlandite-chalcopyrite assemblage is the least common. However, when such assemblage occurs, chalcopyrite dominantly occurs as anhedral blebs (<500μm) on the margins/within granular pentlandite grains **(Figure 7-28 C)**.

Chalcopyrite Fracture Infill

Chalcopyrite less commonly occurs as fine-grained, anhedral grains along fractures that cut silicate grains **(Figure 7-28 D).** Fine-grained chalcopyrite stringers commonly occur amongst brecciated silicate grains (Qz, Bt, Grt, Pl, Kfs) as well as sulfides (Po-Pn-Py-Gdf). Porous space and microfractures in pyrite grains are commonly seen infilled by chalcopyrite. Fine-grained chalcopyrite can occur along fractures in all three chalcopyrite-sulfide assemblages, discussed above.

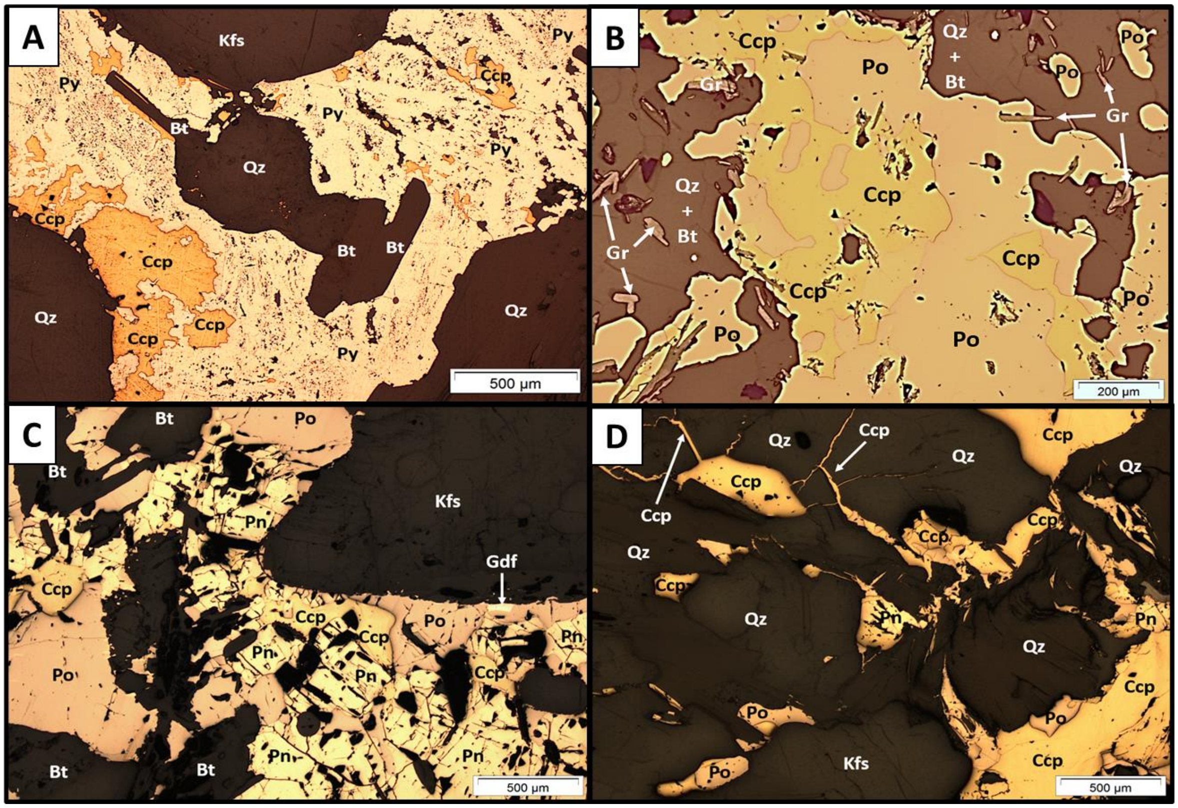

Figure 7-28: Reflected light photomicrographs in PPL of various chalcopyrite assemblages. A: Pyrite-chalcopyrite assemblage showing anhedral blebs of chalcopyrite within massive pyrite (MASV-Py), from thin section 1045397. B: Pyrrhotite-chalcopyrite assemblage showing anhedral blebs of chalcopyrite within a homogenous pyrrhotite matrix (homPo), from thin section 1045339. C: Pentlandite-chalcopyrite assemblage showing anhedral blebs of chalcopyrite on the margins/between pitted granular pentlandite grains (GPnE), from thin section 1045383. D: A chalcopyrite fracture infill texture from thin section 1045364. Chalcopyrite is infilling along fractures in broken up quartz grains. Notice, in all reflected light photomicrographs, silicates are grey to dark-grey, fractures/pits are black. Abbreviations; Qz (quartz), Bt (biotite), Kfs (K-feldspar), Gr (graphite), Ccp (chalcopyrite), Po (pyrrhotite), Pn (pentlandite), Py (pyrite), Gdf (gersdorffite).

7.4.2 Mineral Chemistry

The copper, iron and sulfur compositions in chalcopyrite were determined by EPMA. A total of 22 spot analyses of chalcopyrite from 4 different thin sections were probed in order to determine the composition of chalcopyrite. Weight percent totals of >98.5% and <101.5% were acceptable in order to maintain quality of data. Electron microprobe analysis weight percent and atomic unit data in **Table 7-5,** shows a representative stoichiometric analysis for a pyrite-chalcopyrite assemblage. The other chalcopyrite assemblages; pentlandite-chalcopyrite and pyrrhotite-chalcopyrite, did not vary in chemical compositions and had similar weight percent and stoichiometric values. Thus, the pyrite-chalcopyrite composition in **Table 7-5** serves as a representative analysis for all chalcopyrite assemblages. Chalcopyrite stoichiometry ($CuFeS_2$) was calculated by normalizing to an atomic S of 2.0 and the stoichiometries for all 22 chalcopyrite spot analyses are presented in **Appendix 13.**

Table 7-5: Representative analysis for a chalcopyrite-pyrite assemblage, corroded pyrite enveloped by chalcopyrite (CP-envCcp). The following data is presented in EPMA weight % and atomic units normalized to 2.0 sulfur ($CuFeS_2$). The 'normalization value' along with the molecular weight for each element was used to calculate atomic units.

Sample	1045370
Analysis code	Ccp1_003
Chalcopyrite type	CP-envCcp
	EPMA data (wt%)
Cu	36.3
Fe	32.7
S	31.1
Total wt%	100.1
	Atomic Units
Atomic Cu	1.18
Atomic Fe	1.21
Atomic S	2.00

7.5 Gersdorffite

7.5.1 Mineralogy

Gersdorffite (Gdf) is a nickel arsenide sulfide mineral (NiAsS) that is present in trace amounts within the 1D ores. It occurs as semi-rounded nodules (up to 400μm) that are scattered amongst host pyrrhotite grains **(Figure 7-29 A).** Gersdorffite nodules also occur on the margins or within granular pentlandite **(Figure 7-29 B)** and pyrite grains. Niccolite (NiAs) is commonly present within gersdorffite grains **(Figure 7-29 B).**

Gersdorffite grains host Pd, Rh, Co, Te, Ir and Sb minerals as will be discussed below. It is also important to note that anhedral gersdorffite grains (<30μm) with trace platinum group metals (PGM) are present in several sulfide melt inclusions and will be discussed in the sulfide melt inclusion section (**Section 7.6**).

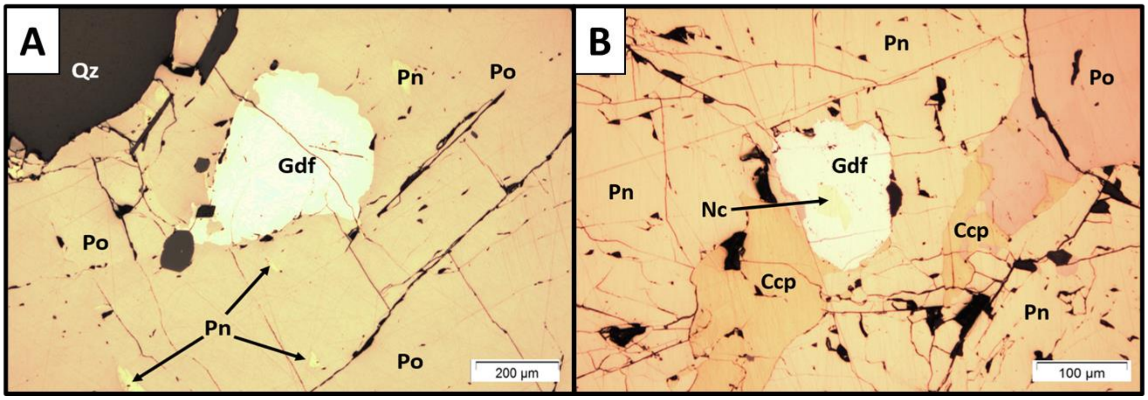

Figure 7-29: Reflected light photomicrographs in PPL of gersdorffite occurrences. A: A subhedral gersdorffite grain within a homogenous pyrrhotite matrix (homPo), from thin section 1045395. B: A subhedral gersdorffite grain in contact with anhedral bleb of chalcopyrite, hosted within granular pentlandite (GPnE), from thin section 1045357. Note the niccolite occurrence within the gersdorffite grain. Silicates are grey, fractures/pits are black. Abbreviations; Po (pyrrhotite), Pn (pentlandite), Gdf (gersdorffite), Qz (quartz), Nc (niccolite), Ccp (chalcopyrite).

7.5.2 Mineral Chemistry

The nickel, arsenic, sulfur, cobalt, iron, palladium and tellurium concentrations in gersdorffite were determined by electron microprobe analysis and were well above the detection limits; 1550 ppm, 240 ppm, 50 ppm, 125 ppm, 115 ppm, 80 ppm and 80 ppm, respectively. The trace element concentrations of platinum, rhodium, iridium, antimony, bismuth, gold, and silver compositions in gersdorffite were also determined by electron microprobe analysis, but were below detection limits; <150 ppm, <80 ppm, <200 ppm, <80 ppm, <140 ppm, <150 ppm and <80 ppm, respectively.

There were 31 spot analyses of 7 gersdorffite grains, from 4 different thin sections and weight percent totals of >98.5% and <101.5% were acceptable. **Table 7-6** shows a representative analysis for a gersdorffite grain hosted in pyrrhotite together with its stoichiometry. Gersdorffite grains hosted in pentlandite have similar compositions, therefore the probe weight percent and atomic unit data in **Table-7-6** is representative of gersdorffite at the 1D orebody. Gersdorffite stoichiometry was calculated by normalizing to an atomic sulfur of 1.0. The stoichiometries for all 31 gersdorffite spot analyses are presented in **Appendix 13.**

No patterns were determined with the accuracy of the electron microprobe. However, it is important to note that some individual spot analyses indicated concentrations of up to 5.7 wt.% Rh, 9450 ppm Ir, 350 ppm Bi and 350 ppm Sb. Future studies can use Laser Ablation Inductively Coupled Mass Spectrometry (LA-ICP-MS) methods to best quantify the concentrations of these elements.

Table 7-6: Representative analysis for a typical gersdorffite composition in the 1D. Analysis is of a subhedral gersdorffite grain within pyrrhotite. The following data is presented in EPMA weight % and atomic units normalized to 1.0 sulfur (NiAsS). The 'normalization value' along with the molecular weight for each element was used to calculate atomic units.

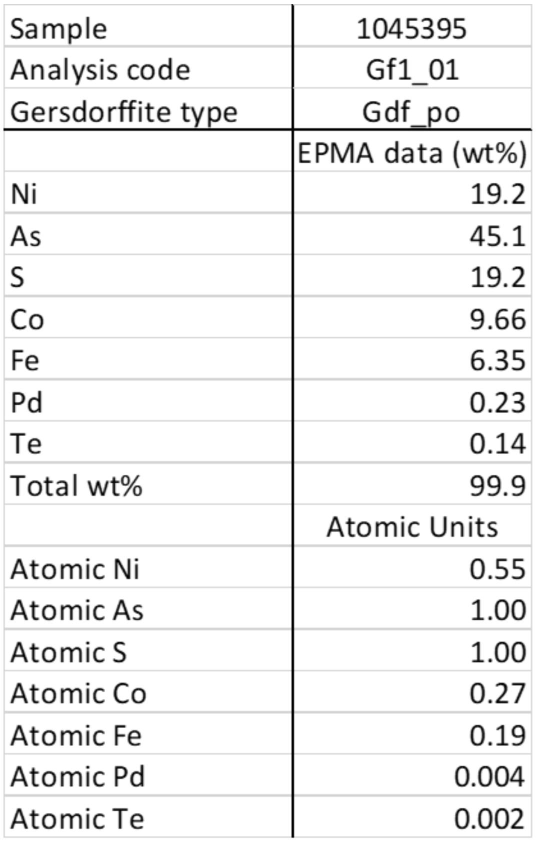

Sample	1045395
Analysis code	Gf1_01
Gersdorffite type	Gdf_po
	EPMA data (wt%)
Ni	19.2
As	45.1
S	19.2
Co	9.66
Fe	6.35
Pd	0.23
Te	0.14
Total wt%	99.9
	Atomic Units
Atomic Ni	0.55
Atomic As	1.00
Atomic S	1.00
Atomic Co	0.27
Atomic Fe	0.19
Atomic Pd	0.004
Atomic Te	0.002

7.5.3 EDS/WDS X-Ray Mapping

EDS X ray maps of elements Au, Bi, Cu, Fe, Ir, Pt, Rh, S, Sb, Te and WDS X ray maps of elements Ni, As, Co, Pd, Ag were examined for 7 different gersdorffite grains. **Figure 7-30 A** shows a backscatter image of a gersdorffite grain that hosts an Ir- and As-bearing PGM grain with additional weight percent level concentrations of Rh, Pt and Au. However, due to poor probe totals (~97%), spot analysis data was omitted for the PGM grain. Cobalt zoning is evident in the gersdorffite grain **(Figure 7-30 B). Figure 7-30 C** and **D** show a WDS-Pd and EDS-Rh maps, respectively. Palladium and to a lesser extent rhodium are at a high enough concentration in gersdorffite grains to be observed during X-Ray mapping and gersdorffite in general, is likely to host of an array of PGM in the 1D orebody.

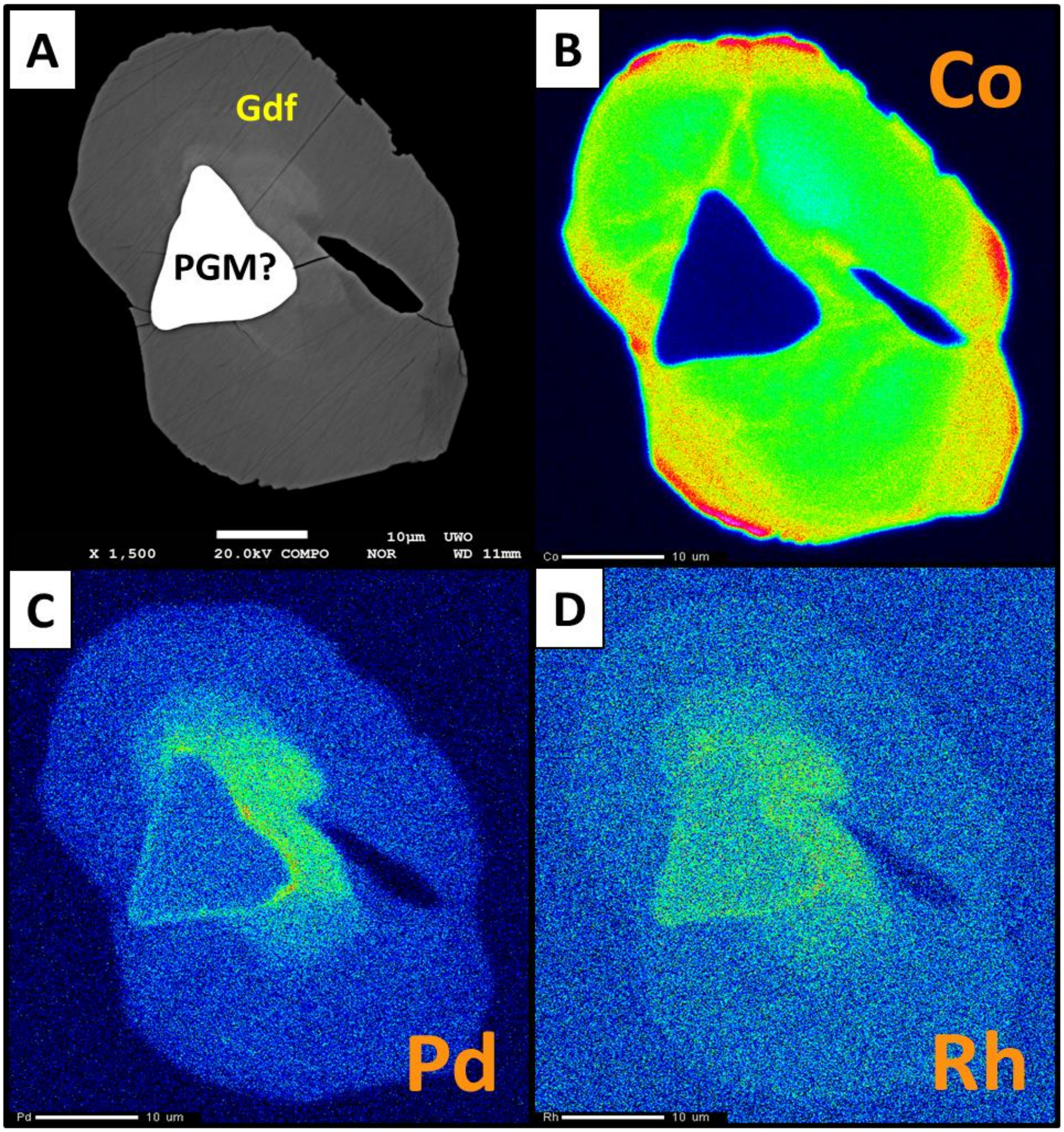

Figure 7-30 A: Backscatter image of a gersdorffite grain (Gdf) with an inclusion of an unknown PGM grain, from thin section 1045357. B: WDS-Co map showing cobalt zoning in the gersdorffite grain. The highest cobalt concentrations are on the outer margins of the grain (red), becoming zoned inwards toward lower cobalt concentrations (light green). C: WDS-Pd map showing palladium concentrations surrounding the unknown PGM grain. D: EDS-Rh map showing concentrations of rhodium dominantly occurring within the unknown PGM grain, as well as overlap with palladium concentrations outside of the PGM grain.

Interestingly, the WDS-Co maps of gersdorffite did show prominent cobalt zoning in most gersdorffite grains **(Figure 7-31 A-C)**. Higher cobalt concentrations towards the grain margins (red), to lower cobalt concentrations towards the centre of the grain (light green), as well as higher cobalt concentrations along fractures in grains resulting a ‘patchy’ appearance **(Figure 7-31 D).** Cobalt concentrations are relatively high in the gersdorffite grains with a mean of 9.72 ± 3.51 wt.% Co, reported to 1σ). Furthermore, nickel zoning is also common in gersdorffite grains, but to a lesser prominence than cobalt zoning.

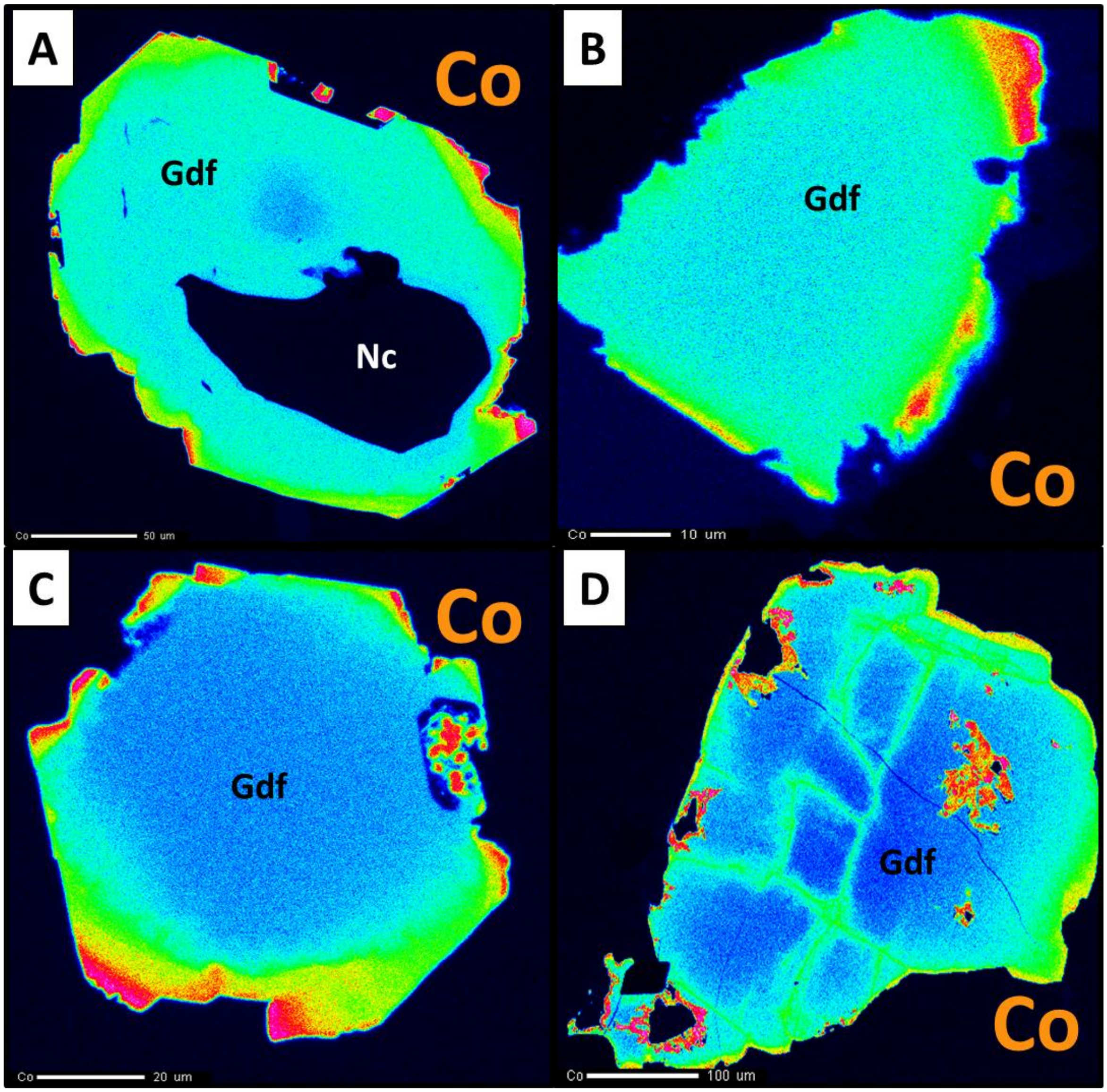

Figure 7-31 A: WDS-Co map of a gersdorffite grain (Gdf) from thin section 1045342. Note the niccolite occurrence (Nc) in the gersdorffite grain. Prominent cobalt zoning is present in the grain. Higher cobalt concentrations towards the margins (red), lower cobalt concentrations towards the centre of the grain (light blue). B: WDS-Co map showing cobalt zoning in a gersdorffite grain from thin section 1045397. C: WDS-Co map showing cobalt zoning in another gersdorffite grain from thin section 1045397. D: WDS-Co map showing higher cobalt concentrations along fractures in the Gdf grain, resulting in a 'patchy' appearance, from thin section 1045395.

7.6 Sulfide Melt Inclusions

All the analytical work completed up to this section was from regular sulfides that fall between silicate grains. In this section, populations in sulfide melt inclusions (SMI) will be compared to the subhedral inclusions (SI-X) in regular sulfides. It is important to first clarify the difference between subhedral sulfide inclusions (SI-X) and sulfide melt inclusions (SMI):

Subhedral sulfide inclusions (SI-X) are products of sulfide having been trapped and incorporated within silicates (eg. metamorphic quartz and garnet grains) during their growth (D_0). They are typically anhedral to subrounded, and monomineralic, but less commonly consist of an intergrowth of two sulfide assemblages. The dominant sulfide inclusion is pyrrhotite; granular pentlandite is the next most common inclusion mineral. Locally subhedral sulfide inclusions (SI-X) occur along fractures, which indicates that some of the inclusions in silicates might post-date peak metamorphism.

In contrary, sulfide melt inclusions (SMI) are products of sulfide partial melt, generated dominantly during peak P-T conditions (late D_2) (**Section 8.5.3**), some of which became trapped in metamorphic silicate phases such as garnet and quartz grains. Sulfide melt inclusions could have also been generated during shear melting (D_3) (**Section 8.5.3**). Sulfide melt inclusions are subrounded, consist of polymetallic sulfide assemblages (Po-Pn-Py-Ccp-Gdf) and possess a complex array of textures.

7.6.1 Mineralogy

Sulfide melt inclusions in the 1D ores are dominantly hosted within metamorphic quartz **(Figure 7-32 A, C, D, E)** and less commonly, within cores of metamorphic garnet grains **(Figure 7-32 B, F).** Sulfide melt inclusions are rounded to semi-rounded, typically <100μm across, but locally are up to 500μm across. Interestingly, graphite occurs as laths commonly attached, or in close proximity to, many polymetallic sulfide melt inclusions **(Figure 7-32 F).** At two locations chlorite, that presumably replaced biotite, is also attached to sulfide melt inclusions.

Cathodoluminescence maps of quartz **(Figure 6-8, Chpt. 6.3.1)** indicate that the sulfide melt inclusions are associated with an older generation of metamorphic quartz; the younger generation lack sulfide melt inclusions **(Figure 6-8, Chpt. 6).** The sulfide melt inclusions are polymineralic and consist of Po>Pn>Py>Ccp>Gdf. They can host flame and lamellae textures of pentlandite **(Figure 7-32 A, E)** and less commonly pyrite, that have exsolved from pyrrhotite, as well as symplectic intergrowths of pyrite-pentlandite, and less commonly pyrite-chalcopyrite **(Figure 7-32 F).**

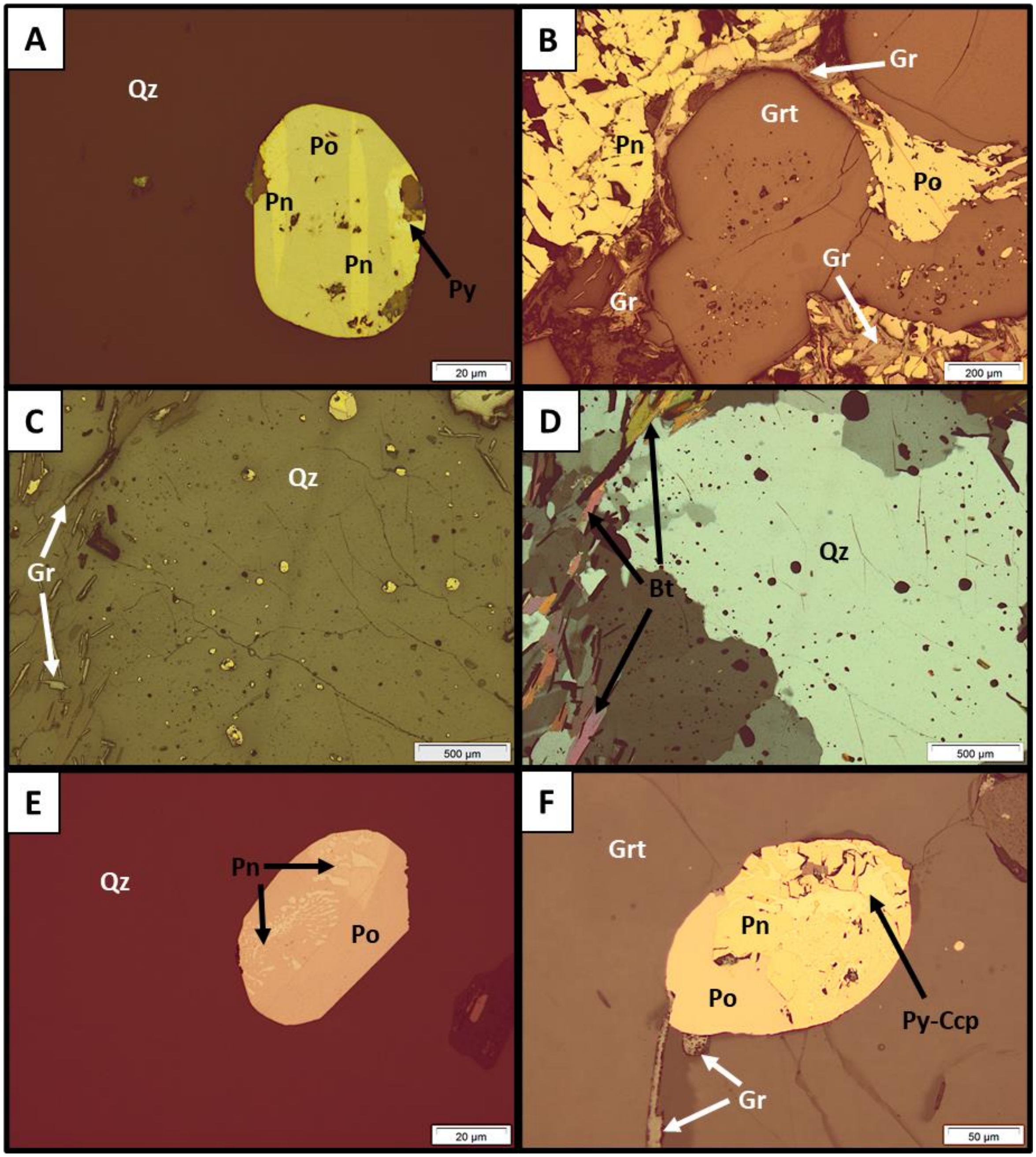

Figure 7-32 A: Reflected light photomicrograph in PPL of a polymetallic, sulfide melt inclusion (SMI) in a metamorphic quartz grain. Dominantly pentlandite lamellae exsolving from a pyrrhotite matrix, with a pyrite occurrence, from thin section 1045386. B: Reflected light photomicrograph in PPL showing numerous sulfide melt inclusions within cores of garnet grains, from thin section 1045395. Note the graphite laths surrounding the garnet grains. C: Reflected light photomicrograph in PPL showing numerous sulfide melt inclusions within a metamorphic quartz grain, from thin section 1045386. Note the graphite laths interlocked with biotite on the outer margins of the grain. D: Same image as (C) but in transmitted light in XPL. The host metamorphic quartz grain has well developed subgrain boundaries. Graphite laths are interlocked with biotite around the grain. E: Reflected light photomicrograph in PPL of a sulfide melt inclusion in a metamorphic quartz grain, from thin section 1045364. Note, pentlandite flames exsolving from a pyrrhotite matrix. F: Reflected light photomicrograph in PPL of a polymetallic sulfide melt inclusion in garnet. A pyrite-chalcopyrite symplectic intergrowth texture (SIT) makes up most of the SMI, from thin section 1045386. Note the graphite laths attached to the SMI. Abbreviations; Qz (quartz), Grt (garnet), Gr (graphite), Bt (biotite), Po (pyrrhotite), Pn (pentlandite), Py (pyrite), Ccp (chalcopyrite).

7.6.2 Mineral Chemistry

The iron, sulfur, nickel, cobalt and copper compositions in sulfide melt inclusions were determined by electron microprobe analysis. A total of 24 pentlandite, 26 pyrite and 23 pyrrhotite spots were analyzed to determine compositions of the sulfide grains in the sulfide melt inclusions. Weight percent totals of >98.5% and <101.5% were acceptable. The probe weight percent and atomic unit data in **Table 7-7** show representative analyses and stoichiometric values for these sulfides. Stoichiometries were calculated assuming atomic concentrations of 8.0 sulfur for pentlandite ($Fe_{4.5} Ni_{4.5} S_8$), 2.0 sulfur for pyrite (FeS_2) and 1.0 sulfur for pyrrhotite ($Fe_{1-x} S$). Due to a small dataset of chalcopyrite and gersdorffite analyses in sulfide melt inclusions, the elemental compositions and stoichiometric calculations of these sulfide minerals were excluded from **Table 7-7.** However, the stoichiometries of all sulfide analyses (Pn, Py, Po, Ccp, Gdf) in sulfide melt inclusions are presented in **Appendix 13.** Arsenic levels in Pn, Py, Po, and Ccp were consistently below the detection limit of the electron microprobe (<350ppm), except for gersdorffite.

The sulfide melt inclusions pentlandite analyses **(Table 7-7)** had similar elemental compositions to the 1D pentlandite analyses **(Table 7-2, Chpt. 7.2.3)** for all elements except copper. Pentlandite in sulfide melt inclusions have just under 600 ppm copper. However, copper concentrations were not analyzed in 1D pentlandite samples. The sulfide melt inclusion pyrite analyses **(Table 7-7)** had a mean of 1.0 ± 0.4 wt.% Co and 1.2 ± 1.4 wt.% Ni, both reported to 1σ. This is ~3000 ppm less Co and ~1000 ppm more Ni than that observed for pyrite in the 1D orebody **(Table 7-4, Ch. 7.3.3).** Pyrite in sulfide melt inclusions also have just under 400 ppm copper. However, copper concentrations were not analyzed in the 1D pyrite analyses. The sulfide melt inclusion pyrrhotite analyses **(Table 7-7)** had similar iron and sulfur compositions to the 1D pyrrhotite analyses **(Table 7-1, Ch. 7.1.3)**. However, the pyrrhotite in sulfide melt inclusions had a mean of 0.34 ± 0.10 wt.% Ni, reported to 1σ. This is ~1400 ppm less Ni compared to 1D pyrrhotite concentrations **(Table 7-1, Ch. 7.1.3)**. In conclusion, there are minor differences in the elemental concentrations of sulfides (Pn-Py-Po) in the sulfide melt inclusions, when compared to concentrations in the sulfide minerals that are described for the 1D mineral zone (**Section 7.1 to 7.5**). However, from 13 observed thin section samples where sulfide melt inclusions occur, the mean whole rock nickel (wt%) and cobalt (ppm) tenor of the ores were; 10.9 wt% Ni and 1573 ppm Co. Thus, sulfide melt inclusions could potentially be linked to high tenor ores.

Table 7-7: Representative analyses for typical sulfide assemblages within sulfide melt inclusions (SMI); pentlandite, pyrite and pyrrhotite. The following data is presented in EPMA weight % and atomic units normalized to 8.0 sulfur for pentlandite ($Fe_{4.5} Ni_{4.5} S_8$), 2.0 sulfur for pyrite (FeS_2) and 1.0 sulfur for pyrrhotite ($Fe_{1-x} S$). The 'normalization value' along with the molecular weight for each element was used to calculate atomic units.

Sample	1045360	1045360	1045395
Analysis code	SMI_3_03	SMI_5_02	SMI_3_04
SMI type	Pn_SMI	Py_SMI	Po_SMI
	EPMA data (wt%)		
Fe	30.5	44.0	60.1
S	33.7	53.6	39.4
Ni	34.5	1.25	0.33
Co	0.32	1.33	n.d.
Cu	0.06	0.04	n.d.
Total wt%	99.1	100.2	99.8
	Atomic Units		
Atomic Fe	4.16	0.94	0.877
Atomic S	8.00	2.00	1.00
Atomic Ni	4.46	0.026	0.005
Atomic Co	0.04	0.027	n.d.
Atomic Cu	0.01	0.001	n.d.
x	n/a	n/a	0.123

7.6.3 EDS/WDS X-Ray Mapping

The EDS X ray map of element S and WDS X ray maps of elements Ni, Co, As, Fe, Cu were examined for sulfide melt inclusions. No zoning of any elements was observed. However, WDS nickel and cobalt analysis, along with the accompanying backscatter maps, helped identify the textural complexity of sulfide melt inclusions **(Figure 7-33 A-H).** Abundant symplectic intergrowth textures between pyrite-pentlandite **(Figure 7-33 A, C, E, F, G, H)** and pyrite-chalcopyrite **(Figure 7-33 A, G)** are observed. Pentlandite and pyrite lamellae exsolved from a pyrrhotite matrix **(Figure 7-33 B** and **H)** and subhedral gersdorffite grains **(Figure 7-33 D)** occur. This contrasts with the rarity of gersdorffite in the 1D sulfides. Gersdorffite is a minor phase in sulfide melt inclusions, generally as subrounded blebs (<10μm) within or on margins of pentlandite grains. Of the mapped sulfide melt inclusions, 2/21 contained between 1-3 gersdorffite grains that were consistently <10μm across. Niccolite (NiAs) and trace PGM have also been detected in gersdorffite grains hosted within sulfide melt inclusions. Spot analysis on the PGM minerals show Fe, Ni, As, Pt peaks. However, more quantitative analyses of platinum group metals is beyond the scope of the study.

It is important to note that symplectic intergrowth textures between pyrite-chalcopyrite are more common than pyrite-pentlandite intergrowths in the 1D sulfide ores. However, the opposite is true in the sulfide melt inclusions, where pyrite-pentlandite symplectites are more common than pyrite-chalcopyrite. However overall, symplectic intergrowth textures occur more frequently across sulfide melt inclusions than in 1D sulfides.

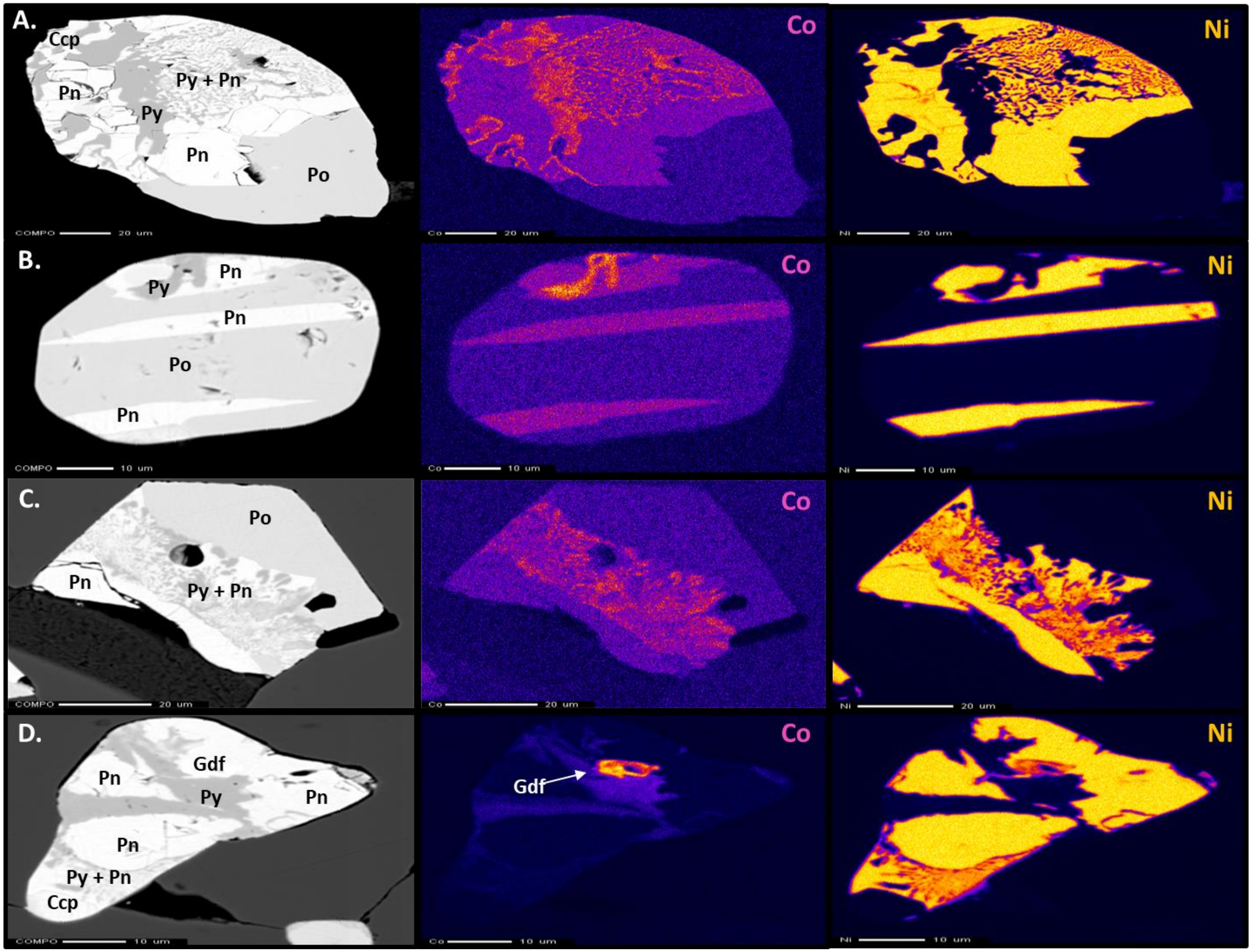
A.
Ccp
Py + Pn
Pn
Py
Pn
Po
COMPO 20 um
Co
Co 20 um
Ni
Ni 20 um
B.
Py
Pn
Pn
Po
Pn
COMPO 10 um
Co
Co 10 um
Ni
Ni 10 um
C.
Po
Pn
Py + Pn
COMPO 20 um
Co
Co 20 um
Ni
Ni 20 um
D.
Gdf
Pn
Py
Pn
Pn
Py + Pn
Ccp
COMPO 10 um
Co
Gdf
Co 10 um
Ni
Ni 10 um

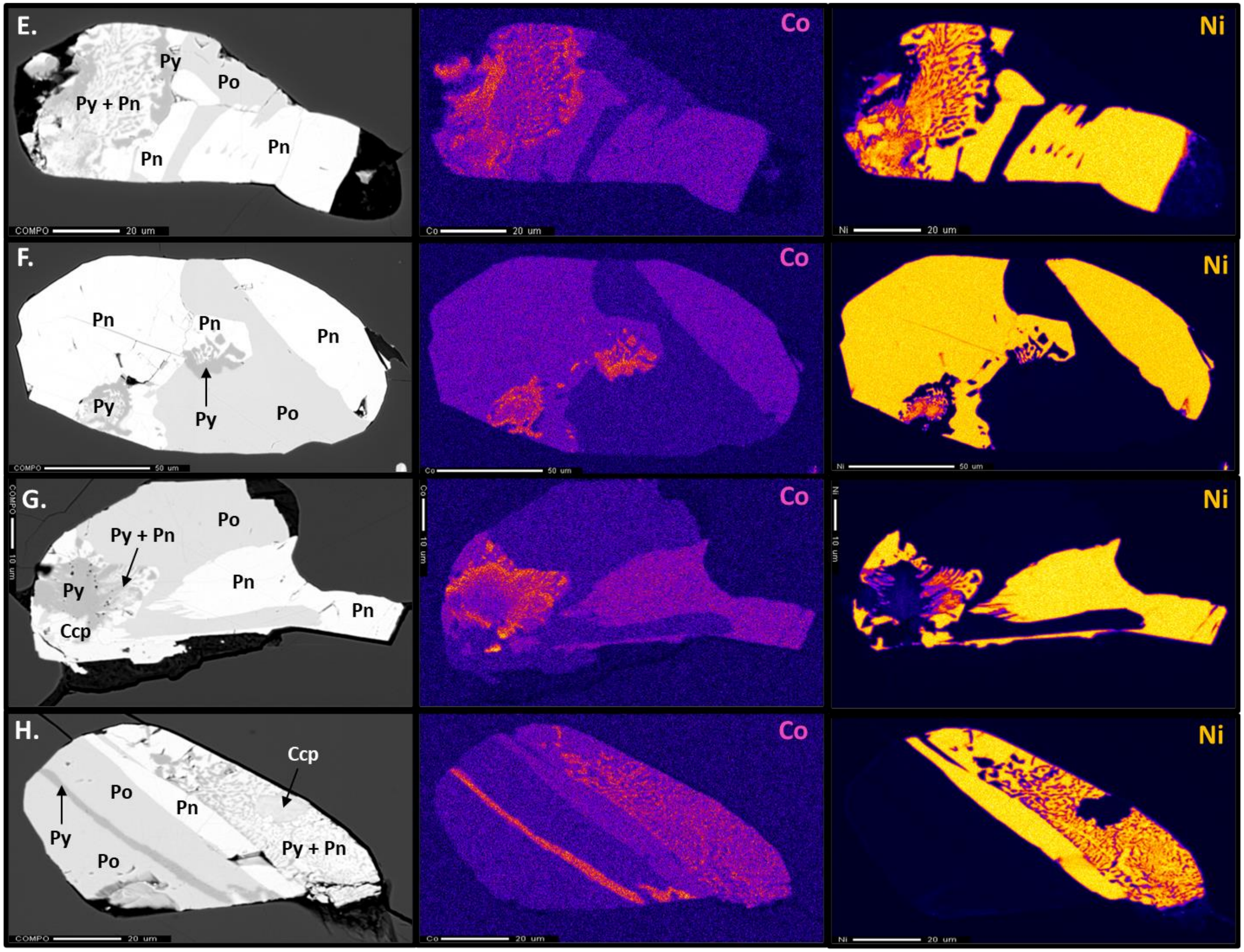
E.
Py
Po
Py + Pn
Pn
Pn
COMPO 20 um
Co
Co 20 um
Ni
Ni 20 um
F.
Pn
Pn
Pn
Py
Py
Po
COMPO 50 um
Co
Co 50 um
Ni
Ni 50 um
G.
Po
Py + Pn
Py
Pn
Pn
Ccp
COMPO 10 um
Co
Co 10 um
Ni
Ni 10 um
H.
Ccp
Po
Pn
Py
Po
Py + Pn
COMPO 20 um
Co
Co 20 um
Ni
Ni 20 um

Figure 7-33 A-H: Eight different polymetallic sulfide melt inclusions (SMI) were mapped by the EPMA. Backscatter images, WDS-Co and WDS-Ni maps are shown for each SMI. Sulfide assemblages present in SMI from most common to least are; Po>Pn>Py>Ccp>Gdf. Symplectic intergrowth textures between pyrite-pentlandite and pyrite-chalcopyrite occur, the former being more common in SMI. Pentlandite and less commonly pyrite flames and lamellae occur in pyrrhotite. Pyrite occurrences are enriched by elevated cobalt concentrations, as in the 1D sulfides. Chalcopyrite usually occurs as anhedral blebs within pyrite or pentlandite grains, or forms a symplectic texture with pyrite. Gersdorffite is quite rare but occurs in multiple SMI. Niccolite and trace PGMs have been detected in gersdorffite grains that are within SMI. Abbreviations; Pn (pentlandite), Py (pyrite), Po (pyrrhotite), Ccp (chalcopyrite), Gdf (gersdorffite).

7.7 Sulfide Paragenetic Sequence

Most of the sulfide assemblages within the 1D orebody at Thompson mine represent a primary magmatic sulfide assemblage of pyrrhotite and pentlandite with minor chalcopyrite, that was subsequently metamorphosed and deformed. Experimental and empirical work on sulfide phase equilibria demonstrate that immiscible magmatic sulfides form from a sulfide-saturated basaltic melt at temperatures of >1200°C. Upon cooling, a monosulfide Fe-Ni-S solid solution (MSS) forms from the sulfide melt that exsolves to form pyrrhotite at ~1100°C (Naldrett et al., 1967, 2004; Li et al., 1996; Barnes et al., 1997, 2001). Continued fractional crystallization of the MSS results in a Ni-enriched residual sulfide liquid (higher partition coefficient) that fractionates a high-temperature polymorph of pentlandite at ~850°C (Sugaki and Kitakaze, 1988; Naldrett, 2004). In most cases, further cooling (~650°C) and fractionation of MSS results in a residual sulfide melt that is progressively more copper-rich (Kullerud et al., 1969; Dutrizac, 1976; Ebel and Naldrett, 1997; Sinyakova and Kosyakov 2009). However, Burnham et al. (2009) and Lightfoot et al., (2017) report that the parental magmatic sulfide melt at Thompson originally had high Ni and low Cu contents. Suggesting that the melt never got to the point of forming a fractionated Cu-liquid and not much potential for Cu-rich stringer zones within country rocks.

All pre-existing sulfide deposits would have been resorbed back to a primarily homogenous MSS during prograde metamorphism and deformation (D_1 to D_2) (Bleeker 1990; Lightfoot and Evans-Lamswood, 2015; Lightfoot et al., 2017), resulting in the destruction of primary magmatic sulfide textures. Therefore, the paragenetic sequence described below, and shown in **Figure 7-34**, represents sulfide textures formed syn- to post-peak D_2 and throughout the retrograde metamorphic realm (D_3 to D_4). For each sulfide mineral section below, the paragenesis is described from the earliest (highest T), to the latest (lowest T), formed textures.

Pyrite is not commonly formed during the crystallization of magmatic sulfides, but usually by secondary processes (Heath et al., 2001; Burnham et al., 2009; Stone et al., 2004; Bailey et al., 2006; Collins et al., 2012; Pina et al., 2013, 2016; Duran et al., 2015, 2016). Pyrite was likely generated after the magmatic phase of evolution in the Thompson deposits (**Section 8.2.1**). However, the origin of pyrite is less certain, and in order to evaluate the possible metamorphic or hydrothermal origins of pyrite, it is necessary to establish a paragenetic sequence of sulfide minerals, based on the textural constraints that were presented in **Chapters 6** and **7**. This paragenetic sequence is together with constraints from phase equilibria and summarized by **Figure 7-34.**

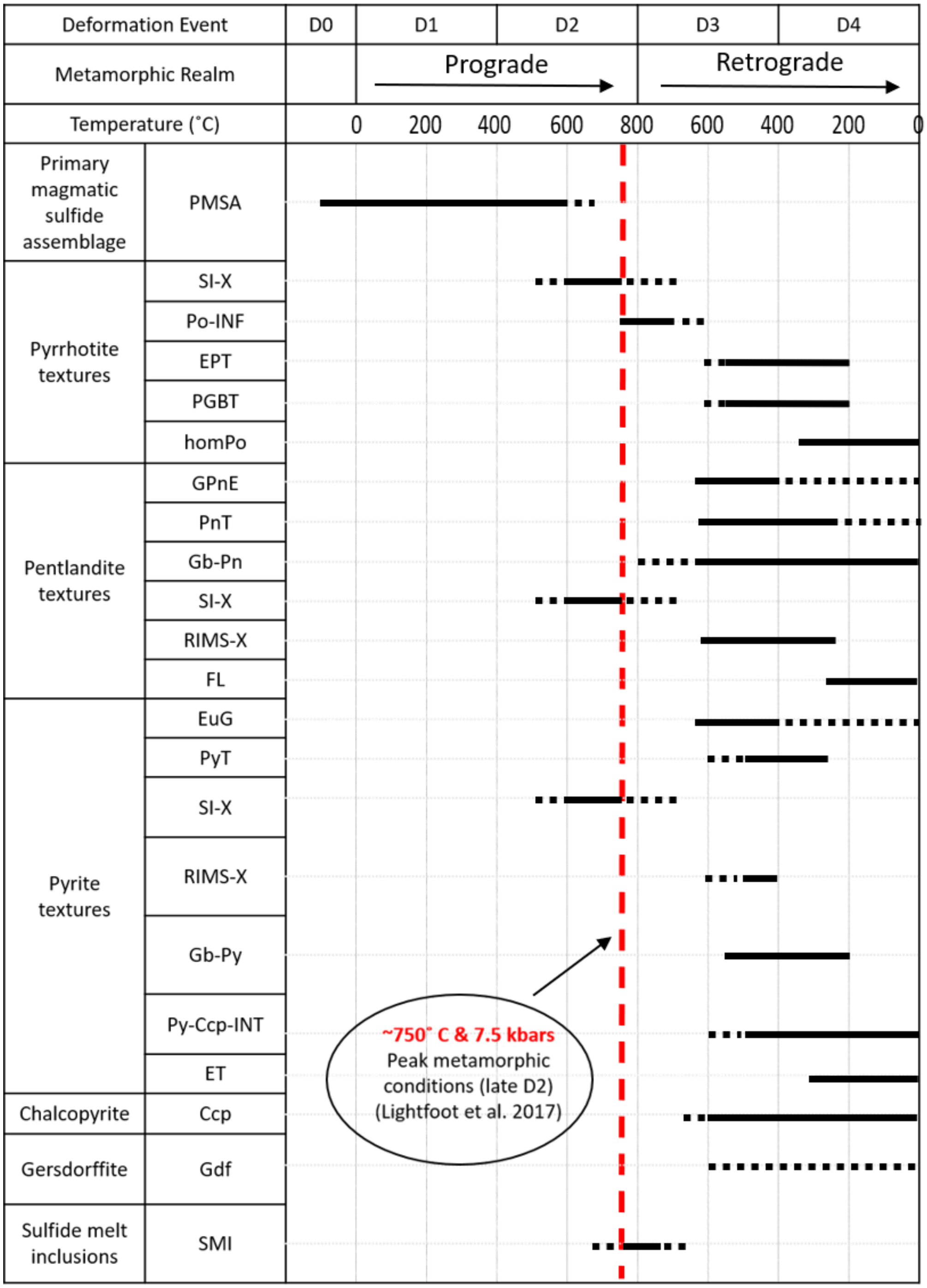

Figure 7-34: Paragenetic sequence outlining the timing of formation of all sulfide textures observed in this study of the Thompson 1D orebody. Red-dotted line (750˚C & 7.5 kbars) marks peak metamorphic conditions at Thompson (Lightfoot et al., 2017). Primary magmatic sulfide assemblage (PMSA) originates in D_0, before onset of D_1 deformation, and carries through to mid-D_2 (~650˚C). Abbreviations; SI-X (subhedral inclusions within silicates); Po-INF (pyrrhotite infilling texture); EPT (elongated pyrrhotite texture); PGBT (polygonal grain boundary texture); homPo (homogenous pyrrhotite matrix); GPnE (granular pentlandite eyes); PnT (pentlandite trails); Gb-Pn (grain boundary pentlandite); RIMS-X (rims around silicates); FL (pentlandite flames); EuG (euhedral pyrite grains); PyT (pyrite trails); Gb-Py (grain boundary pyrite); Py-Ccp-INT (pyrite chalcopyrite intergrowth textures); ET (pyrite exsolution textures – flames and lamellae); Ccp (chalcopyrite); Gdf (gersdorffite); SMI (sulfide melt inclusions).

Primary Magmatic Sulfide Assemblage

A primary magmatic sulfide assemblage (PMSA) would have been present during initial sulfide formation (D_0) before the onset of deformation and metamorphism of the TNB (D_1). The primary magmatic sulfide assemblage would have likely been stable most of the way through D_1, up to D_2, where partial formation of monosulfide solid solution began (~650˚C) and continued with increasing P-T into D_3 (Lightfoot et al., 2017). The primary magmatic sulfide assemblage is depicted in **Figure 7-34.**

Pyrrhotite

SI-X

Monomineralic Po-Pn-Py-Ccp subhedral inclusions (SI-X) dominantly occur within garnet and quartz grains, interpreted to being trapped synchronous with silicate growth, i.e., pre- to syn-peak D_2. Sulfide and silicate inclusions only occur in garnet cores and are absent from garnet rims at Thompson (Bleeker 1990; this study). Garnet cores have yielded consistent prograde temperatures of ~600 ± 50°C and pressures of 5.5 ± 1 kbar at Thompson (Burnham et al., 2009). These ranges have been used on **Figure 7-34** for the Po-Pn-Py subhedral inclusion textures.

Sulfide inclusions are also common in metamorphic quartz grains, hosted within the massive sulfide, that have experienced subgrain development. Plastic deformation and dynamic recrystallization of quartz grains has been interpreted for a wide range of temperatures, from ~700°C to as low as 280°C (Stipp et al., 2002a, 2002b). However, quartz deformation textures have been recorded as high as 850°C in experimental studies of dislocation creep experiments, up to the point of partial melting of the rock (Hirth and Tullis, 1992). Therefore, quartz can undergo dynamic recrystallization progressively over a wide range of temperatures (~850°C to 280°C).

Po-INF

Pyrrhotite infill texture (Po-INF) is interpreted to have been caused by the superplastic behaviour and infiltration of ductile pyrrhotite into fractures and cracks of P_2 host biotite-graphite-schists (Monteiro and Krstic, 2006). It is likely that the pyrrhotite at this stage would of been the most superplastic at the highest P-T and strain rate conditions which were at peak D_2 at ~750°C and 7.5 kbar (Lightfoot et al., 2017) (**Figure 7-34**).

EPT and PGBT

Elongated pyrrhotite texture (EPT), is characterized by intense kinking and twinning, and is interpreted to be caused by high temperature ductile deformation (Monteiro and Krstic, 2006). The polygonal grain boundary texture (PGBT) is coeval with the elongated pyrrhotite texture and is characterized by equant polyhedral subgrains of pyrrhotite that were annealed during recrystallization and reorientation that followed deformation (Monteiro and Krstic, 2006; Lusk and Ostwald, 1983). The development of polygonal subgrain boundaries in pyrrhotite is commonly interpreted to reflect a relaxation process that accompanies kinking and twinning (Clark and Kelly, 1973). Both these pyrrhotite textures are consistent with the brittle-ductile deformation regime that occurred late- to post-F_3 during transpressive deformation (mid-D_3 to early-D_4) at Thompson (Bleeker 1990). The strength and deformation studies on Sudbury pyrrhotite conducted by Clark and Kelly (1973) concluded that twinning and kinking begins ~200°C, and that between 350°C to 550°C the dislocation processes become dominant. Furthermore, diffusion-dominated mechanisms >550°C likely involve continuous polygonization, recrystallization and grain growth of pyrrhotite (McDonald and Paterson, 1980). Consequently, EPT and PGBT pyrrhotite textures are interpreted to having been formed ~200°C to ~550°C **(Figure 7-34),** with dashed-lines reflecting that temperatures of >550°C might also be possible, based on the work of McDonald and Paterson (1980).

homPo

The homogenous pyrrhotite matrix (homPo) texture is interpreted to represent the lowest temperature textural type to crystallize from the monosulfide solid solution. A common characteristic of the homogenous pyrrhotite texture (homPo) is that it lacks subgrain development and resembles a homogenous mass of pyrrhotite. Grain boundaries are difficult to distinguish under reflected light. Similarly, there is a lack of kinking or twinning, therefore this pyrrhotite formation would have last equilibrated at <200°C (Clark and Kelly, 1973). However, a homogenous pyrrhotite matric does exhibit brittle fracture, which is interpreted to occur at low temperatures of <250°C in pyrrhotite (Monteiro and Krstic, 2006). Clark and Kelly (1973) conducted strength and deformation experiments on Sudbury pyrrhotite to show that small-scale brittle deformation in pyrrhotite dominates at temperatures below 350°C.

Pentlandite

Gb-Pn

The experiments of Kelly and Vaughan (1983) demonstrated that Ni, Co and Fe migrate to monosulfide solid solution grain boundaries during exsolution of pentlandite at ~650°C. Naldrett et al. (1967) stated that at temperatures <800°C, depending on the nickel tenor, pentlandite starts exsolving from the monosulfide solid solution. Therefore, grain boundary pentlandite (Gb-Pn) is interpreted to have been the first textural type of pentlandite to heterogeneously nucleate from the MSS. However, Sugaki and Kitakaze (1998) demonstrated that the upper thermal stability of pentlandite is ~865°C and interpreted that pentlandite would dissolve back into MSS during prograde metamorphism, and re-exsolve from the MSS during retrograde metamorphism at this temperature. Furthermore, ‘chain-like’ aggregates of pentlandite occur along boundaries of annealed pyrrhotite grains and are interpreted to have formed from MSS at temperatures between 610°C and 250°C (Naldrett et al., 1967; McQueen, 1979; Durazzo and Taylor, 1982; Burnham et al., 2009). Additionally, Monteiro and Krstic (2006) reported ‘loop textured’ pentlandite, that has similar textural characteristics to what is called grain boundary pentlandite in this study, to exist between the boundaries of annealed pyrrhotite grains at temperatures of <300°C. Therefore, grain boundary pentlandite, or as referred to as ‘loop textured’ pentlandite (Monteiro and Krstic, 2006), or ‘chain-like’ pentlandite (Burnham et al., 2009) has been observed at a wide range of temperatures; from upper limits of 865°C (Sugaki and Kitakaze, 1998), between intermediate temperatures of 650°C to 250°C (Naldrett et al., 1967; McQueen, 1979; Durazzo and Taylor, 1982; Kelly and Vaughan, 1983; Burnham et al., 2009) and at lower limits of <300°C (Monteiro and Krstic, 2006) (**Figure 7-34**).

GPnE

As temperatures fell, grain boundary pentlandite would continue to grow and form coarser-grained pentlandite eyes (GPnE) at temperatures between 650°C to 400°C (Kelly and Vaughan, 1983) (**Figure 7-34**). Kullerud (1963) demonstrated that granular pentlandite exsolves from MSS at temperatures ~610°C and below.

PnT

After granular pentlandite eyes formed, these porphyroblasts underwent annealing, coarsening, and alignment into mm- and cm- scale bands during continued cooling of the MSS between temperatures of <610°C to 250°C (Burnham et al., 2009). During this stage, the pentlandite porphyroblasts became oriented parallel to stress-induced foliation via continued retrograde deformation (Monteiro and Krstic, 2006; Burnham et al., 2009). Pentlandite trails (PnT) are shown to form at these temperatures on **Figure 7-34**.

RIMS-X

Pentlandite rims around silicates (RIMS-X) are characterized by granular pentlandite grains that have annealed into clusters that preferentially surround sericitized quartz and plagioclase grains, but also occur around biotite and muscovite laths. Therefore, these rims would have likely formed via similar annealing processes that granular pentlandite eyes underwent to form mm- to cm- scale pentlandite trails at temperatures between ~610°C to 250°C (Burnham et al., 2009) (**Figure 7-34**).

FL

Upon further cooling of the MSS, continued segregation of pentlandite via homogenous nucleation of pentlandite lamellae and flames (FL) occurred along weak cleavage planes in the pyrrhotite. Kelly and Vaughan (1983) state that pentlandite lamellae are exsolved from the MSS at lower temperatures ~300°C and exsolution flames form <250°C. Naldrett et al. (1967) interpreted that exsolution continues down to below 300°C as fine-grained flame pentlandite within a pyrrhotite matrix. Other authors have also suggested that pentlandite exsolution lamellae and flames formed at low temperatures of 250°C and 150°C, respectively (Gilligan and Marshall, 1987; Monteiro and Krstic, 2006; Burnham et al., 2009). This is due to the lower diffusion rates of iron and nickel at these lower temperatures, causing super saturation than if at higher temperature regimes (Durazzo and Taylor, 1982; Kelly and Vaughan, 1983; Burnham et al., 2009). Both pentlandite lamellae and flames are grouped into the category of pentlandite flames on **Figure 7-34**.

Pyrite

Late-paragenesis of pyrite is common in magmatic sulfide deposits (Craig et al., 1998; Franchuk et al., 2016). In most cases, pyrite forms as a result of post-magmatic sulfidation or oxidation (Craig and Vokes, 1993; Heath et al., 2001; Stone et al., 2004; Burnham et al., 2009; Vukmanovic et al., 2014) and hydrothermal fluid activity during deformation (Collins et al., 2012; Pina et al., 2013, 2016; Duran et al., 2015, 2016). Although a small proportion may form by decomposition of S-rich MSS below 750°C depending on the metal/S ratio of the sulfide melt (Naldrett et al., 1967; Sugaki and Kitakaze, 1998; Farrell and Fleet, 2002; Naldrett, 2004; Dare et al., 2010; Cafagna and Jugo, 2016).

EuG

Euhedral pyrite grains (EuG) commonly occur as overgrowths on granular pentlandite grains (GPnE), pentlandite trails (PnT), pyrrhotite polygonal grain boundary texture (PGBT) and homogenous pyrrhotite texture (homPo), (**Figure 7-34**). Thus, euhedral pyrite grains would have had crystallized after the host pentlandite and pyrrhotite textures were already formed. The presence of euhedral grains in these host sulfide textures indicates that pyrite crystallized relatively late in the paragenetic sequence. Polycrystalline masses of euhedral pyrite are dominantly made up of smaller euhedral pyrite grains that have annealed grain boundaries with triple point junctions at angles between 110° to 130° (Lawrence, 1972). These larger euhedral masses commonly form at temperatures >450°C (Craig and Vokes, 1993) and show remnant pentlandite and mobilized chalcopyrite in adjacent low-pressure triple junction zones (Lawrence, 1972). Cafagna and Jugo (2016) conducted experiments that showed euhedral pyrite grains surrounded by, and having inclusions of chalcopyrite within their cores at 650°C. However, both chalcopyrite and pentlandite inclusions are common in euhedral pyrite grains in the 1D (**Figures 7-17 A; 7-25 A**). Monteiro and Krstic (2006) state that pyrite grains at Thompson underwent brittle modification ~400°C (D_4) which resulted in porous space and microfractures that were infilled by chalcopyrite. Cafagna and Jugo (2016) concluded that in Cu-bearing systems, pyrite can form via reactions involving both MSS and ISS and suggested that euhedral pyrite grains would form after primary magmatic chalcopyrite was introduced into the system, at temperatures below 650°C **(Figure 7-34)** (see also Dare et al., 2010).

PyT

Pyrite trails (PyT) are characterized by annealed, euhedral pyrite bands and single lenses that dominantly occur in granular pentlandite (GPnE), pentlandite trails (PnT), as well as homogenous pyrrhotite (homPo) and elongated pyrrhotite textures (EPT). Thus, euhedral pyrite (EuG) and pyrite trails (PyT) post-dated the crystallization of these pentlandite textures at <650°C (Kullerud 1963; Kelly and Vaughan, 1983; Burnham et al., 2009) and pyrrhotite textures at ~550°C to 200°C (Clark and Kelly, 1973; McDonald and Paterson, 1980). Segregation of euhedral pyrite grains to mm- and cm- scale trails that are oriented parallel to stress-induced foliation would have occurred at temperatures of <600-500°C (Burnham et al., 2009) as shown on **Figure 7-34**.

RIMS-X

Similarly, pyrite rims around silicate (RIMS-X) resemble annealed euhedral pyrite grains that have formed mm- to cm- scale rims around dominantly quartz grains that have developed subgrain boundaries, and rarely around plagioclase grains. Euhedral pyrite grains that annealed into larger polycrystalline masses and pyrite trails formed at temperatures of <600-500°C (Burnham et al., 2009) (**Figure 7-34**). As mentioned earlier, quartz can undergo dynamic recrystallization progressively over a wide range of temperatures ~850°C to 280°C (Stipp et al., 2002a, 2002b; Hirth and Tullis, 1992). Therefore, pyrite rims would have formed around quartz grains that have developed subgrain boundaries over a wide range of temperatures.

Py-Ccp-INT

Massive pyrite (MASV-Py) is dominantly composed of smaller euhedral pyrite grains that have annealed near the margins of the homogenous pyrite mass. Chalcopyrite occurs as abundant inclusions within the triple junction zones of annealed pyrite grains, as well as anhedral bleb overgrowths on the massive pyrite. The massive euhedral pyrite with annealed grain boundaries suggests that the temperature of annealing took place at approximately 650°C to >450°C (Lawrence, 1972). Anhedral blebs of pyrite intergrown with chalcopyrite overgrow pre-existing pentlandite as is supported by the remnant inclusions of pentlandite at the cores of these anhedral grains, which in turn are dominantly hosted within homogenous pyrrhotite matrix and polygonal grain boundary textured-pyrrhotite. This is a unique texture with anhedral pyrite grains resembling augen-shaped grains. Anhedral blebs would have had to originate post-pentlandite introduction at <650°C (Burnham et al., 2009; Kelly and Vaughan, 1983; Durazzo and Taylor, 1982; McQueen, 1979; Naldrett et al., 1967) and post-polygonal grain boundary and homogenous pyrrhotite texture formation <550°C (Clark and Kelly, 1973). The most interesting texture in this subgroup is the symplectic pyrite-chalcopyrite intergrowths and less commonly pyrite-pentlandite. The formation of these textures is discussed in detail in **Section 8.2.4**. However, symplectic pyrite-pentlandite is interpreted at Thompson and elsewhere to have formed at temperatures below 235°C (Craig, 1973; Misra and Fleet, 1973; Waldner and Sitte, 2008; Franchuk et al. 2016), thus it is assumed in this study that symplectites formed at similar temperatures. Furthermore, pyrrhotite, chalcopyrite, and pyrite are known to coexist at temperatures <335°C and can also coexist at temperatures of up to 420°C for bulk-sulfide compositions that contain >10 wt.% Ni (Craig and Kullerud, 1969; Lusk and Bray, 2002; Lorand and Alard, 2010). The pyrite-chalcopyrite symplectic intergrowths are spatially associated with the polycrystalline masses of annealed, euhedral pyrite grains that occur on the margins/within granular pentlandite grains. This suggests that the polycrystalline pyrite masses, overgrew pre-existing pentlandite and in turn were replaced by chalcopyrite that formed the wormy intergrowths. This texture is explained by Barton (1973) who interpreted that symplectic intergrowths between pyrite and chalcopyrite are most likely produced where intermediate solid solution (ISS) replaced polycrystalline pyrite at metamorphic temperatures of <557°C to reform back to chalcopyrite. Supporting evidence for the relative timing of pyrite and chalcopyrite are the corroded pyrite grains that are enveloped by chalcopyrite and anhedral chalcopyrite overgrowing massive pyrite. In the case of the former, the chalcopyrite has surrounded and replaced earlier formed pyrite which has lost its euhedral shape (**Figure 7-18 C**). Regarding the latter, anhedral blebs of chalcopyrite have grown on massive pyrite sections (**Figure 7-18 D**). Pyrite-chalcopyrite intergrowth textures (Py-Ccp-INT) are common in the 1D orebody and occur over a wide range of temperatures, between <600-500°C to <235°C (**Figure 7-34**).

Gb-Py

The grain boundary pyrite texture (Gb-Py) is characterized as fine-grained pyrite along pyrrhotite grain boundaries (PGBT) and at pyrrhotite grain triple junctions. Annealing of pyrrhotite grains occurred between ~550°C and 200°C (McDonald and Paterson, 1980; Clark and Kelly, 1973). Therefore, pyrite diffusion and nucleation along grain boundaries of pyrrhotite would be restricted within this temperature range, <550°C to at least 200°C (**Figure 7-34**).

ET

Pyrite exsolution textures (ET) in the form of lamellae and flames occur dominantly within a homogenous pyrrhotite matrix, pyrrhotite polygonal grain boundary texture, and elongated pyrrhotite texture. Pyrite exsolution textures are considered paragenetically-late as exsolution occurred during cooling. These exsolution textures are uncommon in literature due to the refractory nature of pyrite, especially at low temperatures. However, pyrite flames have been recorded to exsolve from pyrrhotite at temperatures as low as 325°C via supersaturation of iron (Yund and Hall, 1970) (**Figure 7-34**). However, Yund and Hall (1970) state that heterogenous nucleation of pyrite and subsequent growth by volume diffusion tends to precipitate pyrite at grain margins of pyrrhotite. Pyrite flames in the 1D deposit are not necessarily located at visible pyrrhotite grain margins, but instead are distributed across the pyrrhotite matrix.

Pyrrhotite grain boundaries may have once existed where pyrite flames were nucleated (at triple junctions and along grain boundaries) but have since homogenized with decreasing temperatures. Also, Ortega et al. (2004) documented pyrite that nucleated on pre-existing pentlandite flames that exsolved at temperatures below 200°C at the Aguablanca Ni-Cu-PGE deposit in Iberia. This could have been possible in the 1D however, remnant pentlandite has not been observed where pyrite flames currently occur.

Chalcopyrite

Euhedral pyrite grains (EuG) commonly have chalcopyrite inclusions within their cores. Chalcopyrite also dominantly occurs in adjacent low-pressure triple junction zones between annealed pyrite grains that form larger, polycrystalline masses. Both textural types of chalcopyrite suggest a relatively early formation that supports a primary magmatic paragenesis which pre-dates formation and annealing of pyrite grains. Magmatic chalcopyrite (± cubanite) is known to exsolve from ISS at temperatures below 650°C (Kullerud et al., 1969; Dutrizac, 1976; Ebel and Naldrett, 1997; Sinyakova and Kosyakov, 2009). Experimental studies by Cafagna and Jugo (2016) showed that it is possible for euhedral pyrite grains to be surrounded by, and have inclusions of chalcopyrite within their cores at temperatures of ~650°C.

Conversely, chalcopyrite has also infilled brittle fractures in silicate minerals (Qz, Bt, Pl, Grt) as well as sulfides (Po-Pn-Py-Gdf). Porous space and microfractures in pyrite grains are commonly seen infilled by chalcopyrite. Monteiro and Krstic (2006) also observed this in Thompson pyrite and attributed it to brittle modification of the ores in D_4 at ~400°C. Chalcopyrite also commonly surrounds and occurs as anhedral grains within Po-Pn-Py textures (discussed in detail in **Section 7.4.1**), specifically surrounding corroded pyrite grains (CP-envCcp) and as anhedral bleb overgrowths on massive pyrite sections. These textures would suggest a late occurrence of chalcopyrite that post-dates pyrite formation. As per Barton (1973), some chalcopyrite can be interpreted to have been formed when ISS replaced pre-existing, polycrystalline pyrite to reform back to chalcopyrite at temperatures <557°C. This could explain the intimate occurrence between pyrite-chalcopyrite, specifically in the symplectic intergrowths seen between the two sulfide minerals in the 1D orebody.

Therefore, relatively early magmatic chalcopyrite (~650°C) is commonly observed to texturally occur before the formation of pyrite. However, chalcopyrite also occurs later, post-dating pyrite and other sulfide mineral formation. Textural evidence for pyrite reforming back to chalcopyrite at lower metamorphic textures can also be argued (Barton, 1973). Therefore, chalcopyrite can form over a wide range of temperatures, but consistently below ~650°C, as is expressed in **Figure 7-34**.

Gersdorffite

Euhedral to subhedral grains of gersdorffite (Gdf) in 1D ores are usually associated with granular pentlandite and annealed polygonal pyrrhotite grains. Therefore, gersdorffite is interpreted to be paragenetically late and was the result of circulating post-peak metamorphic As- and Pd-bearing fluids that flowed through dilatant shear zone structures at Thompson (Burnham et al., 2009). Hence, gersdorffite is interpreted to have post-dated shearing in the 1D which dominantly occurred in the later stages of the transpressive regimes of D_3 to D_4 (Bleeker, 1990; Burnham et al., 2009).

Sulfide melt inclusions

Subrounded, polymetallic sulfide melt inclusions (Po>Pn>Py>Ccp>Gdf) commonly occur in metamorphic quartz, and less commonly garnet grains throughout the Thompson 1D sulfides (**Section 7.6**). The sulfide melt inclusions display an array of complex textures and are indicative of remobilized primary sulfides having partially re-melted during peak metamorphic conditions (~750˚C & 7.5 kbars; Lightfoot et al., 2017) (late D_2), and shear melting (D_3) **(Figure 7-34),** creating a sulfide melt that was trapped as inclusions during recrystallization of metamorphic silicate phases (**Section 8.5.3**).

Chapter 8: Discussion

8.1 Metal Tenor Variations; Geological Process Controls

8.1.1 Thompson 1D Structural Complexity

The Proterozoic (1.7Ga) Thompson Nickel Belt (TNB) is a collisional domain on the northwestern edge of the Archean Superior province in Northern Manitoba, Canada. Tectonism subjected the TNB rocks to polyphase deformation (D_1 – D_4) and upper amphibolite to lower granulite grade metamorphism, reaching peak P-T conditions of ~750ºC and 7.5 kbars (Bleeker, 1990; Lightfoot et al., 2017).

The TNB and specifically the 1D orebody, was known to have experienced a complex history of retrograde brittle-ductile deformation, resulting in anastomosing shear zone development and wide-scale brecciation (Bleeker, 1990; Liwanag et al., 2001; Burnham et al., 2009; Lightfoot et al., 2017). The structural complexity of the 1D orebody is evidenced by steeply dipping and foliated P_2 schist host rocks, boudinaged pegmatites, and brecciated and highly deformed sulfide mineralization (**Section 5.1**). The presence of high-strain deformation, extensional tension gashes, and large-scale shear structures in the vicinity of high nickel tenor sulfide lenses is observed in the Thompson 1D (**Section 5.2**). Additionally, numerous pegmatites were observed to have been emplaced along shear zones, which also border nickel sulfide mineralization in the 1D orebody (**Section 5.1.3**). Shearing may have created zones of dilatancy that controlled granitoid intrusions and pegmatite emplacement (Machado et al., 2011) while having increased the permeability of the rock thereby providing fluid migration pathways for remobilization of metals in the form of sulfides and sulfosalt minerals (Chen, 1993; Liwanag et al., 2001; Bailey et al., 2006).

The remobilization of primary magmatic sulfide mineralization associated with the Thompson ultramafic intrusions in the TNB is interpreted to be pre-deformation (Heaman et al., 1986, 2009; Bleeker 1990; Burnham et al., 2009; Hulbert et al., 2005; Machado et al., 2011; Lightfoot et al., 2017). Remobilization of these sulfides away from the ultramafic intrusions is interpreted to be syn- or post-D_1 (Lightfoot et al., 2017). The D_2 event involved east-west compression resulting in the folding of the Thompson nappe structure, and the transition from D_2 to D_3 involved transpression and the formation of the dome and basin morphology, doubly-plunging antiforms and synforms, and parasitic folds on the flanks of the domes (Lightfoot et al., 2017). Local shearing started in D_2, but prominent shearing occurred in the later stages of structural evolution of the TNB, during the transpressive ductile regime (D_3 to D_4), synchronous to Thompson Dome formation (Burnham et al., 2009). The 1D ore zone is modified by large-scale shear structures that are typically parallel to steeply dipping limbs of upright F_3 folds (Bleeker, 1990; Bleeker and Macek, 1996; Layton-Matthews et al., 2007); the doubly-plunging F_3 folds are also the dominant ore controlling structures (Lightfoot et al., 2017). Numerous en echelon vein sets (tension gashes) in P_2 schist wall rocks that border these shear zones are kinematic indicators of extensional processes caused by dip-slip displacement along brittle faults and shears reactivated during D_4 deformation (Bleeker, 1990).

The importance of shears, tension gashes and the overall structural complexity of the 1D orebody has been reported to be favourable for remobilization of nickel and other metals during deformation and metamorphism (Bleeker, 1990; Liwanag et al., 2011; Burnham et al., 2009), and is of major importance in exploration for larger ore bodies on the flanks of the Thompson Dome (Lightfoot et al., 2017).

8.1.2 Process Controls on Metal Tenor of Sulfide

Variability in metal contents, especially Ni-Co and platinum group elements (PGE), from various magmatic sulfide deposits across the globe (Western Australia, southern Finland, Thompson and Sudbury) has been discussed extensively in the literature (Keays et al., 1981; Bleeker, 1990; Chen, 1993; Naldrett, 1999; Heath et al., 2001; Liwanag et al., 2001; Seat et al., 2004; Stone et al., 2004; Bailey et al., 2006; Layton-Matthews et al., 2007; Collins et al., 2012; Lightfoot et al., 2017). Tenor variations in Fe-Ni-Cu-S deposits are primarily the result of magmatic processes, specifically the variability in silicate/sulfide ratio (R-factor), being the principal mechanism controlling metal distribution (Campbell and Naldrett, 1979; Naldrett, 1999; Lesher and Campbell, 1993; Lesher and Burnham, 2001). For deposits which have been heavily deformed and metamorphosed or altered in some way, tenor variations in Ni-Cu-PGE have been attributed to post-magmatic structural, hydrothermal and metamorphic processes which overprint originally primary magmatic deposits (Keays et al., 1981; Bleeker, 1990; Chen, 1993; Heath et al., 2001; Liwanag et al., 2001; Seat et al., 2004; Stone et al., 2004; Bailey et al., 2006; Layton-Matthews et al., 2007; Lightfoot et al., 2017).

Within the magmatic sulfide deposits of the TNB, the nickel tenors tend to be higher in the metasedimentary-hosted Thompson deposits (8 to 16 wt% Ni), compared to those found in many of the TNB deposits. For example, the ultramafic-hosted Pipe and Birchtree deposits are lower in nickel tenor (4 to 8 wt% Ni; House, 2009; Lightfoot et al., 2017); whereas the intrusions of the South Manasan deposit have a much higher range in nickel tenor (10 to 39 wt% Ni; Franchuk et al., 2016) relative to the Thompson Deposit.

The Ni tenor of sulfide in the 1D orebody is highly variable, ranging from massive sulfides that are barren of Ni (<200 ppm), to sulfides that are highly nickeliferous (>16 wt% Ni in 100% sulfide) (**Section 5.3.1** and **5.4.2**). The majority of sulfides are hosted by meta-sedimentary rocks rather than ultramafic boudins. The 1D also shows some of the highest Ni/Co (82), Pd/Ir (18), Se/S (0.97) ratios and elevated Pd, Bi, and locally high As values compared to other orebodies within the TNB (Liwanag et al., 2001; Burnham et al., 2009).

Significant concentrations of arsenic are present in Thompson ores due to late-paragenetic phases such as gersdorffite, niccolite and As-bearing pyrite (Bleeker, 1990; Chen, 1993; Liwanag et al., 2001; Franchuk et al., 2016; Lightfoot et al., 2017; this study). Bleeker (1990) indicated anomalously high arsenic concentrations from the Thompson deposit, with >1000 ppm As possible in samples. Burnham et al. (2009) reported high mean arsenic concentrations of samples in the 1D orebody (411-510 ppm), compared to samples from the 1C (34-97 ppm), T1 (13-114 ppm) and Birchtree

(8-96 ppm) deposits. The arsenic concentrations of 1D ore samples in this study are slightly lower, on average 141 ppm As, with up to ~400 ppm As in some samples (**Section 5.4.2**). Therefore, arsenic measurements are quite low in most ores, with locally higher concentrations possible due to concentration of paragenetically-late As-bearing phases (Bleeker, 1990; Burnham et al., 2009). Bismuth contents of ores were not analyzed in this study, but previous work by Burnham et al. (2009) indicates that the 1D ores have higher Bi values (28-41 ppm), than 1C (1-5 ppm), T1 (4-6 ppm) and Birchtree ores (<2 ppm).

Burnham et al. (2009) also indicates that 1D ores have higher Pd contents (1162-2173 ppb), than in 1C (259-977 ppb), T1 (140-942 ppb), and Birchtree (20-143 ppb) ores. Burnham et al. (2009) also reports an average of 133 ppb Pt for Thompson 1D (T3) ore samples. Bleeker (1990) reported 1421 ppb Pd and 708 ppb Pt from nickel sulfide ores (ore type I) within altered metapelite host rocks from T3 mine. Bleeker (1990) also reported 2738 ppb Pd and 1245 ppb Pt from interstitial sulfides around ultramafic boudins in T1 mine. Lightfoot et al. (2017) reported mean compositional data for semi-massive and massive sulfide types in the 1D orebody to be 1500 ppb Pd and 680 ppb Pt (normalized to 100% sulfide). Lightfoot et al. (2017) also reported a wide range of Ni/Co ratios for ore samples from the Thompson deposit, with strong clusters at Ni/Co=48 and a larger cluster from 70-100. This study indicates a Ni/Co ratio of 79 for underground sulfide ores from the 1D (**Figure 7-24**), which agrees with a Ni/Co ratio (82) from Liwanag et al. (2001) and Burnham et al. (2009), as well as a pentlandite-rich Ni/Co trend outlined by Lightfoot et al. (2017).

Platinum group elements (PGE) were not the focus of this study. However, from 78 underground ore samples from the 1D, the mean Pd and Pt tenors (normalized to 100% sulfide) in this study are 2475 ppb and 1200 ppb, respectively (**Section 5.4.2**). The Pd/Pt ratio is 55 (this study), therefore we acknowledge several very high-grade Pt samples have skewed the Pt average, although Pd values stay consistently high. A correlation between Ni (%) and Pd (ppm) exists **(Figure 5-6)**. Burnham et al. (2009) reported a similar positive correlation between Pd-Ni, along with Ni-As and to a lesser extent Ni-Bi of 1D ores. The mean Pd/Pt ratio of 1D ores (55) in this study are slightly lower but comparable to the mean Pd/Pt ratios of 1D (93), 1C (30), T1 (51) and Birchtree (24) deposits reported by Burnham et al. (2009). Thompson ores have been reported to show a Pt-depletion anomaly which was thought to be related to the Cu-poor nature of the deposits (Liwanag et al., 2001; Burnham et al., 2009), as Pt tends to fractionate into a Cu-rich liquid and thus would be concentrated in Cu-bearing sulfides like chalcopyrite and cubanite (Chyi and Crocket 1976). The data in this study shows that there are highly variable metal and metalloid contents (Ni, Co, Pt, Pd, Bi, As) across various Thompson deposits, with the Thompson 1D orebody (T3) showing consistently high contents of Pd than previously recorded, and localized high-grade Pt concentrations.

8.1.3 Highest Ni, Co, Pd Tenors in Shear-Hosted Sulfides

Underground mapping of mineralized stopes identified five main styles of sulfide mineralization: massive, semi-massive, concordant, ultramafic-associated and shear-hosted (**Section 5.2.1**). Geochemical whole rock assay data from underground samples of the various sulfide styles revealed that the shear-hosted mineralization has the highest whole rock Ni (mean 12.8 wt%) and Co tenors (mean 1680 ppm) (**Figure 7-24**), as well as some of the highest Pd tenors (mean 3375 ppb) in the 1D orebody (**Appendix 3**). In contrast, the massive mineralization style has the lowest and most variable whole rock Ni (mean 6.66 wt%), Co (mean 846 ppm) (**Figure 7-24**) and Pd tenors (mean 1660 ppb) (**Appendix 3**). This can partly be attributed to the presence of massive sulfide lenses barren of nickel (**Section 5.1.3**), but also to the presence of massive sulfide bodies that have lower nickel tenors (**Figure 7-24**). The highest nickel tenor sulfide lenses in the 1D tend to occur along the limbs of doubly-plunging F_3 folds versus the fold hinges, in contact with large-scale shear structures (**Section 5.1.4**). The genesis of these coexisting heterogenous sulfide lenses, as observed in this study of the Thompson 1D, can possibly be explained by a ductile translocation process (Monteiro and Krstic, 2006; Lightfoot et al., 2017) (**Section 5.1.4**). Tenor variations are homogenous along a vein, but distinctly heterogenous between different sulfide lenses, as depicted by deposit-scale studies of the Thompson 1D orebody from Lightfoot et al. (2017). Although, possible evidence of Ni tenor gradations along an individual sulfide lens have been speculated at the scale of the stope (this study; **Section 5.1.4**). The highest tenor sulfide packages are shown to be stacked in F_3 fold noses and extending up- and down-dip on limbs of the F_3 folds, along the flank of the Thompson Dome structure (Lightfoot et al., 2017). From underground observations in this study of the Thompson 1D (**Section 5.1.4**), similar observations are drawn in that the highest tenors observed were adjacent to shear structures running along the limbs and structural trend of F_3 folds, less so in the fold hinges (**Section 5.1.4**; **Table 5-1**).

The importance of shears in the 1D orebody for possible remobilization of nickel and other metals during deformation and metamorphism has been documented previously (Bleeker, 1990; Chen, 1993; Burnham et al., 2009; Liwanag et al., 2001; Lightfoot et al., 2017). Variations in nickel tenor have been correlated to intensity of deformation, metamorphism and high strain zones in several Ni deposits at Kambalda, Western Australia (Heath et al., 2001; Seat et al., 2004) and at the Thayer Lindsley deposit in Sudbury, Ontario (Bailey et al., 2006). The data in this report agrees with the above studies and provides additional evidence for an intricate link between the highest Ni and Co tenors in shear-hosted, the most structurally-controlled sulfides in the 1D orebody (**Figure 7-24**). Therefore, this study agrees with Liwanag et al. (2001) and Burnham et al. (2009), in that elevated concentrations of Ni, Co, Pd, Pt, and As of the Thompson 1D orebody suggests the most structurally controlled and heavily deformed deposits of the TNB, specifically those containing abundant shear zones and tension gashes, are most likely to possess some of the highest nickel tenor ores. However, this statement cannot be extrapolated to the whole TNB, as Franchuck et al. (2016) has demonstrated exceptionally high nickel tenor (28 - 39 wt% Ni) and PGE tenor (21 - 28 g/t) in the primary ultramafic-hosted sulfide mineralization of the South Manasan deposit.

8.2 Relationship Between Metal Tenor and Petrographic Observations

8.2.1 Paragenetically Late Pyrite

It has been well documented that the sulfidation of pyrrhotite to form pyrite by late, fluid-assisted replacement processes are common, e.g., the Lac des Iles Pd deposits, Ontario (Duran et al., 2015, 2016), Aguablanca Ni-Cu sulfide deposit, Spain (Pina et al., 2013), and the Great Dyke PGE deposit, Zimbabwe (Pina et al., 2016). Heath et al. (2001) and Stone et al. (2004) reported late, secondary pyrite in several nickel sulfide deposits from the Kambalda ore field in Western Australia. However, as will be discussed in **Section 8.5.1**, most Archean komatiite-associated nickel sulfide deposits from the Kambalda region show metamorphic replacement of pyrrhotite by pyrite via the introduction of oxidising fluids during peak metamorphic conditions. Paragenetically late pyrite that formed from metamorphically remobilized fluids, has also been recorded in the Thayer Lindsley Ni-Cu-PGE deposit in Sudbury (Bailey et al., 2006) and the Flying Fox Ni-Cu-PGE deposit in Western Australia (Collins et al., 2012). The former is similar to the Thompson 1D, in that both report between 5- 10 modal % pyrite in their sheared massive sulfide ores and that the occurrence of pyrite is paragenetically late, having formed as a retrograde alteration product of pyrrhotite.

This study classified pyrite into seven distinct textural types (**Section 7.3.1**). Textural observations from this study indicate that there is some evidence of pyrite having replaced pentlandite, along with the more commonly observed sulfidation of pyrrhotite by pyrite (**Section 8.5.2**). The former is dominantly evidenced by remnant pentlandite that occurs within pyrite porphyroblasts (**Figure 7-25 E,G,H**) and more commonly, remnant pentlandite within symplectic intergrowths of pyrite-chalcopyrite grains (**Figure 7-27 D**). However, the significance of pyrite forming at the expense of pentlandite is not known at this time. The common replacement of pyrrhotite by pyrite is evidenced by: sub- to euhedral porphyroblasts of pyrite that have overprinted both annealed pyrrhotite and pentlandite grains (**Figure 7-17 A, D; Figure 7-25 A,C,D,G**); pyrite filled fractures and have precipitated between pyrrhotite grain boundaries (**Figure 7-17 E**); pyrite overgrowths as rims on silicates (**Figure 7-17 F**); pyrite flames exsolved from pyrrhotite (**Figure 7-17 C; Figure 7-26**); and pyrite involved in complex symplectites (**Figure 7-27**).

Textural relationships between pyrite and other sulfide minerals at 1D are indicative of a complex paragenesis. However, available petrographical evidence points toward pyrite porphyroblasts being paragenetically-late, having formed within the retrograde metamorphic realm (D_3 to D_4) (**Section 7.3**), as is also reported elsewhere for the Thompson deposits (Bleeker, 1990) and more specifically the Thompson 1D ores (Liwanag et al., 2001; Burnham et al., 2009; this study). Pyrite formed during a late-stage high sulfur fugacity event and is interpreted to be secondary/hydrothermal in origin at Thompson (**Section 8.2.2**).

8.2.2 Evidence for Paragenetically Late Ni, Co and Pd-Bismuth telluride Fluids

This study observed strong cobalt, and less commonly nickel zoning, in pyrite grains from the 1D deposit (**Section 7.3.4**). In WDS maps, cobalt- and to a lesser extent nickel-highs, occur along fractures and grain boundaries in pyrite grains (**Figure 7-25 F, H**), indicating that cobalt and nickel could have been mobile elements during deformation. In addition to the seven textural types of pyrite described in **Section 7.3.1**., there are four key geochemical observations of pyrite grains: 1) an early stage of growth defined by nickel-rich and cobalt-poor cores, that were overgrown by cobalt-rich rims (**Figure 7-25 B, C, D, H**); 2) pyrite grains with cobalt- and nickel-poor cores, with nickel-rich outer cores that were overgrown by cobalt-rich rims (**Figure 7-25 E, F, G**); 3) a dominant late-stage pyrite growth formed homogeneously from a cobalt-rich fluid (**Figure 7-25 A**), which also includes generation of all pyrite flames (**Figure 7-26**); and 4) a late-stage pyrite growth that formed symplectic intergrowths with chalcopyrite and pentlandite (**Figure 7-27**).

In conclusion, pyrite paragenesis in the 1D ores is complex. But a commonality between all seven pyrite textural types is that prominent cobalt-rich overgrowths occur on sub-euhedral pyrite and gersdorffite grains from the 1D ores (**Figure 7-25 A, C, F; 7-31**). Additionally, a late-stage (D_4), cobalt-rich pyrite has overgrown and modified an earlier, complexly-zoned pyrite-type (possibly early D_3) (**Figure 7-25 C, D, G**). Pyrite in the 1D orebody dominantly occurs as sub- to euhedral pyrite grains that show a textural and geochemical make-up consistent with an influx of a paragenetically-late, cobalt-rich fluid during the later stages of deformation (D_3 – D_4).

Preservation of complex cobalt and nickel growth zones in pyrite is caused by fast growth and very slow element diffusion rates in pyrite (Cafagna and Jugo, 2016). The growth zones of pyrite could be evidence for sequential removal of nickel and cobalt from a cooling MSS during late-pyrite growth, which could be consistent with a primary magmatic origin for pyrite (Cafagna and Jugo, 2016). Pyrite with weak nickel- but strong cobalt-growth zones, along with late-stage cobalt-rims on grains has been reported at the Craig Ni-Cu-PGE Deposit in Sudbury (Craig and Solberg, 1999). Craig and Solberg (1999) interpret that the growth zones in pyrite are evidence for sequential removal of nickel and cobalt from the host MSS during its contraction as the ores cooled, thus providing a possible primary magmatic signal for pyrite zonation.

However, at other Ni-Cu sulfide and PGE deposits, zoning in pyrite is interpreted to be related to late fluid-assisted replacement of pyrrhotite by pyrite (Collins et al., 2012; Pina et al., 2013, 2016; Duran et al., 2015, 2016). Duran et al. (2015) reported concentric oscillatory zoning and enrichment of pyrite in Co, Rh and IPGE from the Lac des Iles Pd deposits. Duran et al. (2015) concluded that pyrrhotite was converted to pyrite via mineral replacement reactions - that involved fluid-assisted solid-state diffusion processes between pyrite grains and surrounding pentlandite ± pyrrhotite, which led to pyrite enrichment and zoning patterns. Collins et al. (2012) reports the addition of pyrite (1-40 modal %) to the sulfide ores at the Flying Fox Ni-Cu-PGE deposit, cannot be explained by magmatic processes but instead to be a result of circulating Fe-, S-, Cu- and As-enriched fluids syn- to post-peak metamorphism (D_1 – D_3) during deformation of the massive sulfide ore.

Paragenetically late Ni, Co and PGE fluid mobilization in ore zones (**Section 8.5.2**) has been reported in previous studies in the TNB (Bleeker, 1990; Liwanag et al., 2001; Burnham et al., 2009; Layton-Matthews et al., 2007). Mineral chemical data presented by Burnham et al. (2009) indicated that cobalt moved out of pentlandite and into pyrite, and that nickel moved out of pyrite and pyrrhotite into pentlandite during deformation and sulfidation of Thompson ores. Elevated Pd, Bi, As concentrations in the Thompson 1D ores, are contained in Pd-bearing bismuth tellurides that were introduced into the ores during the later stages of deformation and metamorphism. This also resulted in precipitation of paragenetically late phases of sub- to euhedral gersdorffite, niccolite and As-bearing pyrite amongst annealed pyrrhotite and pentlandite (Liwanag et al., 2001; Burnham et al., 2009). Cobalt, nickel and arsenic enriched pyrite (**Section 8.3.2**) along with paragenetically late phases of gersdorffite and niccolite indicate that PGEs and semi-metals were more mobile in the MSS and/or were introduced during fluid assisted alteration of the 1D ores (Liwanag et al., 2001; Burnham et al., 2009).

In conclusion, pyrite paragenesis in the Thompson 1D ores is complex, but evidence points towards a dominantly secondary/hydrothermal origin for pyrite. In addition, a minor pyrite phase also occurs as complexly-zoned, earlier formed pyrite grains (D_3) that have since been modified by later secondary/hydrothermal pyrite (D_4).

8.2.3 Positive Correlation Between Py Abundance and Ni, Co Tenor

This study found that ore samples with elevated modal abundances of pyrite also have the highest nickel and cobalt tenors in the 1D orebody (**Section 7.3.3**; specifically **Figures 7-21, 7-22, 7-24**). This was not previously known in the Thompson ores, nor recorded for other TNB deposits. A comparison of the five main mineralization styles identified from underground mapping (**Section 5.4.1**) of dominantly the 1D Lower (3700 to 4160 levels), showed that shear-hosted styles contained the highest pyrite modal abundances (8.5%), and massive styles had the lowest pyrite modal abundances

(3.2%) (**Figure 7-23**). It was found that ore samples from shear-hosted styles had the highest whole rock nickel, cobalt and palladium tenors (**Section 8.1.3**), and ore samples from massive styles had the lowest and most variable nickel, cobalt and palladium tenors (**Figure 5-3**). Overall, there is a positive dependence of whole rock nickel and cobalt tenor on pyrite modal abundance, thus the control of pyrite is important in the genesis of the mineralization.

Increased abundances of pyrite have been correlated with higher nickel tenors in several Kambalda Ni-Cu-PGE deposits in Western Australia:

Heath et al. (2001) states that higher nickel tenors in the Edwards lode orebody in Western Australia are related to increased abundances of metamorphic pyrite. The study proposes that variations in nickel tenor are a result of intra-orebody redistributions of nickel and sulfidation of the ores during upper-greenschist to lower-amphibolite facies metamorphism. That study provides evidence for an increase of pentlandite abundance (46.6 ± 1.6 wt%) being correlated with an increase in secondary pyrite abundance (27.7 ± 11 wt%), both of which are more abundant than pyrrhotite (22.3 ± 10.9 wt%). The Edwards lode orebody has 5x greater proportions of pyrite compared to the 1D orebody, but similar sulfidation and redistribution processes could have been at play at Thompson.

Stone et al. (2004) conducted a study of ore samples from 14 different nickel sulfide deposits throughout the Western Australian Kambalda ore fields and concluded that nickel tenors are very heterogeneous. The study concluded that pyrite was a major sulfide mineral, particularly of high tenor deposits, and that the bulk of pyrite was secondary rather than primary in origin. They further concluded that pyrrhotite was replaced by metamorphic pyrite + magnetite + chlorite during the ingress of oxidizing fluids that reduced the abundance of pyrrhotite relative to pentlandite and increased the Ni + PGE tenors of the residual sulfides.

By contrast a lack of correlation between pyrite and high nickel tenor ores has also been proposed in several Kambalda deposits: Keays et al. (1981) reported an inverse relationship between pyrite abundance and high tenor ores at the Lunnon Shoot, Kambalda Nickel mine in Western, Australia. They proposed that syn-metamorphic removal of sulfur from matrix ores and addition of S-bearing fluids into thermally contracted and permeable massive ores (Seccombe et al., 1981), resulted in an increased pyrite abundance in the massive ores and higher tenors in the matrix ores.

Seat et al. (2004) also proposed a lack of correlation between pyrite and nickel tenor in the N02 orebody at the Ni-sulfide Wannaway deposit in Western Australia. The nickel tenor of the massive ores of the N02 orebody is highly variable, with the lowest tenor massive sulfides occurring in the most structurally complex parts of the deposit (Seat et al., 2004), which is opposite of that observed in the Thompson 1D. Seat et al. (2004) interpreted that the lack of correlation between pyrite and nickel tenor is inconsistent with the metamorphic sulfidation model, and instead proposes that the variability of nickel tenor of massive ores is a result of relocation of Ni-poor MSS along faults during ductile deformation and metamorphism of heterogenous ores; this mechanical relocation process is also proposed by Monteiro and Krstic (2006) and Lightfoot et al. (2017) for the Thompson ores (**Section 8.4.2**).

In summary, Keays et al. (1981) and Seat et al. (2004) propose that there is a lack of correlation between pyrite and high tenor sulfide at the Lunnon Shoot and

Wannaway deposits in Kambalda. This contrasts with Thompson 1D observations, where increased pyrite abundances are strongly correlated with the highest nickel and cobalt tenor ores in the deposit, as is similarly documented by Heath et al. (2001) and Stone et al. (2004) for several nickel-sulfide deposits in Kambalda. However, similar syn-metamorphic processes of redistribution, fluid-assisted alteration and sulfidation presented by Keays et al. (1981), Heath et al. (2001) and Seat et al. (2004), could have produced the nickel tenor variations seen in the Thompson 1D deposit (**Section 8.7.2**). Although, Stone et al. (2004) agrees with a correlation between pyrite abundance and high nickel tenors at several Kambalda deposits, where mineralization is closely related to ultramafic bodies, the oxidation model he proposes may fall short in explaining tenor variation at Thompson, due to the lack of significant amounts of Fe-oxide (**Section 8.7.1**) and minimal presence of local ultramafic bodies (**Section 3.3**).

8.2.4 Metamorphic and Deformation Textures in the 1D Ores

The Thompson 1D deposit shows features typical of metamorphosed sulfide ores, such as recrystallization, remobilization, deformation, alignment and annealing. However, there is no apparent link between these textures and nickel tenor. The pyrrhotite polygonal grain boundary texture (PGBT) and elongated pyrrhotite texture (EPT) commonly occur in the sulfide ores (**Section 7.1.1**). Monteiro and Krstic (2006) interpret the former as the formation of complex ‘kink bands’ in pyrrhotite, and the latter as pyrrhotite subgrains formed during grain boundary migration in a differential stress-free environment. Both textures attesting to strong ductile deformation recorded by pyrrhotite. The pentlandite trail (**Figure 7-8 B**) and pyrite trail (**Figure 7-17 D**) textures, along with annealed pyrite masses (**Figure 7-25 F**) are interpreted in this study to have been generated syn- to post-peak metamorphism due to the localized alignment of pentlandite grains.

In this study, symplectic ‘wormy’ intergrowths of pyrite-chalcopyrite (Py-Ccp) and to a lesser extent pyrite-pentlandite (Py-Pn), are common in the 1D sulfide samples (**Section 7.3.1**). Pyrite-chalcopyrite symplectic intergrowths have also been reported for Thompson ores by Liwanag et al. (2001) and Burnham et al. (2009); as well as in Western Australian Ni-sulfide ores (Barrett et al., 1977; McQueen, 1981, 1987; Collins et al., 2012). McQueen (1987) stated that preservation of symplectic intergrowths indicate that they likely post-date intense peak metamorphic conditions and thus are post-magmatic in origin. Liwanag et al. (2001) reported the presence of pyrite-chalcopyrite symplectites in the Thompson 1D ores and Burnham et al. (2009) stated that pyrite-chalcopyrite symplectic intergrowths do occur within sulfide ores of the TNB. Both Liwanag et al. (2001) and Burnham et al. (2009) proposed that pyrite-chalcopyrite symplectites are likely formed by chalcopyrite-rich areas that reformed back to pyrite + intermediate solid-solution (ISS) or a Cu-rich ISS that formed out of metamorphic mono-sulfide solution (MSS); chalcopyrite may have then been reformed at lower, retrograde metamorphic temperatures from reaction of ISS with pyrite (Craig & Kullerud, 1969; Barrett et al., 1977).

Franchuk et al. (2016) documented pyrite-pentlandite symplectic intergrowths in sulfides from the South Manasan ultramafic intrusion of the TNB and interpreted them as a low temperature (<235 °C) primary magmatic sulfide assemblage. The experimental study of Mavrogenes et al. (2001) produced myrmekitic intergrowth textures between various sulfide assemblages from rapidly quenching sulfide melts, that very closely resemble symplectic intergrowth textures observed in this study of the Thompson 1D. Frost et al. (2002) also showed that sulfide melts can quench to form complex sulfide mineral intergrowths, which tend to re-equilibrate at very low temperatures, and as a result, sulfide melts are rarely preserved (McQueen, 1987). Therefore, the symplectic intergrowth textures between pyrite-chalcopyrite and pyrite-pentlandite are interpreted in this study as rapid-growth textures indicative of metamorphism or possible sulfide melting (**Section 8.5.3**). However, post-magmatic, Fe-S-Cu-As hydrothermal circulating fluids were interpreted to be responsible for the addition of secondary pyrite creating pyrite-pentlandite intergrowths observed in the sulfide ores at the Flying Fox Ni-Cu-PGE deposit in Western Australia (Collins et al., 2012). There is a lack of consensus on the origin of these symplectic intergrowth textures, being interpreted as; metamorphic MSS-ISS (Craig & Kullerud, 1969; Barrett et al., 1977; Liwanag et al., 2001; Burnham et al., 2009); primary magmatic (Franchuk et al., 2016); product of partial melting (Mavrogenes et al., 2001; Frost et al., 2002); or generated from hydrothermal circulating fluids (Collins et al., 2012). All these hypotheses are plausible explanations for the textures observed in this study.

Furthermore, pyrite-chalcopyrite anhedral blebs (**Figure 7-18 B; 7-25 E**) are interpreted as possible segregations of remnant pentlandite grains overgrown by an assemblage of dominantly pyrite + chalcopyrite. The possibility of pyrite forming at the expense of pentlandite in 1D sulfide ores was discussed in **Section 8.2.1**, but it is not possible to conclude the significance of this texture. Burnham et al. (2009) states that pyrite overgrowth textures are quite common in Thompson ores and suggested that a high sulfidation event occurred syn- to post-deformation, after pentlandite had exsolved from MSS. However, the complex pyrite-chalcopyrite anhedral blebs could also be interpreted as possible ‘partial melt’ textures (Mavrogenes et al., 2001; Frost et al., 2002) that are hosted within a dominant pyrrhotite matrix (**Section 8.5.3**). A third alternative is that the anhedral blebs formed from Fe- and S-saturated hydrothermal fluids, which resulted in late-pyrite growth in ores, as reported by Collins et al. (2012).

In addition to the unique array of post-magmatic textures observed in the Thompson 1D ores, pyrite flames are also common, as exsolution lamellae in pyrrhotite (**Figures 7-17 C; 7-26**). Pyrite flames are uncommon in sulfide ores and have not been previously reported in any TNB deposits. However, Yund and Hall (1970) state that pyrite exsolution from pyrrhotite can occur via volume diffusion at 325°C due to supersaturation of iron in pyrrhotite. Collins et al. (2012) theory of Fe- and S-saturated circulating hydrothermal fluids could also support Yund and Halls (1970) Fe-supersaturation theory, resulting in exsolution of pyrite flames. Electron microprobe analyses indicate that the pyrite flames are cobalt-rich (**Figure 7-26**), with 1.5 – 2.0 wt% Co (**Section 7.3.4**). The implied presence of a cobalt-rich fluid during exsolution is consistent with paragenetically-late, Co-rich pyrite and gersdorffite grains in the 1D ores, as discussed earlier in **Section 8.2.2**.

Section 7.7 summarizes the paragenetic sequence for all sulfide textures observed in the Thompson 1D (this study). In this paragenesis, every sulfide texture is linked to a late-prograde or retrograde realm, and there is nothing left of a magmatic source type material **(Figure 7-34).**

8.2.5 Sulfide Melt Inclusions

This study is the first to provide direct evidence for the existence of a post-emplacement sulfide melt at Thompson. Polymetallic sulfide melt inclusions (Po>Pn>Py>Ccp>Gdf) commonly occur in metamorphic quartz, and less commonly garnet grains throughout the Thompson 1D sulfides (**Section 7.6**). The sulfide melt inclusions are rich in nickel and cobalt, and display an array of complex textures: wormy symplectic intergrowths of pyrite-pentlandite and less commonly pyrite-chalcopyrite, anhedral blebs of pyrite, and both pentlandite and pyrite exsolution lamellae and flames (**Figures 7-32, 7-33**).

Bleeker (1990) reported inclusion-rich cores and inclusion-poor outer rims within garnet grains in Thompson ores. Garnet cores have yielded consistent prograde metamorphic temperature of ~600 ± 50°C and pressure of 5.5 ± 1 kbar at Thompson (Burnham et al., 2009). Bleeker (1990) also notes that garnets are compositionally unzoned, which is attributed to diffusive homogenization of originally zoned garnets at peak-metamorphic conditions. Similarly, X-ray mapping conducted in this study reports very subtle Mn and Mg zoning in silicate-hosted garnet grains (**Section 6.2.3**), all other element maps of garnet were homogenous and did not show zoning of any sort. Additionally, the dominant garnet end member in the Thompson 1D orebody is almandine (Fe-rich) (**Section 6.2.2**). The sulfide melt inclusions in this study are observed within the cores of garnet grains suspended in/around sulfide ore and are interpreted to have been trapped syn-garnet growth (pre- to syn- D_2). It is also important to note that from 13 observed thin section samples where sulfide melt inclusions occur, the mean whole rock nickel (wt%) and cobalt (ppm) tenor of the ore samples were; 10.9 wt% Ni and 1573 ppm Co (**Section 7.6.2**). Interestingly, petrographical and whole rock data observations indicate that sulfide ore samples with modal abundances of >5% garnet in thin sections were reported to have high whole rock nickel tenors (>8%) (**Section 6.2**). Therefore, from the small sample size it can be interpreted that sulfide melt inclusions occur in sulfide ore samples with high tenors.

Furthermore, sulfide melt inclusions within metamorphic quartz are concentrated in areas that have experienced grain-size reduction and recrystallization, as opposed to non-deformed quartz grains. As mentioned in **Section 7.7**, quartz can undergo dynamic recrystallization progressively over a wide range of temperatures (~850°C to 280°C) (Hirth and Tullis, 1992; Stipp et al., 2002a, 2002b). Therefore, it is not possible to determine the exact temperatures at which dynamic recrystallization occurred. Interpretations from cathodoluminescence maps (**Section 6.3.1**) of metamorphosed quartz grains indicate that sulfide melt inclusions are relatively old, trapped within an earlier stage of quartz and overgrown by a later generation. This later generation of quartz post-dates sulfide melt inclusion entrapment and is associated with metamorphic graphite and biotite growth.

These timing relationships indicate that the sulfide melt would have been trapped syn-quartz and garnet growth (syn- D_2) and are linked to a dynamic recrystallization process that could have happened over a wide range of temperatures and pressures (D_2 – D_4). Therefore, it is possible that sulfide melt inclusions could have been trapped in quartz grains that had already experienced grain-size reduction. This implies that a sulfide liquid could have preferentially migrated into pre-existing grain-size reduced quartz grains during peak (late D_2) to post-peak metamorphism.

The sulfide melt inclusions were not the focus of this thesis. Further work needs to be done in order to determine if trapped sulfides are either, primary or secondary compositions. Sulfide inclusions trapped coevally with growth of host minerals are termed primary, whereas sulfide inclusions trapped after the dominant host mineral has crystallized, via melt infiltration through fractures, would be termed secondary inclusions (Roedder, 1984). Whether primary or secondary, a sulfide melt would have been present during the entrapment process in host silicate assemblages. It is proposed here that the sulfide melt inclusions at the Thompson 1D indicate that sulfides may have partially re-melted during peak metamorphic conditions (late D_2), creating a sulfide melt that was trapped as inclusions during recrystallization of metamorphic silicate phases (**Section 8.5.3**).

Numerous examples of multiphase sulfide melt inclusions hosted within high temperature gangue minerals, garnet and biotite, have been recorded in other deposit types, including the Broken Hill-type Pb-Zn-Cu-Ag massive sulfide deposits in Australia as well as at Aggeneys, South Africa (Bailie and Reid, 2005). Bailie and Reid (2005) report sulfide melt inclusions within garnet grains in Broken Hill, South Africa ores that very closely resemble sulfide melt inclusions from this study **(Section 7.6.1).** Bailie and Reid (2005) propose these sulfide melt inclusions are a result of partial melting of the sulfides which could have played a role in upgrading the ores. Similarly, abundant sulfide melt inclusions within garnetite and quartz veins surrounding remobilized ore have been reported in the Pb-Zn-Ag sulfide deposits of Broken Hill (Sparks and

Mavrogenes, 2004; 2005). Broken Hill ore bodies are hosted within highly deformed and metamorphosed Proterozoic metasediments and metavolcanic rocks (Stevens et al., 1988). Sulfide melt inclusions are evidence that partial melting occurred in the highly metamorphosed portions of the Broken Hill deposit (Sparks and Mavrogenes, 2004; 2005). Hofmann (1994) and Hofmann and Knill (1996) reported polyphase sulfide melt inclusions trapped in quartz at the sulfosalt-rich dolomite deposits of Lengenbach, Switzerland, as a result of partial melting during metamorphism. Both Pb-Zn Broken Hill deposits of South Africa and Australia, as well as the Dolomite deposits of Lengenbach Switzerland, report strong enrichment of low-melting point chalcophile elements in the sulfide melt inclusions.

Additionally, the metamorphosed Challenger Au deposit in South Australia also reports polyphase sulfide melt inclusions in peak metamorphic garnet and other silicates (Tomkins and Mavrogenes, 2002). Polyphase sulfide melt inclusions hosted within apatite, plagioclase, olivine and ilmenite have also been reported in the magmatic Ni-Cu-PGE mineralization of the Caribou Lake Gabbro in Northwest Territories (Neyedley et al., 2019). The polyphase sulfide melt inclusions reported by Neyedley et al. (2019) draw comparisons to ones reported in this study **(Section 7.6.1).**

8.3 Geochemistry of Minerals and Relationship to Sulfide Metal Tenor

8.3.1 Mica Geochemistry

Nickel contents of the Pipe Formation, P_2 member pelitic schists near sulfide horizons versus barren sulfide horizons of the TNB were compared in **Section 5.1.1**. The P_2 pelitic schist samples from sulfide barren regional drill holes contained an average whole rock nickel content of 54 ppm. Whereas P_2 pelitic schist samples taken within 5-10m of a sulfide horizon in the 602 ore complex (1D Lower; 3700 to 4160 levels) contained average whole rock nickel values of 178 ppm. Studies of TNB deposits by Burnham et al. (2009) reported that pelitic schists and silicate-facies iron-formations in the Pipe Formation normally contain <75 ppm Ni, whereas sulfide-facies iron-formations contain up to 250 ppm Ni. This study reports slightly higher whole rock nickel contents in P_2 pelitic schist samples near sulfide horizons, whereas distal P_2 pelitic schist samples in sulfide barren zones have comparable whole rock nickel values as reported by Burnham et al. (2009).

Detailed geochemical analyses of biotite laths hosted within 1D sulfide show elevated average nickel and chromium contents, 0.24 and 0.48 wt %, respectively (**Section 6.1.2; Fig. 6-5**). Whereas biotite grains in neighbouring pelitic schists (up to 4.0 metres away from a sulfide horizon) have averages of 0.06 wt% nickel and 0.05 wt% chromium (**Section 6.1.2; Fig. 6-5**). Chromium contents in P_2 schist-hosted biotite fall off strongly beyond 0.5 metres from the sulfide ore contact, whereas nickel contents in P_2 schist-hosted biotite stay elevated up to 2.0 metres within the sulfide ore contact but fall off sharply beyond that (**Figure 6-5**). This study reports elevated nickel and chromium contents in biotite grains hosted within 1D sulfides compared to biotite grains in neighbouring pelitic schists, which has not been documented before. Given the limited size of the anomalous Ni-Cr zone, biotite could potentially be a useful indicator of proximity to a sulfide lens. Future work is needed to address how nickel tenor of the ores may be affected by elevated nickel concentrations in mica and the possible geometallurgical issues that ensue.

8.3.2 Sulfide Geochemistry

The compositions of pyrrhotite (**Table 7-1**), pentlandite (**Table 7-2**), pyrite (**Table 7-4**), chalcopyrite (**Table 7-5**), gersdorffite (**Table 7-6**), also these minerals within sulfide melt inclusions (**Table 7-7**), in the 1D orebody were summarized in Chapter 7. The discussion below focuses on comparing these compositions with other Ni-Cu-PGE deposits in Western Australia, Sudbury and within the TNB.

Western Australia: Donaldson & Bromley (1981) reported a mean of 0.2 wt.% Ni in typical pyrite from Western Australia and Collins et al. (2012) reported 0.5 ± 0.4 wt% Ni in pyrite from Flying Fox. Whereas the cobalt contents of pyrite in Western Australia ranged from below 0.1 wt% Co (Donaldson and Bromley, 1981) to 0.5 – 1.3 wt % Co (Porter and McKay, 1981; Collins et al. 2012). Flying Fox contains pentlandite with 36.3 ± 1.2 wt% Ni and 0.2 ± 0.4 wt% Co, all reported to 2σ (Collins et al., 2012). The Ni and Co values of pyrite and pentlandite from Western Australian are similar to those in the Thompson 1D orebody pyrite (1.1 ± 3.8 wt% Ni and 1.3 ± 1.9 wt% Co in 2σ) and pentlandite (35.3 ± 1.94 wt% Ni and 0.34 ± 0.23 wt% Co in 2σ), however the 1D orebody shows slightly higher Ni and Co values in pyrite.

Sudbury: Hawley (1962) reported a rare nickeloan pyrite with 5-6 wt% Ni at the Worthington, Foy and Milnet deposits. High nickel contents in pyrite, 2.5 wt% Ni, are reported at Creighton ores in Sudbury (Dare et al., 2010) and a nickel-rich pyrite population containing a mean of 4.5 wt% Ni is reported at Thayer Lindsley in Sudbury (Bailey et al., 2006). However, most pyrite in Sudbury ores contain less than 0.7 wt% Ni, including the Craig Ni-Cu mine (Hawley, 1962; Craig and Solberg, 1999). Regarding cobalt, Hawley (1962) reports that Sudbury ores contain pyrite ranging from below detection limit to 0.2 wt% Co (Dare et al., 2010). However, pyrite at the Fecunis Lake deposit contains up to 1.7 wt% Co, a cobalt-rich population at the Thayer Lindsley mine has a mean of 2.63 wt% Co (Bailey et al., 2006) and cobalt contents of up to 3.5 wt% Co are reported for the outer margins of pyrite grains at Craig mine (Craig and Solberg, 1999). Thus, Thompson 1D pyrite nickel and cobalt values (above) are comparable to those reported in other Sudbury deposits, falling within the reported ranges.

Mean pentlandite nickel and cobalt concentrations (wt%) in the Thompson 1D orebody (35.3 wt% Ni, 0.34 wt% Co) are compared with values (wt%) from pentlandite in Sudbury nickel-sulfide deposits: 34.3 wt% Ni, 0.77 wt% Co at Kelly Lake (Huminicki et al., 2005); 35.6 Ni, 1.2 Co at Creighton (Dare et al., 2010); 36.6 wt% Ni, 1.36 wt% Co at Thayer Lindsley (Bailey et al., 2006). Nickel in pentlandite shows similar abundances as the Sudbury deposits, however Thompson 1D orebody shows significantly lower cobalt abundances in pentlandite. Mean pyrrhotite nickel and cobalt values (wt %) in Thompson 1D orebody (0.48 Ni, bdl Co) are compared with values (wt%) from Sudbury deposits: 0.75 Ni, bdl Co at Kelly Lake (Huminicki et al., 2005); 0.7 Ni, bdl Co at Creighton (Dare et al., 2010); and 0.6 - 1.1 Ni, bdl Co at Craig mine (Craig and Solberg, 1999). Two chemically different populations of pyrrhotite are reported at The Thayer Lindsley deposit, with averages of 0.54 Ni and 0.83 Ni, and no reported Co values for either population (Bailey et al., 2006). Thompson 1D pyrrhotite show substantially lower nickel values, but cobalt values are bdl as reported in Sudbury camp deposits. Mean chalcopyrite copper, iron and sulfur values (wt%) in the Thompson 1D orebody (36.3 Cu, 32.6 Fe, 31.0 S) are compared with values (wt%) from Sudbury deposits: 34.3 Cu, 30.0 Fe, 34.9 S at Kelly Lake (Huminicki et al., 2005); 33.7 Cu, 30.7 Fe, 35.2 S at Creighton (Dare et al., 2010). Thompson 1D chalcopyrite show slightly higher copper and lower sulfur concentrations (wt%) compared to the Sudbury camp deposits.

TNB: Burnham et al. (2009) had previously reported elevated cobalt contents in Thompson pyrite, up to 1.4 wt% Co, which is slightly lower than the reported mean values in this study of 1.3 wt% Co or up to 3.55 wt% Co. Burnham et al. (2009) also reported that pyrite can contain up to 400 ppm As, however most pyrite in this study contained <170 ppm As. Pentlandite from Thompson deposits has Ni/Co ratios of 24-113 (Burnham et al., 2009), and significantly higher Ni/Co ratios of 100-275 for Thompson 1D pentlandite (Liwanag et al., 2001). The Ni/Co of pentlandite in this study ranged from 56 to 583 (mean of 124), which are higher than the values reported by both Burnham et al. (2009) and Liwanag et al. (2001). The pentlandite Ni/Co ratios are very high in the 1D ores, which indicates that pentlandite has undergone higher degrees of deformation, accounting for enriched nickel and lower cobalt contents, the latter having diffused into pyrite (Burnham et al., 2009). However, an alternate explanation is that this could also reflect initially low magmatic cobalt concentrations (Liwanag et al., 2001). Nickel values in pyrrhotite reported by Burnham et al. (2009) range from 0.2 to 1.1 wt% Ni. Possibly two distinct pyrrhotite populations were observed in this study of 1D ores (**Section 7.1.4**); a minor nickel-rich (0.7 wt% Ni) and dominantly nickel-poor (0.4 wt%

Ni) pyrrhotite, suggesting the presence of hexagonal pyrrhotite (nickel-rich) that exsolved from monoclinic pyrrhotite (nickel-poor) (Vaughan et al., 1971). This could indicate that during massive sulfide formation, conditions were more favourable for monoclinic pyrrhotite, with hexagonal pyrrhotite having exsolved later at lower temperatures (Liwanag et al., 2001), but further investigations were beyond the scope of this study. Regardless, the mean nickel values of Thompson 1D pyrrhotite (0.48 wt% Ni) are comparable to those reported by Burnham et al. (2009) across Thompson deposits.

The mineral chemical data presented by Burnham et al. (2009), Liwanag et al. (2001) and this study indicate that during polyphase deformation at Thompson, cobalt moved out of pentlandite and into pyrite, whereas nickel was mobilised out of pyrrhotite ± pyrite and into pentlandite. This is confirmed by this study; very high cobalt contents in pyrite, substantially lower cobalt contents in pentlandite and very low nickel contents in pyrrhotite. The nickel values of pyrite at the 1D orebody are quite elevated, which suggests that nickel that was mobilized out of pyrrhotite during deformation may have preferred mobilizing into pyrite over pentlandite.

Lower cobalt values in pentlandite and higher mean nickel and cobalt values in pyrite at Thompson 1D compared to sulfides in Western Australian sulfide deposits, indicate that deformation and remobilization may have been more intense at Thompson compared to Kambalda camp ores. And although elevated nickel and cobalt contents in pyrite are comparable to Sudbury camp deposits, the substantially lower nickel values in both pyrrhotite and cobalt values in pentlandite suggest stronger deformation and remobilization processes were active at Thompson compared to Sudbury sulfide deposits.

8.4 Genetic Models for the TNB Sulfides

8.4.1 Primary Magmatic Model

Primary magmatic as well as post-magmatic and metamorphic processes (**Section 8.5**) have been presented for the Thompson ores.

A primary magmatic origin for sulfide mineralization in the TNB deposits has been widely recognized. The assimilation of komatiitic magma with sulfur from the Ospwagan Group sedimentary rocks that produced immiscible sulfide melt by magmatic processes has been proposed (Peredery, 1982; Bleeker, 1990; Lesher and Burnham, 2001; Layton-Matthews et al., 2007; Burnham et al., 2009; Lightfoot et al., 2012, 2017) although the direct geological evidence for the process is not as compelling as that found in less deformed deposits. Explanations for elevated nickel tenor and platinum group metal contents within remobilized secondary sulfides hosted in meta-sediments (Thompson deposits), compared to lower nickel tenor primary ultramafic associated sulfides (Pipe and Birchtree deposits) have been debated (Bleeker, 1990; Liwanag et al., 2001; Burnham et al., 2009; Layton-Matthews et al., (2007); Lightfoot et al., 2012, 2017; this study), although the evidence for a deformation control is much more evident than magmatic controls.

It has been suggested that the high tenor metasediment-hosted sulfide deposits of the TNB are the result of primary magmatic processes, notably R-factor (Campbell and Naldrett, 1979; Naldrett, 1999; Lesher and Campbell, 1993; Lesher and Burnham, 2001). A sulfide melt that equilibrated with larger amounts of silicate magma (high R-factor) would possess higher metal concentrations than those which interacted with less silicate magma (low R-factor). Platinum and palladium have greater affinities for a sulfide melt than nickel (Barnes et al., 1997), therefore an enrichment in sulfide nickel tenor due to variations in R-factor would have to strongly correlate with an enrichment in PGE. Evidence for nickel tenor variations throughout ultramafic-hosted sulfides (Pipe, Birchtree and South Manasan) and more-so the metasediment-hosted sulfides (Thompson) are recognized in the TNB (Bleeker, 1990; Liwanag et al., 2001; Burnham et al., 2009; Lightfoot et al., 2012, 2017; Franchuk et al., 2016; this study). The Thompson 1D ores show evidence for interfingering of high and low nickel tenor lenses (**Section 5.3.1; Table 5-1**) (Lightfoot et al., 2017) and possess some of the highest Ni-Co-PGE concentrations in sulfides compared to the other TNB deposits (**Section 8.1.2**) (Liwanag et al., 2001; Burnham et al., 2009; Lightfoot et al., 2017). Although PGE were not the focus of this study, a preliminary investigation of PGE abundances in the 1D orebody was presented in **Section 5.4.2**, where a positive correlation between whole rock nickel (%) and palladium (ppm) from underground sulfide ore samples was recognized **(Figure 5-6)**. More importantly, there is a weak variation of palladium concentrations between different mineralization styles in the 1D orebody, although samples with the highest nickel grades contain the highest palladium concentrations (**Figure 5-6**). This supports the argument that primary magmatic processes (R-factor) could have been responsible for nickel and PGE tenor variabilities within Thompson 1D ores.

It is undisputed that primary magmatic processes, following komatiite intrusions into sedimentary Ospwagan sequences, are responsible for the generation of voluminous sulfide deposits in the TNB (Bleeker, 1990). However, the primary magmatic model remains difficult to test and is not confidently understood due to the variably deformed and heterogenous nature of the ores (Lightfoot et al., 2017). The R-factor model can potentially explain the correlation between high nickel and PGE tenors observed in the 1D, however a primary magmatic process control does not explain; the abundance of paragenetically-late pyrite (**Sections 8.2.1**), the variability of Ni-Co in pyrite (**Section 8.2.2**), the intricate link between pyrite abundance and high tenor ores (**Section 8.2.3**), the suite of complex post-magmatic sulfide textures (**Sections 8.24**), or the sulfide melt inclusions that occur in metamorphic silicate assemblages (**Section 8.2.5**).

Extensive remobilization of the primary magmatic sulfides during D_1 - D_2, and tectonic emplacement of these sulfides during high P-T is evidence that post-magmatic and secondary metamorphic processes may have played an important role in repositioning and modifying the Thompson ores (Lightfoot et al., 2017).

8.4.2 Sulfide Kinesis

A post-magmatic deformation model based on the dynamo-thermal metamorphic history of the TNB as it is related to P-T evolution of the system has gained momentum in recent years. McQueen (1987) suggested that Western Australian nickel-sulfide ores could have formed by remobilization of high-temperature, ductile sulfides in relation to less ductile host rocks via mechanical processes in structurally-controlled settings. Similarly, Seat et al. (2004) reports that a lack of correlation between pyrite abundance and nickel tenor is inconsistent with a metamorphic sulfidation model and due to ductility contrasts observed, a more structural approach supporting redistribution of nickel-poor MSS along faults is at cause for primary texture destruction and tenor variations at the N02 orebody at the Wannaway deposit. Seat et al. (2004) states that nickel tenor ores are highly variable, with the lowest tenor massive ores occurring in the most structurally complex areas of the N02 orebody, which is opposite of that observed in the Thompson 1D.

However, models suggesting tenor variations via mechanical processes have been proposed for the TNB. The theory of *sulfide kinesis,* first termed by Monteiro and Krstic (2006) and Lightfoot et al. (2017), suggests mechanical separation of pentlandite from pyrrhotite during the subsolidus flow of ductile sulfide ore during thermal metamorphism and deformation in the TNB. Thompson ores experienced higher degrees of thermal metamorphism (~100 degrees higher; Bleeker, 1990) compared to Pipe and Birchtree ores, which may have facilitated the addition of higher amounts of nickel into the sulfides of the TNB.

Peak metamorphic conditions allowed for pyrrhotite and pentlandite to be resorbed back into a monosulfide solid solution (MSS) (Monteiro and Krstic, 2006). Upon cooling, the physical separation of mobile-pyrrhotite from pentlandite would result in granular pentlandite (less mobile) left behind as the MSS (Po-rich) was transported further away along flanks of folds (Lightfoot et al., 2017). *Sulfide kinesis* suggests the plastic translocation of ductile, primary ultramafic associated sulfides took place over a range of P-T deformation (D_1 – D_2) and involved repeated injections of plastic sulfide, with variable tenor, into the sedimentary country rocks (Lightfoot et al., 2017). This would effectively leave behind nickel-rich areas in the form of pentlandite, while also creating zones low in nickel, dominantly pyrrhotite rich. This process of formation of MSS would generate the heterogenous lenses of neighbouring mineralization observed throughout the Thompson deposits (Lightfoot et al., 2017), with nickel-rich sulfide lenses becoming emplaced beside barren sulfide and intermediate sulfide lenses (**Section 5.1.4**). Additionally, during this translocation process, ductile sulfides would flow into open-space and areas of low-pressure, accumulating in fold hinges, limbs and along transtensional openings (Lightfoot et al., 2017), as would agree with the underground observations described in **Section 5.1.4**.

This mechanical segregation of granular pentlandite from pyrrhotite suggests that the residual MSS (Po-rich) would be enriched in nickel, as nickel resorbed back into the MSS during prograde metamorphism. However, this does not agree with the Ni and Co contents in the Thompson 1D pyrrhotite, which are very low (0.48 wt% and <100ppm, respectively), and much lower than pyrrhotite nickel values reported in most Sudbury camp ores (**Section 8.3.2**). However, the amount of pentlandite the MSS had access to at the time of reformation would dictate this process, and the MSS produced can show a variation in nickel tenor as a function of *sulfide kinesis* (Lightfoot et al., 2017), as can be evidenced by the two-pyrrhotite types (Ni-rich and Ni-poor) documented in the 1D orebody (**Section 7.1.4; Figure 7-7**).

The *sulfide kinesis* model proposed by Monteiro and Krstic (2006), and modified by Lightfoot et al. (2017), provides a viable process which could have repositioned primary sulfides (D_1 - D_2) and generated the heterogenous lenses of sulfide within the Pipe Formation sedimentary stratigraphy. However, the *sulfide kinesis* model does not fully explain several important mineralogical and geochemical constraints associated with the modification of Thompson 1D ores; the highest Ni-Co-Pd tenors associated with shear-hosted sulfides (**Section 8.1.3**), the abundance of paragenetically-late pyrite (**Sections 8.2.1**), the variability of Ni-Co in pyrite (**Section 8.2.2**), the linkage of pyrite abundance to the highest tenor ores in the 1D (**Section 8.2.3**), or the presence of sulfide melt inclusions (**Section 8.2.5**) as indicative of partial melting of ores (**Section 8.5.3**).

8.5 Controls on the Geochemistry of the TNB Mineralization

It is difficult to explain the variability of tenors in metasediment-hosted sulfides solely through primary magmatic and mechanical processes. The primary magmatic theory is required and is responsible for generating the TNB sulfides, whilst *sulfide kinesis* could explain the repositioning of the heterogenous lenses of sulfide via MSS resorption and translocation, but further post-magmatic and metamorphic processes are proposed to have modified the sulfides into the variable tenor ores observed today.

Nickel tenor variability is somehow related to a late-stage high sulfur fugacity event, which created pyrite with enriched, yet variable, nickel and cobalt contents (**Sections 8.2.1; 8.2.2**). Pyrite formation is interpreted to be paragenetically-late and developed at relatively low temperatures, post-dating peak-metamorphic conditions (Bleeker, 1990; Liwanag et al., 2001; Burnham et al., 2009; this study). More importantly, there is an intricate relationship between pyrite abundance and elevated nickel and cobalt tenors of sulfide ore in the Thompson 1D orebody (**Section 8.2.3**).

Duke (1986) stated that nickel and cobalt enrichment of magmatic sulfides at Dumont were due to the importance of sulfur-loss from post-magmatic processes. Three possible geochemical hypotheses that may explain the high sulfidation event and subsequently its relationship to nickel tenor upgrading of the metasedimentary-hosted sulfides in the Thompson 1D are examined below.

8.5.1 Oxidation

It has been observed that the shear-hosted sulfides in the Thompson 1D orebody host the highest pyrite modal abundances amongst all mineralization styles (**Section 8.1.3**). The dependence of whole rock nickel and cobalt tenor on pyrite abundance suggests a high sulfidation event is linked to the genesis of pyrite, which in turn is related to elevated tenors in the metasedimentary-hosted sulfides of the Thompson 1D orebody. Stone et al. (2004) conducted studies on 14 different nickel sulfide deposits throughout the Archean Kambalda ore field in Western Australia and revealed that heterogeneity in nickel tenor variations throughout deposits is difficult to explain solely by magmatic processes. Kambalda experienced a similar dynamo-thermal metamorphic history as Thompson; upper greenschist to amphibolite, and as a result Stone et al. (2004) proposed that retrograde metamorphic modifications on sulfide ores control tenor variations. Positive correlations between nickel tenor and secondary pyrite abundances in several of these komatiite-associated nickel sulfide deposits of Kambalda (Heath et al., 2001; Stone et al., 2004), suggest oxidation as a major control on nickel tenor variation (Stone et al., 2004).

One way to explain a high sulfidation event is by release of S_2 via oxidation of pyrrhotite:

(1)

$$\mathbf{6\ Fe_{(1-x)}S + 4O_2 \rightarrow 2\ Fe_3O_4 + 3\ S_2}$$

(Pyrrhotite + Oxygen → Magnetite + Sulfur degassing)

In theory, oxidizing metamorphic fluids migrating along shears could oxidize neighbouring pyrrhotite and increase the f_{S2} of the system, while producing magnetite and other iron-oxides **(1)**. While excess S_2 undergoes a sulfidation reaction, taking up iron from pyrrhotite to form pyrite:

(2)

$$\mathbf{Fe_{(1-x)}S + \tfrac{1}{2}\ S_2 \rightarrow FeS_2}$$

(Pyrrhotite + excess sulfur → Pyrite)

Although oxidation could have formed some secondary pyrite in the Thompson 1D mineralization **(2)**, there are minimal concentrations of iron-oxides ± ferrochromite and magnetite in the ores (Burnham et al., 2009; this study), which suggests that oxidation is not the major control on nickel tenor variations.

Pyrite in nickel-sulfide Kambalda ores is a major sulfide mineral, particularly of high tenor deposits, consisting of ~27 ± 11 wt% (1σ) abundance of metasomatic pyrite (Heath et al., 2001), whereas Thompson 1D sulfide ores have between 5 – 10 wt% abundance of secondary pyrite (**Section 7.3.3**). Secondary pyrite in several Kambalda deposits is suggested to have formed by replacement of pyrrhotite during introduction of metamorphic oxidizing alteration fluids (Stone at al., 2004). Magmatic oxidation via assimilation of H_2O during emplacement of komatiitic lava into unconsolidated sediments at Kambalda is also proposed (Heath et al., 2001). Variation in oxygen fugacity (f_{O2}) is the major process responsible for nickel tenor variations across several nickel-sulfide deposits from the Archean Kambalda ore field (Stone et al., 2004). However, this process is not favored at Thompson due to the lack of significant amounts of Fe-oxide (**Section 8.7.1**) and minimal presence of local ultramafic bodies in the 1D orebody (**Section 3.3**).

8.5.2 Retrograde Metamorphic Fluid

Flow of metamorphic fluids can result in the transport of mobile elements (Ni, Co, Cu, PGE) along shears and precipitation of late-pyrite enriched in these elements (McQueen, 1987; Bailey et al., 2006; Collins et al., 2012). Modification of sulfide composition by a retrograde metamorphic fluid is supported by the following metamorphic reaction:

$$\mathbf{KAlSi_3O_8 + 3\ Fe_{(1-x)}S + H_2O + 1.5\ O_2 \rightarrow KFe_3^{2+}AlSi_3O_{10}(OH)_2 + 1.5\ S_2} \tag{3}$$

K-feldspar + Pyrrhotite + Water + Oxygen → Fe-biotite (Annite) + Sulfur degassing

The above reaction converts K-feldspar and pyrrhotite into annite while increasing f_{S2} of the metamorphic fluid. The excess S_2 could have been involved in a retrograde sulfidation reaction, to convert pyrrhotite to pyrite:

(4)

$$\mathbf{Fe_{(1-x)}S + \tfrac{1}{2}\,S_2 \rightarrow FeS_2}$$

(Pyrrhotite + excess sulfur → Pyrite)

Reactions **(3)** and **(4)** are consistent with geological and petrographic observations of the Thompson 1D ores. K-feldspar replacement by biotite in reaction **(3)** suggests 'potassic metasomatism', which has been observed to occur in the 1D sulfides (**Section 6.1.1**). However, biotite replacement of all feldspars, including plagioclase, has been observed within the wall rock and pegmatitic inclusions entrained in the 1D ores. Reaction **(3)** and **(4)** also suggests that there is a spatial link between annite and pyrite, as is observed in the geological observations underground in this study (**Section 5.3.2**). Additionally, hydration of ultramafic boudins, especially in the lower 1D orebody (**Section 5.1.2**), would support the presence of fluids and facilitation of these reactions.

Furthermore, these metamorphic reactions support a high-sulfidation event, and possible evidence for a retrograde metamorphic fluid (McQueen, 1987; Bleeker, 1990; Chen, 1993; Liwanag et al., 2001; Heath et al., 2001; Burnham et al., 2009; Bailey et al., 2006; Collins et al., 2012), which could be responsible for: remobilization of paragenetically-late Ni-Co-As-Pd bismuth tellurides (**Section 8.2.2**), generating paragenetically-late pyrite (**Section 8.2.1**) and the zoning/enrichment of several of these elements in Thompson 1D pyrite (**Section 8.2.2**).

Remobilization of metal-bearing metamorphic fluids during deformation and metamorphism has been proposed as the mechanism to cause tenor variations across several nickel-sulfide deposits from Kambalda in Western Australia, Sudbury and the TNB.

Redistribution and sulfidation of nickel ores during deformation and metamorphism of komatiitic sulfides has been proposed at several Kambalda deposits (Keays et al., 1981; Heath et al., 2001). Keays et al. (1981) suggested that tenor variations in the Lunnon shoot, Kambalda are a result of post-metamorphic cooling and thermal contraction of massive ores (Seccombe et al., 1981), which increased permeability and facilitated mobilization of metamorphic sulfur-bearing fluids across various ore shoots. By contrast, nickel tenor variations at the Flying Fox deposit range from 1.4 to 16.8 wt% Ni and are primarily the result of modification of typical komatiite associated magmatic sulfides by hydrothermal fluids during deformation, resulting in dilution of the ores (Collins et al., 2012). Circulating Fe-, S-, As- and Cu-bearing fluids deposited abundant pyrite (1-40% modal), which resulted in the dilution of the original nickel tenor of the ores and creating a variability across the deposit (Collins et al., 2012). This suggests that the role of circulating metamorphic fluids within structurally controlled deposits may not always lead to nickel mobilization (Collins et al., 2012). Collins et al. (2012) also reported that addition of pyrite from hydrothermal circulating fluids resulted in massive pyrite deposition (**Figure 7-18D**) and pyrite-pentlandite intergrowths (**Figures 7-18 A; 7-27**), which could explain several of these post-magmatic textures also observed in the Thompson 1D (**Section 8.2.4**).

Bailey et al. (2006) proposed that remobilization of hydrothermal fluids during amphibolite-grade metamorphism resulted in the mobilization of Ni-Cu-Co along shears and the precipitation of late-pyrite, enriched in these elements, at the Thayer Lindsley mine in Sudbury. Bailey et al. (2006) showed that variations in Ni:S ratio between ore zones correlated with intensity of deformation, and that numerous foliation-parallel quartz veins along ore contacts were conduits for the migration of syn-tectonic metamorphic fluids at Thayer Lindsley. Many similarities can be drawn between the Thompson 1D and the Thayer Lindsley ores: paragenetically-late pyrite enriched in nickel and cobalt (**Section 8.2.2**), variations in nickel tenor across different sulfide mineralization styles (**Section 8.1.3**), and the presence of numerous pegmatites emplaced along shear zones that border nickel-sulfide mineralization, as seen in the Thompson 1D orebody (**Sections 5.1.3; 8.1.1**).

At Thompson, Bleeker (1990) was the first to propose that the enrichment of originally barren sedimentary sulfides in Ni-Co and other metals, was a product of redistribution from initially high-grade magmatic sulfides during peak metamorphism, which resulted in neighbouring sedimentary sulfides to become enriched in these elements. Bleeker (1990) suggested that the redistribution process was variably assisted by a metamorphic fluid. Chen (1993) interpreted mobilization of PGE along structural networks connecting ores to be associated with chlorine-rich and late-hydrothermal fluids, at conditions of 250-300˚C and 3-4 kbar, during a period of dilatancy at Thompson (T1) mine. Chen (1993) also reported PGM and Au-bearing arsenic-rich nickel sulfide ores hosted within some pegmatites in T1 mine, suggesting that Pd-bismuth telluride assemblages, coupled with Au were mobilized in pegmatites at Thompson. Additionally (Bleeker 1990) observed quartz veins (~30m wide) associated with brecciated nickel sulfide ore at Thompson open pit mine and recorded very high arsenic values from samples associated with the quartz veins. Although, pegmatites were not the focus of this study, their propitious existence along shear zones, which also tend to border nickel sulfide mineralization in the 1D orebody, was noted (**Section**

5.1.3). Liwanag et al. (2001) presents a model for fluid-assisted modification and upgrading of ores during deformation and metamorphism in structurally altered deposits of the TNB. Liwanag et al. (2001) proposed that elevated Ni-Co-Pd-As-Bi concentrations in the Thompson 1D sulfides are a result of the strongly deformed nature of the ores, where numerous shear zones and tension gashes act as 'fluid migration pathways' for mobilization of metal-rich fluids and subsequent recrystallization of high-tenor ores. This agrees with observations from this study that the highest Ni, Co, Pd tenors are found in shear-hosted styles of mineralization (**Section 8.1.3**). Furthermore, the structural complexity and metal variability of the ores (**Sections 8.1.1; 8.1.2**) and presence of paragenetically-late phases like gersdorffite, niccolite, Ni- and Co-enriched pyrite (**Section 8.2.1; 8.22**), are consistent with modification of the ores by fluids. Furthermore, Burnham et al. (2009) proposed that deformation at Thompson facilitated mobilization of nickel, palladium, copper and gold in As- and Bi-enriched fluids into massive sulfide ores via structural pathways such as shears and faults. Burnham et al. (2009) stressed the importance of shears and hydrothermal remobilization of elements during deformation and metamorphism, providing evidence that nickel and cobalt diffused into host-rocks to create metasedimentary Thompson ores. Layton-Matthews et al. (2007) also interpreted that primary characteristics of many TNB sulfide deposits have been modified by post-ore deformation and metamorphic processes, specifically that Ni-Cu-Au-Pd appear to have mobilized away from primary ore environments.

The Thompson 1D orebody can draw many comparisons to Kambalda and Sudbury nickel sulfide deposits (Keays et al., 1981; Heath et al., 2001; Bailey et al., 2006; Collins et al., 2012), with post-magmatic remobilization of metal-rich fluids via deformation and metamorphism having also been proposed to explain metal variability and tenor upgrading in TNB deposits (Bleeker, 1990; Chen, 1993; Liwanag et al., 2001; Burnham et al., 2009; Layton-Matthews et al., 2007). Interestingly, as discussed in **Section 8.2.4**, the abundance of several post-metamorphic sulfide textures including; symplectic intergrowths between Py-Pn and Py-Ccp (**Figures 7-18A; 7-27**), anhedral blebs of Py-Ccp overgrowing on remnant pentlandite grains (**Figures 7-18B; 7-25H; 7-25D**), massive pyrite sections (**Figure 7-18D**) and pyrite flames (**Figure 7-26**) could be argued to have formed from Fe- and S-saturated circulating hydrothermal fluids, as reported by Collins et al. (2012) in the Flying Fox deposit. However, the presence of sulfide melt inclusions (**Section 8.2.5**) cannot yet be explained with strictly a retrograde metamorphic fluid. Therefore, complementary post-magmatic processes may have been involved at Thompson.

8.5.3 Localized Partial Melting

Brett and Kullerud (1967) and Lawrence (1967) first hypothesized that a sulfide melt can be generated by partial melting of pre-existing massive sulfide ores during metamorphism and deformation. However, due to lack of field and experimental evidence, the concept was largely ignored.

Since then, partial melting of sulfide bodies during metamorphism has been reported in several deposits around the world, notably the Pb-Zn-Ag Broken Hill deposit in Australia (Sparks and Mavrogenes, 2004; 2005), the Pb-Zn-Cu-Ag Broken Hill deposit of Aggeneys, South Africa (Sparks and Mavrogenes, 2004; Bailie and Reid, 2005), VMS deposits in the Snow Lake district, Manitoba (Frost et al., 2002), the Zn-Pb-Au-Ag Montauban deposit in Quebec (Tomkins et al., 2006; 2007), the Challenger Au mine in South Australia (Tomkins and Mavrogenes, 2002) and in the sulfosalt-rich dolomite deposits of Lengenbach, Switzerland (Hofmann, 1994; Hofmann and Knill, 1996). Partial melting has also been used to explain sulfide and sulfosalt mineral distributions at Hemlo, Ontario (Tomkins et al., 2004). At all the above localities, evidence for the occurrence of polymetallic sulfide melt inclusions have been recorded (**Section 8.2.5**). Interestingly, Frost et al. (2002) recorded multi-phase sulfide melt inclusions in silicates from the highest-grade deposits at the Snow Lake VMS massive sulfide ores, 250 km southwest of Thompson. They interpreted that the sulfides underwent partial melting during metamorphism due to the abundance of arsenopyrite and other chalcophile minerals in the ores. Tomkins et al. (2007) suggested that the deposits near Thompson are possible localities where partial melting could have occurred, due in part to the high P/T metamorphism of the region (upper-amphibolite to lower-granulite facies) and abundance of arsenides, sulfarsenides, Pd-bismuth tellurides and antimonides that are a part of the late-mobilized components of the ores.

The present study is the first to document polymetallic sulfide melt inclusions at Thompson, observed in metamorphic quartz and garnet grains (**Section 8.2.5**). Sulfide melt is interpreted to have been trapped at or near peak D_2 conditions during growth of metamorphic silicate assemblages and thus is evidence for possible localized partial melting of sulfides in the Thompson 1D ores. Polymetallic sulfide melt inclusions tend to occur in sulfide samples with some of the highest nickel and cobalt tenors in the Thompson 1D (**Section 7.6.2**).

Additionally, a localized partial melting theory could also support the complex array of post-magmatic sulfide textures observed in the Thompson 1D ores (**Section 8.2.4**). Experimental results show that sulfide melts can quench to complex sulfide mineral intergrowths, myrmekitic textures, which tend to equilibrate at very low temperatures (Mavrogenes et al., 2001; Frost et al., 2002). These myrmekitic-symplectic textures in the Thompson 1D (**Figures 7-18A; 7-27**) can be interpreted as rapid-growth textures indicative of possible partial melting. Furthermore, a high-sulfidation event is responsible for the late-pyrite textures observed in the 1D; euhedral pyrite grain overgrowths on pyrrhotite-pentlandite assemblages (**Figure 7-17 A; D**), massive-annealed pyrite (**Figure 7-18D**), complex pyrite-chalcopyrite anhedral blebs within a pyrrhotite matrix ± pentlandite remnants (**Figures 7-18B**) and rim textures around silicates (**Figure 7-17F**). The source of sulfur to stabilize late-pyrite could be explained by release of S_2 from partial melting at or near peak P-T of pre-existing ores. Sulfur degassing (S_2) could then be involved in a sulfidation reaction, converting pyrrhotite to form pyrite (**Equation 4, Section 8.5.2**). Therefore, it is plausible that partial melting of sulfides during peak P-T in the most structurally controlled and heavily deformed regions of the Thompson 1D, and possible localized partial melting along shears contributed to the association between high Ni tenors and the presence of pyrite.

However, pyrrhotite, pentlandite, chalcopyrite, pyrite, gersdorffite and minor sphalerite and niccolite are the most common sulfide minerals at Thompson **(Appendix 5).** Chen (1993) reports that platinum group elements (Pd, Pt, Au, Rh, Te) are dominantly in the gersdorffite and niccolite grains at Thompson, which is confirmed in this study (**Section 7.5.3**). For partial melting of dominantly massive pyrrhotite to occur, metamorphic temperatures of 1114 °C at 1bar would need to have been reached (Friedrich, 1907). Peak metamorphic temperatures are well below this required temperature, with Thompson reaching upper amphibolite to lower granulite grade metamorphism (~750ºC and 7.5 kbars - Lightfoot et al., 2017). Tomkins et al. (2006, 2007) states that for massive sulfides to melt, fluxes like As-Bi need to be present in the ores. From **Section 8.1.2**, it is shown that the Thompson 1D ores have some of the highest Ni/Co, Pd/Ir, Se/S ratios and elevated Pd, Pt, Bi and As values compared to other deposits within the TNB (Bleeker, 1990; Liwanag et al., 2001; Burnham et al., 2009; this study). Noticeable concentrations of gersdorffite, niccolite and As-, Ni- Co-enriched pyrite also exist in the 1D ores (Liwanag et al., 2001; Burnham et al., 2009; this study).

Interestingly, the Pipe Formation pelitic schists that host the Thompson metasedimentary sulfides are invariably highly graphitic, made up of 1 - 10% modal graphite, but can be as high as 10 - 20% modal graphite in areas (Bleeker 1990). Graphite abundantly occurs as inclusions within massive and semi-massive ores (**Section 5.1.4**) and invariably occurs in high quantities along shears, faults and gouge zones as slickenside planes (**Section 5.2.1**). Graphite also occurs as laths commonly attached, or in close proximity to, many polymetallic sulfide melt inclusions observed within metamorphic silicate assemblages (**Section 7.6.1; Figure 7-32**). High-pressure experiments by Zhang et al. (2015) conclude that graphite saturation (~0.3 wt% dissolved C) can depress the monosulfide solidus by ~80 ± 25˚C compared to carbon-free conditions up to 8 GPa. The monosulfide composition ($Fe_{0.69}Ni_{0.23}Cu_{0.01}S_{1.00}$) investigated by Zhang et al. (2015) has a low metal/sulfur ratio (0.93) and low Ni/(Fe +

Ni), but states that sulfides with higher M/S ratios and with greater Ni/(Fe + Ni) should melt at lower temperatures. Perhaps, the presence of graphite at Thompson was sufficient to lower the solidus temperatures required to melt massive sulfides. This would suggest that in areas of high graphite abundance, particularly in shears, partial melting was possible at the P-T conditions of regional metamorphism. This is speculative and more experimental studies on the effects of carbon (graphite) on lowering the solidus in S-rich monosulfide systems are needed.

In summary the Thompson 1D ores have: i) elevated concentrations of arsenides, sulfarsenides and Pd-bismuth tellurides; ii) anastomosing shear development; iii) invariably high graphite contents in the host rocks, sulfide ores, shears and sulfide melt inclusions; iv) numerous polymetallic sulfide melt inclusions observed in metamorphic quartz and garnet grains; v) complex post-magmatic ore textures. One model that explains all of these characteristics is localized partial melting during high-temperature metamorphism at Thompson.

8.6 Model for the Thompson Deposits

A model for the formation of the Thompson deposits, specifically the Thompson 1D orebody is proposed in **Figure 8-1** to account for the geological, mineralogical and mineral chemical constraints observed in this study.

The TNB is the collisional craton margin between the Paleoproterozoic Churchill and the Archean Superior Provinces. This region experienced ultramafic magmatism (1880 ± 5 Ma; Hulbert et al., 2005) associated with a continental rifting event that led to the intrusion of fertile komatiitic magmas (Ni- and PGE-bearing) that ascended along fault conduits and were emplaced as sills into Early Proterozoic Ospwagan Group sediments (Barnes and Lightfoot, 2005). The komatiitic magmas intruded along sulfur-rich sediments and sulfide-facies iron formations of the Pipe Formation, where primary magmatic sulfide melt was produced through crustal sulfur saturation and formation of an immiscible sulfide melt that led to the development of TNB ores (Lesher and Burnham, 2001; Layton-Matthews et al., 2007; Lightfoot et al., 2017).

Tectonic activity associated with the Trans-Hudson Orogeny at 1.7 Ga (Machado et al., 2011), subjected the TNB rocks to polyphase deformation (D_1-D_4) and upper amphibolite to lower granulite facies metamorphism (Bleeker, 1990). Magmatic sulfide bodies were folded and stretched during the compressional regimes of D_1 and D_2 into boudin necks/shadow zones of the ultramafic intrusions (Franchuk et al., 2016; Lightfoot et al., 2017). The onset of local shearing started with D_2, during tight to isoclinal F_2 fold development (Burnham et al., 2009; Layton-Matthews et al., 2007) and the start of hydrothermal fluid migration and mobilization along shears (Chen, 1993). During high-grade peak metamorphism (late D_2) sulfide bodies were metamorphosed up to ~750˚C and 7.5 kbars (Lightfoot et al., 2017) and re-equilibrated to a dominantly monosulfide solution (MSS). The translocation of reformed MSS, along with the aid of fluid-assisted migration along strike (Liwanag et al., 2001), remobilized sulfides into fold hinges, limbs and open-space dilation zones in the neighbouring P_2 schists **(Figure 8-1 A)** (Bleeker, 1990; Liwanag et al., 2001; House, 2009; Lightfoot et al., 2017). In the Thompson 1D, the sulfide bodies would be emplaced along, and become structurally controlled by, doubly-plunging F_3 folds on the flanks of the Thompson Dome, which are the dominant ore controlling structures **(Figure 8-1 B).** (Lightfoot et al., 2017). Coevally during late-D_2 to early-D_3, partial melting produced local sulfide melts that were trapped during growth of metamorphic silicate assemblages near peak metamorphic P-T conditions **(Figure 8-1 C).** This is evidenced by polymetallic sulfide melt inclusions that predominantly occur in metamorphic garnet and quartz grains of the Thompson 1D ores (**Section 8.2.5**). Partial melting resulted in the release of S_2 which was mobilized along with Pd-, Pt-, Bi-, Co-, Ni-, As-bearing complexes, sulfarsenide- and bismuth telluride-rich circulating hydrothermal fluids along shears **(Figure 8-1 D).** Mobilization of fluids in anastomosing shear zone networks continued during high-strain deformation of the transpressive ductile regimes D_3 to D_4 (Burnham et al., 2009). Localized partial melting would have ceased early-D_3 as thermal cooling of ores began D_3 – D_4, but circulating hydrothermal fluid alteration intensified during the late-stage ductile-brittle deformation and shear development into D_4. At this point, the fluids in the prominent shear structures would be rich in As-Bi-Te, which could have acted as fluxes (including frictional heat and graphite abundance), for the possible development of local *shear melting* **(Figure 8-1 E),** distinct from the main partial melting event at peak P-T (late D_2). Migration of copper into stringers and deposited along fractures in D_4 took place, with possible Pt-Cu-rich fluids migrating further along structural corridors.

Crystallization of late paragenetic bismuth telluride and arsenic-bearing phases like pyrite, enriched in Ni-Co-As, as well as PGE-rich gersdorffite and niccolite, are interpreted to have been deposited from hydrothermal fluids along sulfide ores dominantly along shear structures, like the 1D ores **(Figure 8-1 F).** Sulfidation of the ores took place dominantly where hydrothermal fluids deposited the sulfur-bearing complexes, specifically along structurally controlled sulfide bodies, creating tenor variabilities between ores.

As ores thermally contracted, fluid-assisted solid-state diffusion of nickel from massive sulfides horizons to the metasediment wall rocks began (Bleeker 1990) and was an ongoing process at low temperatures. However, elevated Ni + Cr concentrations in biotite within wall rock schist units bordering nickel sulfide lenses (**Section 8.3.1**) support redistribution of Cr as well as Ni into schists. This could support why Bleeker (1990) did not observe Cr redistribution across adjacent sulfide bodies, Cr may have redistributed and equilibrated preferentially into micas over sulfides during deformation and metamorphism. This provides evidence of diffusional mixing of elements between cooling sulfides and wall rocks (Bleeker, 1990; this study).

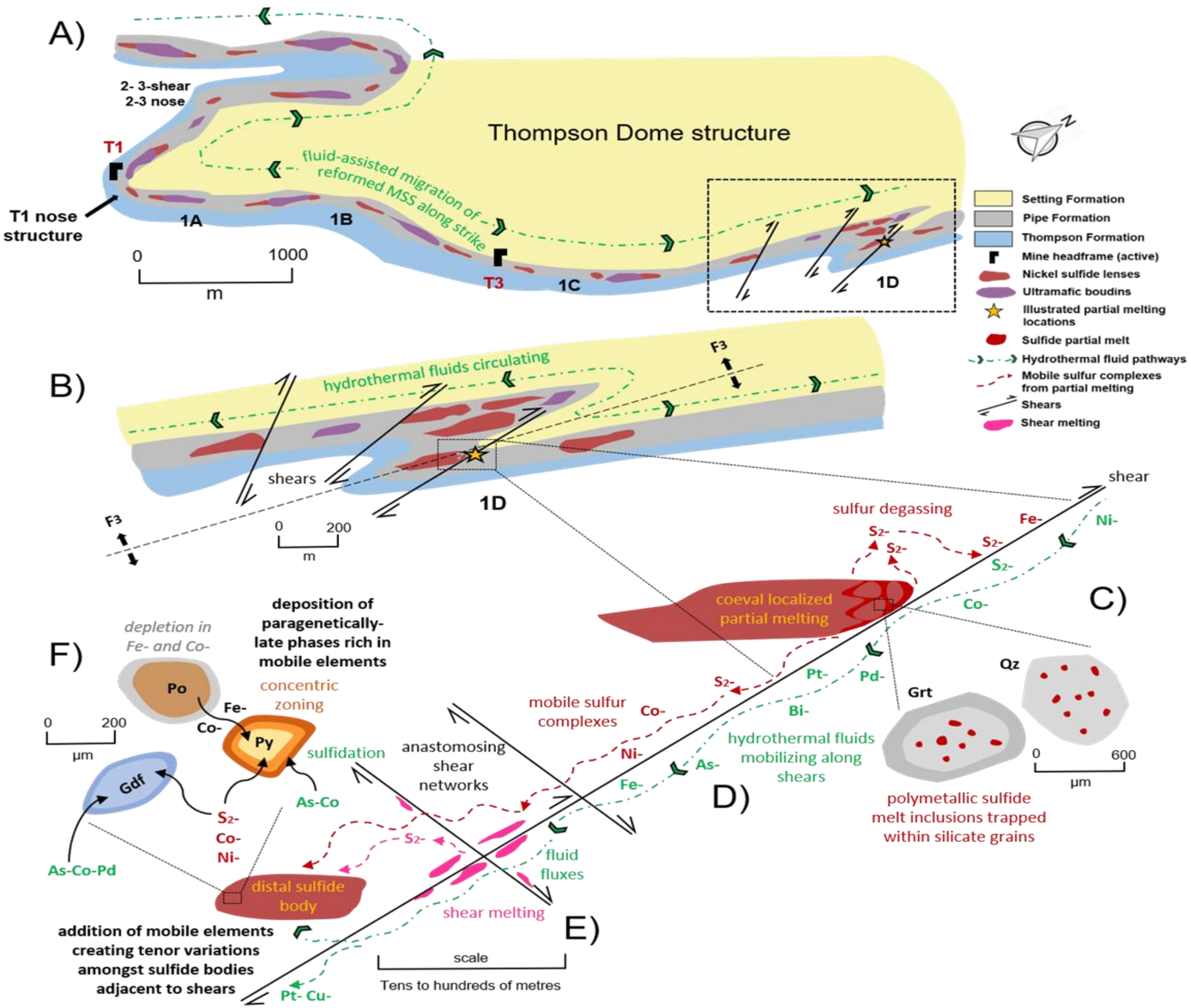
A)
2- 3-shear
2-3 nose
T1
T1 nose structure
1A
1B
T3
1C
1D
0
1000
m
Thompson Dome structure
fluid-assisted migration of reformed MSS along strike
Setting Formation
Pipe Formation
Thompson Formation
Mine headframe (active)
Nickel sulfide lenses
Ultramafic boudins
Illustrated partial melting locations
Sulfide partial melt
Hydrothermal fluid pathways
Mobile sulfur complexes from partial melting
Shears
Shear melting
B)
hydrothermal fluids circulating
F3
shears
1D
F3
0
200
m
shear
sulfur degassing
S2-
S2-
Fe-
S2-
Ni-
S2-
coeval localized partial melting
Co-
C)
Qz
Grt
0
600
µm
polymetallic sulfide melt inclusions trapped within silicate grains
S2-
Pt-
Pd-
Bi-
mobile sulfur complexes
Co-
Ni-
Fe-
As-
hydrothermal fluids mobilizing along shears
D)
anastomosing shear networks
fluid fluxes
shear melting
E)
scale
Tens to hundreds of metres
S2-
Pt- Cu-
F)
depletion in Fe- and Co-
Po
Fe-
Co-
Py
deposition of paragenetically-late phases rich in mobile elements
concentric zoning
sulfidation
As-Co
0
200
µm
Gdf
S2-
Co-
Ni-
As-Co-Pd
distal sulfide body
addition of mobile elements creating tenor variations amongst sulfide bodies adjacent to shears

Figure 8-1: A revised model for the formation of the Thompson deposits, with specific attention on the Thompson 1D orebody. (A) During D2, fluids assisted the translocation of reformed MSS away from primary ultramafic boudins along strike the Pipe Formation meta-sediments, which remobilized ductile sulfides into fold hinges, limbs and open-space dilation zones in P_2 schists (Bleeker 1990; Liwanag et al. 2001; House 2009; Lightfoot et al., 2017). (B) In the Thompson 1D orebody, the sulfide bodies would be emplaced along, and become structurally controlled by, doubly-plunging F_3 folds on the flanks of the Thompson Dome structure. (C) Coevally during late-D_2 to early-D_3, partial melting produced local sulfide melts that were also squeezed into neighbouring sediments along with ductile translocation via sulfide kinesis. Locally, partial melts were trapped within and during the growth of metamorphic silicate assemblages near peak metamorphic, prograde P-T conditions. (D) Partial melting resulted in the release of S_2 which was mobilized along with Pd-, Pt-, Bi-, Co-, Ni-, As-bearing complexes, sulfarsenide- and bismuth telluride-rich circulating hydrothermal fluids along anastomosing shear zone networks. (E) Circulating hydrothermal fluid alteration intensified during the late-stage ductile-brittle deformation and shear development in D3 to D_4. Fluids in the prominent shear structures would be rich in As-Bi-Te, which could have acted as fluxes (including frictional heat and graphite abundance), for the possible development of local shear melting. Possible Pt-Cu-rich complexes could have migrated further along structural corridors. (F) Crystallization of late paragenetic bismuth telluride and arsenic-bearing phases like pyrite, enriched in Ni-Co-As, as well as PGE-rich gersdorffite and niccolite, are interpreted to have been deposited from hydrothermal fluids interacting with sulfide ores dominantly along shear structures. Sulfidation of the ores took place dominantly where hydrothermal fluids deposited the sulfur-bearing complexes, specifically along structurally controlled sulfide bodies, creating tenor variabilities between ores. Abbreviations; Grt (garnet), Qz (quartz), Py (pyrite), Po (pyrrhotite), Gdf (gersdorffite).

Gribbin (2011) suggested a gradational spectrum of deposits exists with increasing deformation and remobilization away from primary ultramafic intrusions: The degree of deformation of primary ores changes, with minimal remobilization of primary ultramafic-hosted disseminated sulfides seen at Pipe and South Manasan deposits. Increased deformation and remobilization of ores is witnessed in the Birchtree deposit, with ultramafic breccia associated mineralization and minor sedimentary-hosted sulfides (Gribbin, 2011). The greatest deformed and remobilized ores are recorded in the Thompson deposits (T1, 1A, 1B, 1C, 1D) where 90% of nickel sulfides are hosted in metasedimentary rocks (Lightfoot et al., 2017). The T1 sulfide ores (2-3 nose, 2-shear, 3-shear, 1A) are structurally located along the fold nose of the Thompson Dome structure to the west **(Figure 8-1 A)** and are the least deformed and most preserved of the Thompson deposits (Gribbin, 2011). Deformation and increased remobilization eastward resulted in breccia-dominated ores of the 1A, 1B and 1C orebodies. With the 1D orebody **(Figure 8-1 B)** being the furthest east and resembling the most structurally complex of the Thompson deposits. The 1D orebody has the highest and most variable nickel tenors (0.2 – 16 wt% Ni) (**Sections 5.31; 5.42**) and hosts brecciated and remobilized sulfides that contain some of the highest As, Bi, PGE, Ni, Co concentrations amongst deposits in the TNB (Chen, 1993; Liwanag et al., 2001; Burnham et al., 2009; Lightfoot et al., 2017; this study). Additionally, ultramafic parent rocks are not common in the Thompson 1D orebody, as compared to the other deposits in the TNB. However, a few larger ultramafic boudins are present in some fold structures, which likely acted as controls on localization of fold hinges (**Section 3.3**) (Lightfoot et al., 2017).

Therefore, this study supports the retrograde metamorphic fluid model and ensuing sulfidation of ores proposed by previous authors on TNB deposits (Bleeker, 1990; Chen, 1993; Liwanag et al., 2001; Burnham et al., 2009; Layton-Matthews et al., 2007). However, this study also supports the speculations of Tomkins et al. (2007), that localized partial melting did indeed occur at Thompson around peak P-T conditions (late D_2), and shortly in D_3 as localized *shear melting*.

The combination of the previously proposed retrograde metamorphic fluid model and the localized partial melting model proposed here **(Figure 8-1)**, is consistent with the geological, petrographical and mineral chemical constraints on the Thompson 1D ores. The localized partial melting model can explain how sulfur-degassing processes at Thompson are linked to tenor variability. The previously proposed models; primary magmatic (R-factor) (Campbell and Naldrett, 1979; Naldrett, 1999; Lesher and Campbell, 1993; Lesher and Burnham, 2001), *sulfide kinesis* (Monteiro and Krstic, 2006; Lightfoot et al., 2017) and oxidation (Stone et al., 2004), cannot explain many of these constraints, as outlined in their respective sections in **Chapter 8**.

A combined retrograde metamorphic fluid and localized partial melting model can explain the multiple high sulfidation events (D_2 – D_4) that occurred during the modification of 1D orebody (**Section 8.1.1**) and consequently responsible for the metal variability across the deposit (**Section 8.1.2**). Release of S_2 from partial melting at peak D_2, where degassed S_2 joined with circulating sulfur-bearing fluids from hydrothermal alteration and hydration of ultramafic boudins, deposited paragenetically-late bismuth telluride and arsenic-bearing phases such as pyrite enriched in Ni, Co, As (**Sections 8.2.1; 8.3.2**) as well as PGE-rich gersdorffite and niccolite (**Section 8.2.2**). One key observation from this study is the correlation between pyrite abundance and ore samples with the highest nickel and cobalt tenors in the 1D orebody (**Section 8.2.3**). Pyrite genesis and abundance can be attributed to both sulfidation from the retrograde metamorphic fluid and localized partial melting models. The Thompson deposits, specifically the shear-hosted mineralization styles in the 1D orebody (**Section 8.1.3**), show the highest Ni/Co, Pd/Ir, Se/S ratios and elevated Pd, Bi and As values of the deposits within the TNB (Bleeker, 1990; Liwanag et al., 2001; Burnham et al., 2009; this study). The mineral chemical data (**Section 8.3.2**) supports data presented by Burnham et al. (2009), that cobalt moved out of pentlandite and into pyrite, and that nickel moved out of pyrrhotite ± pyrite and into pentlandite during deformation and sulfidation of Thompson ores.

The Thompson 1D orebody shows features typical of metamorphosed sulfide ores, such as recrystallization, remobilization, deformation, alignment and annealing (**Section 8.2.4**). A combined retrograde metamorphic fluid and localized partial melting model supports the complex array of post-magmatic sulfide textures in the 1D ores

(**Section 8.2.4**). Genesis of several textures; symplectic intergrowths (**Figures 718B and 7-27**) and pyrite-chalcopyrite anhedral blebs (**Figures 7-18B; 7-25 E and H**), are better supported by the localized partial melting model as similar sulfide melt textures were observed in several nickel sulfide deposits including Broken Hill, where partial melting of the ores occurred (Mavrogenes et al., 2001; Frost et al., 2002). Additionally, the documented occurrence of sulfide melt inclusions at Thompson (**Section 8.2.5**) is supported by the localized partial melting model, which proposes that sulfide ores in the 1D did experience partial melting around peak P-T conditions (late D_2) and via *shear melting* (D_3). Alternatively, a retrograde metamorphic fluid model supports Yund and Halls (1970) Fe-saturation theory, resulting in circulating hydrothermal fluids rich in Fe- and S- and supersaturation of ores in these elements, causing exsolution of pyrite flames.

The present study is the first to evidently document that a contemporaneous localized partial melting model supports partial melting of sulfide ores at peak metamorphic P-T conditions (late D_2) and subsequent *shear melting* (D_3) at Thompson. Both the retrograde metamorphic fluid and localized partial melting models coexist and complement each other, while providing insights on the complex sulfidation processes at play. They add to the reader’s knowledge on the metal variations within the most structurally dominated deposits at Thompson, the 1D orebody.

We provide the first detailed geological, mineralogical and mineral geochemical documentation of the remobilized Thompson 1D ores. The control on nickel tenor of sulfide is still up for debate, but we report that the highest Ni, Co, Pd tenor ores in the Thompson 1D are associated with increased pyrite abundance (**Section 8.2.3**). Of the five main underground mineralization styles (**Section 5.4.1**), the shear-hosted sulfide ores possess the largest pyrite abundances and highest nickel, cobalt and palladium tenors across the 1D orebody. Therefore, tenor upgrading is not entirely explained, but it appears to be related to the abundance of pyrite, and the late tectonic-metamorphic history of the deposit.

The data from this study agrees with; a primary magmatic origin for sulfides in the TNB (Peredery, 1982; Bleeker, 1990; Lesher and Burnham, 2001; Layton-Matthews et al., 2007; Burnham et al., 2009; Lightfoot et al., 2012, 2017), the *sulfide kinesis* theory for the TNB (Monteiro and Krstic, 2006; Lightfoot et al., 2017) and 'mechanical translocation' as described at Wannaway, W.Australia (Seat et al., 2004), as well as a retrograde metamorphic fluid model (McQueen, 1987; Bleeker, 1990; Chen, 1993; Liwanag et al., 2001; Heath et al., 2001; Burnham et al., 2009; Bailey et al., 2006; Collins et al., 2012) with a contemporaneous localized partial melting model (this study). Thus, a staged mechanism for the formation of Thompson sulfide deposits is proposed, in which three principle stages exist:

1) Komatiitic intrusion emplacement into Ospwagan sedimentary stratigraphy and the ensuing primary magmatic model (R-factor) that generated the voluminous amounts of primary magmatic sulfides throughout the TNB (Stage 1; D_0);
2) High P-T repositioning of ductile, primary ultramafic sulfides by repeated injections of plastic to partial melts (late D_2), creating highly variable tenor

lenses emplaced into sedimentary country rocks via *sulfide kinesis* (Stage 2; D_1 - D_2);

3) Post-ore modification of sulfide lenses via partial melting (late D_2) and a contemporaneous retrograde metamorphic fluid model (D_2 - D_4), shear melting (D_3) and ensuing sulfidation of ores during the late-tectonic brittle-ductile deformation of the deposits (D_3 – D_4);

Chapter 9: Conclusions

9.1 Summary

Underground mapping of mineralized stopes identified five main styles of sulfide mineralization: massive, semi-massive, concordant, ultramafic-associated and shear-hosted. Shear-hosted mineralization has the highest whole rock Ni, Co and Pd tenors across the 1D deposit, whereas the massive mineralization style contains some of the lowest and most variable whole rock Ni, Co and Pd tenors.

A primary goal of this thesis was to explain why the tenors are higher in the metasedimentary ores (Thompson) versus primary ultramafic hosted ores (Pipe and Birchtree). A positive correlation between pyrite modal abundance and the occurrence of high tenor nickel and cobalt ores across the 1D orebody was determined. Tenor seems to be related to the occurrence of pyrite. Pyrite is shown to be paragenetically late, formed at the retrograde stage, and is enriched in Co, Ni, ± As. A wide suite of post-magmatic sulfide textures provide evidence for a complex interplay of exsolution, phase dissolution, brittle/ductile deformation, recrystallization and remobilization that occurred in the 1D orebody. Additionally, this study provides evidence for a hydrothermal footprint of the ores and is the first to document the occurrence of polymetallic sulfide melt inclusions at Thompson, which signifies partial melting of sulfide ores occurred throughout the 1D orebody and potentially elsewhere in the TNB.

A primary igneous origin for sulfide liquid immiscibility and the production of voluminous amounts of nickel sulfide mineralization across the TNB is accepted.

However, a primary magmatic theory cannot explain key geological, petrographical and mineral chemical constraints of the metasedimentary-hosted Thompson deposits. Therefore, various ore genesis models are evaluated to better understand the tenor variability across the metasedimentary ores. Models including; *sulfide kinesis*, metamorphic oxidation, retrograde metamorphic fluids and localized partial melting, are discussed and comparisons are drawn between the Thompson 1D, and nickel-sulfide deposits from Kambalda, Sudbury and across the TNB. The data from this study agrees with a well-documented retrograde metamorphic fluid model for Thompson (Bleeker, 1990; Chen, 1993; Liwanag et al., 2001; Burnham et al., 2009; Layton-Matthews et al., 2007) and ensuing sulfidation of ores. The retrograde metamorphic fluid model is modified in this study to include localized partial melting that proposes the sulfide ores underwent partial melting at peak metamorphic P-T (late D_2), and shear-melting (D_3), while contemporaneous hydrothermal fluids were circulating. Numerous polymetallic sulfide melt inclusions hosted within metamorphic silicate assemblages, and possible partial melt textures, are the main streams of evidence for our localized partial melting model.

Although nickel tenor upgrading of ores is not entirely explained, it seems to be related to the late tectonic-metamorphic history of the deposit, linked to a late-stage high sulfur fugacity event, during which pyrite formed. A staged mechanism for the formation of the Thompson deposits is proposed in which; komatiitic emplacement and primary magmatic origin generated sulfide mineralization in the TNB; high P-T MSS reformation and repositioning of primary ultramafic sulfide, and partial melts, into sedimentary country rocks; and modification by hydrothermal fluids, contemporaneous localized partial melting, and shear melting, which further modified the remobilized ores.

9.2 Implications for Grade Recovery

Pyrrhotite is the dominant sulfide mineral in the TNB and in the 1D orebody it contains average concentrations of 0.48 wt% Ni and <100ppm Co. The implication of this is that the nickel contained in pyrrhotite is essentially unrecoverable and this is accounted for in geometallurgical evaluations of mineral zones.

Vale - Northern Manitoba Operations is currently recovering cobalt from pentlandite, the mean cobalt values of pentlandite in the 1D orebody are 0.34 wt% Co, which is comparable to pentlandite from nickel-sulfide deposits in Kambalda, yet significantly lower than cobalt values in pentlandite from Sudbury sulfide ores (~1.0 wt% Co). Additionally, cobalt-rich pentlandite flames are abundant in Thompson 1D pyrrhotite. Flame pentlandite is nickel- and cobalt-rich, with mean abundances of 34.5 wt% Ni and 0.3 wt% Co. Pentlandite flames are on average <75μm across but can be as large as 200μm if related to fractures. The milling of pentlandite-rich feed and recovery processes should continue to assess the abundance and size of pentlandite flames in pyrrhotite, for proper grinding optimization and recovery of nickel and cobalt concentrations in flames that likely report to tailings.

Pyrite is not currently being recovered at the Thompson deposits (T1 and T3) because it is considered a gangue mineral. The pyrite in the Thompson 1D is enriched in nickel and cobalt, with whole rock concentrations of 1.10 wt% Ni and 1.30 wt% Co.

Whereas pyrite is a minor sulfide mineral in the Thompson 1D orebody, with modal abundances between 5 and 10 %, this study showed that pyrite occurs in larger, massive lenses in areas throughout the Thompson deposit. There is substantial weight % levels of nickel and cobalt in pyrite, which currently report largely to tailings.

Mica geochemistry revealed elevated nickel (0.24 wt%) and chromium (0.48 wt%) contents in mica laths within sulfides. Nickel and chromium contents in P_2 schist mica stay elevated up to ~4 metres from a sulfide ore contact, providing a narrow anomalous zone and potential indicator to sulfide mineralization. However, nickel and chromium contents in mica are important to consider when calculating tenors of sulfides to avoid ensuing geometallurgical processing issues.

9.3 Implications for Ni-Cu-PGE Exploration

The success of TNB exploration programs has been recognizing the importance of komatiitic magmas intruding along sulfur-rich sedimentary rocks, as a key requirement for crustal sulfur saturation and generation of voluminous amounts of magmatic sulfides. Therefore, sulfidic sediments with mafic-ultramafic magmatism are of interest for exploration of nickel-sulfide deposits worldwide.

However, the focus of this study was on the 1D Lower zone within the 602 mine-complex at T3 mine. An intricate relationship between pyrite abundance and ore samples with elevated whole rock nickel and cobalt tenors across the 1D deposit has been identified. Similarly, the South End Development (SED) zone, currently being mined at Thompson **(Figure 9-1)**, has a notable increase in pyrite modal abundance and is associated with high tenor Ni+Co ores. Therefore, detailed investigation of pyrite-rich areas in the South End Development zone, and across other Thompson and TNB deposits, should be considered as pyrite abundance is proposed to be a vector towards high tenor mineralization. This key observation can be used to assess the proximity, and tenor ranking, of a fertile sulfide lens in drill-core.

The importance of shears in the 1D orebody has been documented in this study. Shears are associated with hydrothermal mobilization of elements and localized shear melting. Additionally, another key observation is that shear-hosted sulfides contain the highest nickel, cobalt and palladium tenors in the 1D.

Shears in the 1D commonly occur paralleling the steeply, double-plunging limbs of F_3 folds. Deposit-scale studies of the Thompson 1D orebody from Lightfoot et al. (2017) determined that the highest tenor sulfide mineralization occurs as stacked lenses in F_3 fold noses and on F_3 limbs. Thus, ore lenses along shear structures, remobilized further up- and down-dip on the limbs of the doubly-plunging F_3 folds along strike with the Thompson Dome structure, have the potential to host high tenor ores, especially where Pipe formations sediment packages are thickest. Mine and regional exploration programs should target areas of structural complexity, especially areas that are dominated by anastomosing shear and fault networks for exploration of fertile sulfide lenses.

Additionally, Lightfoot et al. (2012) proposed that the 1D North Deep deposit might ‘curve-up’ under the 1D and link up in the area to the south **(Figure 9-1)**. The F_3 fold trend in the 1D North Deep, and extension proposed by Lightfoot et al. (2012), can possibly resurface as a fold hinge underneath the 1B and 1C deposits, extending along strike towards the South End Development zone. This whole area is prospective, as future exploration efforts along strike of this extension, within possible resurfaced F_3 folds, can uncover potential 1B North and 1C North mineralized zones.

Platinum group elements (PGE) have been reported to occur in gersdorffite and niccolite grains. However, these are minor sulfide phases in the Thompson 1D orebody. Areas with elevated arsenic concentrations, especially shear controlled environments, should be targeted for Pd-bismuth telluride, sulfarsenide and arsenide phases with substantial amounts of Ni, Co, PGE, Rh, Ir, Sb and Te, as shown to be the case in the 1D orebody. Potential for PGE-Au complexes related to pegmatites and shears (Chen, 1993), may have also remobilized via late-fluids along anastomosing structural networks.

Evidence for polymetallic sulfide melt inclusions indicates that pre-existing sulfide bodies melted during peak metamorphic conditions (late D_2), and during shear melting (D_3), producing localized sulfide melt that was trapped in metamorphic silicate assemblages. From deposit-scale studies of the Thompson 1D, Lightfoot et al. (2017) noticed a homogeneity in tenor along sulfide veins, but a heterogeneity between different sulfide lenses. It is proposed that partial melts (late D_2) may have been squeezed during the high P-T relocation (D_1 – D_2), along with reformed monosulfide solid solution, into Pipe formation country rocks. This could have added to the tenor variability, along with post-ore modifying hydrothermal alteration along structural networks, observed between sulfide lenses. Recognizing that sulfide melting occurred, even if partially, has important implications for the genesis and modification of Ni-Cu-PGE deposits in the TNB.

Furthermore, during metamorphism and melting, precious metals may have been remobilized and concentrated into localized pockets of high-grade ore, called *dropper zones*, instead of becoming disseminated across the deposit (Lawrence, 1967; Sparks and Mavrogenes, 2005). These discrete, high-grade pockets of trace and precious metals may be locally remobilized and concentrated in massive sulfide deposits (Frost et al., 2002), or occur as high-grade off-shoots in country rocks, extending away from main ore bodies (Lawrence, 1967; Sparks and Mavrogenes, 2005). Additionally, Lawrence (1967) proposed sulfide dikes (known as *droppers*) formed as a product of 'sulfide neomagmas', where sulfide partial melts created during syn- to post-peak metamorphism behave like dikes that crosscut country-rocks. These *droppers* can have higher precious metal contents than the main lodes from which they originated form. Therefore, a proper understanding of the proposed staged mechanism model, and the coeval processes of partial melting and hydrothermal alteration, on the combined effect of remobilization of metal-bearing fluids and modification of ore lenses is required. Potential formation of these high-grade *dropper zones* is important to address for future exploration programs, as well as for the economic assessment of komatiitic nickel-sulfide deposits in the highly metamorphosed TNB.

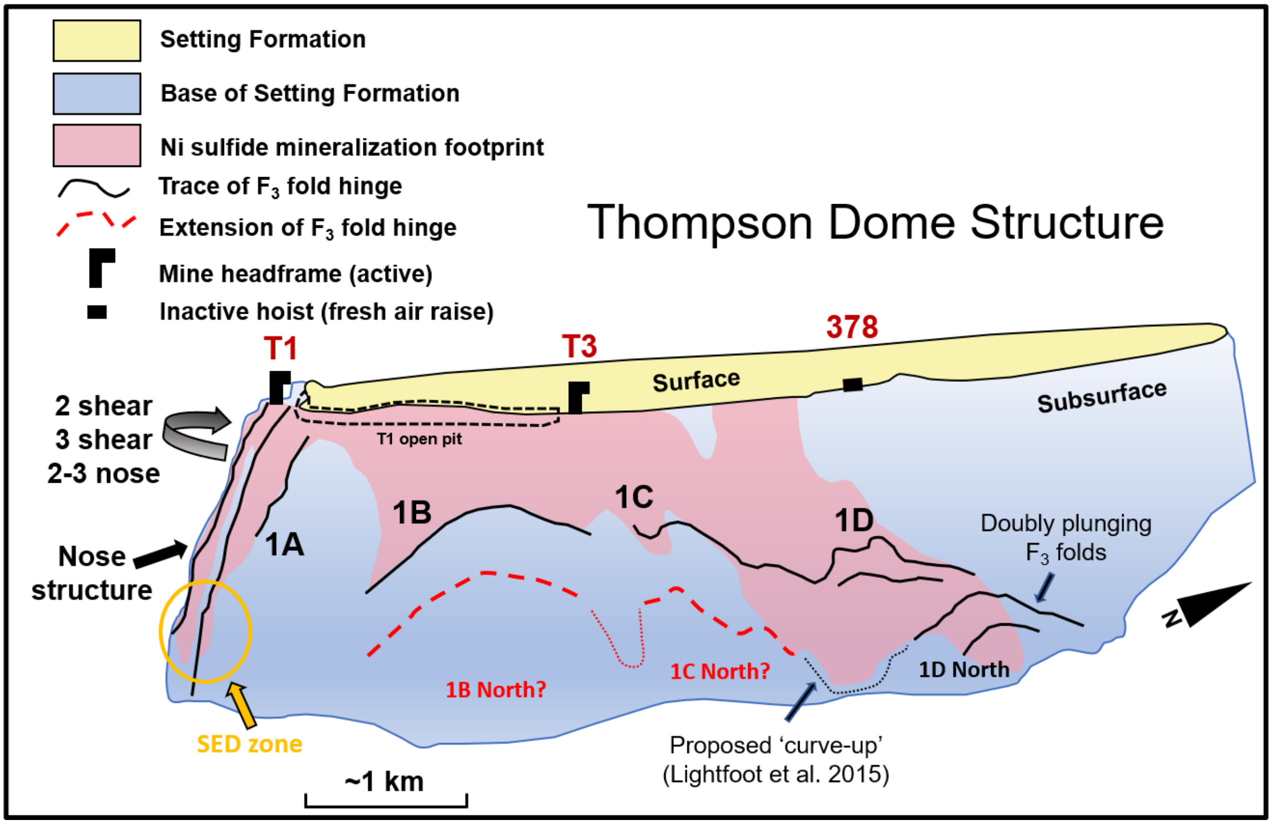

Figure 9-1: A 3D diagram showing the surface of the Setting Formation (yellow), base of the Setting Formation (blue) and the footprint of Ni sulfide mineralization (pink), in a 3D view of the Thompson Dome structure. F_3 fold hinges are depicted as 'bolded black lines'. At the 1D orebody, the location of doubly-plunging F_3 structures are shown – high tenor Ni sulfide mineralization aligns along the doubly-plunging F_3 folds. 'Red dashed lines' represent a possible extension and resurface of the F_3 fold hinge, along strike from the 1D, towards the SED zone on the Nose structure. Prospective exploration areas are highlighted by '1B North' and '1C North' locations, along the hinge and limbs of a possible extensional F_3 fold structure. (Modified from Lightfoot et al., 2012, 2017).

9.4 Future Work

Carbon, in the form of graphite, is abundant within the host, Pipe Formation schist units. Graphite is also abundant along shears and as laths entrained within sulfide ore and attached to polymetallic sulfide melt inclusions. Although carbon-rich sulfide systems, as opposed to carbon-free systems, have been shown to play an important role in depressing monosulfide solidus temperatures (Zhang et al., 2015), future experimental studies on the effects of graphite on the solidus temperature of sulfur-rich monosulfide systems needs to be investigated, as carbon can potentially act as a flux for partial melting of sulfides.

Pyrite has been shown to be an important component of high tenor sulfide ores within the Thompson 1D orebody. Additional geochemical investigations on understanding the complex paragenesis of pyrite are necessary to refine the estimations of the abundances of primary versus secondary (hydrothermal) pyrite and how exactly they relate to high tenor mineralization. Additionally, future geochemical work on the different pyrite textures is necessary, due to the variability and complex zoning patterns of nickel and cobalt found in pyrite.

Lastly, pegmatites were not the focus of this study, however, their propitious existence along shear zones that tend to border high tenor sulfide lenses in the 1D orebody has been documented. Brecciated nickel sulfide ore associated with pegmatites was observed to host the highest arsenic contents in the T1 open pit mine (Bleeker, 1990). Additionally, Chen (1993) reported evidence for mobilization of Pd-bismuthtelluride + Au sequences in pegmatites by reporting PGM + Au bearing arsenic-rich nickel sulfide mineralization within pegmatites at T1 mine. Therefore, work should be undertaken to understand the link between pegmatites and hydrothermal fluid alteration, and the role of pegmatites as a potential source of leaching and remobilization of metals across Thompson 1D ores.

References

Abramoff, M.D., Magelhaes, P.J., Ram, S.J., 2004. Image Processing with ImageJ. Biophotonics Int. 11(7), 36-42.

Ansdell, K.M., 2005. Tectonic evolution of the Manitoba-Saskatchewan segment of the Palaeoproterozoic Trans-Hudson Orogen, Canada. Can. Jour. Earth Sci. 42, 741–759.

Bailey, J., McDonald, A.M., Lafrance, B., 2006. Variations in Ni Content in Sheared Magmatic Sulfide Ore at the Thayer Lindsley Mine, Sudbury, Ontario. Can. Min. 44, 1063-1077.

Bailie, R., Reid, D.L., 2005. Ore textures and possible sulphide partial melting at Broken Hill, Aggeneys, South Africa I: Petrography. South African Jour. Geol. 108, 51-70.

Barnes, S.J., Lightfoot, P.C., 2005. Formation of magmatic nickel-sulfide ore deposits and processes affecting their copper and platinum-group element contents. In Hedenquist, J.W., Thompson, J.F.H., Goldfarb, R.J. and Richards, J.P. (eds.) Econ. Geol. 100th Anniversary Volume, p. 179-213.

Barnes, S.-J., Acterberg, E., Makovicky, E., and Li, C., 2001. Proton probe results for partitioning of platinum group elements between monosulphide solid solution and sulphide liquid: South African Jour. Geol. 104, 337–351.

Barnes, S.J., Makovicky, E., Makovicky, M., Rose-Hansen, J., Karup-Moller, S., 1997. Partition coefficients for Ni, Cu, Pd, Pt, Rh, and Ir between monosulphide solid solution and sulphide liquid and the formation of compositionally zoned Ni-Cu sulphide bodies by fractional crystallization of sulphide liquid: Can. Jour. Earth Sci. 34, 366–374.

Barnes, S.J., Staude, S., Le Vaillant, M., Pina, R., Lightfoot, P.C., 2018. Sulfide-silicate textures in magmatic Ni-Cu-PGE sulfide ore deposits: Massive, semi-massive and sulfide-matrix breccia ores. Ore. Geol. Rev. 101, 629-651.

Barrett, F.M., Binns, R.A., Groves, D.I., Martson, R.J., McQueen, K.G., 1977. Structural History and Metamorphic Modification of Archean Volcanic-Type Nickel Deposits, Yilgarn Block, Western Australia. Econ. Geol. 72, 1195-1223.

Barton, P.B., 1973. Solid solutions in the system Cu-Fe-S. Part I: The Cu-S and CuFe-S joins. Econ. Geol. 68, 455-465.

Bleeker, W., 1990. Evolution of the Thompson Nickel Belt and its Nickel Deposits, Manitoba, Canada. Unpublished Ph.D. thesis, Fredericton, New Brunswick, Department of Earth Sciences, University of New Brunswick.

Bleeker, W., Hamilton, M.A., 2001. New SHRIMP U-Pb ages for the Ospwagan Group: implications for the SE margin of the Trans-Hudson Orogen. Geol. Assoc. Can. Min. Assoc Can., Program Abstr. 26, p. 15.

Bleeker, W., Macek, J., 1996. Evolution of the Thompson nickel belt, Manitoba: setting of Ni-Cu deposits in the western part of the Circum-Superior boundary zone, (Field Trip Guidebook A-1), Geol. Assoc. Can. Min. Assoc. Can. Joint Ann. Meeting, 1996, 44.

Brett, R., Kullerud, G., 1967. The Fe–Pb–S system. Econ. Geol. 62, 354-369.

Burnham, O.M., Halden, N., Layton-Matthews, D., Lesher, C.M., Liwanag, J., Heaman, L., Hulbert, L., Machado, N., Michalak, D., Pacey, M., Peck, D., Potrel, A., Theyer, P., Toope, K., and Zwanzig, H., 2009. CAMIRO Project 97E–02, Thompson Nickel Belt: final report March 2002, revised and updated 2003. Manitoba Geol. Surv., Open file OF2008-11.

Cafagna, F., Jugo, P.J., 2016. An experimental study on the geochemical behavior of highly siderophile elements (HSE) and metalloids (As, Se, Sb, Te, Bi) in a mss-iss-pyrite system at 650˚C: A possible magmatic origin for Co-HSE-bearing pyrite and the role of metalloid-rich phases in the fractionation of HSE. Geochimica et Cosmochimica Acta. 178, 233-258.

Campbell, I.H., Naldrett, A.J., 1979. The influence of silicate: sulfide ratios on the geochemistry of magmatic sulfides. Econ. Geol. 74, 1503–1505.

Canil, D., 1999. The Ni-in-garnet geothermometer: calibration at natural abundances. Contrib. Min. Petrol. 136, 240-246.

Chen, Y., 1993. Precious-metal Mineralization and Sulfide-silicate Relationships In Some Canadian Nickel-copper Sulfide Deposits: Thompson Mine, Manitoba; Sudbury, Ontario; Dundonald Beach, Ontario. Unpublished Ph.D. thesis, London, Ontario, Department of Earth Sciences, University of Western Ontario.

Chyi, L.L., and Crocket, J.H., 1976. Partition of platinum, palladium, iridium, and gold among coexisting minerals from the deep ore zone, Strathcona Mine, Sudbury, Ontario. Econ. Geol. 71, 1196–1205.

Clark, B.R., Kelly, W.C., 1973. Sulfide Deformation Studies: I. Deformation of Pyrrhotite and Sphalerite to 2,000 Bars and 500˚C. Econ. Geol. 68, 332-352.

Collins, Z.J.E., Barnes, S.J., Hagemann, S.G., Campbell, T., McCuag, T.C., Frost, K.M., 2012. Postmagmatic variability in ore composition and mineralogy in the T4 and T5 ore shoots at the high-grade Flying Fox Ni-Cu-PGE Deposit, Yilgarn Craton, Western Australia. Econ Geol. 107, 859–879.

Corrigan, D., Hajnal, N., Ne'Meth, B., Lucas, S.B., 2005. Tectonic framework of a Palaeoproterozoic arc-continent to continent-continent collisional zone, Trans-Hudson Orogen, from geological and seismic reflection studies. Can. Jour. Earth Sci. 42, 421–434.

Couëslan, C.G., Pattison, D.R.M., Dufrane, S.A., 2013. Paleoproterozoic metamorphic and deformation history of the Thompson Nickel Belt, Superior Boundary Zone, Canada, from in situ U–Pb analysis of monazite. Precambr. Res. 237, 13–35.

Craig, J.R., 1973. Pyrite-Pentlandite Assemblages and Other Low Temperature Relations in the Fe-Ni-S System. American Jour. Earth Sci., Cooper. 273A, 496-510.

Craig, J. R., and Kullerud, G., 1969. Phase relations in the Cu-Fe-Ni-S system and their application to magmatic ore deposits: Econ. Geol. Mon. 4, p. 344-358.

Craig, J.R., Solberg, T.N., 1999. Compositional Zoning in Ore Minerals at the Craig Mine, Sudbury, Ontario, Canada. Can. Min. 37, 1163-1176.

Craig, J.R., Vokes, F.M., 1993. The metamorphism of pyrite and pyritic ores: an overview. Min. Mag. 57, 3-18.

Craig, J.R., Vokes, F.M., Solberg, T.N., 1998. Pyrite: physical and chemical textures. Min. Deposita. 34, 82-101.

Dare, S.A.S., Barnes, S.-J., Prichard, H.M., 2010. The distribution of platinum group elements (PGE) and other chalcophile elements among sulfides from the Creighton Ni-Cu-PGE sulfide deposit, Sudbury, Canada, and the origin of palladium in pentlandite. Miner Dep. 45, 765-793.

Donaldson, M.J., Bromley, G.J., 1981. The Honeymoon Well nickel sulphide deposit, Western Australia. Econ. Geol. 76, 1550 - 1564.

Duke, J.M., 1986. Petrology and economic geology of the Dumont Sill: An Archean intrusion of komatiitic affinity in northwestern Quebec. Geological Survey of Canada. 35, 1-56.

Duran, C.J., Barnes, S.-J., Corkery, J.T., 2015. Chalcophile and platinum-group element distribution in pyrites from the sulfide-rich pods of the Lac des Iles Pd deposits, Western Ontario, Canada: Implications for post-cumulus re-equilibration of the ore and the use of pyrite compositions in exploration. Jour. Geochem. Exp. 20.

Duran, C.J., Barnes, S.J., Corkery, J.T., 2016. Geology, petrography, and genesis of sulfide-rich pods in the Lac des Iles palladium deposits, western Ontario, Canada. Min. Deposita. 51, 509-532.

Durazzo, A., Taylor, L.R., 1982. Exsolution in the mss-pentlandite system: Textural and genetic implications for Ni-sulfide ores. Miner. Deposita. 17, 313-332.

Dutrizac. J.E., 1976. Reactions in cubanite and chalcopyrite. Can. Mineral. 14, 172-181.

Ebel, D.S., and Naldrett A.J., 1997. Crystallization of sulfide liquids and the interpretation of ore composition. Can. Jour. Earth Sci. 34, 352–365.

Elphick, S.C., 1972. Geology of the Mynarski-Notigi lakes area; Manitoba Department of Mines, Resources and Environmental Management, Mines Branch, Publication 71-2C, 48 p., 2 maps, scale 1:50 000.

Farrell, S.P., Fleet, M.E., 2002. Phase separation in (Fe, Co) (sub1 − x) S monosulfide solid-solution below 450 degrees C, with consequences for coexisting pyrrhotite and pentlandite in magmatic sulfide deposits. Can. Min. 40, 33–46.

Franchuk, A., Lightfoot, P.C., Kontak, D., 2016. High tenor Ni–PGE sulfide mineralization in the South Manasan ultramafic intrusion, Paleoproterozoic Thompson Nickel Belt, Manitoba, Canada. Ore Geol. Rev. 72, 434–458.

Fraser, H.S., 1985. A Journey North: The Great Thompson Nickel Discovery: Inco Ltd., p. 388.

Friedrich, K., 1907. Die Schmelzdiagramme der binären systeme schwefelsilber-kupfersulfür und bleiglanz- kupfersulfür. Metallurgie. 4, 671–673.

Frost, B.R., Mavrogenes, J.A., Tomkins, A.G., 2002. Partial Melting of Sulphide Ore Deposits During Medium-And High-Grade Metamorphism. Can. Min. 40, 1-18.

Gilligan, L.B., Marshall, B., 1987. Textural evidence for remobilization in metamorphic environments. Ore Geol. Rev. 2, 205–229.

Golder Associates Limited, 2010. Vale Limited, External Audit of Mineral Reserves, Vol. 2, Sec. 2, Report No. 10-1117-0032, Phase 2000. Manitoba Operations. Presentation.

Gribbin, G., 2011. Geology and Mine Exploration: An Overview of the Ni Sulfide Deposits of the Vale Thompson Manitoba Operations. Canadian Institute Mining Metallurgy, Toronto. Abstract.

Hawley, J.E., 1962. The Sudbury ores: their mineralogy and origin. University of Toronto Press. Canadian Min. 7, 1 - 206.

Heaman, L.M., Machado, N., Krogh, T.E., Weber, W., 1986. Precise U-Pb zircon ages for the Molson dyke swarm and the Fox River sill: Constrains for early Proterozoic crustal evolution in northeastern Manitoba, Canada. Contrib. Mineral. Petrol. 94, 82–89.

Heaman, L.M., Peck, D., Troope, K., 2009. Timing and geochemistry of 1.88 Ga Molson Igneous Events, Manitoba: insights into the formation of a craton-scale magmatic and metallogenic province. Precamb. Res. 172, 143–162.

Heath, C., Lahaye, Y., Stone, W.E., Lambert, D.D., 2001. Origin of variations in nickel tenor along the strike of the Edwards lode nickel sulfide orebody, Kambalda, Western Australia. Can. Mineral. 39, 655–671.

Hirth, G., Tullis, J., 1992. Dislocation creep regimes in quartz aggregates. Jour. Struct. Geol. 14 (2), 145–159.

Hoatson, D.M., Jaireth, S., Jaques, A.L., 2006. Nickel sulfide deposits in Australia: characteristics, resources, and potential. Ore Geol. Rev. 29, 177–241.

Hofmann, B.A, 1994. Formation of a sulfide melt during Alpine metamorphism of the Lengenbach polymetallic sulfide mineralization, Bintal, Switzerland. Miner. Depos. 29, 439–442.

Hofmann, B.A., Knill, M.D., 1996. Geochemistry and genesis of the Lengenbach Pb-Zn-As-Tl-Ba-mineralization, Binn Valley, Switzerland. Miner. Depos. 31, 319–339.

House, G.L., 2009. PGE distribution in the Thompson Nickel Belt, Manitoba, Canada. M.Sc. thesis, Department of Earth Sciences, Laurentian University, Sudbury, ON.

Hubregtse, J.J.M.W., 1980. The Archean Pikwitonei granulite domain and its position at the margin of the northwestern Superior Province, central Manitoba: Manitoba Mines Branch, Geol. Paper 80–3, p. 16.

Hulbert, L.J., Hamilton, M.A., Horan, M.F., Scoates, R.F.J., 2005. U–Pb zircon and Re-Os isotope geochronology of mineralized ultramafic intrusions and associated nickel ores from the Thompson Nickel belt, Manitoba, Canada. Econ. Geol. 100, 29–41.

Huminicki, M.A.E., Sylvester, P.J., Cabri, L.J., Lesher, C.M., Tubrett, M., 2005. Quantitative mass balance of platinum-group elements in the Kelly Lake Ni–Cu–PGE deposit, Copper Cliff Offset, Sudbury. Econ. Geol. 100, 1631–1646.

Keays, R.R., Ross, J.R., Woolrich, P., 1981. Precious metals in volcanic peridotite-associated nickel sulfide deposits in western Australia. II: distribution within the ores and host rocks at Kambalda. Econ. Geol. 76, 1645-1674.

Kelly, D.P., Vaughan, D.J., 1983. Pyrrhotite-pentlandite ore textures: a mechanical approach. Min. Mag. 47, 453-463.

Kerr, A., 2003. Guidelines for the Calculation and use of Sulphide Metal Contents in Research and Mineral Exploration. Newfoundland Department of Mines and Energy Geological Survey, Report 03-1. 223-229.

Kullerud, G., 1963. Thermal stability of pentlandite. Can. Mineral. 7, 353–366.

Kullerud, G., Yund, R. A., and Moh, G., 1969, Phase relations in the Fe-Ni-S, Cu-Fe-S and Cu-Ni-S systems: Econ. Geol. Mon. 4, p. 323-343.

Lawrence L.J., 1967. Sulphide neomagmas and highly meta-morphosed sulphide deposits. Min. Dep. 2, 5-10.

Lawrence, L.J., 1972. The Thermal Metamorphism of Pyritic Sulfide Ore. Econ. Geol. 67, 487-496.

Layton-Matthews, D., Lesher, C.M., Burnham, O.M., Liwiang, J., Halden, N., Hulbert, L., Peck, D., 2007. Magmatic Ni–Cu deposits of the Thompson Nickel Belt. In: Goodfellow, W.D. (ed.), Mineral Resources of Canada: A Synthesis of Major Deposit-types, District Metallogeny, the Evolution of Geological Provinces, and Exploration Methods, Geological Survey of Canada and Mineral Deposits Division of the Geological Association of Canada Special Publication, pp. 409–432.

Lesher, C.M., Burnham, O.M., 2001. Multicomponent Elemental and Isotopic Mixing in Ni-Cu-(PGE) ores at Kambalda, Western Australia. Can. Min. 39 (2), p. 421-446.

Lesher, C.M., Campbell, I.H., 1993. Geochemical and fluid dynamic modeling of compositional variations in Archean komatiite-hosted nickel sulfide ores in Western Australia. Econ. Geol., 88: 804–816.

Lesher, C.M., Keays, R.R., 2002. Komatiite-associated Ni-Cu-(PGE) deposits; Mineralogy, geochemistry, and genesis. In Cabri, L.J., (ed.), The Geology, Geochemistry, Mineralogy, and Mineral Beneficiation of the Platinum-Group Elements: Canadian Institute of Mining, Metallurgy and Petroleum, Special Volume 54, pp. 579–617.

Lesher, C.M., Burnham, O.M., Keays, R.R., Barnes, S.J., and Hulbert, L., 2001. Geochemical discrimination of barren and mineralized komatiites associated with magmatic Ni-Cu-(PGE) sulphide deposits, Can. Min., vol. 39, p. 673-696.

Li, C., Barnes, S.-J., Makovicky, E., Rose-Hansen, J., Makovicky, M., 1996. Partitioning of nickel, copper, iridium, platinum and palladium between monosulfide solid solution and sulfide liquid: Effects of composition and temperature. Geochimica et Cosmochimica Acta. 60, 1231-1238.

Lightfoot, P.C., 2016. Nickel Sulfide Ores and Impact Melts: Origin of the Sudbury Igneous Complex. Elsevier, Amsterdam, p. 71.

Lightfoot, P.C., Evans-Lamswood, D., 2015. Structural controls on the primary distribution of mafic-ultramafic intrusions containing Ni-Cu-Co-(PGE) mineralization in the roots of large igneous provinces. Ore Geol. Rev. 64, 354–386.

Lightfoot, P.C., Stewart, R., Gribbin, G., Mooney, S.J., 2012. A Geological Model for the Thompson Ni-Co Sulfide Ore Deposits, Manitoba, Canada. Short Course. Manitoba Mining, Winnipeg. http://www.gov.mb.ca/iem/convention/previous/2015.html#shortcourse.

Lightfoot, P.C., Stewart, R., Gribbin, G., and Mooney, S.J., 2017. Relative contribution of magmatic and post-magmatic processes in the genesis of the Thompson Mine Ni-Co sulphide ores, Manitoba, Canada. Ore Geol. Rev., 83: 258-286.

Liwanag, J., 2001. Post-Magmatic Modification of the Sulphide Deposits from the Thompson Nickel Belt, Manitoba, Canada. M.Sc. thesis, Winnipeg, Manitoba, Department of Geological Sciences, University of Manitoba.

Lorand, J.-P., Alard, O., 2010. Pyrite tracks assimilation of crustal sulfur in Pyrenean peridotites. Miner. Petrol. 101, 115-128.

Lucas, S.B., Stern, R.A., Syme, E.C., Reilly, B.A., and Thomas, D.J., 1996. Intraoceanic tectonics and the development of continental crust: 1.92–1.84 Ga evolution of the Flin Flon Belt, Canada. Geological Society of America Bulletin. 108, 602–629.

Lusk, J., Bray, D., 2002. Phase relations and the electrochemical determination of sulfur fugacity for selected reactions in the Cu– Fe–S and Fe–S systems at 1 bar and temperatures between 185 and 460°C. Chem. Geol. 192, 227–248.

Lusk, J., Ostwald, J., 1983. Analysis of pyrrhotite properties accompanying recrystallization of metamorphosed nickel sulfide ore from Kambalda, Western Australia. Can. Jour. Earth Sci. 20, 113-119.

Macek, J.J, McGregor, C.R., Zwanzig, H.V., 2004. Thompson Nickel Belt Project, Manitoba (part of NTS 63P): geology of the South pit, Thompson mine; in Report of Activities 2004, Manitoba Industry, Economic Development and Mines, Manitoba Geological Survey, pp. 135–148.

Macek, J.J., Zwanzig, H.V., Pacey, M., 2006. Thompson Nickel Belt geological, Manitoba compilation map (parts of NTS 63G, J, O, P and 64A and B): Manitoba Science, Technology, Energy and Mines, Geological survey, Open File Report 2006–33, 1 CD-ROM.

Machado, N., Krogh, T.E., and Weber, W., 1990. U–Pb geochronology of basement gneisses in the Thompson Belt (Manitoba): evidence for pre-Kenoran and Pikwitonei-type crust and Early Proterozoic basement reactivation in the western margin of the Archean Superior Province. Can. J. Earth Sci. 27: 794–802.

Machado, N., Gapais, D., Potrel, A., Gauthier, G., and Hallot, E., 2010. Chronology of transpression, magmatism and sedimentation in the Thompson Nickel Belt (Manitoba, Canada) and timing of Trans-Hudson Orogen – Superior Province collision. Can. Jour. Earth Sci. 48, 295-324.

Machado, N., Heaman, L.M., Krogh, T.E., and Weber, W., 1987. U–Pb geochronology program: Thompson belt and Northern Superior Province. In Report of Field Activities 1987, Manitoba Energy and Mines, pp. 145–147.

Machado, N., Heaman, L.M., Krogh, T.E., Weber, W., Corkery, M.T., 2011. Timing of Paleoproterozoic granitoid magmatism along the northwestern Superior Province margin: implications for the tectonic evolution of the Thompson Nickel Belt. Can. F. Earth Sci. 48: 325-346.

Martyn, J.E., Johnson, G.I., 1986. Corrigendum: Geological setting and origin of fuchsite-bearing rocks near Menzies, Western Australia. Aus. Jour. Earth Sci. 33 (3), 373-390.

Mavrogenes, J.A., MacIntosh, I.W., Ellis, D.J., 2001. Partial Melting of the Broken Hill Galena-Sphalerite Ore: Experimental Studies in the System PbS-FeS-ZnS-(Ag_2S). Econ. Geol. 96, 205-210.

McDonald, J.A., Paterson, M.S., 1980. Experimental deformation of nickel sulfide ores and their host rocks, Lunnon Shoot, Kambalda, Western Australia. Unpubl. Rep., Australian Natl. Univ., Canberra, A.C.T. 46.

McQueen, K.G., 1979. Experimental heating and diffusion effects in Fe-Ni sulfide ore from Redross, Western Australia: Econ. Geol., 74, 140-148.

McQueen, K.G., 1981. Volcanic-associated Nickel Deposits from around the Widgiemooltha Dome, Western Australia. Econ. Geol. 76, 1417-1443.

McQueen, K.G., 1987. Deformation and remobilization in some western Australian nickel ores. Ore Geol. Rev. 2, 269–286.

McRitchie, W.D., 1995. Mineral Development Potential in Manitoba – Nickel in

Southwest Extension of the Thompson Nickel Belt. Manitoba Energy and Mines, Geological Services: Econ. Geol. Rep. ER95-2.

Misra, K.C., Fleet, M.F., 1973. The chemical compositions of synthetic and natural pentlandite assemblages. Econ. Geol. 68 (4), 518-539.

Monteiro, R., Krstic, S., 2006. Ore Shape: Solid-state Deformation and Translocation of Massive Sulphides. Inco Exploration: Structural Economic Geology Newsletter 2(4).

Mudd, G.M., 2010. Global trends and environmental issues in nickel mining: sulfides versus laterites. Ore Geol. Rev. 38, 9–26.

Munoz, J.L., 1984. F–OH and Cl–OH exchange in micas with applications to hydrothermal ore deposits. In: Bailey, S.W. (Ed.), Micas. Reviews in Mineralogy, Vol.13. Min. Soc. Amer., Washington, DC. 469–493.

Naldrett, A. J., 1999. World class Ni-Cu-PGE deposits: key factors in their genesis. Min. Deposita. 34, 227-240.

Naldrett, A.J., 2004. Magmatic Sulfide Deposits; Geology, Geochemistry and Exploration. Springer, 725.

Naldrett, A.J., Craig, J.R., Kullerud, G., 1967. The central portion of the Fe-Ni-S system and its bearing on pentlandite exsolution in iron-nickel sulfide ores. Econ. Geol. 62, 826-847.

Naldrett, A.J., Asif, M., Krstic, S., Li, C., 2000. The Composition of Mineralization at the Voisey's Bay Ni-Cu Sulfide Deposit, with Special Reference to Platinum-Group Elements. Econ. Geol. 95, 845-865.

Neyedley, K., Hanley, J.J., Hendrik, F., Bodnar, R.J., Fedele, L., Fayek, M., Sharpe, R., 2019. Sulfide melt inclusions associated with magmatic Ni-Cu-platinum-group element (PGE) mineralization in the Caribou Lake Gabbro, Blatchford Lake intrusive suite, Northwest Territories, Canada. Ore Geol. Rev. 107, 513-531.

Ortega, L., Lunar, R., Garcia-Palomero, F., Moreno, Teresa, Martin-Estevez, J.R., Prichard, H.M., Fisher, P.C., 2004. The Aguablanca Ni-Cu-PGE Deposit, Southwestern Iberia: Magmatic Ore-Forming Processes and Retrograde Evolution. Can. Min. 42, 325-350.

Percival, J.A., Whalen, J.B., and Rayner, N., 2004. Pikwitonei – Snow Lake Manitoba

Transect (parts of NTS 63J, 63O, and 63P), Trans-Hudson Orogen – Superior Margin Metallotect Project: new results and tectonic interpretation. In Report of Activities 2004, Manitoba Industry, Economic Development and Mines, Manitoba Geological Survey, 120-134.

Peredery, W.V., Geological Staff., 1982. Geology and nickel sulfide deposits of the Thompson Belt, Manitoba. In: Precambrian sulfide deposits, H.S. Robinson memorial volume R.W. Hutchinson, C. D. Spence, J.M. Franklin (Eds.), Geological association of Canada, Special Paper. 25, 165–209.

Piña, R., Gervilla, F., Barnes, S.-J., Oberthür, T., Lunar, R., 2016. Platinum-group element concentrations in pyrite from the Main Sulfide Zone of the Great Dyke of Zimbabwe. Miner Deposita. 51, 853-872.

Piña, R., Gervilla, F., Barnes, S.-J., Ortega, L., Lunar, R., 2013. Platinum-group elements bearing pyrite from the Aguablanca Ni-Cu sulfide deposit (SW Spain): a LA-ICP-MS study. Eur. Jour. Min. 25, 241–252.

Porter, D.J., McKay, K.G., 1981. The nickel sulphide mineralization and metamorphic setting of the Forrestania area, Western Australia. Econ. Geol. 76, 1524-1549.

Reed, S.J.B., 2005. Electron microprobe analysis and scanning electron microscopy in geology. Cambridge University Press, New York, 189 pp.

Roedder, E., 1984. Fluid inclusions. Mineralogical Society of America. Rev. Min. 12, 644.

Ross, C.R., Keppler, H., Canil, D., O'Neil, H.St.C., 1996. Structure and crystal-field spectra of $Co_3Al_2(SiO_4)_3$ and $(Mg, Ni)_3Al_2(SiO_4)_3$ garnet. Amer. Min. 81, 61-66.

Scoates, R.F.J., Macek, J.J., Russell, J.K., 1977. Thompson Nickel Belt project; in Report of Field Activities 1977, Manitoba Department of Mines, Resources and Environmental Management; Mineral Resources Division, pp. 47–54.

Seat, Z., Stone, W.E., Mapleson, D.B., Daddow, B.C., 2004. Tenor variation within komatiite-associated nickel sulphide deposits: insights from the Wannaway Deposit, Widgiemooltha Dome, Western Australia. Min. Pet. 82, 317-339.

Seccombe, P.K., Groves, D.I., Marston, R.J., Barrett, F.M., 1981. Sulfide paragenesis and sulfur mobility in Fe-Ni-Cu sulfide ores at Lunnon and Juan main shoots, Kambalda: textural and sulfur isotopic evidence. Econ. Geol. 76, 1675 - 1685.

Sinyakova, E., Kosyakov, V., 2009. Experimental modeling of zonality of copper-rich sulfide ores in copper-nickel deposits. Dokl Earth Sci. 427, 787-792.

Sparks, H.A., Mavrogenes, J.A., 2004. Evidence in Support of Sulfide Partial Melting at Broekn Hill Australia and Broken Hill, South Africa. AGU Spring Meeting Abstracts.

Sparks, H.A., Mavrogenes, J.A., 2005. Sulfide Melt Inclusion as Evidence for the Existence of a Sulfide Partial Melt at Broken Hill, Australia. Econ. Geol. 100, 773-779.

Stevens, B.P.J., Barnes, R.G., Brown, R.E., Stroud, W.J., and Willis, I.L., 1988. The Willyama Supergroup in the Broken Hill and Euriowie blocks, New South Wales. Prec. Res. 40-41, 297-327.

Stipp, M., Stünitz, H., Heilbronner, R., Schmid, S.M., 2002a. Dynamic recrystallization of quartz; correlation between natural and experimental conditions. Geol. Soc. Spec. Publ. 200, 171–190.

Stipp, M., Stünitz, H., Heilbronner, R., Schmid, S.M., 2002b. The eastern Tonale fault zone; a ‘natural laboratory’ for crystal plastic deformation of quartz over a temperature range from 250 to 700 ˚C. Jour. Struct. Geol. 24 (12), 1861–1884.

Stone, W.E., Heydari, M., Seat, Z., 2004. Nickel tenor variations between Archaean komatiite-associated nickel sulfide deposits, Kambalda ore field, Western Australia: the metamorphic modification model revisited. Min. Petrol. 82, 295–316.

Sugaki, A., Kitakaze, A., 1998. High form of pentlandite and its thermal stability. Am. Mineral. 83, 133–140.

Tomkins, A.G., and Mavrogenes, J.A., 2002. Mobilization of gold as a polymetallic melt during pelite anatexis at the Challenger deposit, South Australia: A metamorphosed Archean gold deposit. Econ. Geol. 97, 1249–1271.

Tomkins, A.G., Frost, B.R., Pattison, D.R.M., 2006. Arsenopyrite Melting During Metamorphism of Sulphide Ore Deposits. Can. Min. 44, 1045-1062.

Tomkins, A. G., Pattison, D. R. M., & Frost, B. R., 2007. On the initiation of metamorphic sulphide anatexis. Jour. Pet. 48 (3), 511-535.

Tomkins, A. G., Pattison, D.R.M., Zaleski, E., 2004. The Hemlo gold deposit, Ontario:

an example of melting and mobilization of a precious metal-sulfosalt assemblage during amphibolite facies metamorphism and deformation. Econ. Geol. 99, 1063-1084.

Vaughan, D. J., Schwarz, E. J., Owens, D., 1971. Pyrrhotite from Strathcona mine, Sudbury, Canada; a thermal magnetic mineralogical study. Econ. Geol. 66, 1131-1144.

Vukmanovic, Z., Reddy, S.M., Godel, B., Barnes, S.J., Fiorentini, M.L., Barnes, S.-J., Kilburn, M.R., 2014. Relationship between microstructures and grain-scale trace element distribution in komatiite-hosted magmatic sulphide ores. Lithos 184-187, 42-61.

Waldner, P., Sitte, W., 2008. Thermodynamic modeling of Fe-Ni pentlandite. Jour. Phys. Chem. Sol. 69, 923-927.

Yund, R.A., Hall, H.T., 1970. Kinetics and Mechanism of Pyrite Exsolution from Pyrrhotite. Jour. Petrol. 11 (2), 381-404.

Zeh, A., 2006. Calculation of Garnet Fractionation in Metamorphic Rocks, with Application to a Flat-Top, Y-rich Garnet Population from the Ruhla Crystalline Complex, Central Germany. Jour. Pet. 47 (12), 2335-2356.

Zhang, Z., Lentsch, N., Hirschmann, M.M., 2015. Carbon-saturated monosulfide melting in the shallow mantle: solubility and effect on solidus. Contrib. Min. Petrol. 170 (47).

Zwanzig, H.W., 2005. Geochemistry, Sm–Nd isotope data and age constrains of the Bah Lake assemblage, Thompson Nickel belt and Kisseynew Domain margin: relation to Thompson-type ultramafic bodies and a tectonic model (NTS 63J, O and P); in Report of activities 2005, Manitoba Industry, Economic Development and Mines, Manitoba Geological Survey, pp. 40–53.

Zwanzig, H.V., Böhm, C.O., 2002. Tectonostratigraphy, Sm–Nd isotope and U–Pb age Data of the Thompson Nickel Belt and Kisseynew north and east margins (NTS 63J, 63P, 63Q, 64A, 64B), Manitoba; in Report of Activities 2002, Manitoba Industry, Trade and Mines, Manitoba Geological Survey, pp. 102–114.

Zwanzig, H.V., Böhm, C.O., Potrel, A., and Machado, N. 2003. Field relations, U–Pb zircon ages and Nd model ages of granitoid intrusions along the Thompson Nickel Belt – Kisseynew Domain boundary, Setting Lake area, Manitoba (NTS 63J15 and 63O2). In Report of Activities 2003, Manitoba Industry, Economic Development and Mines, pp. 1

Curriculum Vitae

Name: Povilas G. Grigutis

Post-secondary education and degrees:

M.Sc. Geology (2017 – present)
B.Sc. Geology (2011 – 2017)
Western University (London, Ontario, Canada)

Related Work Experience:

Geologist
True Point Exploration
2020 – present

Production Geology Intern
Newmont-Goldcorp (RLGM)
May – Sept 2018

Graduate Teaching Assistant
Western University
2017 – 2019

Production/Exploration Geology Intern
Vale (Manitoba Operations)
May – Sept 2017

Geological Assistant - Exploration
De Beers Canada Inc.
June – Sept 2016; June – Sept 2015

Research Assistant
Western University – Dr.Micha Pazner
Sept 2014 – April 2016

Publications:

Grigutis, G.P., Linnen, R., Lightfoot, P.C. 2019. The Importance of pyrite to Ni tenor in the metasedimentary-hosted 1D orebody at the Thompson (T3) mine, Northern Manitoba, Canada. PDAC 2019. (Poster)

Grigutis, G.P., Linnen, R., Lightfoot, P.C. 2019. Controls on Ni tenor in the 1D orebody at Vale's Thompson mine (T3), Northern Manitoba, Canada. AME RoundUp 2020. (Poster)